

**ORGANOMETALLIC COMPLEXES THAT MODEL  
THE ACTIVE SITES OF  
THE [FeFe]- AND [Fe]-HYDROGENASES**

A Dissertation

by

TIANBIAO LIU

Submitted to the Office of Graduate Studies of  
Texas A&M University  
in partial fulfillment of the requirements for the degree of

DOCTOR OF PHILOSOPHY

December 2009

Major Subject: Chemistry

**ORGANOMETALLIC COMPLEXES THAT MODEL  
THE ACTIVE SITES OF  
THE [FeFe]- AND [Fe]-HYDROGENASES**

A Dissertation

by

TIANBIAO LIU

Submitted to the Office of Graduate Studies of  
Texas A&M University  
in partial fulfillment of the requirements for the degree of

DOCTOR OF PHILOSOPHY

Approved by:

Chair of Committee,	Marcetta Y. Darensbourg
Committee Members,	Michael B. Hall
	Manuel P. Soriaga
	David P. Barondeau
	Perla B. Balbuena
Head of Department,	David H. Russell

December 2009

Major Subject: Chemistry

## ABSTRACT

Organometallic Complexes That Model the Active Sites of  
the [FeFe]- and [Fe]-Hydrogenases. (December 2009)

Tianbiao Liu, B.S., Hubei University of Technology;

M.S., Dalian University of Technology

Chair of Advisory Committee: Dr. Marcetta Y. Darensbourg

My research primarily focuses on biomimetics of the active sites of the [FeFe]- and [Fe]-hydrogenases ( $H_2ase$ ) and is classified into three parts.

Part A: The one-electron oxidation of asymmetrically disubstituted  $Fe^I Fe^I$  models of the active site of the [FeFe]- $H_2ase$ ,  $(\mu-pdt)[Fe(CO)_2PMe_3][Fe(CO)_2NHC]$  ( $pdt = 1,3$ -propanedithiolate,  $NHC = N$ -heterocyclic carbene) generates mixed valent  $Fe^{II} Fe^I$  models of the  $H_{ox}$  state of [FeFe]-hydrogenase. The spectroscopic properties, structures, reactivities and relative stabilities of the one-electron oxidized mixed valent complexes,  $(\mu-pdt)(\mu-CO)[Fe^{II}(CO)_2PMe_3][Fe^I(CO)NHC]^+$  are discussed in the context of experimental and theoretical data and biological relevance.

Part B: DFT computations find the Fe-Fe bond in the  $Fe^I Fe^I$  diiron models  $((\mu-pdt)[Fe(CO)_2L][Fe(CO)_2L'])$  ( $L, L' = CO, PPh_3, \text{ or } PMe_3$ ) is thermodynamically favored to produce the  $\mu$ -oxo or oxidative addition product,  $Fe^{II}-O-Fe^{II}$ , nevertheless the sulfur-based HOMO-1 accounts for the experimentally observed mono- and bis-O-atom adducts at sulfur. The  $Fe^{II}(\mu-H)Fe^{II}$  diiron model,  $(\mu-pdt)(\mu-H)[Fe(CO)_2PMe_3]_2$  (**IV-5**),

for which the HOMO is largely of sulfur character, exclusively yields S-oxygenation. Deoxygenation with reclamation of the  $\mu$ -pdt parent complexes occurs in a proton/electron coupled process. The possible biological relevance of oxygenation and deoxygenation studies is discussed.

Comprehensive investigations of intramolecular CO site change and intermolecular CO/L (L =  $\text{PMe}_3$  or  $\text{CN}^-$ ) exchange of  $(\mu\text{-pst})[\text{Fe}(\text{CO})_3]_2$  (**IV-1-O**),  $(\mu\text{-pdt})[\text{Fe}(\text{CO})_3]_2$  (**V-1**), and their mono- $\text{CN}^-/\text{PMe}_3$  substituted derivatives indicated that the factors influencing the rate of the CO/L exchange reaction of such diiron carbonyls are intramolecular structural rearrangement (or fluxionality) and nucleophilic attack by the incoming ligand.

Part C: X-ray diffraction and spectroscopic studies of a series of mono- and di-substituted complexes,  $\text{FeI}_2(\text{CO})_x\text{L}_{4-x}$ ,  $x = 2$  or  $3$ , showed them to be rudimentary structural models of the  $[\text{Fe}]\text{-H}_2\text{ase}$  active site in native ( $\text{Fe}^{\text{II}}(\text{CO})_2$ ) or CO-inhibited ( $\text{Fe}^{\text{II}}(\text{CO})_3$ ) states. Full characterization of the advanced model complexes ( $(\text{NS})\text{FeI}(\text{CO})_2\text{P}$ , NS = 2-amidophenothiolate; P = phosphine) including x-ray diffraction, DFT computations, and Mössbauer studies revealed the interesting “non-innocent” character of these complexes due to the NS ligand. Ligand-based protonation with a strong acid,  $\text{HBF}_4 \cdot \text{Et}_2\text{O}$ , interrupted the  $\pi$ -delocalization over Fe and ligand of complex **VII-1** and switched on CO uptake (1 bar) and  $^{12}\text{CO}/^{13}\text{CO}$  exchange of **VII-1**. The intermediate, **VII-1-H<sup>+</sup>**, capable of CO uptake, was defined by DFT calculations.

## **DEDICATION**

I dedicate this dissertation to my parents and my wife. Their unwavering love and support gave me the courage and strength to conquer challenges which occurred along my journey, and helped me to reach my goals.

## ACKNOWLEDGEMENTS

During my doctoral study at Texas A&M University, I have been blessed to have met many nice people and developed numerous precious friendships. I would like to take this opportunity to acknowledge help and support that I received.

First, I wish to thank my advisor, Professor Marcetta Y. Darensbourg, for mentoring me through the rigors of a Ph.D. program and supporting me over the last four years. You have directed me on how to be a successful chemist by looking at alternative routes. Your passion in research and teaching is one of most valuable things I have learned from you and also has engendered my research to become something I enjoyed each day. Your broad vision in chemical research has made me aim for big goals while your attention to detail has educated me to pay attention to **small things** and be **patient**. I appreciate your strong recommendations in my applications for postdoctoral position. Furthermore, I've learned many things from you outside the lab. An important life lesson I learned is "take a look before you leap". Finally, I would like to thank you for giving me many opportunities to attend conferences so that I could meet other excellent scientists and learn new American cultures. P. S., Marcetta, I apologize for pumping gasoline into your cute Beetle when Ben arrived in College Station.

I acknowledge Professor Michael B. Hall, Professor Manuel P. Soriaga, Professor David P. Barondeau and Professor Perla B. Balbuena for serving as my committee members. Special thanks goes to Professor Hall for his insightful guidance on DFT calculations and constructive suggestions for my research. I am thankful for the excellent

support staff in the Department of Chemistry: Dr. Joseph Reibenspies and Dr. Nattamai Bhuvanesh for solving tricky crystal structures; Dr. Lisa M. Pérez for her immense help in DFT calculations; Miss Vanessa Santiago for her timely treatment of my sensitive MS samples; Dr. Vladimir Bakhmoutov and Dr. K. P. Sarathy for their training in the use of NMR instruments; Professor Paul Lindahl and Mr. Ren Miao for their assistance in EPR measurements; our former group secretary, Sue Winters, the current group secretary, Ethelyn Mejia and departmental graduate student assistant, Sandra Manning, for their help with the paperwork. I thank Professor Codrina Popescu and Mr. Andrey Bilko from Ursinus College for their help on Mössbauer studies. My thanks also go to Dr. Yubo Fang and Dr. Xinzheng Yang for their helpful discussions in theoretical chemistry.

I would like to thank Professor Donald J. Darensbourg and his group. I have learned a lot from Don on kinetic studies and IR spectroscopy. Thank you for the encouraging words and smiles in the hallway when I needed it most. Your laugh and sarcastic wit brought many a smile to my face. Don's group gave me a sense of family and belongingness. We had lots of great times together. I owe much gratitude to Eric Frantz, Osit "Pop" Karroonnirun, Adriana Moncada, Wonsook Choi, Jeremy Andreatta, Shawn Fitch, Sheng-Hsuan "Sunshine" Wei, Ross Poland and other DJD group members for their help. Eric, thank you for teaching me how to use x-ray instruments and cheering me up on bad days. I miss your laughter when you were in Sunshine's position. Pop and Adriana, before I leave, we should go to more places for delicious meals. Jeremy, you are "cool beans" because whenever I needed weird experimental stuff, such as the small  $^{13}\text{C}$ O gas regulator, I could get them from you.

I appreciate all the help I received from the former MYD members in my earlier time. Each of you taught or mentored me in some form by shaping my scientific development and maturity: Drs. Joy Chiang, Marilyn Rampersad, Jesse Tye, Kayla Green, Elky Almaraz, Stephen Jeffery and Christine Thomas. I thank the current members of the MYD group: Mike Singleton, Bin Li, Jason Denny, Roxanne Jenkins, Tiffany Pinder, Scott Brothers, Jen Hess, William Foley and Ryan Bethel. Your friendships have meant a lot to me. We had lots of great times in and out of the lab. Thanks very much for your encouraging words and help that I couldn't exemplify in detail here. Special thanks to my research co-workers, Dr. Christine Thomas, Mike Singleton and Bin "Ben" Li. It has been great fun to work with and discuss research with you. Your ideas have inspired me in many ways and your contributions to my research are tremendous as evident in papers we co-authored. Definitely, without your help, I couldn't have done so much. Mike, many thanks for your strong support besides research. We had wonderful times together in Washington D.C. and in Colorado with our families. Ben, it is a pity that you will not attend my final defense. I wish you do best in your defense in China. Scott, thanks for answering my questions on DFT calculations. Roxanne, thanks for your help with my English. You, Elky and other MYD members have proofread my manuscripts many times. By the way, Amelia, our little angel, brought me lots of joy. I would like to share some of my experience with the current MYD members. If you get stressed or feel frustrated in your research, please first relax with some beers or spend some time with your family. Then hold yourself and fight back. The only thing you need is energy—you can get it from your soul—to overcome



barriers. Later on, you will enjoy the sense of fulfillment when you look back at your starting point and transition states you have crossed.

I must give thanks to my friends, Dr. Jubo Zhang, Gang Liu, Ye Zhu, Chiyuan Tsao, Ren Miao, Zeyun Wu and their families for their help while living in College Station.

No words can express my sincere thanks and appreciation to my parents and my wife, Xiang Jin. My parents have always told me to be nice, diligent and strong. My wife gave up her opportunity to pursue her doctoral study in Japan and came to stay with me in the United States. She has been taking care of me on a daily basis. For me, she, a spoiled girl in her family, learned how to handle all kinds of house work. I am very happy she is a good cook now. I have gained more than 30 pounds since she joined me in Texas. She is my best listener whenever I speak. She is also a good support when I am down or excited. Sometimes, I joke with her, “you are the untitled second-author in my papers”. One thing that makes me a little comfortable, is she finally learned how to drive.

Life is a kind of chemistry, which is about changes between atoms. It is hard to say farewell to all of you, even the hot weather in Texas. I will do my best to keep in touch.

## TABLE OF CONTENTS

	Page
ABSTRACT .....	iii
DEDICATION .....	v
ACKNOWLEDGEMENTS .....	vi
TABLE OF CONTENTS .....	x
LIST OF FIGURES.....	xiii
LIST OF TABLES .....	xix
 CHAPTER	
I INTRODUCTION.....	1
Energy crisis.....	1
Biological functions of hydrogenases .....	2
Biophysical studies of hydrogenases and mechanisms .....	7
Chemical models of hydrogenases.....	17
Research conducted in this dissertation .....	29
II EXPERIMENTAL.....	30
Materials and techniques.....	30
Experimental for chapter III.....	33
Experimental for chapter IV.....	40
Experimental for chapter V .....	46
Experimental for chapter VI.....	47
Experimental for chapter VII .....	52
III NHC CARBENE SUPPORTED MIXED-VALENT Fe <sup>II</sup> Fe <sup>I</sup> , DIIRON COMPLEXES THAT MODEL THE H <sub>ox</sub> STATE OF THE [FeFe] HYDROGENASE ACTIVE SITE.....	56

CHAPTER	Page
Introduction .....	56
Results and discussion.....	59
Conclusions and comments .....	97
 IV    SULFUR OXYGENATES OF BIOMIMETICS OF THE DIIRON	
SUBSITE OF THE [FeFe]-HYDROGENASE ACTIVE SITE.....	102
Introduction .....	102
Results and discussion.....	105
Conclusions and comments.....	131
 V     THE INFLUENCE OF SULF-OXYGENATION ON CO/L	
SUBSTITUTION AND Fe(CO) <sub>3</sub> ROTATION IN THIOLATE-	
BRIDGED DIIRON COMPLEXES .....	133
Introduction .....	133
Results and discussion.....	136
Conclusions and comments.....	156
 VI    IRON CARBONYL COMPLEXES FeI <sub>2</sub> (CO) <sub>3</sub> L (L = NHC	
CARBENES, PHOSPHINES, PYRIDINE) AND FeI <sub>2</sub> (CO) <sub>2</sub> N <sub>2</sub> (N <sub>2</sub> =	
α-DIAMINES) REVELANT TO THE [Fe]-HYDROGENASE .....	163
Introduction .....	163
Results and discussion.....	165
Conclusions and comments.....	179
 VII   THE [Fe]-HYDROGENASE MODELS: PENTA-COORDINATE	
IRON DICARBINYLS SUPPORTED BY A NONINNOCENT NS	
LIGAND.....	182
Introduction .....	182
Results and discussion.....	183
Conclusions .....	200

CHAPTER	Page
VIII CONCLUSIONS .....	201
Mixed valence .....	201
Oxygenates and deoxygenation.....	205
Mono-Fe models .....	208
REFERENCES .....	210
VITA .....	233

## LIST OF FIGURES

		Page
Figure I. 1	The active sites of the [FeFe]- (A), [NiFe]- (B), and [Fe]-H <sub>2</sub> ases (C).....	2
Figure I. 2	The vertical distribution of different redox reactions of <i>anaerobic respiration</i> and other biological processes involving H <sub>2</sub> metabolism via hydrogenases found in microorganisms (adapted from ref. 8, 11 and 23).....	4
Figure I. 3	The catalytic mechanism of the [NiFe]-H <sub>2</sub> ase proposed by Hall <i>et al.</i> <sup>43</sup> .....	11
Figure I. 4	The catalytic mechanism of the [FeFe]-H <sub>2</sub> ase. ....	14
Figure I. 5	A suggested mechanism for the [Fe]-H <sub>2</sub> ase, i.e., stereoselective hydride abstraction from ( $\eta^2$ -H <sub>2</sub> )Fe <sup>II</sup> by the H <sub>4</sub> MPT <sup>+</sup> substrate (see text). <sup>67</sup> .....	16
Figure I. 6	Selected model complexes of the [NiFe]-H <sub>2</sub> ase. See text for references. ....	19
Figure I. 7	Selected model complexes of the [FeFe]-H <sub>2</sub> ase. See references in text.....	24
Figure I. 8	Selected model complexes of the [Fe]-H <sub>2</sub> ase. See references in text. ....	28
Figure III.1	Cyclic voltammograms of ( $\mu$ -pdt)[Fe(CO) <sub>2</sub> PMe <sub>3</sub> ][Fe(CO) <sub>2</sub> IMes] (III-1, black), ( $\mu$ -pdt)[Fe(CO) <sub>2</sub> PMe <sub>3</sub> ][Fe(CO) <sub>2</sub> IMesMe] (III-2, red), and ( $\mu$ -pdt)[Fe(CO) <sub>2</sub> PMe <sub>3</sub> ][Fe(CO) <sub>2</sub> IMe] (III-3, blue) in CH <sub>3</sub> CN (top) and CH <sub>2</sub> Cl <sub>2</sub> (bottom).. ....	64
Figure III. 2	Solution IR spectra (CH <sub>2</sub> Cl <sub>2</sub> ) showing the reversibility of the one-electron oxidation of III-1 (A), III-2 (B), and III-3 (C).....	67
Figure III. 3	Experimental (black) and simulated (red) EPR spectra of III-1 <sub>ox</sub> (top), III-2 <sub>ox</sub> (middle), and III-3 <sub>ox</sub> (bottom).....	69
Figure III. 4	Solid state molecular structures (ball and stick representation) of complexes III-2 <sub>NHC</sub> , III-1, III-2 and III-3. ....	72

	Page
Figure III. 5 Solid state molecular structure (ball and stick representation) of III-1 <sub>ox</sub> .....	72
Figure III. 6 Assignment of infrared CO stretches for complex III-1 <sub>ox</sub> .....	74
Figure III. 7 Infrared spectra (recorded at ca. 22°C) of CH <sub>2</sub> Cl <sub>2</sub> solutions of III-1 <sub>ox</sub> (top), III-2 <sub>ox</sub> (middle), and III-3 <sub>ox</sub> (bottom) following CO sparging at -78 °C.....	75
Figure III. 8 Experimental (top) and simulated (bottom) EPR spectrum of III-ox <sup>CO</sup> (in CH <sub>2</sub> Cl <sub>2</sub> at 10 K, X band).....	77
Figure III. 9 Infrared spectra of (A) III-1 <sub>ox</sub> upon exposure to <sup>13</sup> CO at -78 °C in CH <sub>2</sub> Cl <sub>2</sub> (in the dark) after 0 (black), 15 (red) and 45 (blue) min, (B) III-1 <sub>ox</sub> after warming to room temperature under 1 atm of <sup>13</sup> CO, and (C) <sup>13</sup> CO-labeled product obtained via treatment of III-1 <sub>ox</sub> with <sup>13</sup> CO at room temperature followed by reduction with Cp <sub>2</sub> Co. Carbonyl region of the <sup>13</sup> C NMR spectrum of (D) the regioselectively labeled product generated upon exposure of III-1 <sub>ox</sub> to <sup>13</sup> CO at -78 °C for 30 minutes followed by Cp <sub>2</sub> Co reduction and (E) the fully <sup>13</sup> CO-labeled product obtained by addition of Cp <sub>2</sub> Co to the labeled product generated upon exposure of III-1 <sub>ox</sub> to <sup>13</sup> CO at room temperature. ....	79
Figure III. 10 IR spectra monitoring the reaction of III-2 <sub>ox</sub> with <sup>13</sup> CO at -78 °C in CH <sub>2</sub> Cl <sub>2</sub> over a 1 hour time period in the absence of light. ....	83
Figure III. 11 IR spectra of the mixture of isotopically-labeled product formed upon exposure of III-2 <sub>ox</sub> to <sup>13</sup> CO (black), and the products of reaction of this mixture with CoCp <sub>2</sub> (blue) and excess <sup>12</sup> CO (red). ....	84
Figure III. 12 Pictorial representations of the highest occupied molecular orbitals (or singly occupied molecular orbital, in the case of III-1 <sub>ox</sub> ) of the neutral complex III-1, the rotated transition state III-1 <sup>‡</sup> , and the cation III-1 <sub>ox</sub> . ....	86
Figure III. 13 Top: unpaired spin density surface (isodensity = 0.03) of III-3 <sub>ox</sub> <sup>CO</sup> and III-3 <sub>ox</sub> <sup>*CO</sup> ; Bottom: comprehensive frontier orbitals (isovalue = 0.03) of III-3 <sub>ox</sub> <sup>CO</sup> .....	96
Figure IV. 1 Sketches of the [NiFe]- and [FeFe]-H <sub>2</sub> ase active sites.....	104

	Page
Figure IV. 2	Frontier molecular orbitals (with isovalue = 0.04) of complex IV-1, $(\mu\text{-pdt})[\text{Fe}(\text{CO})_3]_2$ ..... 106
Figure IV. 3	Frontier molecular orbitals (with isovalue = 0.04) of IV-5 <sup>+</sup> , $\{(\mu\text{-pdt})(\mu\text{-H})[\text{Fe}(\text{CO})_2(\text{PMe}_3)]_2\}^+$ ..... 109
Figure IV. 4	CV and DPV (inset) curves of the sulfur oxygenated complex IV-1-O in CH <sub>3</sub> CN. All potentials are referenced vs Fc <sup>+</sup> /Fc (scan rate = 100 mV/s, 0.1 M [ <sup>n</sup> Bu <sub>4</sub> N] <sup>+</sup> [BF <sub>4</sub> ] <sup>-</sup> , 22 °C)..... 116
Figure IV. 5	Molecular structures of the sulfur oxygenated complexes (IV-1-O, IV-2-O, IV-2-O <sub>2</sub> , IV-4-O and IV-6) given in two perspectives: along the Fe-Fe bond and perpendicular to the Fe-Fe vector. For IV-2-O and IV-2-O <sub>2</sub> , the PPh <sub>3</sub> ligand is in the front..... 119
Figure IV. 6	Top: variable temperature <sup>13</sup> C NMR studies of complex IV-1-O from -60 to 30 °C (CD <sub>2</sub> Cl <sub>2</sub> solution, in CO region); signals indicated with “*” are unknown impurities. Bottom: Variable temperature <sup>13</sup> C NMR studies of complex IV-1 from -80 to 30 °C..... 122
Figure IV. 7	Ground state and transition state structures of IV-1-O (top) and IV-1 (bottom) with corresponding energies given in kcal/mol obtained by DFT computations (In parenthesis, for e.g., (13.97/ 14.27): the former value obtained from the level of B3LYP/D95&LANL2DZ and the later value from the level of B3LYP/cc-pVDZ&LANL2DZ) for one Fe(CO) <sub>3</sub> unit rotation..... 125
Figure IV. 8	IR monitor of deoxygenation of IV-1-O with Cp* <sub>2</sub> Co in CH <sub>3</sub> CN in the presence of H <sub>2</sub> O (2% V/V)..... 126
Figure IV. 9	CV (top), DPV (top, inset) and IR measurements (bottom) of deoxygenation studies of IV-4-O via bulk electrolysis..... 128
Figure IV. 10	CV (top), DPV (top, inset) and IR measurements (bottom) of deoxygenation studies of IV-1-O via bulk electrolysis..... 128
Figure V. 1	Representation of events along reaction coordinate for cyanide nucleophilic attack on diiron carbonyl, L = CO or CN <sup>-</sup> , n = 0 or -1, and the equation describing contributing factors to the overall activation energy barrier..... 135

	Page
Figure V. 2	Infrared spectra, in the 1800 – 2150 $\text{cm}^{-1}$ region, as CO / $\text{PMe}_3$ exchange takes place to produce (a) IV-1- $\text{PMe}_3$ from IV-1; and (b) to produce IV-1-( $\text{PMe}_3$ ) <sub>2</sub> from IV-1- $\text{PMe}_3$ . ..... 140
Figure V. 3	(a) Example of plot of $\ln(A_0/A_t)$ vs time over five half-lives, Entry 4, Table V. 2. (b) Plot of $k_{\text{obs}}$ vs $[\text{PMe}_3]$ for the formation of complex IV-1- $\text{PMe}_3$ from complex 1 measured at 22°C. .... 141
Figure V. 4	Infrared spectra, in the 1800 – 2150 $\text{cm}^{-1}$ region, as CO / $\text{PMe}_3$ exchange takes place to produce complex IV-1-O- $\text{PMe}_3$ from IV-1-O. .... 143
Figure V. 5	(a) Example of plot of $\ln(A_0/A_t)$ vs. time over four half-lives, Entry 7, Table V. 3 (b) Plots of $k_{\text{obs}}$ vs. $[\text{PMe}_3]$ for the formation of IV-1-O- $\text{PMe}_3$ from IV-1-O measured at 90°C. .... 144
Figure V. 6	Left: Eyring plots for the formation of complex IV-1- $\text{PMe}_3$ from complex IV-1 ( $\square$ ) and for the formation of IV-1-( $\text{PMe}_3$ ) <sub>2</sub> from IV-1- $\text{PMe}_3$ ( $\Delta$ ). Right: Arrhenius plot for the formation of IV-1- $\text{PMe}_3$ from ( $\mu$ -pdt)[ $\text{Fe}(\text{CO})_3$ ] <sub>2</sub> (1) ( $\square$ ) and for the formation of IV-1-( $\text{PMe}_3$ ) <sub>2</sub> from IV-1- $\text{PMe}_3$ ( $\Delta$ ). .... 145
Figure V. 7	Eyring plot (left) and Arrhenius plot (right) for the formation of ( $\mu$ -pst)[ $\text{Fe}(\text{CO})_3$ ][ $\text{Fe}(\text{CO})_2\text{PMe}_3$ ] ( <b>1-O-<math>\text{PMe}_3</math></b> ) from ( $\mu$ -pst)[ $\text{Fe}(\text{CO})_3$ ] <sub>2</sub> ( <b>1-O</b> ) follow dissociative path ( $\square$ ) and associative path ( $\Delta$ ). .... 147
Figure V. 8	Infrared spectra, in the 1850 – 2150 $\text{cm}^{-1}$ region, as CO / $\text{CN}^-$ exchange takes place: (a) to produce IV-1-O- $\text{CN}^-$ from IV-1-O at 0 °C in $\text{CH}_3\text{CN}$ , and (b) to produce (IV-1-O- $\text{CN}_2$ ) <sup>2-</sup> from IV-1-O- $\text{CN}^-$ at 40 °C in $\text{CH}_3\text{CN}$ . .... 148
Figure V. 9	(a) Example of plot of $\ln(A_0/A_t)$ vs. time over three half-lives; (b) Plot of $k_{\text{obs}}$ vs. $[\text{CN}^-]$ for the formation of (IV-1-O- $\text{CN}_2$ ) <sup>2-</sup> from IV-1-O- $\text{CN}^-$ measured at 40°C. .... 150
Figure V. 10	Eyring plot (left) for the formation of complex IV-1-O-( $\text{CN}$ ) <sub>2</sub> <sup>2-</sup> from complex IV-1-O- $\text{CN}^-$ . Arrhenius plot (right) for the formation of complex IV-1-O-( $\text{CN}$ ) <sub>2</sub> <sup>2-</sup> from complex IV-1-O- $\text{CN}^-$ ..... 152



Figure V. 11	Variable temperature $^{13}\text{C}$ NMR studies of complex <b>IV-1-O-CN<math>^-</math></b> from $-100\text{ }^\circ\text{C}$ to $20\text{ }^\circ\text{C}$ ( $\text{CD}_2\text{Cl}_2$ solution, in CO region); signal indicated with “*” are impurities .....	153
Figure V. 12	Ground state and transition state structures for the rotation of $\text{Fe}(\text{CO})_3$ and $\text{Fe}(\text{CO})_2\text{CN}^-$ units in the complex <b>IV-1-O-CN<math>^-</math></b> with corresponding energies given in kcal/mol from DFT computations; see text for parameters used. ....	155
Figure V. 13	Mechanism for CN $^-$ /CO exchange reaction in $(\mu\text{-pdt})[\text{Fe}(\text{CO})_3]_2$ ( <b>IV-1-O</b> ). ....	159
Figure V. 14	Reaction profiles of CN $^-$ /CO substitution reaction of (a) $(\mu\text{-pdt})[\text{Fe}(\text{CO})_3]_2$ ( <b>IV-1</b> ) <sup>1</sup> and (b) $(\mu\text{-pst})[\text{Fe}(\text{CO})_3]_2$ ( <b>IV-1-O</b> ). ....	160
Figure V. 15	Structures of [Fe]-H <sub>2</sub> ase active site (a) <sup>46, 59</sup> and transition state of $\text{Fe}(\text{CO})_3$ rotation in $(\mu\text{-pdt})[\text{Fe}(\text{CO})_3]_2$ (b), <sup>1</sup> and $(\mu\text{-pst})[\text{Fe}(\text{CO})_3]_2$ (c). ....	162
Figure VI. 1	The active site of Hmd or [Fe]-H <sub>2</sub> ase with its CO stretching frequencies. ....	164
Figure VI. 2	The infrared spectra of mono-Fe <sup>II</sup> complexes <b>VI-1</b> , <b>VI-6</b> , <b>VI-8</b> , <b>VI-10</b> and <b>VI-12</b> . ....	168
Figure VI. 3	Infrared spectral monitoring of $\text{CH}_2\text{Cl}_2$ solution of complex <b>VI-5</b> at $22^\circ\text{C}$ . (A) Immediately after dissolving complex <b>VI-5</b> ; (B) IR spectrum recorded 2 h later; (C) IR spectrum after overnight (RT and in the dark). ....	170
Figure VI. 4	Infrared spectral monitoring of $\text{CH}_2\text{Cl}_2$ solution of complex <b>VI-5</b> at $22^\circ\text{C}$ . (A) Immediately after dissolving complex <b>VI-5</b> ; (B) IR spectrum recorded 2 h later; (C) IR spectrum after overnight (RT and in the dark). ....	171
Figure VI. 5	$\nu(\text{CO})$ region of IR spectra of complex <b>VI-4</b> in THF under $^{13}\text{CO}$ atmosphere: (A) IR spectra of complex <b>VI-4</b> in THF. (B) IR spectra of complex <b>VI-4</b> in THF under $2\text{atm }^{13}\text{CO}$ after 3 h. (C) IR spectra of complex <b>4</b> in THF under $2\text{atm }^{13}\text{CO}$ after 18 h. ....	172
Figure VI. 6	6 K Mössbauer spectra for complexes <b>VI-1</b> , <b>VI-6</b> , and <b>VI-7</b> in an applied field of $0.03\text{ T}$ . ....	173

	Page
Figure VI. 7 Thermal ellipsoid representations of the molecular structures of mono-iron complexes as indicated; hydrogen atoms omitted. ....	177
Figure VII. 1 Formulation of the active site of the [Fe]-H <sub>2</sub> ase and a suggested mechanism of action. ....	183
Figure VII. 2 IR spectra ( $\nu(\text{CO})$ region) of complexes VII-1, VII-2 and VII-3 in CH <sub>2</sub> Cl <sub>2</sub> . ....	184
Figure VII. 3 Molecular structures of complexes VII-1 (top) and VII-2 (bottom) as thermal ellipsoid representations, 50% probability, hydrogen atoms omitted. ....	186
Figure VII. 4 Comparison of DFT and experimental metric parameters for complex VII-1. Additional metric parameters are in the SI. ....	188
Figure VII. 5 Frontier molecular orbitals (HOMO, left, and LUMO, right, isovalue = 0.05) of complex VII-1 obtained from DFT calculations. ....	191
Figure VII. 6 Frontier orbitals (isovalue = 0.05) of the free ligand forms: (a) NS <sup>2-</sup> , 2-amidothiophenolate; (b) NS <sup>1-</sup> , 2-iminothionebenzosemiquinonate; and (c) NS <sup>0</sup> : 6-iminocyclohexa-2,4-dienethione. ....	191
Figure VII. 7 Mössbauer spectra of nujol suspensions of polycrystalline complexes VII-1~VII-3 in an applied field of 300 Gauss. Two impurities accounting for ~15% of the total iron in this sample, were simulated and subtracted from the original spectrum of VII-3. The solid lines through the spectra are least-square fits, with the parameters listed in Table VII. 2, text. ....	193
Figure VII. 8 Protonation/deprotonation of complex VII-1 in the presence of exogeneous CO to yield VII-1(CO)-H <sup>+</sup> . ....	195
Figure VII. 9 $\nu(\text{CO})$ IR monitor of concomitant <sup>12</sup> CO/ <sup>13</sup> CO exchange and <sup>13</sup> CO uptake of complex VII-1 and the reclamation of complex VII-1 completely labeled with <sup>13</sup> CO. ....	196
Figure VII. 10 Top: DFT optimized structures and relative energy of the isomers of VII-1-NH <sup>+</sup> and a tautomer, VII-1-SH <sup>+</sup> (Isomer a of VII-1-NH <sup>+</sup> is defined as G = 0.0 kcal/mol). Bottom: Calculated frontier orbitals (isovalue = 0.05) of VII-1-NH <sup>+</sup> (b). ....	198

## LIST OF TABLES

		Page
Table III. 1	Infrared spectroscopic data for $(\mu\text{-pdt})[\text{Fe}(\text{CO})_2(\text{L})]_2$ , derivatives (reported in THF solution unless otherwise noted). .....	61
Table III. 2	Electrochemical potentials (V vs $\text{Fc}^+/\text{Fc}$ ) as determined by cyclic voltammetry for $(\mu\text{-pdt})[\text{Fe}(\text{CO})_2(\text{NHC})][\text{Fe}(\text{CO})_2(\text{L})]$ complexes, III-1 <sub>NHC</sub> ~III-3 <sub>NHC</sub> and III-1~III-3 (recorded in $\text{CH}_3\text{CN}$ or $\text{CH}_2\text{Cl}_2$ with 0.1 M $[\text{nBu}_4\text{N}][\text{BF}_4]$ ; scan rate = 100 mV/s, 22 °C). The data for III-3 <sub>NHC</sub> was taken from ref. 40. ....	63
Table III. 3	Selected interatomic distances (Å) and angles (deg) for III-2 <sub>NHC</sub> , III-1, III-2, III-3 and III-1 <sub>ox</sub> . ....	71
Table III. 4	Unpaired spin density and relevant geometrical parameters calculated for III-1 <sub>ox</sub> ~III-3 <sub>ox</sub> , starting from the crystallographic coordinates of III-1 <sub>ox</sub> . ....	89
Table III. 5	Calculated <sup>a</sup> and experimental $\nu(\text{CO})$ stretching frequencies for complexes III-1 <sub>ox</sub> ~ III-3 <sub>ox</sub> . ....	89
Table III. 6	Relevant geometrical parameters calculated for the 8 possible conformational isomers of III-3 <sub>ox</sub> in both rotated and unrotated structures. ....	90
Table III. 7	Calculated $\nu(\text{CO})$ stretching frequencies for isomers A-H (using a scaling factor of 1.0107). ....	93
Table III. 8	Relevant bond distances and angles calculated for the two possible CO adducts, $3_{\text{ox}}^{\text{CO}}$ and $3_{\text{ox}}^{*\text{CO}}$ . ....	95
Table IV. 1	Total free energy (kcal/mol) comparison between sulfur oxygenated species and corresponding metal oxygenated isomers from the computations with functional and basis sets of B3LYP/D95&LANL2DZ (in parentheses, B3LYP/cc-PPVDZ&LANL2DZ). ....	107
Table IV. 2	Infrared spectroscopic data, $\nu(\text{CO})$ region, for sulfur-oxygenated complexes (IV-1-O, IV-2-O, IV-2-O <sub>2</sub> , IV-4-O, IV-5-O and IV-6) in $\text{CH}_2\text{Cl}_2$ , and their corresponding precursors in solvents as listed. ....	114

	Page
Table IV. 3	Cyclic voltammetry data versus $Fc^+/Fc$ for the sulfur-oxygenated complexes (IV-1-O, IV-2-O, IV-2-O <sub>2</sub> and IV-4-O) and reference complexes in CH <sub>3</sub> CN electrolyte (0.1 mM Bu <sub>4</sub> N <sup>+</sup> BF <sub>4</sub> <sup>-</sup> ; scan rate, 100 mV/s)..... 115
Table IV. 4	Selected metric data for the sulfur oxygenated complexes (IV-1-O, IV-2-O, IV-2-O <sub>2</sub> and IV-4-O). In parenthesis and italics are the values of Fe-Fe distance of parent non-oxygenates. .... 120
Table V. 1	Infrared spectroscopic ( $\nu(CO)$ and $\nu(CN)$ ) data for ( $\mu$ -pdt)[Fe(CO) <sub>2</sub> (L)] <sub>2</sub> and ( $\mu$ -pst)[Fe(CO) <sub>2</sub> (L)] <sub>2</sub> derivatives (reported in toluene solution unless otherwise noted). .... 138
Table V. 2	Rate data for determination of rate expression for the reaction of PMe <sub>3</sub> with complex IV-1 measured at 22 °C and with IV-1-PMe <sub>3</sub> measured at 50 °C in toluene solution..... 139
Table V. 3	Rate data for the reaction of PMe <sub>3</sub> with ( $\mu$ -pst)[Fe(CO) <sub>3</sub> ] <sub>2</sub> (IV-1-O) as a function of temperature in Toluene..... 143
Table V. 4	Temperature dependence of reaction of PMe <sub>3</sub> with ( $\mu$ -pdt)[Fe(CO) <sub>3</sub> ] <sub>2</sub> (IV-1), ( $\mu$ -pdt)[Fe(CO) <sub>3</sub> ][Fe(CO) <sub>2</sub> PMe <sub>3</sub> ] (IV-1-PMe <sub>3</sub> ) and ( $\mu$ -pst)[Fe(CO) <sub>3</sub> ] <sub>2</sub> (IV-1-O). .... 146
Table V. 5	Rate data for the reaction of Et <sub>4</sub> N <sup>+</sup> CN <sup>-</sup> with complex IV-1-O measured at 0 °C and with IV-1-O-CN <sup>-</sup> measured at 40 °C in CH <sub>3</sub> CN solution..... 149
Table V. 6	Temperature dependence of reaction of Et <sub>4</sub> N <sup>+</sup> CN <sup>-</sup> with complex (IV-1-O-CN <sup>-</sup> )..... 151
Table VI. 1	Infrared Spectroscopic ( $\nu(CO)$ ) Data For FeI <sub>2</sub> (CO) <sub>3</sub> L, FeI <sub>2</sub> (CO) <sub>2</sub> N <sub>2</sub> and FeI(CO) <sub>2</sub> LPyS Derivatives (reported in CH <sub>2</sub> Cl <sub>2</sub> solution unless otherwise noted). .... 167
Table VI. 2	Selected metric data for complexes VI-1, VI-2, VI-3, VI-4, VI-10 and VI-12..... 178
Table VII. 1	Calculated distances (Å) within the NS ligand in three redox levels and within the ligand in complexes VII-1 and VII-2. .... 189

	Page
Table VII. 2 Relative energies (kcal / mol) of complex VII-1 found by DFT calculations at different levels. ....	190
Table VII. 3 Selected Mössbauer parameters at 6 K, in an applied magnetic field of 0.03 T. ....	194
Table VII. 4 Selected structural parameters of the lowest energy isomer of VII-1-NH <sup>+</sup> (b) found by DFT calculation. ....	199

# CHAPTER I

## INTRODUCTION

### Energy crisis

Due to the imminent depletion and environmental problems related to fossil fuels, energy alternatives are critically needed to address global requirements.<sup>1-3</sup> Energy forms such as hydroelectric energy, wind power, biomass and nuclear energy, etc. are auxiliary means to offer power that are limited by access, ease of operation and security.<sup>3</sup> Solar energy (energy source) and hydrogen (energy carrier) have been widely accepted as an ideal combined solution for long term energy development that is friendly to the environment. Basically, the paradigm consists of two coupled components: a solar H<sub>2</sub>O splitting system and a H<sub>2</sub> fuel cell system.<sup>2</sup> Among many technical problems, critical to this new technology are the production of hydrogen through solar energy conversion and the use of hydrogen as a fuel at cheap cost. The technical aspects, namely water electrolysis and the fuel cell technology are particular concerns of the research. At present, the most common material used in industries and laboratories for hydrogen technologies is platinum metal.<sup>4</sup> Even though the catalytic ability of Pt<sup>0</sup> is the best among all catalysts currently, it has some serious problems. First, Pt<sup>0</sup>, a trace metal on earth, is very expensive as it is seriously resource limited. Secondly, Pt is easily poisoned on exposure to CO and loses its catalytic ability for either H<sub>2</sub> oxidation or proton reduction. Therefore, finding a good substitute for Pt<sup>0</sup> is essential.

---

This dissertation follows the style of *the Journal of the American Chemical Society*.

While the electrolysis of water (Hofmann voltameter) and the fuel cell technology have been developed since the 19th century,<sup>5</sup> nature has been utilizing a specific family of enzymes, hydrogenases, for billions of years. These can function in hydrogen generation and reversible activation, i.e.  $\text{H}_2 \rightleftharpoons 2\text{H}^+ + 2\text{e}^-$ , at an efficiency comparable with that of Pt.<sup>6</sup> Hydrogenases and the chemistry they perform have inspired biologists and chemists to develop cheap and reliable  $\text{H}_2$ -fuel techniques.

### Biological functions of hydrogenases

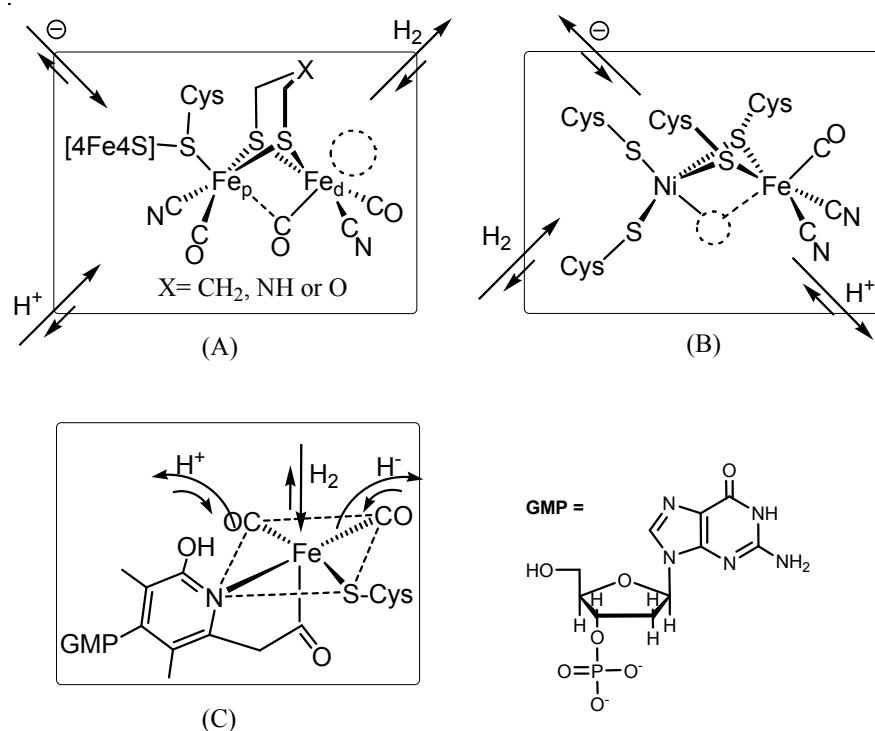
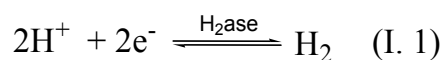


**Figure I. 1** The active sites of the [FeFe]- (A), [NiFe]- (B), and [Fe]- $\text{H}_2$ ases (C).

Depending on the metal components of enzymatic active sites as sketched in Figure I. 1, there are three phylogenetically unrelated classes of these enzymes: (A) the [FeFe]-

(B) the [NiFe]-, and (C) the [Fe]-H<sub>2</sub>ases.<sup>7</sup> In microorganisms belonging to archaea, bacteria, and eukaryotes domains of life, the utilization of hydrogen as a source of reducing power or of protons as final electron acceptors (Equation I. 1) via hydrogenases play a central role in microbial energy metabolism, “*respiration*”. It should be mentioned that a complex array of functions involving by hydrogenases can occur in one microorganism. A brief review of hydrogenase-related biological processes is presented in this section. For more detailed information, reviews on the topic were reported by P. Vignais *et al.*<sup>8,9</sup> and R. Conrad,<sup>10</sup> and a book was written by R. Cammack *et al.*<sup>11</sup>



It is now known that oxygen respiration (*aerobic respiration*) universally found in eukaryotes and prokaryotes, uses O<sub>2</sub> as terminal electron acceptor and involves electron transfer between redox components of a respiratory chain located in a membrane coupled to a vectorial proton transfer across the membrane.<sup>8,9</sup> For most prokaryotes, non-oxygen respiration (*anaerobic respiration*) can take place in the presence of alternative electron acceptors such as nitrate, fumarate, ferric ion, or sulfate, more specifically termed as nitrate respiration, fumarate respiration, or sulfate respiration, respectively. In Figure I. 2, an illustrative scheme demonstrates various redox reactions of *anaerobic respiration* and other biological processes involving hydrogen production



and consumption by anaerobes and aerobes typically found in stagnant water environment of ponds or damp soils.<sup>10, 11</sup> From bottom to top of the H<sub>2</sub> metabolism community, the reducing power decreases upward while the redox potential at the top is more positive. Hydrogenases mediate H<sub>2</sub> uptake or production to couple various redox reactions while utilizing specific proton channels, electron transfer relays, such as FeS (Fe<sub>4</sub>S<sub>4</sub> or Fe<sub>2</sub>S<sub>2</sub>) clusters and other cell membrane-bound redox couples.

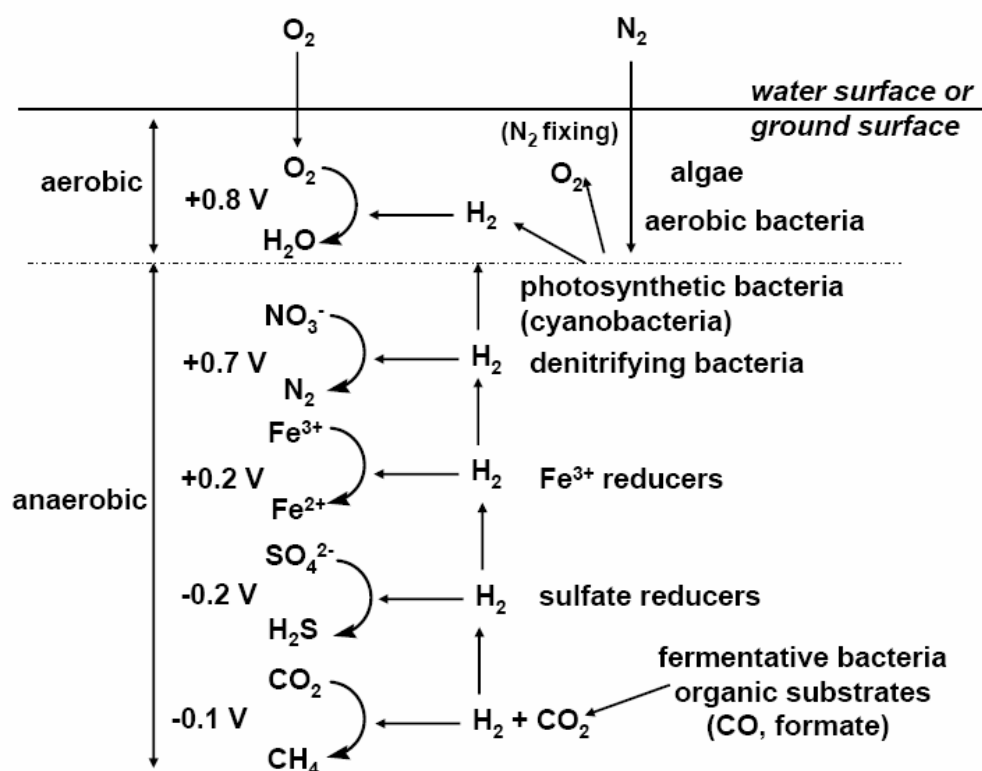


**Figure I. 2** The vertical distribution of different redox reactions of *anaerobic respiration* and other biological processes involving H<sub>2</sub> metabolism via hydrogenases found in microorganisms (adapted from ref. 8, 11 and 23).

The [NiFe]-H<sub>2</sub>ase consists of a large subunit hosting the bimetallic active site and a small subunit containing the FeS clusters. According to amino-acid sequences of subunits and biological functions of the enzymes, the [NiFe]-H<sub>2</sub>ases can be classified into four groups.<sup>8,9</sup>

(1) Periplasmic respiratory (H<sub>2</sub> uptake) [NiFe]-H<sub>2</sub>ases found in bacteria and archaea. In this group, the membrane-bound hydrogenases conduct hydrogen oxidation to reduce quinone and are further related to the anaerobic reductions of NO<sub>3</sub><sup>-</sup> to N<sub>2</sub>, SO<sub>4</sub><sup>2-</sup> to H<sub>2</sub>S, fumarate to succinate, CO<sub>2</sub> to CH<sub>4</sub> or the aerobic reduction of O<sub>2</sub> to H<sub>2</sub>O with the reservation of energy in the form of trans-membrane proton gradients.<sup>8,9</sup> For example, in *Wolinella succinogenes*, the electrons released from H<sub>2</sub> uptake by the [NiFe]-H<sub>2</sub>ase are transferred via FeS clusters to membrane redox mediators of the proximal di-heme cytochrome b group, the quinone / quinol, the distal di-heme cytochrome b group and then transferred outside to cytoplasm where fumarate is reduced to succinate by fumarate reductase.<sup>12</sup> Also there are some periplasmic and membrane-bound hydrogenases coupled with different redox mediators.<sup>8</sup>

(2) Cyanobacterial uptake [NiFe]-H<sub>2</sub>ases (a) and H<sub>2</sub> sensors (b) found in cyanobacteria and proteobacteria, respectively. This group is distinct from group 1 by the amino-acid sequences in the small subunit. The *cyanobacterial* uptake [NiFe]-H<sub>2</sub>ases (group 2a) from the cyanobacteria *Nostoc* and *Anabaena variabilis* are related to nitrogenases.<sup>13</sup> These enzymes are capable of H<sub>2</sub> uptake, a byproduct in nitrogen fixation and therefore they facilitate the N<sub>2</sub>-fixation process. The H<sub>2</sub> sensors (group 2b) of hydrogenases are not directly involved into energy transducing reactions. Their role is to

detect the presence of H<sub>2</sub> and to trigger a series of cellular reactions controlling the biosynthesis of the respiratory [NiFe]-H<sub>2</sub>ases.<sup>9</sup>

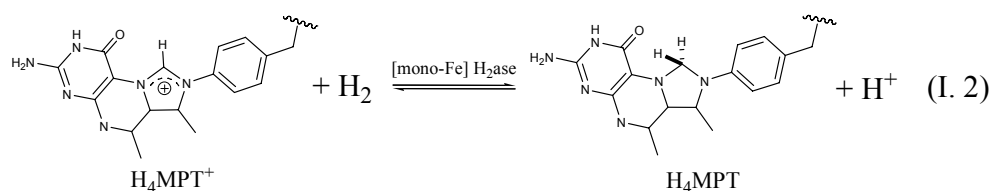
(3) The bidirectional heteromultimeric cytoplasmic [NiFe]-H<sub>2</sub>ases are found in archaea and bacteria. In this group, the dimeric core is associated with other subunits bound with soluble cofactors such as F420 (8-hydroxyl-5-deazaflavin),<sup>14</sup> NAD or NADP.<sup>15</sup> This type of the bacterial [NiFe]-H<sub>2</sub>ases can perform H<sub>2</sub> production from water and reversible H<sub>2</sub> uptake under anaerobic conditions involving energy transfer reactions.

(4) H<sub>2</sub>-evolving, energy-conserving membrane-associated [NiFe]-H<sub>2</sub>ases found in archaea and bacteria. The multimeric enzymes ( $\geq 6$  subunits) produce H<sub>2</sub> from water to reserve excess electron power produced from the anaerobic oxidation of low potential single carbon organic compounds such as CO or formate. For example, the CO-induced [NiFe]-H<sub>2</sub>ase of *Rhodospirillum (abbreviated as R.) rubrum* is a component of the CO-oxidation system that allows *R. rubrum* to grow in the dark by utilizing CO as energy source.<sup>16</sup> The H<sub>2</sub> production process is coupled to a Ni-containing CO-dehydrogenase.

The [FeFe]-H<sub>2</sub>ases are found in anaerobic prokaryotes and some anaerobic eukaryotes. Many [FeFe]-H<sub>2</sub>ases are monomeric and only have the active subunit. Unlike the [NiFe]-H<sub>2</sub>ases, the [FeFe]-H<sub>2</sub>ases are mainly H<sub>2</sub>-evolving enzymes using protons as final electron acceptors. In comparison to the [NiFe]-H<sub>2</sub>ases, the [FeFe]-H<sub>2</sub>ases commonly found in anaerobes such as *Clostridium (abbreviated as C.) pasteurianum* and *Megasphaera elsdeni* are strictly O<sub>2</sub> sensitive.<sup>17</sup> In the green algae of *Chlamydomonas reinhardtii* and *Chlorella fusca*, the [FeFe]-H<sub>2</sub>ase located in the chloroplast utilizes protons as the electron terminals in photosynthetic electron transfer

chain.<sup>18, 19</sup> There are exceptions, such as that the periplasmic [FeFe]-H<sub>2</sub>ase of *Desulfovibrio* (abbreviated as *D.*) *vulgaris* functions as uptake-hydrogenase is thought to protect against oxidative stress.<sup>20</sup>

The [Fe]-H<sub>2</sub>ase is a type of non-redox active enzyme.<sup>21</sup> The enzyme found in *Methanothermobacter marburgensis* has been the most studied. Different from the [FeFe]- and [NiFe]-H<sub>2</sub>ases directly utilizing H<sub>2</sub> and H<sup>+</sup> as substrates, the [Fe]-hydrogenase catalyzes the reversible reduction of N<sup>5</sup>,N<sup>10</sup>-methenyl-tetrahydromethanopterin (methenyl-H<sub>4</sub>MPT<sup>+</sup>, or MPT<sup>+</sup>) with H<sub>2</sub> to N<sup>5</sup>,N<sup>10</sup>-methylene-tetrahydromethanopterin (methylene-H<sub>4</sub>MPT, or HMPT) and a proton (Equation I. 2). This is an intermediate reaction in the process of CO<sub>2</sub> reduction to methane.



### Biophysical studies of hydrogenases and mechanisms

In this section, biophysical investigations on three hydrogenases by biologists, biophysicalists and biochemists are summarized to emphasize the substantial progress that has been made in defining the structures and crucial catalytic states of these enzymes and further proposing the corresponding enzymatic mechanisms. Physical methods

applied in the area include x-ray crystallography, IR spectroscopy, electrochemical voltammetry, EPR spectroscopy, Mössbauer spectroscopy, and other advanced magnetic spectroscopic techniques. There is a series of good reviews published in *Chemical Reviews* in 2007 exclusively on the physical studies of hydrogenases: x-ray crystallography by J. Fontecilla-Camps,<sup>7</sup> IR spectroscopy by A. De Lacey *et al.*,<sup>22</sup> electrochemical voltammetry by K. Vincent *et al.*,<sup>23</sup> and magnetic spectroscopies by W. Lubitz *et al.*<sup>24</sup>

**The [NiFe]-H<sub>2</sub>ase.** The first crystal structure of the [NiFe]-H<sub>2</sub>ase isolated from *D. gigas* was reported with a resolution of 2.8 Å in 1995 by Volbeda, *et al.*<sup>25</sup> Subsequently, four additional crystal structures were reported by other groups.<sup>26-29</sup> There are two subunits in the protein: the large subunit contains the active site and the small subunit hosts one 3Fe4S and two 4Fe4S clusters. The Ni site of the active site was defined, however, the Fe site was unclear and the ligands about the Fe were assigned as three water molecules. The Fe site was later determined with improved x-ray diffraction techniques.<sup>26, 30</sup> Establishment of the diatomic ligands as CO and CN<sup>-</sup> was achieved by IR spectroscopy as summarized below. As generally accepted, the active site (see Figure I. 1 (B)) of the [NiFe]-H<sub>2</sub>ase consists of a bimetallic Ni and Fe construct, in which the metals are bridged by two cysteinyl S ligands; the other two cysteinyl S ligands coordinate to the distorted square planar Ni site. One apical CO and two basal CN<sup>-</sup> coordinate to the Fe site in a square pyramidal geometry. It cannot be determined whether the structure reported by Volbeda, *et al* corresponds to Ni-C or Ni-R state, since the bridged H can not be identified by x-ray diffraction (see Figure I. 3). Other states

including aerobically prepared Ni-A<sup>30</sup> and Ni-B<sup>31</sup> were also crystallographically characterized. Overall, crystallographical studies have provided the structural base to interpret data obtained from other physical and chemical approaches and provide the starting point to theoretical investigations.

The redox active [NiFe]-H<sub>2</sub>ase was first investigated by EPR spectroscopy. Early in 1982, the EPR spectra of the <sup>61</sup>Ni labeled [NiFe]-H<sub>2</sub>ases were reported simultaneously by three groups and established Ni as an essential component in the enzyme.<sup>32-34</sup> These studies revealed three paramagnetic states: Ni-A (g-values, 2.31, 2.23 and 2.01 for *D. gigas*), Ni-B (g-values, 2.33, 2.16 and 2.01 for *D. gigas*), and Ni-C (g-values, 2.19, 2.16 and 2.01 for *D. gigas*). Ni-A and Ni-B states as two standard redox states also were observed in the [NiFe]-H<sub>2</sub>ases isolated from other bacteria including *A. vinosum*, *D. fructosovorans* and *D. vulgaris*. Later it was shown that the EPR signals correlate with the reactivity of the enzyme: Ni-A (unready oxidized state, slow to reactivation) and Ni-B (ready oxidized state, easily reactivated under reduction conditions) were inert to dihydrogen while Ni-C (active state) was active with dihydrogen. Electrochemical titrations of these EPR active states led to other EPR silent states, Ni-SI (oxidized, EPR silent state) and Ni-R (reduced EPR silent state).<sup>22</sup> These EPR silent states were however examined with vibrational spectroscopy in the diatomic ligand region (see below).

The intrinsic diatomic ligands in the active site of the [NiFe]-H<sub>2</sub>ase isolated from *A. vinosum* were first detected by IR spectroscopy in the region ca. 2000 cm<sup>-1</sup>.<sup>35,36</sup> Later IR studies of the enzymes isotropically labeled with <sup>13</sup>C or <sup>15</sup>N permitted assignment of diatomic ligands as one CO (1945 cm<sup>-1</sup>) and two CN<sup>-</sup> (2082 and 2093 cm<sup>-1</sup>) respectively.

<sup>37, 38</sup> The combination of IR spectroscopy and electrochemical titration called IR spectroelectrochemistry were applied to study various redox states of the [NiFe]-H<sub>2</sub>ase from *D. gigas* <sup>39</sup> and *A. vinosum* <sup>40</sup> in order to obtain deeper understandings of EPR results as mentioned above. Using IR monitoring together with electrochemical titrations at different redox levels and different pH values, a total of 11 states were identified for the [NiFe]-H<sub>2</sub>ase from *D. gigas*: <sup>39</sup> Ni-A (CO, 1945 cm<sup>-1</sup>; CN<sup>-</sup>, 2082 and 2093 cm<sup>-1</sup>), Ni-B (CO, 1943 cm<sup>-1</sup>; CN<sup>-</sup>, 2079 and 2090 cm<sup>-1</sup>), Ni-SU (CO, 1948 cm<sup>-1</sup>; CN<sup>-</sup>, 2088 and 2100 cm<sup>-1</sup>), Ni-SI<sub>I</sub> (CO, 1910 cm<sup>-1</sup>; CN<sup>-</sup>, 2052 and 2067 cm<sup>-1</sup>), Ni-SI<sub>II</sub> (CO, 1931 cm<sup>-1</sup>; CN<sup>-</sup>, 2073 and 2084 cm<sup>-1</sup>), Ni-C (CO, 1951 cm<sup>-1</sup>; CN<sup>-</sup>, 2073 and 2085 cm<sup>-1</sup>), Ni-R<sub>I</sub> (CO, 1936 cm<sup>-1</sup>; CN<sup>-</sup>, 2059 and 2072 cm<sup>-1</sup>), Ni-R<sub>II</sub> (CO, 1921 cm<sup>-1</sup>; CN<sup>-</sup>, 2048 and 2064 cm<sup>-1</sup>), Ni-R<sub>III</sub> (CO, 1913 cm<sup>-1</sup>; CN<sup>-</sup>, 2043 and 2058 cm<sup>-1</sup>), Ni-CO (CO, 1929 and 2060 cm<sup>-1</sup>; CN<sup>-</sup>, 2069 and 2082 cm<sup>-1</sup>) and Ni-L (CO, 1989 cm<sup>-1</sup>; CN<sup>-</sup>, 2044 and 2060 cm<sup>-1</sup>). IR studies of the [NiFe]-H<sub>2</sub>ase from other bacteria, *D. fructosovorans* <sup>41</sup> and *D. vulgaris* <sup>42</sup> showed similar spectroscopic data for the various states. A detailed comparison is available in reference 22. Electrochemical potentials applied for interconversion between the redox states are -210 mV for Ni-A/Ni-SU, -135 mV for Ni-B/Ni-SI, -365 mV Ni-SI/Ni-C, and -430 mV for Ni-C/Ni-R. <sup>39</sup> All redox conversions are coupled with proton transfer. Two Ni-SI states and three Ni-R states are pH dependent instead of redox potential dependent. The assay of D<sub>2</sub>/H<sup>+</sup> exchange indicated Ni-SI, Ni-R and Ni-C are active states. <sup>39</sup>

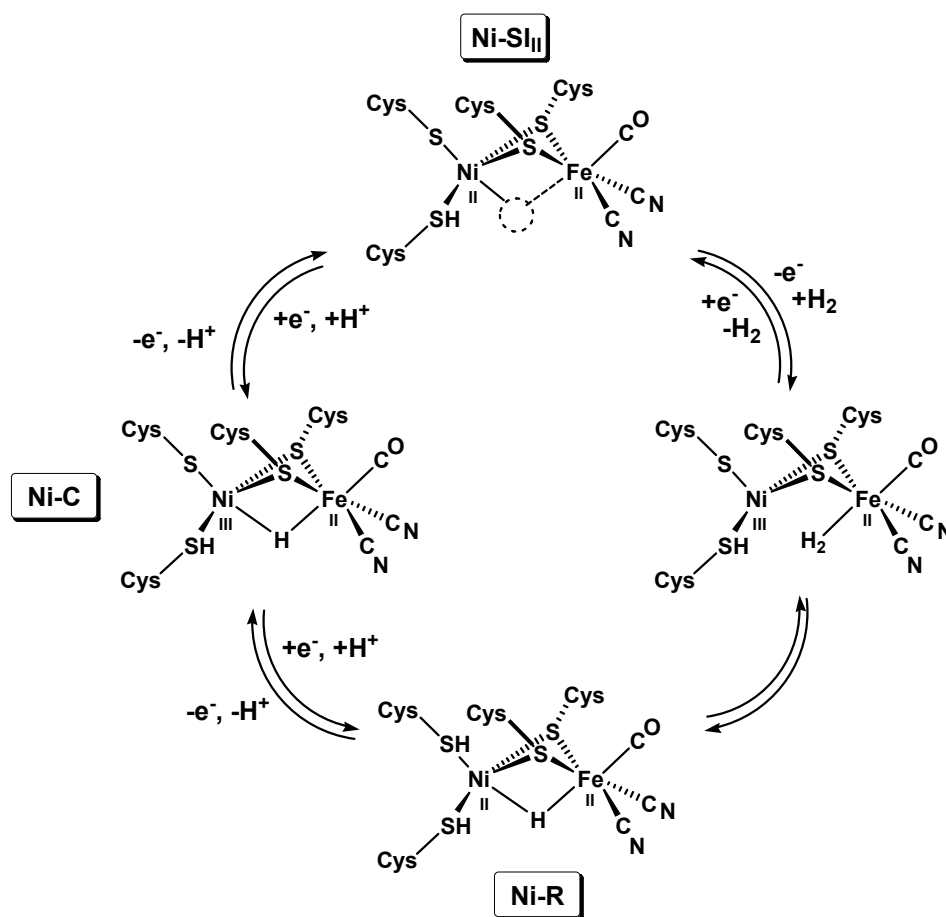


**Figure I. 3** The catalytic mechanism of the [NiFe]-H<sub>2</sub>ase proposed by Hall *et al.*<sup>43</sup>

Although bio-physical studies and biological assays have provided understanding of the enzyme, the catalytic mechanism is still uncertain. Questionable is whether the binding site of substrates, H<sub>2</sub> or H<sup>+</sup>, is Ni or Fe. Figure I. 3 gives a catalytic mechanism of the [NiFe]-H<sub>2</sub>ase according to Hall's theoretical investigation.<sup>43</sup> In this mechanism, one electron oxidation of Ni-SI state permits uptake H<sub>2</sub> at the Fe site to form a  $\eta^2$ -H<sub>2</sub>-adduct. Then, a terminal cysteinyl-S on the Ni site serves as a base to promote hetero- H<sub>2</sub> cleavage to generate the diamagnetic Ni-R state, a Ni-H-Fe bridged hydride.



Subsequently, a proton-coupled electron transfer (PCET) leads to the formation of Ni-C state. Another PCET finishes the catalytic cycle and ends up with the Ni-SI state. The counter-route is for H<sub>2</sub> production.

**The [FeFe]-H<sub>2</sub>ase.** The first crystallographic model of the active site of the [FeFe]-H<sub>2</sub>ase isolated from *C. pasteurianum* was reported by J. Peters *et al.* in 1998.<sup>44</sup> Soon thereafter, J. Fontecilla-Camps and coworkers reported their structure of the [FeFe]-H<sub>2</sub>ase isolated from *D. desulfuricans*.<sup>45</sup> Based on these two reports, a consensus structure of the active site of the [FeFe]-H<sub>2</sub>ase was agreed on as sketched in Figure I. 1 (A). The enzymatic active site contains two Fe atoms, assigned as Fe<sub>p</sub> and Fe<sub>d</sub> according their positions relative to an attached 4Fe4S cluster. One CO and one CN<sup>-</sup> are at the Fe<sub>d</sub> center; one CO, one CN<sup>-</sup> and a cysteinyl S ligand are at the Fe<sub>p</sub> center. A third CO ligand and a dithiolate bidentate ligand bridge between the two Fe sites, and a Fe<sub>4</sub>S<sub>4</sub> cluster is bridged to the Fe<sub>p</sub> center via the cysteinyl S. The vacancy on the Fe<sub>d</sub> center was proposed for binding substrates of H<sub>2</sub> or H<sup>+</sup>. The center atom of the bridging dithiolate has remained uncertain between C, N and O. Most likely, it is a N<sup>46, 47</sup> or O<sup>48</sup> atom instead of a C atom. The structures of H<sub>ox</sub>-CO and H<sub>red</sub> were reported subsequently.<sup>46, 49</sup> In the H<sub>red</sub> structure, the bridged CO in the H<sub>ox</sub> structure became a terminal ligand at the Fe<sub>d</sub> site (see Figure I. 4). And in the structure of H<sub>ox</sub>-CO, the vacancy on the Fe<sub>d</sub> center was replaced by a CO group.

The redox states of the active site of the [FeFe]-H<sub>2</sub>ase were first studied by EPR and Mössbauer spectroscopies in the 1980s.<sup>50-52</sup> The non-heme iron of the [FeFe]-H<sub>2</sub>ase from *D. vulgaris* was first detected with EPR signals at 2.06 and 2.00 by B. Huynh *et al.*

while EPR signals and Mössbauer data indicated the presence of the Fe<sub>4</sub>S<sub>4</sub> cluster as well.<sup>50</sup> Later the unique rhombic EPR signals (2.10, 2.05, 2.00) observed in the more air sensitive [FeFe]-H<sub>2</sub>ase from *C. pasterianum* was assigned to H<sub>ox</sub> state of the enzyme.<sup>51</sup> B. Huynh *et al.* revisited the [FeFe]-H<sub>2</sub>ase from *D. vulgaris* and observed one isotropic signal at 2.02 from the isolated enzyme and two rhombic signals, 2.10, 2.05, 2.00 (-110 mV) and 2.10, 2.04, 2.00 (-300 mV) using electrochemical titrations.<sup>52</sup> The rhombic signals were attributed to different redox states of H<sub>trans</sub> (2.06) and H<sub>ox</sub> (2.10).<sup>53, 54</sup> A more recent study<sup>55</sup> indicated the isotropic signal at 2.02 caused by H<sub>ox</sub>-CO state was due to degradation in purification. This study also established detailed redox chemistry between paramagnetic states and diamagnetic states: H<sub>inac</sub> to H<sub>trans</sub>, one electron reduction; H<sub>trans</sub> to H<sub>ox</sub>, two electron reduction; H<sub>ox</sub> to H<sub>red</sub>, one electron reduction. The H<sub>red</sub> state is also EPR active (1.93) due to the FeS clusters. Under CO, H<sub>ox</sub> state can be converted to H<sub>ox</sub>-CO with a rhombic signal of 2.06, 2.00, and 2.00.

Similar to the biophysical studies of the [NiFe]-H<sub>2</sub>ase, IR spectroscopy has offered major contributions to the assignment of the diatomic ligands as CO and CN<sup>-</sup>, and provided details of the EPR silent states of H<sub>inact</sub> (the isolated inactive state) and other states. The first IR studies of the [FeFe]-H<sub>2</sub>ase of *D. vulgaris* was reported in 1996 as for H<sub>inact</sub> state with  $\nu$  (CO) at 2008, 1983, and 1847 cm<sup>-1</sup> and H<sub>red</sub> state with with  $\nu$ (CO) at 2041, 1964, 1916 and 1894 cm<sup>-1</sup>.<sup>56</sup> Later, in a high quality IR study, two CN<sup>-</sup>s were identified as intrinsic ligands in the enzymatic site of *D. vulgaris*.<sup>57</sup> In the 2000's, IR studies carried out under electrochemical titration conditions allowed accurate assignment of H<sub>inact</sub> ( $\nu$ (CN<sup>-</sup>), 2106 and 2087;  $\nu$ (CO), 2007, 1983 and 1834 cm<sup>-1</sup>), H<sub>trans</sub> ( $\nu$

(CN<sup>-</sup>), 2100 and 2075;  $\nu(\text{CO})$ , 1983, 1977 and 1836  $\text{cm}^{-1}$ ), H<sub>ox</sub> ( $\nu(\text{CN}^-)$ , 2093 and 2079;  $\nu(\text{CO})$ , 1965, 1940 and 1802  $\text{cm}^{-1}$ ), H<sub>ox</sub>-CO ( $\nu(\text{CN}^-)$ , 2096 and 2088;  $\nu(\text{CO})$ , 2016, 1971, 1963 and 1810  $\text{cm}^{-1}$ ), H<sub>red</sub> ( $\nu(\text{CN}^-)$ , 2093 and 2079, 2041;  $\nu(\text{CO})$ , 1965, 1916 and 1894  $\text{cm}^{-1}$ ).<sup>55</sup> In CO uptake and <sup>13</sup>CO/<sup>12</sup>CO exchange experiments,<sup>58</sup> the  $\nu(\text{CO})$  position and pattern helped to assign specific CO binding sites and also to suggest the oxidation state assignment of proximal Fe, +2 and distal Fe, +1 (termed as Fe<sub>p</sub> and Fe<sub>d</sub> respectively in Figure I. 1) although Mössbauer studies at first suggested an Fe<sup>III</sup>Fe<sup>II</sup> assignment.<sup>59, 60</sup>

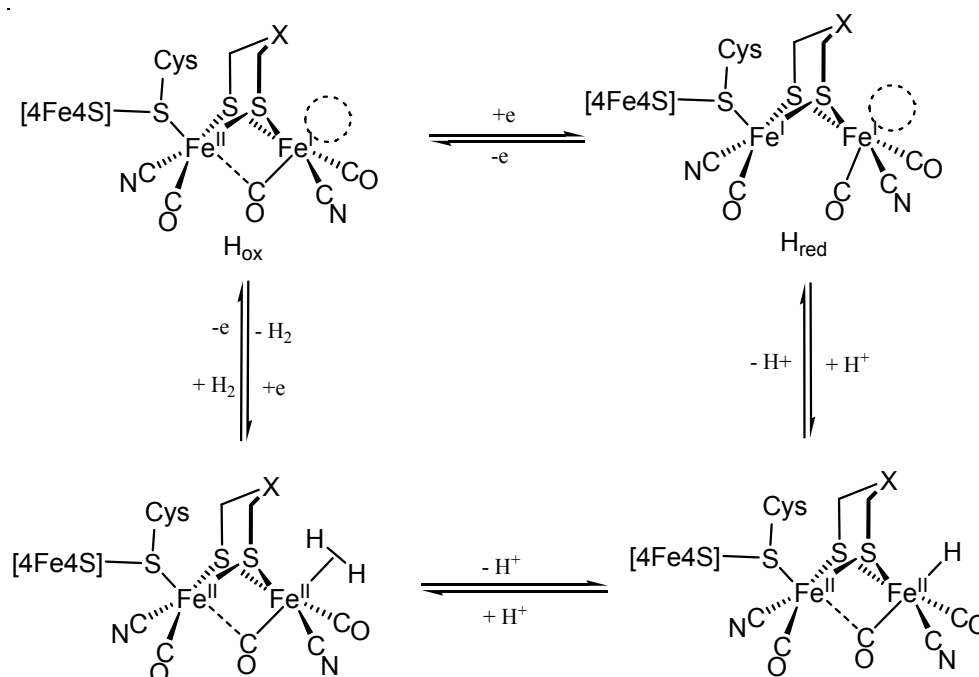


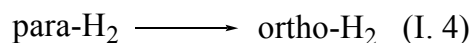
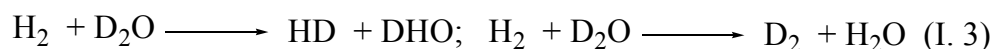
**Figure I. 4** The catalytic mechanism of the [FeFe]-H<sub>2</sub>ase.

A proposed mechanism of the [FeFe]-H<sub>2</sub>ase is given in Figure I. 4.<sup>43</sup> H<sub>ox</sub> is the resting state. Through one electron reduction or oxidation, the active states of H<sub>red</sub> or

unsaturated  $\text{Fe}^{\text{II}}\text{Fe}^{\text{II}}$  state are formed to uptake substrates of  $\text{H}^+$  or  $\text{H}_2$ , respectively. In either case, H-H bond formation or cleavage is governed in a heterolytic hydride/proton fashion.

**The [Fe]-H<sub>2</sub>ase.** The [Fe]-H<sub>2</sub>ase (alternatively called **Hmd** or **H<sub>2</sub>-forming methylene-H<sub>4</sub>MPT dehydrogenase**) was first assessed to be a metal-free enzyme.<sup>21, 61</sup> Most likely, missing the Fe metal as an active component was due to the extreme light sensitivity of the enzyme.<sup>62, 63</sup> Among the three types of hydrogenases, the crystal structure of the [Fe]-H<sub>2</sub>ase was the last one determined by S. Shima, *et al.* in 2008.<sup>64</sup> According to this report, the active site of the [Fe]-H<sub>2</sub>ase consists of a low-spin  $\text{Fe}^{\text{II}}$ , two cis-oriented CO ligands, a cysteinyl-S, an organic pyridinol N ligand, a H<sub>2</sub>O (or an open site) trans to pyridinol N ligand, and an unknown ligand trans to the cysteinyl-S. In 2009, based on the crystal structure of the cysteinyl-S mutant enzyme and XAS spectroscopic data,<sup>65</sup> a new model sketched in Figure I. 1 (C) was proposed for the wild type enzyme first reported in 2008.<sup>64</sup> The active site is composed of a low-spin  $\text{Fe}^{\text{II}}$ , two cis-oriented CO ligands, a cysteinyl-S, an organic pyridone bidentate ligand (N and acyl carbon), and a H<sub>2</sub>O (or an open site) trans to the acyl group as sketched in Figure I. 1.<sup>65</sup>

No EPR signal has been detected in the active state of the non-redox active [Fe]-H<sub>2</sub>ase.<sup>21</sup> The diatomic CO ligands were defined by IR spectroscopy in 2004 by Lyon E. *et al.* Mössbauer studies indicated the oxidation state of the Fe center is low spin  $\text{Fe}^{\text{II}}$ .<sup>66</sup>



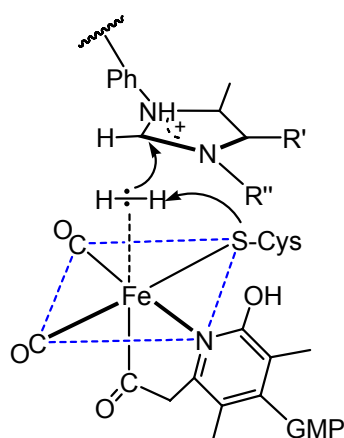


**Figure I. 5** A suggested mechanism for the [Fe]-H<sub>2</sub>ase, i.e., stereoselective hydride abstraction from ( $\eta^2$ -H<sub>2</sub>)Fe<sup>II</sup> by the H<sub>4</sub>MPT<sup>+</sup> substrate (see text).<sup>67</sup>

Biological assays<sup>68</sup> of the activities of the [Fe]-H<sub>2</sub>ase revealed the enzyme catalyzes isotopic H/D exchange (Equation I. 3) and the conversion of para-H<sub>2</sub>/ortho-H<sub>2</sub> (Equation I. 4) only in the presence of MPT<sup>+</sup> while other two hydrogenases catalyze the same reactions without an exogenous electron acceptor.<sup>67</sup> Illustrated in Figure I. 5 is an appealing ternary-complex mechanism put forth by Thauer, Shima, *et al.* that uses the d<sup>6</sup>, Fe<sup>II</sup> catalytic center as an H<sub>2</sub> trapping site, with the carbonium ion of the H<sub>4</sub>MPT<sup>+</sup> substrate strategically positioned to abstract hydride with concurrent proton transfer a nearby base.<sup>21</sup> This mechanism does not invoke an Fe-H intermediary, however, DFT calculations have suggested that a hydride transfer mechanism involving Fe-H cannot be ruled out.<sup>69</sup> In the former view, the Fe behaves like a H<sub>2</sub> trapping site much like the function of the Fe site in the [NiFe]-H<sub>2</sub>ase. In the case involving a hydride intermediate, the [Fe]-H<sub>2</sub>ase and the [FeFe]-H<sub>2</sub>ase should follow a similar hetero-H<sub>2</sub> cleavage or formation mechanism.

## Chemical models of hydrogenases

Applications of hydrogenases as functional electrode materials have been pioneered by the F. Armstrong group<sup>6, 23, 70-77</sup> and other groups.<sup>78-80</sup> However, the enzymatic materials have downsides: they are difficult to produce in large quantities; and, mainly due to O<sub>2</sub> sensitivity, they lack long-term stability. The unique dihydrogen chemistry of hydrogenases and the challenges encountered with biological materials inspires and stimulates chemists to prepare robust synthetic analogues of the active sites with high performance in the absence of the protein matrix. The well developed organometallic chemistry on dihydrogen complexes,<sup>81, 82</sup> metal hydrides<sup>83-86</sup> and metal carbonyls<sup>87-91</sup> has provided fundamental principles and excellent precedents to prepare model complexes of hydrogenases and understand their physical and chemical properties. Since the structural determinations of the [NiFe]-H<sub>2</sub>ase and [FeFe]-H<sub>2</sub>ase, many model complexes have been made that exhibit structural and/or functional similarities as the active sites of enzymes. In the last decade, biomimetics of hydrogenases including experimental and theoretical investigations has made tremendous contributions to mechanistic understandings of these enzymes but also has enriched the areas mentioned above in organometallics. The field has been extensively reviewed by several groups.<sup>43, 68, 92-101</sup> Because the structure of the [Fe]-H<sub>2</sub>ase was reported very recently, synthetic analogues of this enzyme are very few. In this section, experimental studies on model complexes will be briefly summarized to highlight important advances. Theoretical modeling can be referred to reviews.<sup>43, 94</sup>

**The [NiFe]-H<sub>2</sub>ase model complexes.** Before the [NiFe]-H<sub>2</sub>ase structure was

determined, many sulfur-rich mono-Ni complexes in a general form of  $[\text{Ni}(\text{SR})_4]^{2-}$  and, binuclear Ni complexes were developed as putative models of the enzyme in that the active sites of the enzyme was thought to only consist of mono- or binuclear Ni centers. The period was reviewed by A. Halcrow *et al.*, A. Marr *et al.*, and E. Bouwman *et al.*<sup>96, 100, 102</sup> These early studies lent reference compounds or understanding of the spectroscopic information of the enzyme and also provided foundations to later hetero-NiFe bimetallic models. For example, complex **I-1**,  $[\text{Ni}(\text{p-ClC}_6\text{H}_4\text{S}^-)_4][\text{Et}_4\text{N}^+]_2$  was reported by Rosenfield *et al.* early in 1986, in which  $\text{Ni}^{\text{II}}$  has a distorted tetrahedral coordination with four chloro-benzenethiols satisfactorily replicating the Ni site.<sup>103</sup>

Shortly after the structural elucidation of the  $[\text{NiFe}]\text{-H}_2\text{ase}$  revealed the active site of the enzyme contains an unusual  $\text{Fe}(\text{CO})(\text{CN}^-)_2$  moiety, several mono-Fe complexes were prepared in order to examine physical and chemical properties of such moieties. Generally, there are three types of formulas: octahedral  $\text{Fe}(\text{CO})_x(\text{CN}^-)_y$  complexes by S. Koch *et al.*,<sup>104-106</sup> piano stool complexes,  $\text{Cp}^*\text{Fe}(\text{CO})_x(\text{CN}^-)_y$  or  $\text{CpFe}(\text{CO})_x(\text{CN}^-)_y$  by M. Y. Darensbourg *et al.*<sup>107</sup> and other octahedral  $\text{Fe}(\text{CO})_x(\text{CN}^-)_y\text{L}_z$  complexes by W. Liaw *et al.*<sup>108-110</sup> and other groups (L= RS- or phosphine etc.).<sup>93, 101</sup> The  $(\text{Et}_4\text{N}^+)_2[\text{Fe}(\text{CO})_2(\text{CN}^-)_4]$  demonstrated the influence of hydrogen bonding on vibrational energy of CO and  $\text{CN}^-$  stretches.<sup>106</sup> In Figure I. 6, a mononuclear Fe complex, **I-2**, published in 1998 by the Darensbourg group mimicking the iron site of the  $[\text{NiFe}]\text{-H}_2\text{ase}$ , showed similar CO and CN stretching frequencies as that from the enzyme.<sup>107</sup>

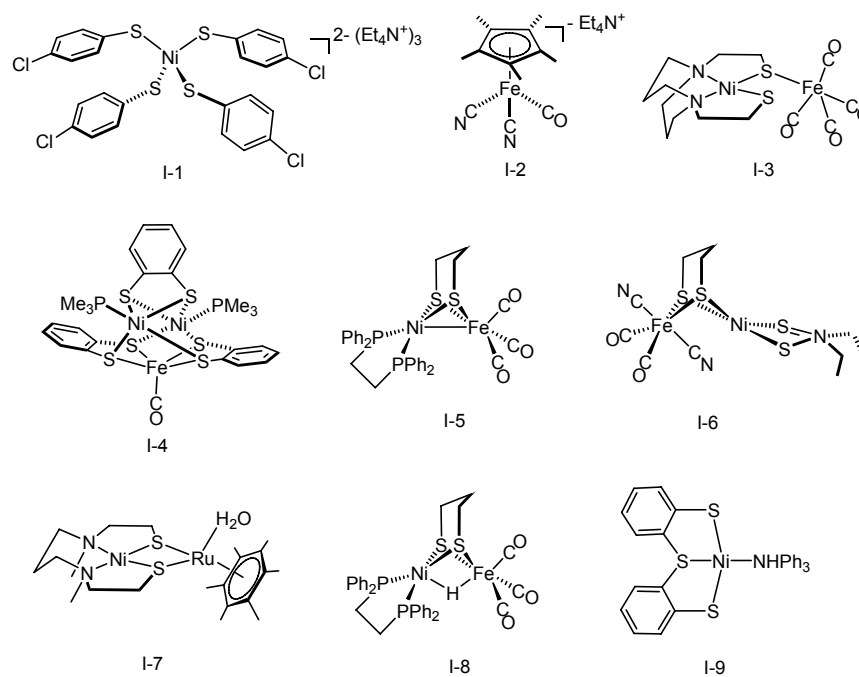


**Figure I. 6** Selected model complexes of the [NiFe]-H<sub>2</sub>ase. See text for references.

The biomimetic advances of mono-Ni and mono-Fe complexes led to the development of more authentic hetero-NiFe bimetallic or multinuclear model complexes. Complex **I-3**, the first complex consisting of both Ni and Fe was reported by M. Darensbourg group in 1998. As one of a few functional models,<sup>111-113</sup> trinuclear complex **I-4** prepared by D. Sellmann's group in 2004 exhibited the ability to catalyze the reduction of protons into dihydrogen. Complex **I-5** reported by M. Schroder's group was synthesized by assembling NiS<sub>2</sub>P<sub>2</sub> and "Fe<sup>0</sup>(CO)<sub>3</sub>" together in an elegant approach.<sup>114</sup> Very recently, this complex was shown by Rauchfuss, et al., to be a very useful precursor to make the first Ni-H-Fe hydride species, **I-8**.<sup>113</sup> The structural model **I-6** satisfying both Ni and Fe environments was published by Tatsumi in 2005 although

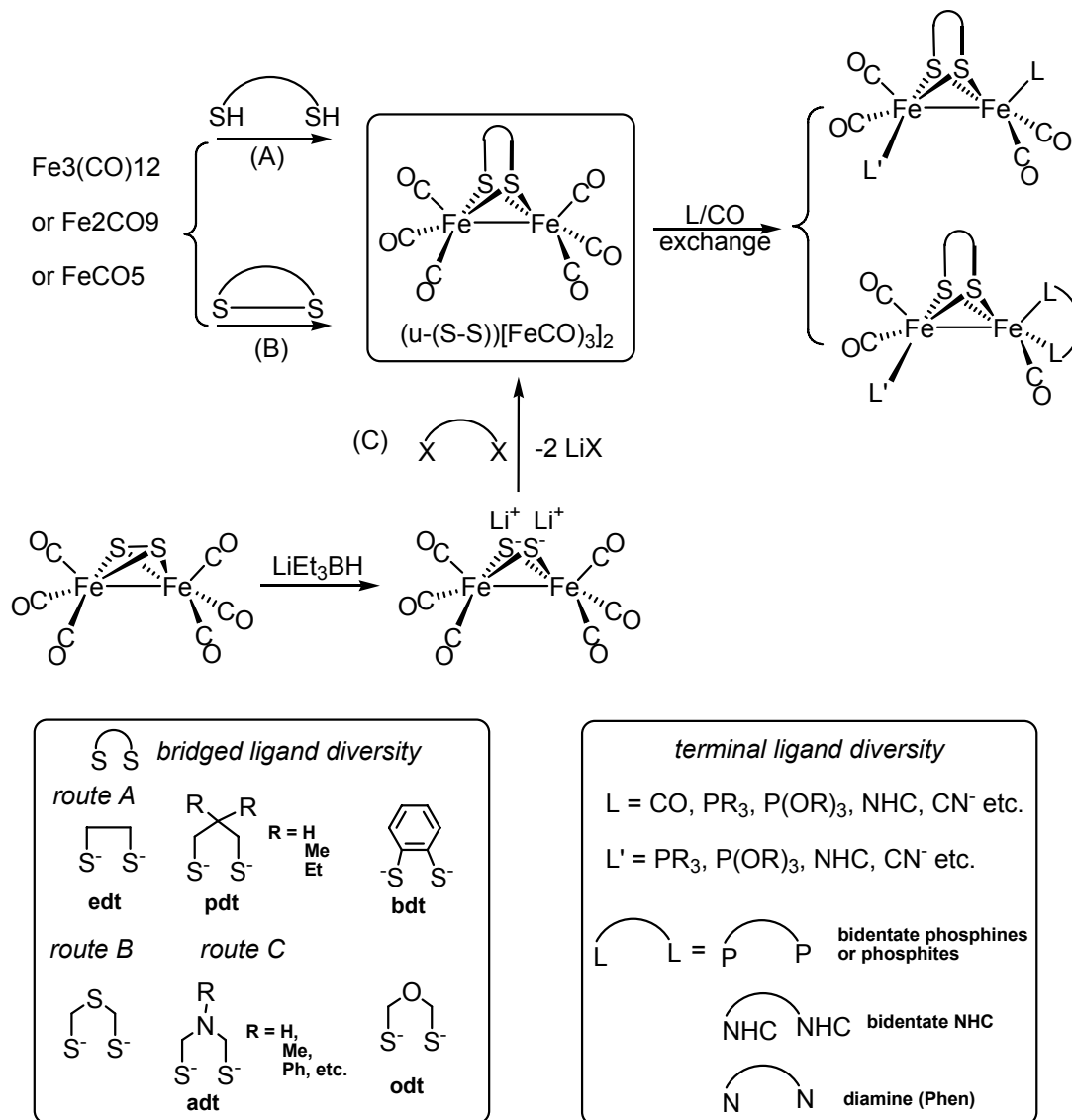


the Ni site has a square planar geometry in contrast to the highly distorted NiS<sub>4</sub> adduct.<sup>115</sup> Among bio-inspired Ni-Ru complexes, Ogo's complex (**I-7**) is very interesting.<sup>116</sup> This complex was shown to activate H<sub>2</sub> in H<sub>2</sub>O under ambient conditions.

Functional models of the [NiFe]-H<sub>2</sub>ase are relatively less developed in comparison to many synthetic models. Few models are functional as electrocatalysts for H<sub>2</sub> production from strong acids.<sup>111-113</sup> There is only one mono-Ni complex, **I-9**, prepared by D. Sellmann *et al.* that catalyzes D<sub>2</sub>/H<sub>2</sub>O exchange, indicating Ni<sup>II</sup> without redox change is enough for H<sub>2</sub> heterolysis.<sup>117</sup> However, Ni and Fe based bimetallic complexes are not known for H<sub>2</sub> activation. Still new designs are required for screening the functions of Ni vs Fe in the processes of H<sub>2</sub> activation and production. It should be mentioned that mono-Ni complexes supported by bidentate phosphine ligand with pending amines developed by D. DuBois *et al.* exhibited capability for both H<sub>2</sub> uptake and production.<sup>118</sup><sup>119</sup> Additionally, the hydride chemistry of the [NiFe]-H<sub>2</sub>ase models is not well understood.

**The [FeFe]-H<sub>2</sub>ase model complexes.** The surprisingly structural resemblance of the diiron subunit of the active site of the [FeFe]-H<sub>2</sub>ase in the so-called H-cluster and the well known organometallic complexes, (μ-SR)<sub>2</sub>[Fe(CO)<sub>3</sub>]<sub>2</sub>,<sup>120</sup> enables synthetic chemists to skillfully construct numerous model complexes of the H-cluster. Likely due to convenient preparations of diiron dithiolate hexacarbonyls as precursors (see Scheme I. 1) of model complexes, biomimetics of the [FeFe]-H<sub>2</sub>ase has attracted much more attention than that of the [NiFe]-H<sub>2</sub>ase.

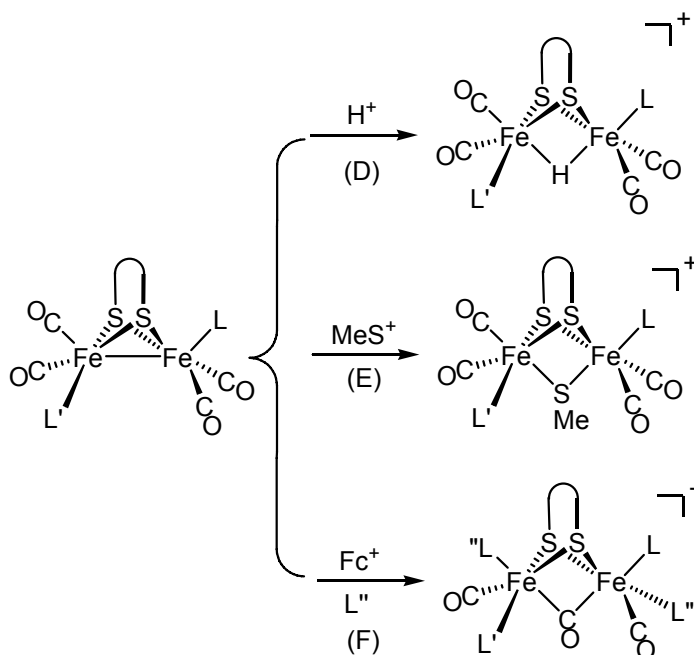
In comparison to diverse synthetic approaches to the [NiFe]-H<sub>2</sub>ase models, the synthetic chemistry of the [FeFe]-H<sub>2</sub>ases is highly formulated as shown in Scheme I. 1 and Scheme I. 2. Representative synthetic approaches to Fe<sup>I</sup>Fe<sup>I</sup> diiron models are given in Scheme I. 1. Three methods (route A,<sup>120, 121</sup> route B<sup>122, 123</sup> and route C<sup>124</sup>) to prepare precursor A,  $\mu$ -(S-S)[Fe(CO)<sub>3</sub>]<sub>2</sub>, were reported in literatures.<sup>125</sup> The reaction nature of route A and route B are almost identical, i.e. oxidative addition of dithiol or cyclic disulfide to Fe<sup>0</sup> carbonyl (Fe<sub>3</sub>(CO)<sub>12</sub>, Fe<sub>2</sub>(CO)<sub>9</sub>, Fe(CO)<sub>5</sub>). Route C is an electrophilic [2+2] cyclo-addition reaction of dihalide and  $\mu$ -(S<sup>-</sup>Li<sup>+</sup>)<sub>2</sub>[Fe(CO)<sub>3</sub>]<sub>2</sub>. The diversity of the S-S linkage is summarized in Scheme I. 1: edt, (-S(CH<sub>2</sub>)<sub>2</sub>S-, 1,2-ethyldithiolate), pdt (R = H, -S(CH<sub>2</sub>)<sub>3</sub>S-, 1,3-propanedithiolate; dmpdt, R = methyl, 2-dimethyl-1,3-propanedithiolate; depdt, R = ethyl, 2-diethyl-1,3,1,3-propanedithiolate), bdt (-S(C<sub>6</sub>H<sub>4</sub>)<sub>3</sub>S-, 1,2-benzylidithiolate), adt (-SCH<sub>2</sub>NRCH<sub>2</sub>S-, azadithiolate) and odt (-SCH<sub>2</sub>OCH<sub>2</sub>S-, oxadithiolate). Among them,  $\mu$ -(S-S)[Fe(CO)<sub>3</sub>]<sub>2</sub> with edt (-S(CH<sub>2</sub>)<sub>2</sub>S-, 1,2-ethyldithiolate), pdt (-S(CH<sub>2</sub>)<sub>3</sub>S-, 1,3-propanedithiolate) and adt (-SCH<sub>2</sub>NRCH<sub>2</sub>S-, azadithiolate) have been mostly utilized to construct ligand modified Fe<sup>I</sup>Fe<sup>I</sup> diiron models via L/CO exchange reactions. The diversity of ligands used in the ligand exchange is also summarized in Scheme I. 1. Depending on the extent of ligand substitution (1, 2 or higher number L/CO substitution) and the type of ligand (monodentate ligand or bidentate ligand), structural components of Fe<sup>I</sup>Fe<sup>I</sup> diiron models are very easily varied. The electronic and steric properties of models can be delicately modulated by careful selection of the S-S linkage and terminal ligands.

**Scheme I. 1** Synthetic routes to  $\text{Fe}^{\text{I}}\text{Fe}^{\text{I}}$  models


Starting from the electron-rich  $\text{Fe}^{\text{I}}\text{Fe}^{\text{I}}$  diiron complexes coordinated with good donors such as phosphines or NHC (N-heterocyclic carbene),  $\text{Fe}^{\text{II}}\text{Fe}^{\text{II}}$  diiron complexes can be

prepared through outersphere or innersphere oxidation (see Scheme I. 2). Specifically,  $\text{Fe}^{\text{II}}\text{Fe}^{\text{II}}$  diiron hydride in the formula of  $(\mu\text{-H})(\mu\text{-S-S})[\text{Fe}(\text{CO})_2\text{L}]_2$ , is made by protonation of  $\text{Fe}^{\text{I}}\text{Fe}^{\text{I}}$  diiron complexes with acids such as  $\text{HCl}$  and  $\text{HBF}_4$  etc. Oxidative addition of  $(\mu\text{-S-S})[\text{Fe}(\text{CO})_2\text{L}]_2$  with  $\text{MeS}^+$  generates  $(\mu\text{-SMe})(\mu\text{-S-S})[\text{Fe}(\text{CO})_2\text{L}]_2$ . Another class of  $\text{Fe}^{\text{II}}\text{Fe}^{\text{II}}$  diiron complexes,  $(\mu\text{-CO})(\mu\text{-S-S})(\text{Fe}_2(\text{CO})_x\text{L}_y)$ , are prepared through electron transfer reaction of  $(\mu\text{-S-S})[\text{Fe}(\text{CO})_2\text{L}]_2$  with the oxidant,  $\text{Fc}^+\text{BF}_4^-$ , in the presence of additional ligands.

**Scheme I. 2** Synthetic routes to  $\text{Fe}^{\text{II}}\text{Fe}^{\text{II}}$  models



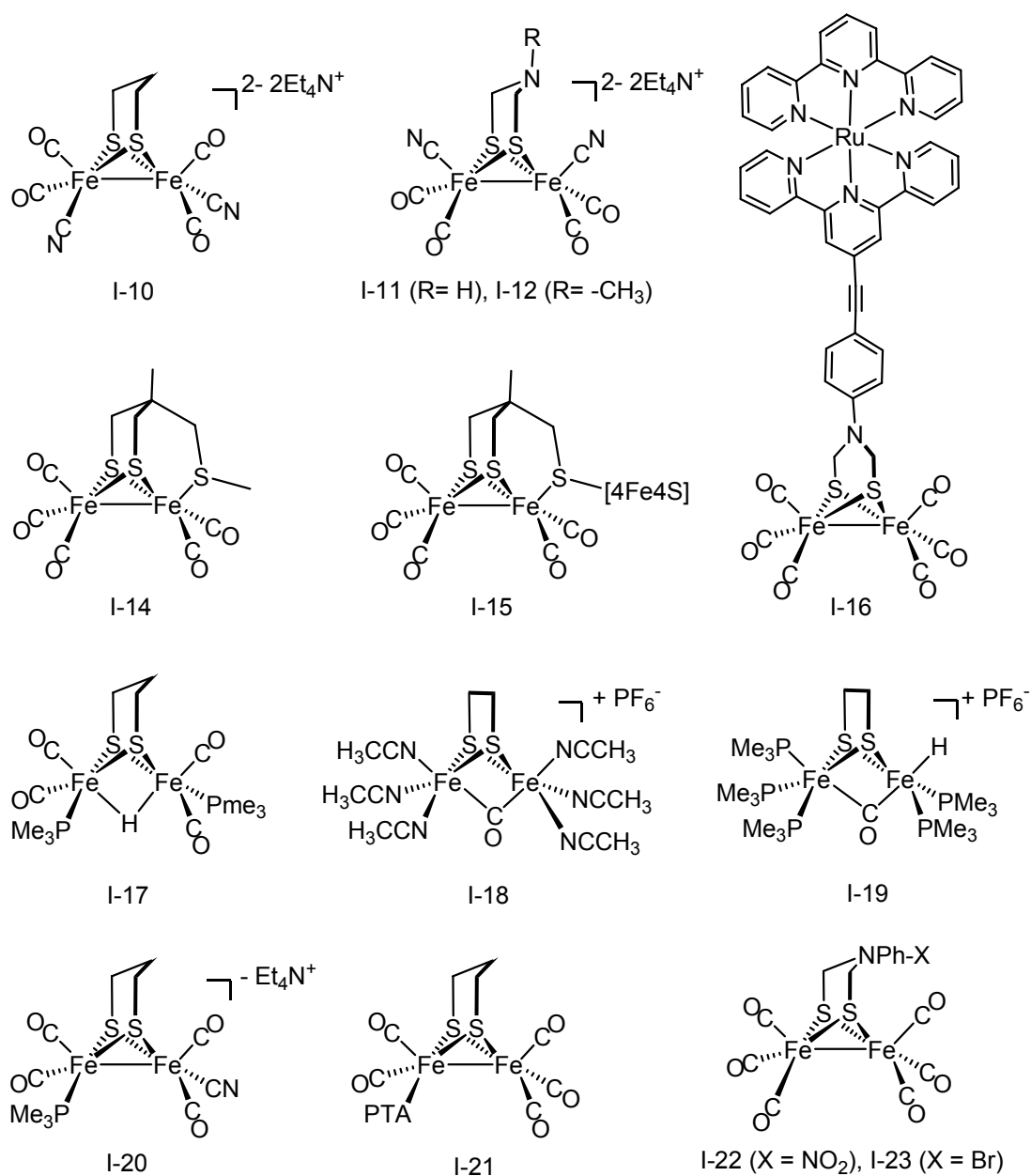


**Figure I. 7** Selected model complexes of the [FeFe]-H<sub>2</sub>ase. See references in text.

Significant progresses of the [FeFe]-H<sub>2</sub>ase models are addressed by examples shown in Figure I. 7. Complex **I-10** was reported simultaneously in 1999 by three groups (Rauchfuss, Darensbourg and Pickett; Scheme I. 1, route A)<sup>126-128</sup> which stands for the

first model and possesses a similar structure framework of the active site. As reported by Rauchfuss *et al.* in 2001, complexes **I-11** and **I-12** with the same coordination conformation as complex **I-10** are the first adt (azadithiolate,  $-\text{SCH}_2\text{NRCH}_2\text{S}-$ , R= H, Me) bridged diiron complexes and are thought to be more faithful to the diiron cofactor of H-cluster (Scheme I. 1, route C).<sup>129</sup> The synthetic approach<sup>130</sup> to the complexes provides a versatile methodology for more complex N-functionalized azadithiolate models reported by other groups. In the same year, Pickett's group reported the first  $\text{Fe}_2\text{S}_3$  models such as complex **I-13** by following route A in Scheme I. 1. This group applied the synthetic strategy to synthesize a more sophisticated complex, **I-15**, which contains a  $4\text{Fe}4\text{S}$  cluster attached to the Fe of diiron subunit.<sup>131</sup>

Complex **I-17** was the first  $\text{Fe}^{\text{II}}\text{Fe}^{\text{II}}$  hydride model complex to mimic the enzymatic active site (Scheme 1, route D).<sup>132</sup> This work led to the synthesis of other diiron hydride complexes. In 2004, structurally characterized complex **I-18**<sup>133</sup> and other  $\text{Fe}^{\text{II}}\text{Fe}^{\text{II}}$  derivatives synthesized by Rauchfuss' group according to their previous exploration (Scheme I. 1, route F),<sup>134</sup> were featured with a bridging CO ligand and were assumed to mimic  $\text{H}_{\text{air}}$  state of the enzyme. Based on this synthetic advance, the first  $\text{Fe}^{\text{II}}\text{Fe}^{\text{II}}$  terminal hydride, **I-19**, to mimic  $\text{H}_{\text{red}}$  state, was reported by the same group.<sup>135</sup> The structure of the complex features a terminal hydride and a hemi-bridged CO underneath the Fe-Fe vector. However, this terminal hydride species is thermally unstable and easily isomerized to the bridged hydride species. It was proved later that the form of terminal hydride is an isomer occurring in the protonation of  $\text{Fe}^{\text{I}}\text{Fe}^{\text{I}}$  complexes.<sup>136</sup>

Since 2003, other groups have joined the area of biomimetic of the [FeFe]-H<sub>2</sub>ase. Sun's group built Ru photosynthesizers into azadithiolate diiron models through covalent attachment to assemble a conceptual supramolecule (for example, complex **I-16**) designed for photo-induced H<sub>2</sub> production.<sup>137, 138</sup> Similar diiron supramolecules including other dye units were reported later.<sup>139-141</sup>

Early attempts to use the [FeFe]-H<sub>2</sub>ase models for functional studies were pioneered by Darensbourg's group and Rauchfuss' group. Darensbourg's group reported that complex **I-17** demonstrated the ability of H/D exchange in the mixture of D<sub>2</sub> and H<sub>2</sub>O, showing function as H<sub>2</sub> activation.<sup>132</sup> In their later reports, other Fe<sup>II</sup>Fe<sup>II</sup> hydrides and a thiolate bridged Fe<sup>II</sup>Fe<sup>II</sup> complex (see Scheme I. 2, route E) exhibited similar catalytic capability for D<sub>2</sub>/H<sub>2</sub>O or D<sub>2</sub>/C<sub>2</sub>H<sub>4</sub> exchange.<sup>142-144</sup> In Rauchfuss's investigation, complex **I-20** was shown to electrochemically catalyze H<sub>2</sub> production in the presence of strong acids, HCl or HOTs.<sup>145</sup> Subsequently, Darensbourg *et al.* reported other simple Fe<sup>I</sup>Fe<sup>I</sup> models (such as complex **I-21**) as electrocatalysts for H<sub>2</sub> production from a weak acid, HOAc.<sup>146, 147</sup> Azadithiolate Fe<sup>I</sup>Fe<sup>I</sup> models, complexes **I-22** and **I-23**, were also reported to be functional for H<sub>2</sub> production, in which the built-in amine was thought to facilitate the proton transfer and decrease overpotential.<sup>148, 149</sup> Later numerous diiron model complexes were shown to be functional for electrochemical H<sub>2</sub> production.

Additionally, in pursuit of more practical applications of model complexes, the immobilization of model complexes onto glassy carbon electrodes for heterogeneous H<sub>2</sub> production was attempted by several groups.<sup>150-152</sup> But the efficiency of these systems is poor for proton reduction.

Reported by Sun and Song with their respective coworkers, dye-diiron supramolecules as mentioned above were able to photo-catalyze proton reduction at moderate efficiency in the presence of appropriate sacrificial electron donors.<sup>139, 140, 153</sup>

To summarize the advances made in the last decade for the chemical modeling of the [FeFe]-H<sub>2</sub>ase, some comments and perspectives are given here. In terms of structural and function modeling as well as constructive insights into the enzymatic chemistry, the biomimetic studies of the [FeFe]-H<sub>2</sub>ase are much more fruitful than that of the [NiFe]-H<sub>2</sub>ase. As for structural models, unsaturated mixed-valent Fe<sup>I</sup>Fe<sup>II</sup> complexes remained unknown prior to this dissertation work, which is described in detail in Chapter III. Hydride chemistry of diiron models needs further exploration. Preventing the terminal hydride from isomerizing to a bridged hydride is a target of new model designs with consideration of the second coordination sphere since the similar terminal hydride state of the active site is most likely stabilized by surrounding protein matrix. Concerned with functional models, direct H<sub>2</sub> uptake by diiron models is a challenge. A recent communication from Rauchfuss' group made a good attempt to activate H<sub>2</sub> under harsh conditions.<sup>154</sup> It is commonly accepted that diiron model are capable of catalyzing H<sub>2</sub> production. However, model complexes normally function at their Fe<sup>I</sup>Fe<sup>0</sup> redox level that is not the desired state proposed for the enzymatic activity, and therefore, have a large overpotential.<sup>155</sup> The second major problem is the stability of models in electrocatalysis. Furthermore, water soluble models or hydrophilic models are needed for proton reduction from neutral pH = 7 aqueous media. To solve these problems and



achieve more practical materials, close consideration of structure and function relationships should be addressed by new synthetic designs.

**The [Fe]-H<sub>2</sub>ase model complexes.** Synthetic analogues (see Figure I. 8) recently developed for the [Fe]-H<sub>2</sub>ase include octahedral Fe<sup>II</sup> dicarbonyls (complexes **I-24** and **I-25**) that mimic the denatured state of the enzyme.<sup>156, 157, 158</sup> Rauchfuss' group reported an unstable hexa-coordinate (PhS)(Ph<sub>2</sub>PC<sub>6</sub>H<sub>4</sub>C(=O))Fe(CO)<sub>3</sub>,<sup>159</sup> complex **I-26**, which has the acyl carbonyl built in as analogue of the CO-inhibited state.<sup>156</sup> Rare examples of pentacoordinate, presumably Fe<sup>II</sup> dicarbonyl were reported earlier by Holland's group and Liaw's group. Liaw's complex, **I-28**, is supported by a good  $\pi$  donating bidentate ligand, 2-amido-phenothiolate.<sup>160</sup> Holland's (acetyl)Fe<sup>II</sup> complex (**I-27**) was derived from carbonylation of a 3-coordinate Fe-Me species.<sup>161</sup>

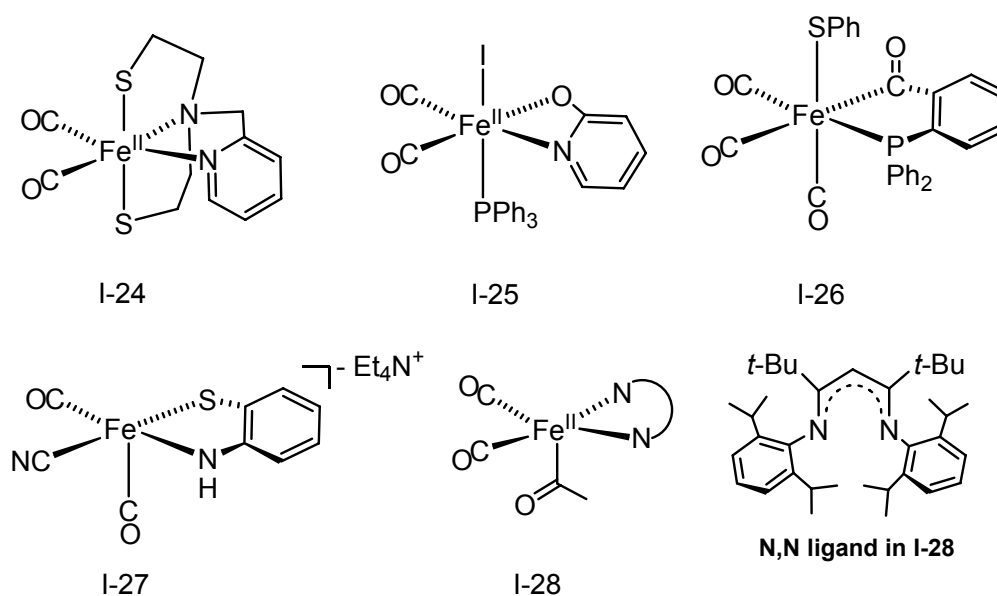


**Figure I. 8** Selected model complexes of the [Fe]-H<sub>2</sub>ase. See references in text.

### Research conducted in this dissertation

This dissertation describes synthesis, reactivities and theoretical investigations of binuclear and mononuclear Fe carbonyl complexes that model the active site of the [FeFe]- and [Fe]-H<sub>2</sub>ases. In Chapter III, a series of mixed-valent Fe<sup>I</sup>Fe<sup>II</sup> complexes, as (μ-CO)(μ-pdt)[Fe<sub>2</sub>(CO)<sub>3</sub>PMe<sub>3</sub>NHC], developed to mimic the structure and function of the H<sub>ox</sub> state of the [FeFe]-H<sub>2</sub>ase will be discussed. In Chapter IV, sulfur oxygenation of (μ-pdt)[Fe<sub>2</sub>(CO)<sub>3</sub>]<sub>2</sub> and its phosphine derivatives and deoxygenation of the corresponding sulfur oxygenates provides synthetic models relevant to the oxygen sensitivity of the [FeFe]-H<sub>2</sub>ase. In Chapter V, the intramolecular CO site exchange and intermolecular CO/L exchange of (μ-pdt)[Fe<sub>2</sub>(CO)<sub>3</sub>]<sub>2</sub> and its sulfur oxygenate, (μ-pst)[Fe<sub>2</sub>(CO)<sub>3</sub>]<sub>2</sub> (pst = -S(O)(CH<sub>2</sub>)<sub>3</sub>S-), will be discussed, which provides insight into the fundamental chemistry related to the CO/L exchange reaction of (μ-(S-S))[Fe<sub>2</sub>(CO)<sub>3</sub>]<sub>2</sub>. In Chapters VI and VII, the coordination chemistry of Fe(CO)<sub>4</sub>I<sub>2</sub> and mono-Fe complexes as models of the [Fe]-H<sub>2</sub>ase active site will be presented. Interesting results on electronic structure and reactivities of non-innocent mono-Fe complexes, (NS)Fe(CO)<sub>2</sub>P (NS = 2-aminophenothiolate; P = PCy<sub>3</sub>, PPh<sub>3</sub>, P(OEt)<sub>3</sub>), are analyzed.

## CHAPTER II

### EXPERIMENTAL

#### Materials and techniques

All reactions and operations were conducted on a double-manifold Schlenk vacuum line under N<sub>2</sub> or Ar atmosphere. Hexane, tetrahydrofuran (THF), CH<sub>2</sub>Cl<sub>2</sub>, Ether, acetone, MeOH, CH<sub>3</sub>CN and toluene were first degassed with N<sub>2</sub> for 30 minutes and then purified by an MBraun Manual Solvent Purification System packed with Alcoa F200 activated alumina desiccant. Hexane and toluene were freshly collected from the solvent system and used in experiments. The purified THF, CH<sub>2</sub>Cl<sub>2</sub> and CH<sub>3</sub>CN were stored over molecular sieves under N<sub>2</sub> for 24 hrs prior to further purification: THF was distilled under N<sub>2</sub> from sodium/benzophenone; CH<sub>2</sub>Cl<sub>2</sub>, CaCl<sub>2</sub>, and CH<sub>3</sub>CN was first stirred with CaH<sub>2</sub> at 22 °C for 5 hrs and then distilled. The collected CH<sub>2</sub>Cl<sub>2</sub> and CH<sub>3</sub>CN were stored over molecular sieves under Ar for experimental uses.

The known complexes, (μ-pdt)[Fe(CO)<sub>3</sub>]<sub>2</sub> (pdt = 1,3-propanedithiolate),<sup>162</sup> (μ-pdt)[Fe(CO)<sub>2</sub>PMe<sub>3</sub>]<sub>2</sub>,<sup>132</sup> (μ-pdt)(μ-H)[Fe(CO)<sub>2</sub>PMe<sub>3</sub>]<sub>2</sub>,<sup>132</sup> (μ-pdt)[Fe(CO)<sub>3</sub>][Fe(CO)<sub>2</sub>PPh<sub>3</sub>],<sup>163</sup> (μ-pdt)[Fe(CO)<sub>3</sub>][Fe(CO)<sub>2</sub>PMe<sub>3</sub>],<sup>164</sup> (μ-pdt)[Fe(CO)<sub>3</sub>][Fe(CO)<sub>2</sub>(IMes)],<sup>165</sup> 1,3-bis(methyl)imidazolium iodide,<sup>166</sup> methyl,3-(2,4,6-trimethylphenyl)imidazolium iodide,<sup>167</sup> DDO (dimethyldioxirane)<sup>168</sup> and FeI<sub>2</sub>(CO)<sub>4</sub><sup>169</sup> were prepared according to published procedures. The following materials were of reagent grade and were directly used as purchased from Sigma-Aldrich or TCI Chemical Companies: NaO*t*-Bu, KO*t*-Bu, Fe(CO)<sub>5</sub>, Fe<sub>3</sub>(CO)<sub>12</sub>, PMe<sub>3</sub>, PCy<sub>3</sub>, PPh<sub>3</sub>,

P(OEt)<sub>3</sub>, pyridine, 2,2'-bipyridine and 1,10-phenanthroline, 1,3-propanedithiol, 2-aminophenethiol, 1,3-Bis(2,4,6-trimethylphenyl)imidazolium chloride, trimethylphosphine, FcPF<sub>6</sub>, Cp<sub>2</sub>Co Cp\*<sub>2</sub>Co, m-chloroperoxy-benzoic acid (m-CPBA), H<sub>2</sub>O<sub>2</sub>,

**Spectroscopy.** <sup>1</sup>H- and <sup>31</sup>P NMR spectra were measured on a Unity+ 300 MHz superconducting NMR instrument. Variable temperature <sup>13</sup>C NMR spectra were collected on natural abundance samples using a Unity+ 500 MHz superconducting NMR instrument operating at 125.9 MHz. Solution infrared spectra were measured on a Bruker Tensor 27 FTIR spectrometer using 0.1 mm NaCl sealed cells. The X-band EPR spectrum was recorded at 10 K on a Bruker EMX spectrometer using a Hewlett-Packard 5352B microwave frequency counter, the ER4102ST cavity, and the Oxford Instruments ESR900 cryostat. The simulated spectrum was obtained by use of the WINEPR Simfonia program Version 1.25. Mössbauer spectra were collected with a spectrometer model CCR4K, in constant acceleration mode, cooled to cryogenic temperatures by a closed-cycle refrigerator and fitted with a permanent 300 Gauss magnet. The spectra were analyzed with the program WMOSS (Thomas Kent, SeeCo.us, Edina, Minnesota).

**X-ray structure determinations.** For all reported structures a Bausch and Lomb 10x microscope was used to identify suitable crystals of the same habit. Each crystal was coated in paratone, affixed to a Nylon loop and placed under streaming nitrogen (110K) in a Bruker SMART 1000 CCD, Bruker Gadds or Bruker-AXS APEXII diffractometer. The space groups were determined on the basis of systematic absences and intensity statistics. The structures were solved by direct methods and refined by full-

matrix least squares on  $F^2$ . Anisotropic displacement parameters were determined for all nonhydrogen atoms. Hydrogen atoms were placed at idealized positions and refined with fixed isotropic displacement parameters. The following is a list of programs used: data collection and cell refinement, SMART WNT/2000 Version 5.632<sup>63</sup> or FRAMBO<sup>111</sup> Version 4.1.05 (GADDS); data reductions, SAINTPLUS Version 6.63;<sup>161</sup> absorption correction, SADABS;<sup>62</sup> structural solutions, SHELXS-97;<sup>115</sup> structural refinement, SHELXL-97;<sup>66</sup> graphics and publication materials, X-Seed Version 1.5.<sup>170</sup> All x-ray structures are available in the Cambridge Crystallographic Data Centre.

**Electrochemistry.** Measurements were carried out using a BAS 100A electrochemical analyzer. All voltammograms were obtained in a conventional and gastight three-electrode cell under Ar atmosphere at 22 °C. The working electrode was a glassy carbon disk (0.071 cm<sup>2</sup>) which was successively polished with 15- $\mu$ m, 3- $\mu$ m and 1- $\mu$ m diamond paste three times and alternately cleaned with deionized water after each polish treatment. Then the electrode was sonicated in MeOH for 15 min prior to use. The supporting electrolyte was 0.1 M *n*-Bu<sub>4</sub>NBF<sub>4</sub> in CH<sub>3</sub>CN. The experimental reference electrode was Ag/Ag<sup>+</sup> prepared by anodizing a silver wire in a CH<sub>3</sub>CN solution of 0.01 M AgNO<sub>3</sub>/0.1 M *n*-Bu<sub>4</sub>NBF<sub>4</sub>. The counter electrode was a platinum wire. All potentials were measured in CH<sub>3</sub>CN solutions which were 0.1 M in *n*-Bu<sub>4</sub>NBF<sub>4</sub>, and reported relative to Fc<sup>+</sup>/Fc as an internal standard.

**Theoretical details.** DFT calculations were performed using a hybrid functional [the three parameter exchange functional of Becke (B3)<sup>171</sup> and the correlation functional of Lee, Yang, and Parr (LYP)<sup>172</sup> (B3LYP) as implemented in Gaussian 03.<sup>173</sup> The effective

core potentials and associated basis set of Hay and Wadt (LANL2DZ)<sup>174, 175</sup> were used on the iron, sulfur and phosphorus atoms. For iron, the two outermost p functions were replaced by the reoptimized 4p functions as suggest by Couty and Hall.<sup>176</sup> For sulfur and phosphorus, the basis set was augmented by the d polarization function of Höllwarth et al.<sup>177</sup> All carbon, nitrogen, oxygen and hydrogen atoms were represented using Dunning's double zeta valence basis (D95)<sup>178, 179</sup> or Dunning's correlation-consistent polarized valence double- $\zeta$  basis set (cc-pVDZ)<sup>180</sup>. For some complexes, calculations were also examined with different functionals or basis sets to support the results obtained from the B3LYP functional (In such cases, the computational details are described in corresponding chapters). The geometries of ground state or transition state of all species were fully optimized and confirmed as minima or first-order saddle point by analytical frequency calculations at the same levels.

### Experimental for chapter III

**( $\mu$ -pdt)[Fe(CO)<sub>2</sub>IMes][Fe(CO)<sub>3</sub>] (III-1<sub>NHC</sub>) and ( $\mu$ -pdt)[Fe(CO)<sub>2</sub>IMe][Fe(CO)<sub>3</sub>] (III-3<sub>NHC</sub>).** Mono-substituted complexes, **III-1<sub>NHC</sub>** and **III-3<sub>NHC</sub>**, were prepared in an improved procedure according to earlier reports.<sup>165, 181</sup> Solid ( $\mu$ -pdt)[Fe(CO)<sub>3</sub>]<sub>2</sub> (2.32g, 6 mmol) and the imidazolium salt (6 mmol) were combined and dissolved in THF (50 mL). After stirring for 30 min, 12 mmol of KO<sup>t</sup>Bu in 20 mL THF was added and the resulting mixture was stirred for an additional 30 min, monitoring by IR spectroscopy to confirm that the reaction had reached completion. Solid byproducts were removed from the reaction mixture by filtration through a sintered glass frit. After removal of THF

from the filtrate under vacuum, the crude product was extracted into 50 mL ether, dried in vacuo and then washed with methanol (2 x 10 mL). Yield: **1**<sub>NHC</sub> (85%), **3**<sub>NHC</sub> (83%).

**( $\mu$ -pdt)[Fe(CO)<sub>2</sub>IMesMe][Fe(CO)<sub>3</sub>] (III-2<sub>NHC</sub>).** Solid 1-methyl,3-(2,4,6-trimethylphenyl)imidazolium iodide (0.653 g, 2.00 mmol) was suspended in THF (50 mL). To this was added solid KO<sup>t</sup>Bu (0.248 g, 2.21 mmol) and the resulting mixture was stirred for 2.5 hours at 22°C. To this cloudy yellow solution was added solid ( $\mu$ -pdt)[Fe(CO)<sub>3</sub>]<sub>2</sub> (0.771 g, 2.00 mmol). The solution immediately darkened to red/brown. After 2 h, the solution was filtered through Celite and dried in vacuo. The resulting red solids were dissolved in toluene and loaded onto a silica gel column (12 in x 1 in). Elution with petroleum ether removed excess starting material. The product was then eluted with 1:1 petroleum ether/THF. Solvent was evaporated from the dark red eluant to yield spectroscopically pure product (0.77 g, 69%). Crystals suitable for X-ray diffraction were grown via slow diffusion of Et<sub>2</sub>O into a concentrated CH<sub>2</sub>Cl<sub>2</sub> solution at -35 °C. IR (THF, cm<sup>-1</sup>): 2035 (m), 2025 (m), 1970 (vs), 1949 (m), 1916 (w). <sup>1</sup>H NMR (300 MHz, acetone-*d*<sub>6</sub>):  $\delta$  = 7.65 (s, 1H, NCH), 7.27 (s, 1H, NCH), 7.05 (s, 2H, *m*-Mes), 4.16 (s, 3H, Me), 2.33 (s, 3H, *p*-Mes), 2.13 (m, 2H, pdt), 2.09 (s, 6H, *o*-Mes), 1.82 (m, 4H, pdt). Anal. Calcd for C<sub>21</sub>H<sub>22</sub>N<sub>2</sub>Fe<sub>2</sub>S<sub>2</sub>O<sub>5</sub>: C, 45.18; H, 3.97; N, 5.02. Found: C, 45.39; H, 4.50; N, 4.87.

**( $\mu$ -pdt)[Fe<sup>I</sup>(CO)<sub>2</sub>IMes][Fe<sup>I</sup>(CO)<sub>2</sub>PMe<sub>3</sub>] (III-1).** Excess PMe<sub>3</sub> was added into a solution of complex **III-1**<sub>NHC</sub> (200.0 mg, 0.3 mmol) in toluene. The mixture was stirred and refluxed overnight under N<sub>2</sub>. Following solvent removal in vacuo, the dark red crude product was purified by column chromatography with hexane as the eluent. The second

band was collected and stripped of solvent, recovering a dark red solid as a slightly air sensitive product, which was further purified by recrystallization from hexane. Yield: 83.3 % (177.9 mg, 0.25 mmol). Dark red crystals, suitable for X-ray analysis, were grown by cooling a hexane solution. IR ( $\nu$  (CO) region in  $\text{CH}_2\text{Cl}_2$ ,  $\text{cm}^{-1}$ ) 1972 (s), 1933 (vs), 1897 (s), 1882 (m,sh);  $^1\text{H}$  NMR (ppm, acetone- $d_6$ ) 7.17 (s, 2 H), 7.06(s, 2H), 2.86 (d, 2 H,  $J_{\text{H-H}} = 10$  Hz), 2.36 (s, 6 H), 2.26 (s, 12H), 1.58 (br, 4H) 1.44 (br, 2H), 1.31 (d, 9H,  $J_{\text{P-H}} = 9$  Hz);  $^{31}\text{P}$  NMR (ppm, acetone- $d_6$ ) 25 ppm. Elemental analysis, found (calculated for  $\text{C}_{31}\text{H}_{39}\text{Fe}_2\text{N}_2\text{O}_4\text{PS}_2$ ) %: C, 52.89 (52.33); H, 5.59 (5.67), N, 3.99 (3.94).

**( $\mu$ -pdt)[Fe(CO) $_2$ IMesMe][Fe(CO) $_2$ PMe $_3$ ] (III-2).** To a stirred solution of **III-2**<sub>NHC</sub> (0.226 g, 0.406 mmol) in toluene (25 mL) was added PMe $_3$  (0.21 mL, 2.0 mmol), followed by reflux for 16 h. The solution, devoid of starting material as monitored by IR, was filtered through a plug of silica gel and volatiles were removed from the resulting dark red solution in vacuo to yield analytically pure product (0.144 g, 58%). IR ( $\text{CH}_2\text{Cl}_2$ ,  $\text{cm}^{-1}$ ): 1974 (m), 1934 (s), 1899 (m), 1884 (w).  $^1\text{H}$  NMR (300 MHz, acetone- $d_6$ ):  $\delta = 7.63$  (s, 1H, NCH), 7.21 (s, 1H, NCH), 6.99 (s, 2H, *m*-Mes), 4.25 (s, 3H, Me), 2.31 (s, 3H, *p*-Mes), 2.07 (s, 6H, *o*-Mes), 1.75 (m, 4H, pdt), 1.51 (m, 2H, pdt), 1.37 (m, PMe $_3$ ).  $^{31}\text{P}$  NMR (121 MHz, acetone- $d_6$ ):  $\delta = 25.3$  (s).  $^{13}\text{C}$  NMR (300 MHz,  $\text{CD}_2\text{Cl}_2$ ):  $\delta = 219$  (CO at Fe2), 216 (d,  $J_{\text{C-P}} = 19$  Hz, CO at Fe1). 193 (:C(NR $_2$ ) $_2$ ), 167 (Mes), 139 (Mes), 137 (Mes), 136 (Mes), 129 (Mes), 124 (NHC), 124 (NHC), 39 (Me), 30 (pdt), 25 (pdt), 21 (Mes), 20 (PMe $_3$ ), 18 (Mes). Anal. Calcd for  $\text{C}_{23}\text{H}_{31}\text{N}_2\text{Fe}_2\text{PS}_2\text{O}_4$ : C, 45.56; H, 5.15; N, 4.62. Found: C, 45.59; H, 5.02; N, 4.66.



**( $\mu$ -pdt)[Fe(CO)<sub>2</sub>IMe][Fe(CO)<sub>2</sub>PMe<sub>3</sub>] (III-3).** The synthetic procedure is similar to that of **III-3** typically using ~1 g of the **III-3**<sub>NHC</sub> precursor. The reaction time is 24 h as indicated by *in situ* IR spectroscopy, and a different purification procedure was required. After the toluene reaction solution was filtered through Celite, removal of the volatiles from the filtrate in vacuo provided a dark red sticky residue. To the crude product methanol (5 mL) was added to solidify the product. The product was then collected as a solid on a sintered glass frit and washed with pentane (2 x 10 mL). Single crystals and samples for combustion analysis were obtained through crystallization in layered CH<sub>2</sub>Cl<sub>2</sub>/pentane. Yield: 60.0 %. IR (CH<sub>2</sub>Cl<sub>2</sub>, cm<sup>-1</sup>): 1974 (s), 1934 (s), 1898 (m), 1884 (m, sh). <sup>1</sup>H NMR (300 MHz, acetone-*d*<sub>6</sub>):  $\delta$  = 7.38 (s, 2H, NCH), 4.08 (s, 6H, NMe), 1.92 (t, 4H, pdt), 1.53 (br, 2H, pdt), 1.46 (d, PMe<sub>3</sub>). <sup>31</sup>P NMR (121 MHz, acetone-*d*<sub>6</sub>):  $\delta$  = 29.5 (s). <sup>13</sup>C NMR (300 MHz, CD<sub>2</sub>Cl<sub>2</sub>):  $\delta$  = 219 (CO at Fe-NHC), 216 (d, *J*<sub>C-P</sub> = 19 Hz, CO at Fe-PMe<sub>3</sub>). Anal. Calcd for C<sub>23</sub>H<sub>31</sub>N<sub>2</sub>Fe<sub>2</sub>PS<sub>2</sub>O<sub>4</sub>: C, 35.88; H, 4.62; N, 5.58. Found: C, 36.00; H, 4.80; N, 5.57.

**{( $\mu$ -pdt)[Fe<sup>II</sup>(CO)<sub>2</sub>IMes][Fe<sup>I</sup>(CO)<sub>2</sub>PMe<sub>3</sub>]}PF<sub>6</sub><sup>-</sup> (III-1<sub>ox</sub>).** The oxidation of complex **III-1** was performed at -70 °C under Ar. Complex **III-1** (142.5 mg, 0.2 mmol) was dissolved in 5 mL CH<sub>2</sub>Cl<sub>2</sub> and the solution was cooled to -70 °C. The pre-cooled solution of FcPF<sub>6</sub> (66.2 mg, 0.2 mmol) in 5 mL CH<sub>2</sub>Cl<sub>2</sub> was transferred to the above solution via cannula. The mixture was stirred at -70 °C for 0.5 hour until the IR monitor indicated there was no starting material remaining. 20 mL of pre-cooled hexane was added to form precipitates and the supernatant was filtered with a cannula fitted with a PTFE membrane. The dark brown crude product was washed successively by 5 mL benzene

and 5 ml pentane to further remove impurities. Yield: 95.0 % (162.5 mg, 0.19 mmol). Recrystallization in CH<sub>2</sub>Cl<sub>2</sub>/pentane at -40 °C afforded crystals of **III-1<sub>ox</sub>** suitable for X-ray crystallography study. The crystal for X-ray analysis was mounted at -40 °C under protection of epoxy oil in 30 seconds. IR (ν (CO) region in CH<sub>2</sub>Cl<sub>2</sub>, cm<sup>-1</sup>) 2037 (s), 1997 (vs), 1886 (w). MS (ESI): m/z: 710 [D<sub>ox</sub>]<sup>+</sup>. The sensitivity of the product to heat has thus far precluded elemental analysis.

**{(μ-pdt)[Fe(CO)<sub>2</sub>IMesMe][Fe(CO)<sub>2</sub>PMe<sub>3</sub>]}PF<sub>6</sub><sup>-</sup> (III-2<sub>ox</sub>)**. The synthetic procedure is similar to that for **III-1<sub>ox</sub>**. Solid **(III-2)** (0.035 g, 0.058 mmol) was dissolved in CH<sub>2</sub>Cl<sub>2</sub> (25 mL) and cooled to -78 °C. While stirring, a solution of FcPF<sub>6</sub> (0.019 g, 0.058 mmol) in CH<sub>2</sub>Cl<sub>2</sub> (10 mL) was added dropwise. Upon addition, the solution darkened in color from red to burgundy and IR spectroscopy revealed complete consumption of starting material after ~ 20 minutes. Pre-cooled hexane (20 mL) was added to precipitate the product and the supernatant was removed with a cannula fitted with a PTFE membrane. The dark brown solid was washed successively by 5 mL benzene and 5 mL pentane to further remove impurities. The product was stored at -80 °C. IR (CH<sub>2</sub>Cl<sub>2</sub>, cm<sup>-1</sup>): 2036(s), 2000 (vs), 1929 (w).  $\mu_{eff}$  (Evans' method, CD<sub>2</sub>Cl<sub>2</sub>, 298 K): 1.87  $\mu_B$ . The thermal sensitivity of the product has thus far precluded elemental analysis.

**{(μ-pdt)[Fe(CO)<sub>2</sub>IMe][Fe(CO)<sub>2</sub>PMe<sub>3</sub>]}PF<sub>6</sub><sup>-</sup> (III-3<sub>ox</sub>)**. The preparation of **III-3<sub>ox</sub>** followed a similar procedure as that described for **III-1<sub>ox</sub>** and **III-2<sub>ox</sub>**. At -78 °C under Ar, complex **III-3** (103.9 mg, 0.2 mmol) dissolved in CH<sub>2</sub>Cl<sub>2</sub> (5 mL) was treated with a pre-cooled solution of FcPF<sub>6</sub> (66.2 mg, 0.2 mmol) in 5 mL CH<sub>2</sub>Cl<sub>2</sub>. The mixture was stirred at -78 °C for 0.5 hour until *in situ* IR spectroscopy indicated there was no starting

material remaining. Following precipitation with pre-cooled hexanes (20 mL) and removal of the supernatant via filtration as described above, the dark brown crude product was washed successively by 5 mL benzene and 5 mL pentane. The product obtained was stored at -80 °C for further use. IR (CH<sub>2</sub>Cl<sub>2</sub>, cm<sup>-1</sup>): 2036(s), 2005 (vs), 1981(s), 1929 (w).  $\mu_{eff}$  (Evans' method, CD<sub>2</sub>Cl<sub>2</sub>, 298 K): 1.89  $\mu_B$ . The thermal sensitivity of the product has thus far precluded elemental analysis.

**Reversibility of oxidation study.** The oxidation of complex **III-1** and the reversible reduction were monitored by FTIR *in situ*. All operations were performed at -70 °C under Ar. Both of the oxidant, FcPF<sub>6</sub> and the reductant, Cp<sub>2</sub>\*Co were used as solids to avoid the concentration change of the reaction solution to influence IR measurement. The IR spectrum of complex **III-1** (71.0 mg, 0.1 mmol in 10 mL CH<sub>2</sub>Cl<sub>2</sub>) was recorded before being transferred into a Schlenk tube containing one equivalent of pre-cooled Fc<sup>+</sup>PF<sub>6</sub><sup>-</sup> solids. After 0.5 h, the second IR spectrum was recorded, which indicated all complex **III-1** starting material was converted to its oxidized form, **III-1<sub>ox</sub>**. **III-1<sub>ox</sub>** was completely reduced back to complex **III-1** by an equivalent amount of Cp<sub>2</sub>\*Co within 0.5 h as shown by the IR monitor.

Similar procedure was applied to complexes **III-2** and **III-3**.

**Standard procedure <sup>13</sup>C<sub>O</sub> exchange experiments.** **III-1<sub>ox</sub>** was prepared *in situ* at -78 °C via addition of a solution of FcPF<sub>6</sub> (0.015 g, 0.045 mmol) in CH<sub>2</sub>Cl<sub>2</sub> (5 mL) to a stirring solution of **III-1** (0.032 g, 0.045 mmol) in CH<sub>2</sub>Cl<sub>2</sub> (10 mL) in a dry ice/acetone bath. After stirring for 15 minutes at -78 °C, the resulting brown solution was frozen with liquid N<sub>2</sub>. The headspace above this frozen solution was evacuated, then back-filled

with  $^{13}\text{CO}$ . The reaction mixture was then allowed to thaw and warm to  $-78\text{ }^\circ\text{C}$ , and  $^{13}\text{CO}$  exchange progress was monitored via IR spectroscopy of aliquots of this solution.

Similar procedure was applied to complexes **III-2<sub>ox</sub>** and **III-3<sub>ox</sub>**.

**Standard procedure for  $\text{Cp}_2\text{Co}$  reduction experiments after  $^{12}\text{CO}/^{13}\text{CO}$  exchange.**  $^{13}\text{CO}$  was removed from the reaction vessel via brief exposure of the solution to vacuum while maintaining the temperature at  $-78\text{ }^\circ\text{C}$ . Under  $\text{N}_2$ , a pre-cooled solution of  $\text{Cp}_2\text{Co}$  (0.009 g, 0.05 mmol) in  $\text{CH}_2\text{Cl}_2$  (5 mL) was added to the reaction mixture. After 15 minutes, the solution was allowed to warm to room temperature and solvent was removed in vacuo. The resulting red solids were extracted with 1:1 toluene/hexanes and filtered through a plug of silica gel. Solvent was removed and  $^{13}\text{C}$  NMR (75 MHz, acetone- $d_6$ ) spectra were recorded on the resulting solid without further purification.

**Reversibility of  $^{13}\text{CO}/^{12}\text{CO}$  exchange.** To confirm the reversibility of the CO ligand exchange process, a fully  $^{13}\text{CO}$ -labeled solution of **III-1<sub>ox</sub>** in  $\text{CH}_2\text{Cl}_2$  at  $-78\text{ }^\circ\text{C}$  (generated by briefly warming a solution of **III-1<sub>ox</sub>** to room temperature under  $^{13}\text{CO}$ ) was exposed to 1 atm  $^{12}\text{CO}$  and allowed to warm to room temperature. After 30 minutes at room temperature, the IR revealed that the unlabeled starting material **III-1<sub>ox</sub>** had been regenerated. A small amount of neutral **III-1<sub>ox</sub>** (unlabeled) was also formed as a result of the temperatures required to achieve complex exchange.

**Generation of  $\{(\mu\text{-pdt})(\mu\text{-CO})[\text{Fe}^{\text{I}}(\text{CO})_2\text{IMesMe}][\text{Fe}^{\text{II}}(\text{CO})_2\text{PMe}_3]\}\text{PF}_6^-$  (**III-2<sub>ox</sub>-CO**) and  $\{(\mu\text{-pdt})(\mu\text{-CO})[\text{Fe}^{\text{I}}(\text{CO})_2\text{IME}][\text{Fe}^{\text{II}}(\text{CO})_2\text{PMe}_3]\}\text{PF}_6^-$  (**III-3<sub>ox</sub>-CO**).** At  $-78\text{ }^\circ\text{C}$ , solutions of **III-2<sub>ox</sub>** or **III-3<sub>ox</sub>** (0.020 mmol) in  $\text{CH}_2\text{Cl}_2$  were sparged with CO. The CO uptake was monitored by *in situ* solution IR spectroscopy.

**Treatment of  $\{(\mu\text{-pdt})(\mu\text{-CO})[\text{Fe}^{\text{I}}(\text{CO})\text{IMesMe}][\text{Fe}^{\text{II}}(\text{CO})_2\text{PMe}_3]\}\text{PF}_6^-$  (III-2<sub>ox</sub>) with  $^{13}\text{CO}$ .** A solution of III-2<sub>ox</sub> (0.020 mmol) in 10 mL  $\text{CH}_2\text{Cl}_2$  was frozen with liquid  $\text{N}_2$ . The reaction flask was evacuated and refilled with 1 atm  $^{13}\text{CO}$ . The temperature was raised to  $-78\text{ }^\circ\text{C}$  and the solution was magnetically stirred. The IR spectrum of the resulting reaction mixture was monitored by taking aliquots of this solution over the course of 1 hour.

#### Experimental for chapter IV

**Synthesis of  $(\mu\text{-pst})[\text{Fe}(\text{CO})_3]_2$  (IV-1-O).** Method A: Complex IV-1-O was synthesized by slightly modifying the reported procedure for  $(\mu\text{-est})[\text{Fe}(\text{CO})_3]_2$ .<sup>182</sup> To a toluene solution of  $(\mu\text{-pdt})[\text{Fe}(\text{CO})_3]_2$  (IV-1) (1.00 g, 2.59 mmol in 50 mL) was added dropwise 1.5 equiv of oxidant, m-CPBA dissolved in 50 mL toluene. The mixture was stirred for 0.5 h at  $22\text{ }^\circ\text{C}$ . Subsequently, the reaction solution was bubbled with ammonia gas for 20 min to remove excess m-CPBA and the m-chlorobenzoic acid byproduct. After filtration and in vacuo removal of toluene, the crude product (0.99 g, 95% yield) was dissolved in a minimum of MeOH and crystallized at  $-30\text{ }^\circ\text{C}$  to give analytically pure product (0.87 g, 84% yield). Crystals suitable for X-ray analysis were grown from  $\text{CH}_2\text{Cl}_2$  solution layered with hexane.  $^1\text{H}$  NMR (ppm, acetone- $d_6$ ), 3.6 (t, 2 H, -S(O)CH<sub>2</sub>), 2.3 (p, 2H, -CH<sub>2</sub>CH<sub>2</sub>CH<sub>2</sub>-), 2.1 (t, 2 H, -CH<sub>2</sub>CH<sub>2</sub>S-). MS (ESI): m/z: 402.82 [M+H<sup>+</sup>]; Elem. Anal. found (calc'd for C<sub>9</sub>H<sub>6</sub>Fe<sub>2</sub>O<sub>7</sub>S<sub>2</sub>) %: C 26.89 (26.93), H 1.50 (1.50).

Method B: To an acetone solution of complex IV-1 (0.20 g, 0.52 mmol in 20 mL) was added dropwise 20 mL of DDO (dimethyldioxirane) acetone solution (ca. 0.05 mM). The mixture was stirred for 10 minutes at  $22\text{ }^\circ\text{C}$  to reach completion as indicated

by IR monitor. After removing solvent, the product was obtained in a yield of 92 %, 192 mg.

**Synthesis of  $(\mu\text{-pst})[\text{Fe}(\text{CO})_3][\text{Fe}(\text{CO})_2\text{PPh}_3]$  (IV-2-O).** Method A: The procedure used to synthesize complex IV-1-O was applied to prepare complex IV-2-O from complex IV-2 (1.00 g, 1.61 mmol) to provide crude product (93%). Further purification was achieved by precipitation from the saturated solution in  $\text{CH}_3\text{CN}$  at 0 °C. The final yield was 82% (0.84 g). Single crystals were grown from a solvent mixture of  $\text{CH}_2\text{Cl}_2$  and pentane at -30 °C.  $^1\text{H}$  NMR (ppm, acetone- $d_6$ ) 7.74 (br, 6H,  $\text{PPh}_3$ ), 7.63 (br, 9H,  $\text{PPh}_3$ ) 3.23 (br 2 H,  $-\text{S}(\text{O})\text{CH}_2$ ), 2.69 (br, 2H,  $-\text{CH}_2\text{CH}_2\text{CH}_2-$ ), 1.95 (br, 2 H,  $-\text{CH}_2\text{CH}_2\text{S}-$ );  $^{31}\text{P}$  NMR (ppm, acetone- $d_6$ ), 63.86. MS (ESI): m/z: 636.91  $[\text{M}+\text{H}^+]$ ; Elem. Anal. found (calc'd for  $\text{C}_{26}\text{H}_{21}\text{Fe}_2\text{N}_2\text{O}_6\text{PS}_2$ ) %: C 48.83 (49.08), H 3.40 (3.33).

Method B: An orange solution of IV-1-O (0.50 g, 1.24 mmol) in 30 mL  $\text{CH}_3\text{CN}$  was treated with an equal amount of  $\text{Me}_3\text{NO}$  (94 mg, 1.24 mmol) in 5 mL  $\text{CH}_3\text{CN}$ . The solution color turned dark red indicating the formation of the intermediate ( $(\mu\text{-pst})[\text{Fe}(\text{CO})_3][\text{Fe}(\text{CO})_2\text{NMe}_3]$ ) within 15 min as suggested by the IR monitor. To this solution was added 1 equiv of  $\text{PPh}_3$  (0.327 g, 1.24 mmol) in 10 mL  $\text{CH}_3\text{CN}$ , followed by heating at 80 °C for 5 h. After removing volatiles under vacuum, the remaining red solids were washed with pentane ( $2 \times 10$  mL) and re-dissolved in  $\text{CH}_3\text{CN}$ . Pure product (0.67 g, 85%) precipitated from  $\text{CH}_3\text{CN}$  solution at -30 °C.

**Synthesis of  $(\mu\text{-pds})[\text{Fe}(\text{CO})_3][\text{Fe}(\text{CO})_2\text{PPh}_3]$ , (IV-2-O<sub>2</sub>).** To complex IV-2-O (0.50 g, 0.78 mmol) in 30 mL toluene was added dropwise 1.5 equiv of m-CPBA in 30 mL toluene. The solution was stirred at 22 °C for 0.5 h to convert all IV-2-O as

monitored by IR. The crude product (0.26 g, 50%) was obtained after treatment with  $\text{NH}_3$  gas for 20 min and removal of solvent under vacuum. Then the crude product was dissolved in 10 mL hot MeOH and crystallized by cooling to 22 °C to give analytically pure product as orange needles (0.15 g, 29%). Crystals suitable for X-ray analysis were grown from  $\text{CH}_2\text{Cl}_2$  solution layered with pentane.  $^1\text{H}$  NMR (ppm,  $\text{CH}_2\text{Cl}_2\text{-d}_2$ ) 7.65 (br, 6H,  $\text{PPh}_3$ ), 7.55 (br, 9H,  $\text{PPh}_3$ ) 3.42 (d, 4 H,  $-\text{S}(\text{O})\text{CH}_2$ ), 3.14 (br, 2H,  $-\text{CH}_2\text{CH}_2\text{CH}_2-$ );  $^{31}\text{P}$  NMR (ppm,  $\text{CH}_2\text{Cl}_2\text{-d}_2$ ), 64.4. MS (ESI):  $m/z$ : 653.90  $[\text{M}+\text{H}^+]$ ; Elem. anal. Found (calc'd for  $\text{C}_{26}\text{H}_{21}\text{Fe}_2\text{N}_2\text{O}_7\text{PS}_2$ ) %: C 47.86 (47.88), H 3.31 (3.25).

**Synthesis of  $(\mu\text{-pst})[\text{Fe}(\text{CO})_2\text{PMe}_3]_2$  (IV-4-O).** Method A: An oily crude product of **IV-4-O** was obtained from complex **IV-4** (1.00 g, 2.07 mmol) by following the oxygenation procedure used to prepare complex **IV-1-O**. Silica gel column chromatography with toluene eluent was performed under  $\text{N}_2$ . The red band was collected and concentrated to give a red residue. Over the course of a week, pure **IV-4-O** precipitated from a -30 °C hexane solution in a yield of (83 mg, 8 %). Single crystals for x-ray analysis were grown from the saturated solution in  $\text{CH}_2\text{Cl}_2$  at -30 °C.  $^1\text{H}$  NMR (ppm,  $\text{CH}_2\text{Cl}_2\text{-d}_2$ ) 3.27 (br, 2 H,  $-\text{S}(\text{O})\text{CH}_2$ ), 2.18 (br, 2H,  $-\text{CH}_2\text{CH}_2\text{CH}_2-$ ), 1.76 (br, 2 H,  $-\text{CH}_2\text{CH}_2\text{S}-$ ), 1.53 (d, 18 H,  $\text{P}(\text{CH}_3)_3$ );  $^{31}\text{P}$  NMR (ppm,  $\text{CH}_2\text{Cl}_2\text{-d}_2$ ), 24.54. MS (ESI):  $m/z$ : 498.93  $[\text{M}+\text{H}^+]$ ; Elem. anal. found (calc'd for  $\text{C}_{13}\text{H}_{24}\text{Fe}_2\text{N}_2\text{O}_5\text{PS}_2$ ) %: C 30.88 (31.35), H 4.83 (4.86).

Method B: Starting materials of complex **IV-1-O** (1.00 g, 2.49 mmol) and excess  $\text{PMe}_3$  (0.57 g, 8.07 mmol) were dissolved in 50 mL toluene at 22 °C. The mixture was stirred at reflux temperature (110 °C) for 24 h, followed by filtration through a sintered

glass frit to remove solid byproducts and subsequent evaporation of the filtrate to remove toluene. The resulting red product was subjected to silica gel column chromatography under N<sub>2</sub>. Hexane was used as the first eluent to remove trace byproduct ( $\mu$ -pst)[Fe(CO)<sub>3</sub>][Fe(CO)<sub>2</sub>PMe<sub>3</sub>] (**3**). The second band was collected using toluene as eluent to give analytically pure complex **IV-4-O** (0.77 g, 62%).

**Isolation of Fe(CO)<sub>2</sub>(PMe<sub>3</sub>)<sub>2</sub>(*m*-Cl-PhCOO<sup>-</sup>)<sub>2</sub> (**IV-6**).** After the oxygenation of **IV-4** and workup with ammonia gas as stated in method A to prepare **IV-4-O**, solvent was removed under vacuum. Then the obtained residue was extracted with 20 mL hexane followed by filtration through celite. The hexane solution was slowly evaporated at 22 °C in 5 days to provide yellow green crystals (**IV-6**) at the top of the crystallization tube and red crystals (**IV-4-O**) at the bottom. The crystals of **6** were manually chosen for x-ray and IR spectroscopic analyses.

**Synthesis of {( $\mu$ -pst)( $\mu$ -H)[Fe(CO)<sub>2</sub>PMe<sub>3</sub>]<sub>2</sub>}<sup>+</sup>PF<sub>6</sub><sup>-</sup> (**IV-5-O**).** To complex **IV-5** (0.50 g, 0.78 mmol) in 50 mL CH<sub>2</sub>Cl<sub>2</sub> was added dropwise 1.5 equiv of *m*-CPBA in 50 mL CH<sub>2</sub>Cl<sub>2</sub>. The solution was stirred at 22 °C for 0.5 h to convert all **5** as monitored by IR. After removing solvent, the remaining yellow solids were washed with ether 50 mL × 2 to remove excess oxidant and the *m*-chlorobenzoic acid byproduct. The crude product was dissolved in 10 mL CH<sub>2</sub>Cl<sub>2</sub> and then filtered through a sintered glass frit. The solution was layered with hexane yielding the pure product as precipitate (0.36 g, 70%) at -30 °C in 3 days. <sup>1</sup>H NMR (ppm, CD<sub>2</sub>Cl<sub>2</sub>) 3.91 (br, 2 H, -S(O)CH<sub>2</sub>), 2.62 (br, 2H, -CH<sub>2</sub>CH<sub>2</sub>CH<sub>2</sub>-), 2.4 (br, 2 H, -CH<sub>2</sub>CH<sub>2</sub>S-), 1.66 (q, 18 H, P(CH<sub>3</sub>)<sub>3</sub>), -13.33 (q, 1 H, Fe<sub>2</sub>H); <sup>31</sup>P NMR (ppm, CH<sub>2</sub>Cl<sub>2</sub>-d<sub>2</sub>), 25.8 (s, PMe<sub>3</sub>), 149.2 (q, PF<sub>6</sub><sup>-</sup>); MS (ESI): m/z:



498.93 [M-PF<sub>6</sub>]<sup>+</sup>; Elem. anal. found (calc'd for C<sub>13</sub>H<sub>25</sub>Fe<sub>2</sub>S<sub>2</sub>O<sub>5</sub>P<sub>3</sub>F<sub>6</sub>) %: C 24.67 (24.24), H 3.93 (3.91).

**Deoxygenation of (μ-pst)[Fe(CO)<sub>3</sub>]<sub>2</sub> (IV-1-O).** To a suspension of Cp\*<sub>2</sub>Co (0.33 g, 1 mmol) in a solvent mixture (10 mL, CH<sub>3</sub>CN:H<sub>2</sub>O, 50:1, V/V), complex **1-O** (0.2 g, 0.5 mmol), dissolved in the same solvent mixture (20 mL), was added dropwise. The mixture was stirred at 22 °C for 30 min to reach completion as indicated by the IR monitor. Solvent was removed *in vacuo* and solids obtained were extracted with 20 mL hexane. The concentrated hexane solution was cooled at -30 °C to give complex **1** (96.5 mg, 50%). Complex **1** was further identified by <sup>1</sup>H NMR and FTIR spectroscopies.

**Deoxygenation of (μ-pst) [Fe(CO)<sub>3</sub>] [Fe(CO)<sub>2</sub>PPh<sub>3</sub>] (IV-2-O) and (μ-pds) [Fe(CO)<sub>3</sub>] [Fe(CO)<sub>2</sub>PPh<sub>3</sub>] (IV-2-O<sub>2</sub>).** The procedure used to successfully deoxygenate complex **IV-1-O** was applied to complexes **IV-2-O** and **IV-2-O<sub>2</sub>**. Based on 0.20 g starting material, complex **IV-2** was isolated, 20 mg (10%) from **IV-2-O** and 17 mg (9%) from **IV-2-O<sub>2</sub>**. The identity of complex **IV-2** was confirmed by <sup>1</sup>H NMR and FTIR spectroscopies.

**Deoxygenation of {(μ-pst)(μ-H)[Fe(CO)<sub>2</sub>(PMe<sub>3</sub>)<sub>2</sub>]<sup>+</sup>PF<sub>6</sub><sup>-</sup> (IV-5-O).** The deoxygenation procedure as described for **IV-1-O** was applied. A 0.27 g (0.04 mmol) sample of **IV-5-O** was dissolved in the mixture solvent (5 mL, CH<sub>3</sub>CN:H<sub>2</sub>O = 50:1, V/V) and treated with 2 equiv of Cp\*<sub>2</sub>Co. The reaction was monitored by IR spectroscopy, indicating the generation of complex **IV-5** and complex **IV-4-O**.

**Electrochemical deoxygenation of sulfur-oxygenated complexes (IV-1-O and IV-4-O).** Bulk electrolyses for electrochemical deoxygenation of sulfur-oxygenated

complexes (**IV-1-O** and **IV-4-O**) were performed using a gas tight 75 mL BASI bulk electrolysis cell equipped with four electrodes (Ag/Ag<sup>+</sup> reference electrode, platinum counter electrode loaded in a fritted glass tube, glassy carbon working electrode, and a reticulated vitreous carbon (RVC) working electrode.). During electrochemical experiments, the glassy carbon working electrode and RVC working electrode were switched between cyclic voltammetry (CV) & differential pulse voltammetry (DPV) and bulk electrolysis modes. Complex **IV-1-O** (32 mg, 2 mmol), or **IV-4-O** (40 mg, 2 mmol), was dissolved in 40 mL electrolyte solution (CH<sub>3</sub>CN:H<sub>2</sub>O, 50:1, V/V, 0.1 M *n*-Bu<sub>4</sub>NBF<sub>4</sub>) in the cell. The first IR was measured before commencement of electrochemical experiments. The first CV and DPV was recorded using the glassy carbon working electrode. Then the RVC working electrode was engaged to carry out bulk electrolysis at -1.7 V vs Fc<sup>+</sup>/Fc (2.3 V for complex **IV-4-O**). After each equivalent of electrons passed through the RVC working electrode, the IR, CV and DPV were measured to detect species present in electrolyte solution. It was found that ca. 2 equiv electrons were required to complete the electrochemical deoxygenation for complex **IV-1-O** while 3 equiv electrons were needed for electrochemical deoxygenation of complex **IV-4-O**.

#### **Experimental for chapter V**

**[Et<sub>4</sub>N]{(μ-pst)[Fe(CO)<sub>3</sub>][Fe(CO)<sub>2</sub>CN]} (IV-1-O-CN<sup>-</sup>)**. To a solution of complex **V-1-O** (402 mg, 1.0 mmol) in 10 mL CH<sub>3</sub>CN was added a solution of Et<sub>4</sub>N<sup>+</sup>CN<sup>-</sup> (156 mg, 1.0 mmol) in 10 mL of CH<sub>3</sub>CN; the reaction mixture was heated to 60°C and stirred for 0.5 h. The solvent was removed under vacuum and the dark red residue was

recrystallized from 5 mL of CH<sub>2</sub>Cl<sub>2</sub> by gradual addition of 30 mL of Et<sub>2</sub>O. The resulting red solid was washed with 3×20 mL Et<sub>2</sub>O and dried under vacuum. Yield: 387 mg (73%). <sup>1</sup>H NMR ( DMSO-d<sub>6</sub>, 300MHz ): δ = 3.18 (m, 8H, N(CH<sub>2</sub>CH<sub>3</sub>)<sub>4</sub>), 2.07 (br, 2H, O=SCH<sub>2</sub>), 1.92 (br, 2H, SCH<sub>2</sub>), 1.63 (br, 2H, CH<sub>2</sub>CH<sub>2</sub>CH<sub>2</sub>), 1.15 (m, 12H, N(CH<sub>2</sub>CH<sub>3</sub>)<sub>4</sub>). IR (CH<sub>3</sub>CN, cm<sup>-1</sup>): ν (CN) = 2099(w); ν (CO) = 2042(m), 1993(s), 1975(s), 1958(m), 1934(m). ESI-MS ( CH<sub>2</sub>Cl<sub>2</sub>, *m/z*): 399.9, [M-Et<sub>4</sub>N<sup>+</sup>]; 371.9, [M-Et<sub>4</sub>N<sup>+</sup>-CO]; 343.9, [M-Et<sub>4</sub>N<sup>+</sup>-2CO]; 315.9, [M-Et<sub>4</sub>N<sup>+</sup>-3CO].

**[Et<sub>4</sub>N]<sub>2</sub>{(μ-pst)[Fe(CO)<sub>2</sub>CN]<sub>2</sub>} (IV-1-O-(CN)<sub>2</sub><sup>2-</sup>)**. To a solution of compound **V-1-O** (80 mg, 0.2 mmol) in 10 mL CH<sub>3</sub>CN was added Et<sub>4</sub>N<sup>+</sup>CN<sup>-</sup> (188 mg, 1.2 mmol) dissolved in 10 mL of CH<sub>3</sub>CN; the reaction mixture was heated to reflux and stirred overnight. The excess Et<sub>4</sub>N<sup>+</sup>CN<sup>-</sup> was removed by precipitation on gradual addition of Et<sub>2</sub>O. After filtration the filtrate was dried under vacuum. The crude product was purified by recrystallization from 5 mL of CH<sub>2</sub>Cl<sub>2</sub> layered with Et<sub>2</sub>O. Yield, ~70%. <sup>1</sup>H NMR ( DMSO-d<sub>6</sub>, 300MHz ): δ = 3.20 (m, 16H, N(CH<sub>2</sub>CH<sub>3</sub>)<sub>4</sub>), 1.93 (br, 2H, O=SCH<sub>2</sub>), 1.75 ( m, 2H, SCH<sub>2</sub>), 1.64 (br, 2H, CH<sub>2</sub>CH<sub>2</sub>CH<sub>2</sub>), 1.15 (m, 24H, N(CH<sub>2</sub>CH<sub>3</sub>)<sub>4</sub>). IR ( CH<sub>3</sub>CN, cm<sup>-1</sup>): ν (CN) = 2075(m); ν (CO) = 1979(s), 1939(s), 1903(s).

**Kinetic measurements.** Pseudo-first-order reaction conditions were employed for all kinetic studies, using 20-fold and greater excesses of PMe<sub>3</sub> or Et<sub>4</sub>N<sup>+</sup>CN<sup>-</sup>. Reactions were monitored by infrared spectroscopy. Typically, 10 mL of a toluene (or CH<sub>3</sub>CN for the Et<sub>4</sub>N<sup>+</sup>CN<sup>-</sup> substitution) solution containing the diiron complex (0.10 mmolar) in a Schlenk flask under N<sub>2</sub> was placed in a temperature-controlled bath. Following temperature equilibration, 10 mL of a toluene solution of PMe<sub>3</sub> (or an CH<sub>3</sub>CN solution

of  $\text{Et}_4\text{N}^+\text{CN}^-$ ) at the same temperature was rapidly transferred into the flask. While being magnetically stirred, samples were removed and IR spectra were taken at 2 to 40 min intervals typically through four half-lives. Rates of reaction were measured by following the decrease in absorption of the reactant's most intense non-overlapping  $\nu(\text{CO})$  vibration, which centered at ca.  $2073\text{ cm}^{-1}$  for complex **IV-1**;  $2036\text{ cm}^{-1}$  for **IV-1-PMe<sub>3</sub>**;  $2083\text{ cm}^{-1}$  for complex **IV-1-O**; and  $2042\text{ cm}^{-1}$  for **IV-1-O-CN<sup>-</sup>**. Rate constants were calculated from plots of  $\ln(A_0/A_t)$  versus time typically using >30 data points over 4 to 5 half-lives giving correlation constant of 0.99. Reproducibility of a run under identical conditions was 95% or better. Activation parameters  $\Delta H^\ddagger$ ,  $\Delta S^\ddagger$  were obtained from Eyring plots; activation energies,  $E_a$ , were obtained from Arrhenius plots.

## Experimental for chapter VI

**Synthetic procedures.** Note: All complexes (**VI-1~VI-12**) are light and heat sensitive, therefore preparations, isolation and manipulations were conducted in the dark. The isolated complexes were stored under argon at  $-40^\circ\text{C}$  in a freezer within the glovebox.

**FeI<sub>2</sub>(CO)<sub>3</sub>IMes. (VI-1)** 1, 3- Bis-(2, 4, 6- trimethylphenyl)imidazolium chloride (750 mg, 1.8 mmol), KO*t*-Bu (500 mg, 3.6 mmol), and THF (30 mL) were added to a 50 mL flask and stirred at room temperature for 1 h. The solvent was removed under reduced pressure, and the residual solid was extracted with hexane (30 mL). The resulting suspension was filtered through celite and the filtrate of free carbene was added to a hexane (20 mL) solution of FeI<sub>2</sub>(CO)<sub>4</sub> (750 mg, 1.8 mmol). The reaction mixture was stirred for 1h at room temperature in dark. The product precipitated and the solid

was collected by filtration, washed with two 25 mL portions of Hexane, and dried under vacuum to give a dark red powder. Crude yield: 1.086 g (86.4 %); recrystallization from Et<sub>2</sub>O gave analytically pure crystals used for analysis and X-ray diffraction studies. <sup>1</sup>H NMR (ppm, acetone-d<sub>6</sub>): δ = 7.68 (s, 2H, NCH), 7.21 (s, 4H, *m*-Mes), 2.39 (d, 6H, *p*-Mes), 2.24 (s, 12H, *o*-Mes). IR (CH<sub>2</sub>Cl<sub>2</sub>, cm<sup>-1</sup>): 2087 (w), 2040 (s), 2018 (m). Elemental analysis, found (calc'd for C<sub>24</sub>H<sub>25</sub>N<sub>2</sub>FeO<sub>3</sub>I<sub>2</sub>) %: C, 40.78 (41.29); H, 3.21 (3.47); N, 3.61 (4.01).

**FeI<sub>2</sub>(CO)<sub>3</sub>SIMes. (VI-2)** Deprotonation of the imidazolium salt and isolation of the free carbene was performed precisely as described above for (1), using 342.9 mg, 1 mmol, of 1, 3- Bis (2, 4, 6- trimethylphenyl)imidazolium chloride and 224 mg, 2 mmol, of KO*t*-Bu . Reaction with FeI<sub>2</sub>(CO)<sub>4</sub> (421.6 mg, 1 mmol) and workup as described above gave a grey powder. Crude yield: 500 mg (72 % ); analytically pure crystals were obtained as for complex 1. <sup>1</sup>H NMR (ppm, acetone-d<sub>6</sub>): δ 7.13 (s, 4H, *m*-Mes), 4.73(s, 1H, NCH), 4.59(s, 1H, NCH), 4.14(s, 2H, NCH), 2.47(s, 12H, *o*-Mes), 2.34(s, 6H, *p*-Mes). IR (CH<sub>2</sub>Cl<sub>2</sub>, cm<sup>-1</sup>): 2082 (w), 2039 (s), 2019 (m). Elemental analysis, found (calc'd for C<sub>24</sub>H<sub>27</sub>N<sub>2</sub>FeO<sub>3</sub>I<sub>2</sub>) %: C, 40.9 (41.2); H, 3.76 (3.74); N, 3.57 (4.00).

**FeI<sub>2</sub>(CO)<sub>3</sub>IMe. (VI-3)** As described above, the 1, 3- dimethylimidazolium iodide (224 mg, 1 mmol) salt was deprotonated with KO*t*-Bu (224 mg, 2 mmol), and the filtrate of the free carbene was added to a hexane (20 mL) solution of FeI<sub>2</sub>(CO)<sub>4</sub> (421.6 mg, 1 mmol). A red powder was ultimately obtained. Crude yield: 250 mg ( 51 % ); recrystallization from ether gave analytically pure crystals. <sup>1</sup>H NMR (ppm, acetone-d<sub>6</sub>): δ = 7.45 (d, 2H, NCH), 3.95 (d, 6H, NMe). IR (CH<sub>2</sub>Cl<sub>2</sub>, cm<sup>-1</sup>): 2082 (w), 2034 (s), 2023

(sh). Elemental analysis, found (calc'd for  $C_8H_8N_2FeO_3I_2$ ) %: C, 19.2 (19.6); H, 2.09 (1.65); N, 5.31 (5.72).

**FeI<sub>2</sub>(CO)<sub>2</sub>bipy. (VI-4)** To a solution of FeI<sub>2</sub>(CO)<sub>4</sub> (1.0 g, 2.4 mmol) in 30 mL of hexane was added a solution of 2, 2'-bipyridine (375 mg, 2.4 mmol) in 25 mL of hexane. The reaction mixture was stirred for 1h at room temperature in the dark. The resulting precipitate was collected by filtration, washed with two 25 mL portions of hexane, and dried under vacuum to give a dark red powder. Yield: 1.12 g (89.4 %); crystals were grown by layering a CH<sub>2</sub>Cl<sub>2</sub> solution with hexane. <sup>1</sup>H NMR (ppm, CD<sub>3</sub>CN): δ 8.50 (d, 2 H), 8.10 (m, 2 H), 7.39 (d, 4 H). IR (CH<sub>2</sub>Cl<sub>2</sub>, cm<sup>-1</sup>) of cis-(CO),cis-(I)-FeI<sub>2</sub>(CO)<sub>2</sub>bipy: 2043 (s), 2002 (s). IR (CH<sub>2</sub>Cl<sub>2</sub>, cm<sup>-1</sup>) of cis-(CO),trans-(I)-FeI<sub>2</sub>(CO)<sub>2</sub>bipy: 2077 (s), 2025 (s). ESI-MS (CH<sub>2</sub>Cl<sub>2</sub>, *m/z*): 521 [M-H]<sup>-</sup>, 495 [M-CO+H]<sup>+</sup>. Elemental analysis, found (calc'd for C<sub>12</sub>H<sub>8</sub>N<sub>2</sub>FeO<sub>2</sub>I<sub>2</sub>) %: C, 26.6 (27.6); H, 1.81 (1.55); N, 5.84 (5.37).

**FeI<sub>2</sub>(CO)<sub>2</sub>phen (VI-5)** To a solution of FeI<sub>2</sub>(CO)<sub>4</sub> (1.5 g, 3.6 mmol) in 25 mL of CH<sub>2</sub>Cl<sub>2</sub>, was added a solution of 1,10-phenanthroline (0.648 g, 3.6 mmol) in 25 mL of CH<sub>2</sub>Cl<sub>2</sub>. The reaction mixture was stirred for 0.5 h at room temperature in dark. The solvent was removed under reduced pressure. The residual solid was washed with two 25 mL portions of hexane and dried under vacuum to give a dark red powder. Yield: 1.6 g (81%). <sup>1</sup>H NMR (ppm, CD<sub>3</sub>CN): δ 8.61 (d, 2 H), 8.26 (s, 2 H), 7.63 (m, 4 H). IR (CH<sub>2</sub>Cl<sub>2</sub>, cm<sup>-1</sup>) of cis-(CO),cis-(I)-FeI<sub>2</sub>(CO)<sub>2</sub>phen: 2044 (s), 2003 (s). IR (CH<sub>2</sub>Cl<sub>2</sub>, cm<sup>-1</sup>) of cis-(CO),trans-(I)-FeI<sub>2</sub>(CO)<sub>2</sub>phen: 2077 (s), 2025 (s). Elemental analysis, found (calc'd for C<sub>14</sub>H<sub>8</sub>N<sub>2</sub>FeO<sub>2</sub>I<sub>2</sub>) %: C, 29.8 (30.8); H, 1.52 (1.48); N, 5.18 (5.13).

**Preparation of  $\text{FeI}_2(\text{CO})_3\text{P}$  (  $\text{P} = \text{PMe}_3$  (VI-6),  $\text{PPh}_3$  (VI-7)  $\text{PCy}_3$  (VI-8) and  $\text{P(OEt)}_3$  (VI-9))** A general procedure was used to prepare these complexes.<sup>183-185</sup> To a solution of  $\text{FeI}_2(\text{CO})_4$  (2.0 g, 4.74 mmol) in 30 mL of hexane was added of a solution of the phosphine (4.74 mmol) in 20 mL of hexane. The reaction mixture was stirred for 1 h at room temperature in the dark. The solvent was removed in vacuo to give a dark red residue. The product was purified by washing with 2 x 5 mL portions of hexane and dried under vacuum to give a dark brown solid.

**$\text{FeI}_2(\text{CO})_3\text{PMe}_3$  (VI-6)** Yield: 460 mg (83 %).  $^1\text{H}$  NMR (ppm, acetone- $d_6$ ):  $\delta = 2.20$  (d, 9H,  $\text{PMe}_3$ ).  $^{31}\text{P}$  NMR (ppm, acetone- $d_6$ ):  $\delta = 30.7$  (s). IR ( $\text{CH}_2\text{Cl}_2$ ,  $\text{cm}^{-1}$ ): 2093 (s), 2047 (s), 2022 (s). Elemental analysis, found (calc'd for  $\text{C}_6\text{H}_9\text{FeO}_3\text{PI}_2$ ) %: C, 15.5 (15.3); H, 1.86 (1.93).

**$\text{FeI}_2(\text{CO})_3\text{PPh}_3$  (VI-7)** Yield: 1.5 g ( 95 % ).  $^1\text{H}$  NMR (ppm, acetone- $d_6$ ): 7.80 (m, 6H,  $\text{PPh}_3$ ), 7.61 (m, 9H,  $\text{PPh}_3$ ).  $^{31}\text{P}$  NMR (ppm, acetone- $d_6$ ): 64.2 (s). IR (THF,  $\text{cm}^{-1}$ ): 2093 (w), 2045 (s), 2032 (m). Elemental analysis, found (calc'd for  $\text{C}_{21}\text{H}_{15}\text{FeO}_3\text{PI}_2$ ) %: C, 38.3 (38.4); H, 2.41 (2.30).

**$\text{FeI}_2(\text{CO})_3\text{PCy}_3$  (8)** Yield: 3.0 g (94 % ).  $^1\text{H}$  NMR (ppm, acetone- $d_6$ ): 2.58 (br, 3H, -CH-), 1.93 (br, 12 H, - $\text{CH}_2$ -), 1.76 (br, 12 H, - $\text{CH}_2$ -), 1.36 (br, 6 H, - $\text{CH}_2$ -).  $^{31}\text{P}$  NMR (ppm, acetone- $d_6$ ): 76.25 (s). IR (THF,  $\text{cm}^{-1}$ ): 2081 (w), 2031 (vs), 2017 (s, sh). Elemental analysis, found (calc'd for  $\text{C}_{21}\text{H}_{33}\text{FeO}_3\text{PI}_2$ ) %: C, 37.26 (37.42); H, 4.90 (4.93).

**$\text{FeI}_2(\text{CO})_3\text{P(OEt)}_3$  (VI-9)** Yield: 1.8 g (68 %).  $^1\text{H}$  NMR (ppm, acetone- $d_6$ ): 4.36 (m, 6 H,  $\text{OCH}_2\text{CH}_3$ ), 1.40 (t, 9 H,  $\text{OCH}_2\text{CH}_3$ ).  $^{31}\text{P}$  NMR (ppm, acetone- $d_6$ ): 159.31 (s). IR

(THF,  $\text{cm}^{-1}$ ): 2104 (w), 2053 (s). Elemental analysis, found (calc'd for  $\text{C}_9\text{H}_{15}\text{FeO}_6\text{PI}_2$ ) %: C, 18.8 (19.3); H, 2.74 (2.70).

**$\text{FeI}_2(\text{CO})_3\text{Py}$  (VI-10)** To a solution of  $\text{FeI}_2(\text{CO})_4$  (1.0 g, 2.4 mmol) in 30 mL hexane was added a solution of pyridine (0.2 mL, 2.4 mmol) in 30 mL of hexane. The reaction mixture was stirred for 1 h at room temperature in the dark. The precipitated solid product was collected by filtration, washed with 2 x 25 mL hexane, and dried under vacuum to give a grey powder. Yield: 0.88 g (77 %); crystals for analyses and x-ray diffraction were obtained as described for complex VI-1.  $^1\text{H}$  NMR (ppm, acetone- $d_6$ ): 9.63 (s, 2H), 8.12 (s, 1H), 7.65 (s, 2H). IR ( $\text{CH}_2\text{Cl}_2$ ,  $\text{cm}^{-1}$ ): 2095 (s), 2050 (ms), 2041 (ms). Elemental analysis, found (calc'd for  $\text{C}_8\text{H}_5\text{NFeO}_3\text{I}_2$ ) %: C, 20.8 (20.3); H, 1.39 (1.07); N, 3.47(2.96).

**$\text{FeI}(\text{CO})_2\text{PPh}_3\text{PyS}$  (VI-11)** To a solution of  $\text{FeI}_2(\text{CO})_3\text{PPh}_3$  (400 mg, 0.61 mmol) in 20 mL THF was added a solution of  $\text{PyS}^-\text{Na}^+$  (81 mg, 0.61 mmol) in 10 mL THF. The reaction mixture was stirred for 12 h at room temperature in dark. After remove of solvent the residue solid was extracted with 50 mL  $\text{Et}_2\text{O}$ . After concentration of the filtrate, a red powder solid product precipitated upon addition of 50 mL hexane. Yield: 156 mg (42 % ); recrystallization from ether gave analytically pure crystals.  $^1\text{H}$  NMR (ppm, acetone- $d_6$ ): 8.17 (d, 1H, PyS), 7.45 (m, 15H,  $\text{PPh}_3$ ), 7.15 (t, 1H, PyS), 6.75 (t, 1H, PyS), 6.13 (d, 1H, PyS),  $^{31}\text{P}$  NMR (ppm, acetone- $d_6$ ):  $\delta = 77.69$  (s). IR ( THF,  $\text{cm}^{-1}$ ): 2031 (s), 1983 (s). Elemental analysis, found (calc'd for  $\text{C}_{24}\text{H}_{19}\text{NFeO}_2\text{PSI}$ ) %: C, 49.07 (49.13); H, 3.11 (3.13); N, 2.08(2.29).



**FeI(CO)<sub>2</sub>PCy<sub>3</sub>PyS (VI-12)** The preparation of **VI-12** was identical to that of **VI-11**. Yield: 140 mg (37 %). <sup>1</sup>H NMR (ppm, acetone-d<sub>6</sub>): 8.62 (d, 1H, PyS), 7.56 (t, 1H, PyS), 6.99 (t, 1H, PyS), 6.71 (d, 1H, PyS), 2.38 (m, 3H, PCy<sub>3</sub>), 1.68 (br, 18 H, PCy<sub>3</sub>), 1.21 (br, 12H, PCy<sub>3</sub>). <sup>31</sup>P NMR (ppm, acetone-d<sub>6</sub>): 76.44 (s). IR (THF, cm<sup>-1</sup>): 2019 (s), 1971 (s). Elemental analysis, found (calc'd for C<sub>24</sub>H<sub>37</sub>NFeO<sub>2</sub>PS) %: C, 48.03 (47.7); H, 6.41 (5.93); N, 1.91 (2.23).

### Experimental for chapter VII

**(NS)Fe(CO)<sub>2</sub>(PCy<sub>3</sub>) (VII-1)** To a mixture of FeI<sub>2</sub>(CO)<sub>3</sub>PCy<sub>3</sub> (300 mg, 0.45 mmol) and 2-aminothiophenol (57 mg, 0.45 mmol) in 30 mL THF was dropwise added 2 equivalents of sodium *t*-butoxide (87 mg, 0.9 mmol) in 30 mL THF over 3 hours. The reaction was monitored to completeness by IR. THF was removed under vacuum and the obtained dark solids were extracted with 30 mL ether. The ether solution was dried under vacuum and washed with 2 x 10 mL pentane to remove byproduct **Fe(CO)<sub>3</sub>(PCy<sub>3</sub>)<sub>2</sub>** (1960 (s, sh) and 1952 (s) cm<sup>-1</sup> in ether). Then the crude product was re-dissolved in 20 mL ether. The solution was cooled at -30 °C to afford dark crystals of product **4** suitable for all characterizations (yield, 70%, 161mg.). <sup>1</sup>H NMR (ppm, CD<sub>2</sub>Cl<sub>2</sub>): 10.12 (s, 1H, PhNHS), 7.82 (s, 1H, *Ph*NHS), 7.47 (s, 1H, *Ph*NHS), 7.09 (s, 2H, *Ph*NHS), 2.08 (br, 3H, Cy), 1.75 (br, 12H, Cy), 1.60 (br, 6H, Cy), 1.06 (br, 12 H, Cy); <sup>31</sup>P NMR (ppm, CD<sub>2</sub>Cl<sub>2</sub>): 89.59 (s). IR (CH<sub>2</sub>Cl<sub>2</sub>, cm<sup>-1</sup>): 1985 (s), 1927 (s). Elemental analysis, found, (calculated, based on complex **VII-1**, C<sub>26</sub>H<sub>38</sub>FeNO<sub>2</sub>PS, *calculated, based on complex 4-Et<sub>2</sub>O*, C<sub>30</sub>H<sub>48</sub>FeNO<sub>3</sub>PS) %: C, 61.15 (60.58, 61.11); H, 7.56 (7.43, 8.21), N, 2.68 (2.72, 2.38).

**(NS)Fe(CO)<sub>2</sub>PPh<sub>3</sub> (VII-2)** and *trans*-**Fe(CO)<sub>3</sub>(PPh<sub>3</sub>)<sub>2</sub>** To a mixture of FeI<sub>2</sub>(CO)<sub>3</sub>PPh<sub>3</sub> (600 mg, 0.92 mmol) and 2-aminothiophenol (114 mg, 0.92 mmol) in 30 mL THF was dropwise added 2 equivalents of sodium *t*-butoxide (177 mg, 1.84 mmol) in 30 mL THF over 3 hours. THF was removed under vacuum and the dark solids obtained were extracted by 30 mL ether. Overnight cooling of the ether solution at -30 °C afforded dark brown crystals of complex **VII-2** suitable for all characterizations (yield, 64 mg, 14%). Extending crystallization yielded crystals of **(VII-2)** and red crystals of byproduct, **trans-Fe(CO)<sub>3</sub>(PPh<sub>3</sub>)<sub>2</sub>** (IR (CH<sub>2</sub>Cl<sub>2</sub>, cm<sup>-1</sup>): 1886 (s)) as determined by X-ray diffraction.

Complex **VII-2**: <sup>1</sup>H NMR (ppm, CD<sub>2</sub>Cl<sub>2</sub>): 9.46 (s, 1H, PhNHS), 7.84 (d, 1H, PhNHS), 7.44 (multi-peaks, 15H, PPh), 7.15 (t, 2H, PhNHS), 7.05 (d, 1H, PhNHS); <sup>31</sup>P NMR (ppm, CD<sub>2</sub>Cl<sub>2</sub>): 97.42 (s). IR (CH<sub>2</sub>Cl<sub>2</sub>, cm<sup>-1</sup>): 2002 (s), 1942 (s). Elemental analysis, found (calc'd for C<sub>26</sub>H<sub>20</sub>FeNO<sub>2</sub>PS) %: C, 60.82 (62.79); H, 4.01 (4.05), N, 3.26 (2.82). The low quality of this elemental analysis is likely a result of some decomposition due to its extreme thermal and light sensitivity.

**(NS)Fe(CO)<sub>2</sub>P(OEt)<sub>3</sub> (VII-3)** To a mixture of FeI<sub>2</sub>(CO)<sub>3</sub>P(OEt)<sub>3</sub> (300 mg, 0.54 mmol) and 2-aminothiophenol (67 mg, 0.54 mmol) in 30 mL THF was dropwise added 2 equivalents of sodium *t*-butoxide in 30 mL THF (104 mg, 1.08 mmol) over 3 hours. THF was removed under vacuum and the obtained dark residues were extracted by 30 mL ether. The ether solution was concentrated to 10 mL and placed at -30 °C overnight afforded dark precipitates as products (160 mg, 74%) . <sup>1</sup>H NMR (ppm, CD<sub>2</sub>Cl<sub>2</sub>): 10.24 (s, 1H, PhNHS), 7.85 (q, 1H, PhNHS), 7.49 (q, 1H, PhNHS), 7.13 (q, 2H, PhNHS), 3.79

(q, 6H,  $-OCH_2CH_3$ ), 1.21 (t, 9H,  $-OCH_2CH_3$ );  $^{31}P$  NMR (ppm,  $CD_2Cl_2$ ): 173.61 (s). IR ( $CH_2Cl_2$ ,  $cm^{-1}$ ): 2012 (s), 1952 (s). Elemental analysis, found (calc'd for  $C_{14}H_{20}FeNO_5PS$ ) %: C, 42.58 (41.91); H, 5.76 (5.02), N, 3.12 (3.49). The low quality of this elemental analysis is likely a result of some decomposition due to its extreme thermal and light sensitivity.

**CO uptake of VII-1 in the presence of  $Et_2O \cdot HBF_4$**  In a CO (1 bar) atmosphere, complex **VII-1** (20 mg, 0.04 mmol) dissolved in 5 mL acetone was treated with  $Et_2O \cdot HBF_4$  by dropwise addition. The reaction was monitored by IR to indicate the generation of  $[VII-4(CO)-H]^+BF_4^-$  (2102(w) and 2046(vs)  $cm^{-1}$ ) accompanied by a color change from dark brown to orange within 15 minutes. The treatment of  $[VII-4(CO)-H]^+BF_4^-$  with  $Et_3N$  led to CO liberation and stoichiometric regeneration of complex **VII-1** as monitored by IR.

**Concomitant CO uptake and  $^{12}CO/^{13}CO$  exchange of VII-1 in the presence of  $Et_2O \cdot HBF_4$**  When the experiment (in the presence of the acid,  $Et_2O \cdot HBF_4$ ) described above was conducted in a  $^{13}CO$  atmosphere (1 bar), the  $^{13}CO$  labeled  $[VII-1(CO)-H]^+BF_4^-$  ((2056(w) and 2002(vs)  $cm^{-1}$ ) was formed within 15 minutes. Base treatment ( $NEt_3$ ) led to the reformation of **VII-1** completely  $^{13}CO$  labeled (1982(s), and 1938(s)  $cm^{-1}$ ).

**Direct  $^{12}CO/^{13}CO$  exchange of complex VII-1 without acid** In a  $^{13}CO$  (1 bar) atmosphere, complex **VII-1** (20 mg, 0.04 mmol) dissolved in 5 ml acetone was monitored by IR up to 3 days. The IR monitor indicated direct  $^{12}CO/^{13}CO$  exchange of

complex **VII-1** was slow and stepwise as one  $^{13}\text{CO}$  and two  $^{13}\text{CO}$  labeled species were observed.

## CHAPTER III

### NHC CARBENE SUPPORTED MIXED-VALENT Fe<sup>II</sup>Fe<sup>I</sup>, DIIRON COMPLEXES THAT MODEL THE H<sub>ox</sub> STATE OF THE [FeFe]- HYDROGENASE ACTIVE SITE\*

#### Introduction

There is an impressive concurrence of the diiron sub-unit of the six-iron H-cluster in [FeFe]Hydrogenase, [FeFe]H<sub>2</sub>ase, **A**, with a classic Fe<sup>I</sup>Fe<sup>I</sup> organometallic, (μ-pdt)[Fe(CO)<sub>3</sub>]<sub>2</sub> (pdt = propane dithiolate, <sup>-</sup>S(CH<sub>2</sub>)<sub>3</sub>S<sup>-</sup>), **B**.<sup>7, 186</sup> In the protein crystal structure of the “Hox” state, the 2Fe site is currently assigned as a mixed-valent Fe<sup>I</sup>Fe<sup>II</sup> redox level;<sup>46, 59, 187</sup> however, exact Fe oxidation states under various conditions remain questionable.<sup>55</sup> From the structures of **A** and **B** in Scheme III. 1 significant discrepancies are obvious, including, in **A**, the apparent open site on an otherwise octahedral iron and the CO group that toggles between bridging or semi-bridging, dependent on the redox level of the enzyme active site (eas) or adjacent 4Fe4S clusters. The ease of manipulation of complex **B** has led to extensive efforts in the synthesis of

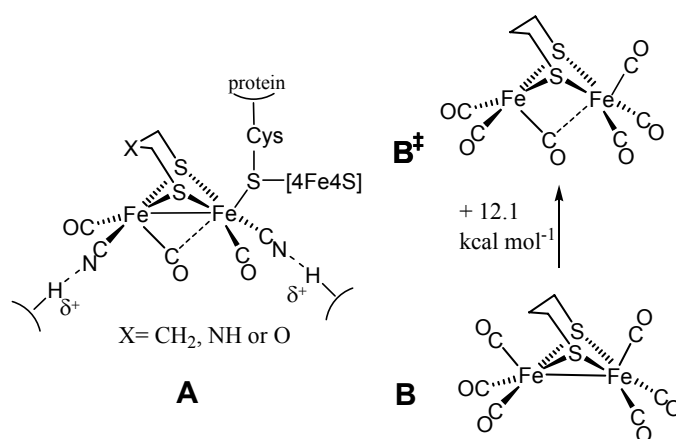
---

\*Reprinted with permission from three manuscripts. (1) Liu, T.; Darensbourg, M. Y. A Mixed-Valent, Fe(II)Fe(I), Diiron Complex Reproduces the Unique Rotated State of the [FeFe]Hydrogenase Active Site. *J. Am. Chem. Soc.* **2007**, *129* (22), 7008-7009, Copyright [2007] by the American Chemical Society. (2) Thomas, C. M.; Liu, T. B.; Hall, M. B.; Darensbourg, M. Y. Regioselective (CO)-C-12/(CO)-C-13 exchange activity of a mixed-valent Fe(II) Fe(I) model of the H-ox state of [FeFe]-hydrogenase. *Chem. Commun.* **2008**, (13), 1563-1565, Copyright [2008] by the Royal Chemical Society. (3) Thomas, C. M.; Liu, T.; Hall, M. B.; Darensbourg, M. Y. Series of Mixed Valent Fe(II)Fe(I) Complexes That Model the Hox State of [FeFe]Hydrogenase: Redox Properties, Density-Functional Theory Investigation, and Reactivities with Extrinsic CO. *Inorg. Chem.* **2008**, *47* (15), 7009-7024, Copyright [2008] by the American Chemical Society.

derivatives aiming to reproduce structural and spectroscopic features of the eas, and to exploit the models for electrocatalysis.<sup>131, 135, 188</sup>

Steady progress made since the definitive report of the H-cluster structure has called upon fundamental principles of organometallic chemistry to guide designs of small molecule analogues with first coordination sphere ligands taking the place of the elaborate protein scaffold. Still there is great difficulty in stabilizing a synthetic analog with the entatic state or “rotated” structure, **B<sup>‡</sup>**, which is computed to exist only as the transition state in CO site exchange processes of  $(\mu\text{-SRS})[\text{Fe}^{\text{I}}(\text{CO})_3]_2$ .<sup>162</sup> Furthermore, examples of the mixed valent  $\text{Fe}^{\text{II}}\text{Fe}^{\text{I}}$  state that is observed as a prominent redox level in the enzyme are rare.<sup>55, 188</sup> The synthesis of mixed valent  $\text{Fe}^{\text{II}}\text{Fe}^{\text{I}}$  compounds were presaged by computational studies<sup>189</sup> and by the efforts of Rauchfuss and coworkers, who reported  $\text{Fe}^{\text{II}}\text{Fe}^{\text{II}}$  dithiolates in which a terminal hydride was characterized,<sup>135</sup> mimicking the structural features of an expected key intermediate of the enzymatic catalysis and highlighting the occurrence of a terminal hydride in the catalytic cycle.

### Scheme III. 1



We and others have explored the possibility that the unique properties of N-heterocyclic carbene (NHC) ligands,<sup>165, 181</sup> such as IMes, 1,3-bis(2,4,6-trimethylphenyl)imidazol-2-ylidene, in  $(\mu\text{-pdt})[\text{Fe}(\text{CO})_3][\text{Fe}(\text{CO})_2(\text{IMes})]$ , complex **III-1<sub>NHC</sub>**, might be useful in the preparation of  $\text{Fe}^{\text{I}}\text{Fe}^{\text{I}}$  electrocatalysts for  $\text{H}_2$  production.

In the course of extending the redox activity of NHC complexes into the  $\text{H}_2$  uptake and oxidation regime, we have prepared the unsymmetric disubstituted derivative  $(\mu\text{-pdt})[\text{Fe}(\text{CO})_2(\text{PMe}_3)]\text{-}[\text{Fe}(\text{CO})_2(\text{IMes})]$ , complex **III-1**.<sup>190</sup> The  $\text{Fe}^{\text{I}}\text{Fe}^{\text{I}}$  precursor, **III-1**, was initially designed according the following assumptions: (1) asymmetric coordination might differentiate the two Fe sites with respect to their redox activities upon one electron oxidation; (2) good donor ligands are needed for stabilization of the  $\text{Fe}^{\text{II}}$  oxidation state; and (3) sterically encumbering ligand substituents could potentially protect an open coordination site. A combination of  $\text{PMe}_3$  and the N-heterocyclic carbene IMes fulfilled these requirements. The  $\text{PMe}_3$  ligand has been used extensively in  $[\text{FeFe}]\text{H}_2\text{ase}$  active site synthetic analogues as a ligand that emulates the donor properties of the biological  $\text{CN}^-$  ligand, without the complications of reactivity at the cyanide nitrogen. The IMes ligand is a strong  $\sigma$ -donor ligand with dynamic steric properties as a result of the low rotation barrier about the M-C bond in its metal complexes.<sup>191</sup> Its fully reversible  $\text{Fe}^{\text{I}}\text{Fe}^{\text{I}} \rightleftharpoons \text{Fe}^{\text{II}}\text{Fe}^{\text{I}}$  couple as expected inspired efforts to isolate the first unsaturated mixed-valent  $\text{Fe}^{\text{II}}\text{Fe}^{\text{I}}$  complex, **III-1<sub>ox</sub>**,<sup>190, 192</sup> via one electron oxidation as described in this chapter.

In a collaboration with Dr. Christine M. Thomas, a systematic investigation of other asymmetrically disubstituted diiron complexes,  $(\mu\text{-$

pdt)[Fe<sup>I</sup>(CO)<sub>2</sub>PMe<sub>3</sub>][Fe<sup>I</sup>(CO)<sub>2</sub>(NHC)], with a selection of N-heterocyclic carbene (NHC) ligands with different N-atom substituents (NHC = IMem (**III-2**), IMe (**III-3**)) was conducted to address the questions posed below through a combination of experimental and computational approaches.<sup>193, 194</sup>

(1) What steric role is played by the carbene's N-atom substituents in protecting the open coordination site on the rotated Fe center?

(2) What combination of steric/electronic factors and configurational isomers control the semi-bridging nature of the CO ligand?

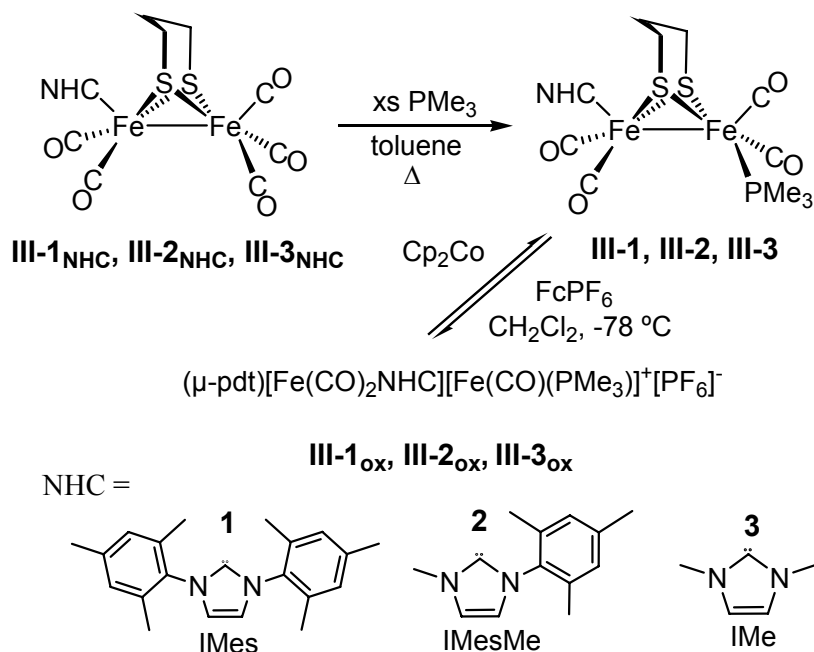
(3) Do these mixed valent synthetic analogues mimic the CO uptake and exchange reactivity of the H<sub>ox</sub> state of the biological active site?

## Results and discussion

Spectroscopic characterization of complexes (μ-pdt)[Fe(CO)<sub>2</sub>NHC][Fe(CO)<sub>3</sub>] (**III-1**<sub>NHC</sub>, **III-2**<sub>NHC</sub> and **III-3**<sub>NHC</sub>) and (μ-pdt)[Fe(CO)<sub>2</sub>NHC][Fe(CO)<sub>2</sub>PMe<sub>3</sub>] (**III-1**, **III-2** and **III-3**). The mono-substituted Fe<sup>I</sup>Fe<sup>I</sup> precursors were synthesized via NHC ligand displacement of CO from (μ-pdt)[Fe(CO)<sub>3</sub>]<sub>2</sub>. Subsequent thermal substitution with PMe<sub>3</sub> ultimately led to product as deep red crystals as described in the Experimental section (Chapter II) and shown in Scheme III. 2. These complexes are at least moderately soluble in both nonpolar and polar organic solvents ranging from pentane to methanol. Solubility in polar solvents increases in the order of **III-1**, **III-2** and **III-3**.



Scheme III. 2



The FTIR data for the mono- and di-substituted complexes in the diatomic ligand region are listed in Table III. 1. In THF solution, the mono-substituted NHC complexes display similar IR patterns with five  $\nu(\text{CO})$  stretches at very similar frequencies. The second and third bands of **III-1<sub>NHC</sub>** and **III-2<sub>NHC</sub>** are well-defined while those of **III-3<sub>NHC</sub>** significantly overlap. Very similar IR patterns and  $\nu(\text{CO})$  values were also observed for complexes **III-1~III-3**. The increased electron density at Fe with sequential CO substitution results in shifts of  $\nu(\text{CO})$  to lower values by 40 to 60  $\text{cm}^{-1}$  compared to  $(\mu\text{-pdt})[\text{Fe}(\text{CO})_3]_2$  and  $(\mu\text{-pdt})[\text{Fe}(\text{CO})_3][\text{Fe}(\text{CO})_2\text{NHC}]$ , respectively. The donating ability of NHC ligands compared to phosphine and  $\text{CN}^-$  ligands can be evaluated using  $\nu(\text{CO})$  IR stretches as an indicator of metal electrophilicity. The  $\nu(\text{CO})$  values of complexes **III-1<sub>NHC</sub>~III-3<sub>NHC</sub>** are slightly lowered from those of ( $\mu$ -

pdt)[Fe(CO)<sub>3</sub>][Fe(CO)<sub>2</sub>PMe<sub>3</sub>], but higher than that of (μ-pdt)[Fe(CO)<sub>3</sub>][Fe(CO)<sub>2</sub>CN]<sup>-</sup>. A simple conclusion is that the electron-donating ability of the NHC's and PMe<sub>3</sub> are similar, and that both ligands create an environment about iron that is slightly less electron-rich than is that of the cyanide analogue.

**Table III. 1** Infrared spectroscopic data for (μ-pdt)[Fe(CO)<sub>2</sub>(L)]<sub>2</sub>, derivatives (reported in THF solution unless otherwise noted).

Complex	ν(CO) (cm <sup>-1</sup> )
<sup>a</sup> (μ-pdt)[Fe(CO) <sub>3</sub> ] <sub>2</sub> <sup>162</sup>	2074 (m), 2036 (vs), 1995 (s)
<sup>a</sup> (μ-pdt)[Fe(CO) <sub>3</sub> ][Fe(CO) <sub>2</sub> PMe <sub>3</sub> ] <sup>163</sup>	2037 (s), 1980 (s), 1919 (m)
<sup>a</sup> (μ-pdt)[Fe(CO) <sub>2</sub> PMe <sub>3</sub> ] <sub>2</sub> <sup>142</sup>	1979 (m), 1942 (s), 1898 (s)
(μ-pdt)[Fe(CO) <sub>3</sub> ][Fe(CO) <sub>2</sub> CN] <sup>-127</sup>	2027 (m), 1977 (s), 1944 (s), 1919 (m)
(μ-pdt)[Fe(CO) <sub>2</sub> PMe <sub>3</sub> ][Fe(CO) <sub>2</sub> CN] <sup>-127</sup>	1971 (s), 1931 (s), 1895 (s), 1880 (sh)
<sup>b</sup> (μ-pdt)[Fe(CO) <sub>3</sub> ][Fe(CO) <sub>2</sub> IMes] ( <b>III-1</b> <sub>NHC</sub> )	2035(s), 2027(s), 1969(vs), 1947(m), 1916(m)
<sup>b</sup> (μ-pdt)[Fe(CO) <sub>3</sub> ][Fe(CO) <sub>2</sub> IMeM] ( <b>III-2</b> <sub>NHC</sub> )	2035 (s), 2025 (s), 1970 (vs), 1949(s), 1916(m)
<sup>b</sup> (μ-pdt)[Fe(CO) <sub>3</sub> ][Fe(CO) <sub>2</sub> IMe] ( <b>III-3</b> <sub>NHC</sub> )	2039 (s), 2031 (s), 1970(vs), 1950 (s), 1916 (m)
<sup>b</sup> (μ-pdt)[Fe(CO) <sub>2</sub> PMe <sub>3</sub> ][Fe(CO) <sub>2</sub> IMes] ( <b>III-1</b> )	1972 (s), 1933 (vs), 1897 (s), 1882 (m,sh)
<sup>b</sup> (μ-pdt)[Fe(CO) <sub>2</sub> PMe <sub>3</sub> ][Fe(CO) <sub>2</sub> IMesMe] ( <b>III-2</b> )	1974 (s), 1934 (s), 1899 (m), 1884 (m, sh)
<sup>b</sup> (μ-pdt)[Fe(CO) <sub>2</sub> PMe <sub>3</sub> ][Fe(CO) <sub>2</sub> IMe] ( <b>III-3</b> )	1974 (s), 1934 (s), 1898 (m), 1884 (m, sh)
<sup>b</sup> {(μ-pdt)[Fe(CO) <sub>2</sub> PMe <sub>3</sub> ][Fe(CO) <sub>2</sub> IMes]} <sup>+</sup> ( <b>III-1</b> <sub>ox</sub> )	2037 (s), 1997 (vs), 1987 (s,sh), 1886 (w)
<sup>b</sup> {(μ-pdt)[Fe(CO) <sub>2</sub> PMe <sub>3</sub> ][Fe(CO) <sub>2</sub> IMesMe]} <sup>+</sup> ( <b>III-2</b> <sub>ox</sub> )	2036(s), 2000 (vs), 1983(s, sh),1929 (w)
<sup>b</sup> {(μ-pdt)[Fe(CO) <sub>2</sub> PMe <sub>3</sub> ][Fe(CO) <sub>2</sub> IMes]} <sup>+</sup> ( <b>III-3</b> <sub>ox</sub> )	2036(s), 2005 (vs), 1981(s), 1929 (w)

<sup>a</sup>Spectrum recorded in acetonitrile; <sup>b</sup> Reported in this work.

**Cyclic voltammetry of complexes III-1<sub>NHC</sub>~III-3<sub>NHC</sub> and III-1~III-3.** The redox behavior of the complexes was investigated using cyclic voltammetry (CV) for comparative purposes and to enable us to choose an appropriate chemical oxidant (and reductant) for solution redox chemistry (*vide infra*). Electrochemical data (referenced to

$\text{Fc}^+/\text{Fc} = 0.00 \text{ V}$ ) are compared in Table III. 2 and assigned according to a previous report.<sup>95, 145, 146, 195</sup> To explore the effects of solvent on the different redox couples, especially the  $\text{Fe}^{\text{II}}\text{Fe}^{\text{I}}/\text{Fe}^{\text{I}}\text{Fe}^{\text{I}}$  couple of interest, CV measurements were performed in both coordinating ( $\text{CH}_3\text{CN}$ ) and relatively non-coordinating solvent ( $\text{CH}_2\text{Cl}_2$ ) for complexes **III-1~III-3**. The CV's of complexes **III-1~III-3** in  $\text{CH}_3\text{CN}$  (0.1 M [ $^n\text{Bu}_4\text{N}$ ][ $\text{BF}_4$ ], scan rate = 100 mV/s, 22 °C) display several redox events (Figure III. 1) that shift cathodically relative to those of **III-1<sub>NHC</sub>**, consistent with the increase in electron density at the diiron centers with the  $\text{PMe}_3/\text{CO}$  substitution. Under the conditions reported here, the cyclic voltammograms of all six complexes feature an irreversible reduction at negative potentials in  $\text{CH}_3\text{CN}$  ( $< -2 \text{ V}$  vs  $\text{Fc}/\text{Fc}^+$ ), with the disubstituted complexes **III-1~III-3** being more difficult to reduce by 0.2-0.5 V and at the limit of the solvent window. From a detailed electrochemical investigation of **III-3<sub>NHC</sub>** by Capon, et al. the conclusion was made that the reduction is a two-electron process and partially reversible. In the presence of weak acid ( $\text{HOAc}$ ), the current at the reduction potential of complex **III-1~III-3** increases with increasing concentrations of acid, indicative of electrocatalytic  $\text{H}^+$  reduction by these diiron dithiolate models,<sup>193</sup> as reported for **III-1<sub>NHC</sub>**.<sup>165</sup>

The cyclic voltammograms of both mono-substituted **III-1<sub>NHC</sub>~III-3<sub>NHC</sub>** and di-substituted **III-1~III-3** display irreversible oxidations at  $E_{pa} \sim 0.7 \text{ V}$ ., There is an additional additional oxidative process in all complexes, attributed to an  $\text{Fe}^{\text{II}}\text{Fe}^{\text{I}}/\text{Fe}^{\text{I}}\text{Fe}^{\text{I}}$  couple, which shows a degree of reversibility and whose position depends on the degree of substitution, Table III. 2. The  $\text{Fe}^{\text{II}}\text{Fe}^{\text{I}}/\text{Fe}^{\text{I}}\text{Fe}^{\text{I}}$  couple ( $E_{1/2} = -0.47 \text{ V}$ ) of complex **III-1**

in CH<sub>3</sub>CN was also observed in CH<sub>2</sub>Cl<sub>2</sub> solution ( $E_{1/2} = -0.50$  V) with a slight cathodic shift (Figure III. 1). , The reversibility of this redox couple was well maintained at a slower scan rate (50 mV/s) in both solvents. The CV of complex **III-2** features a similar reversible Fe<sup>II</sup>Fe<sup>I</sup>/Fe<sup>I</sup>Fe<sup>I</sup> couple in both CH<sub>3</sub>CN and CH<sub>2</sub>Cl<sub>2</sub> solution, although this couple is shifted anodically by ca. 0.15 V from that of **III-1**. In contrast to complexes **III-1** and **III-2**, in CH<sub>3</sub>CN solution, complex **III-3** shows a quasi-reversible Fe<sup>II</sup>Fe<sup>I</sup>/Fe<sup>I</sup>Fe<sup>I</sup> couple ( $E_{1/2} = -0.24$  V). In CH<sub>2</sub>Cl<sub>2</sub>, however, this process becomes fully reversible. No additional events or changes in the Fe<sup>II</sup>Fe<sup>I</sup>/Fe<sup>I</sup>Fe<sup>I</sup> couple are observed when the CV's of complexes **III-1~III-3** are measured under a CO atmosphere rather than Ar.

**Table III. 2** Electrochemical potentials (V vs Fc<sup>+</sup>/Fc) as determined by cyclic voltammetry for ( $\mu$ -pdt)[Fe(CO)<sub>2</sub>(NHC)][Fe(CO)<sub>2</sub>(L)] complexes, **III-1<sub>NHC</sub>~III-3<sub>NHC</sub>** and **III-1~III-3** (recorded in CH<sub>3</sub>CN or CH<sub>2</sub>Cl<sub>2</sub> with 0.1 M [<sup>n</sup>Bu<sub>4</sub>N][BF<sub>4</sub>]; scan rate = 100 mV/s, 22 °C). The data for **III-3<sub>NHC</sub>** was taken from ref. 40.

Complex	CH <sub>3</sub> CN			CH <sub>2</sub> Cl <sub>2</sub>		
	Further oxidation(s)	Fe <sup>II</sup> Fe <sup>I</sup> /Fe <sup>I</sup> Fe <sup>I</sup>	Fe <sup>I</sup> Fe <sup>I</sup> /Fe <sup>I</sup> Fe <sup>0</sup>	Further oxidation(s)	Fe <sup>II</sup> Fe <sup>I</sup> /Fe <sup>I</sup> Fe <sup>I</sup>	Fe <sup>I</sup> Fe <sup>I</sup> /Fe <sup>I</sup> Fe <sup>0</sup>
<b>III-1<sub>NHC</sub></b>	0.72	0.11	-2.10	—	—	—
<b>III-2<sub>NHC</sub></b>	0.77	0.23	-2.12	—	—	—
<b>III-3<sub>NHC</sub></b>		0.11	-2.01	—	—	—
<b>III-1</b>	0.77, 0.14	-0.47	-2.36	0.85	-0.50	—
<b>III-2</b>	0.70, -0.11	-0.33	-2.52	-0.12	-0.38	-2.50
<b>III-3</b>	0.84, 0.37	-0.24	-2.53	0.49	-0.33	—

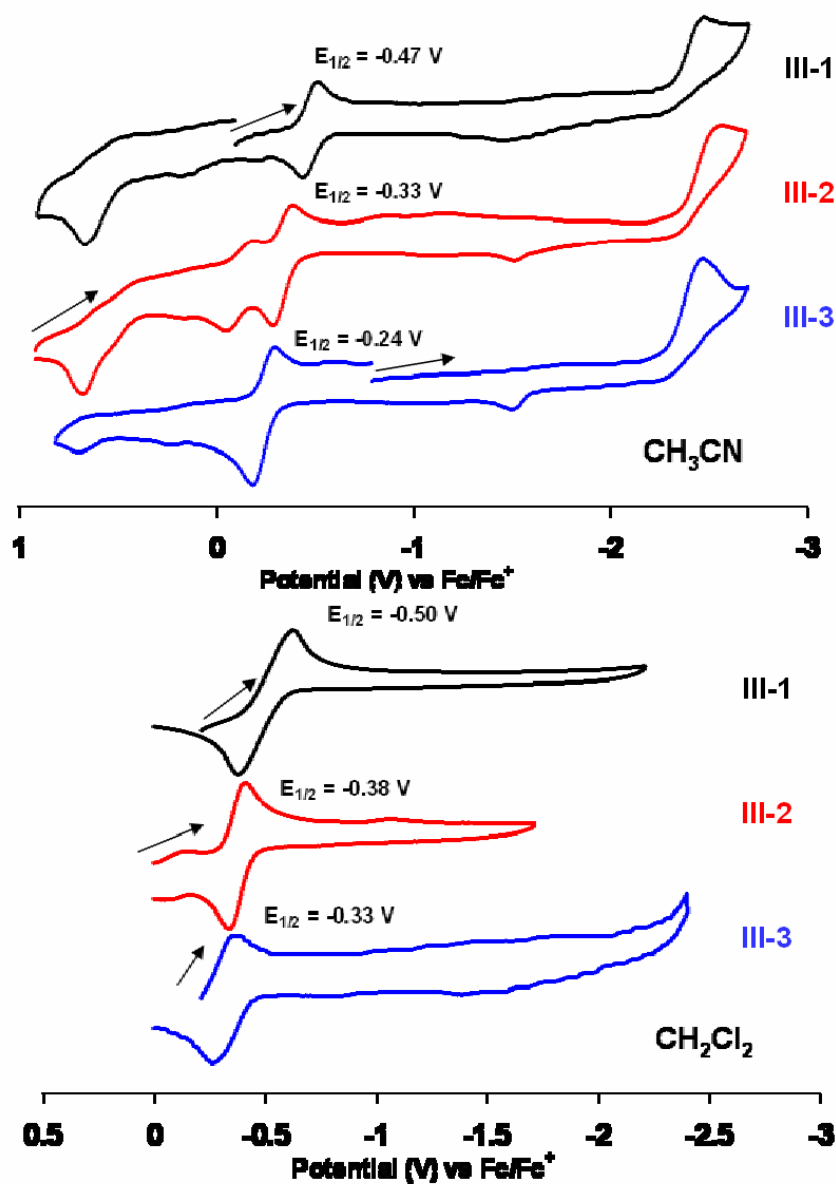


**Figure III. 1** Cyclic voltammograms of  $(\mu\text{-pdt})[\text{Fe}(\text{CO})_2\text{PMe}_3][\text{Fe}(\text{CO})_2\text{IMes}]$  (**III-1**, black),  $(\mu\text{-pdt})[\text{Fe}(\text{CO})_2\text{PMe}_3][\text{Fe}(\text{CO})_2\text{IMesMe}]$  (**III-2**, red), and  $(\mu\text{-pdt})[\text{Fe}(\text{CO})_2\text{PMe}_3][\text{Fe}(\text{CO})_2\text{IME}]$  (**III-3**, blue) in CH<sub>3</sub>CN (top) and CH<sub>2</sub>Cl<sub>2</sub> (bottom). All potentials are reported vs. Fe<sup>+</sup>/Fe (0.1 M [<sup>n</sup>Bu<sub>4</sub>N][BF<sub>4</sub>], scan rate = 100 mV/s, 22 °C).

Notably, the  $\text{Fe}^{\text{II}}\text{Fe}^{\text{I}}/\text{Fe}^{\text{I}}\text{Fe}^{\text{I}}$  couple of **III-1** occurs at a more positive potential than that of **III-2** or **III-3**, but the reduction for **III-2** and **III-3** occurs at potentials more negative than that of **III-1**. As the IR data is convincing of the similar electron-donating ability of the three NHC ligands, this difference in oxidation potentials between **III-1** vs. **III-2** and **III-3** must be ascribed to the steric differences in the ligands. The steric control of such a thermodynamic property may be a result of stabilization of the rotated forms or of different configurational/conformational isomers, as explored below by DFT calculations. Note that complex **III-2** which has the possibility of rotational isomers of the NHC shows yet another oxidative event, at ca. 0.1 V, possibly reflecting the presence of another stable form.

**Synthesis and spectroscopic characterization of complex III-1<sub>ox</sub>~III-3<sub>ox</sub>.** Based on the electrochemical data regarding the  $\text{Fe}^{\text{II}}\text{Fe}^{\text{I}}/\text{Fe}^{\text{I}}\text{Fe}^{\text{I}}$  couple of complexes **III-1~III-3**, one electron oxidation was performed at -78 °C to isolate  $\text{Fe}^{\text{I}}\text{Fe}^{\text{II}}$  mixed-valent species with subsequent back-reduction to confirm reversibility.<sup>190</sup>

In  $\text{CH}_2\text{Cl}_2$ , oxidation of the red  $\text{Fe}^{\text{I}}\text{Fe}^{\text{I}}$  complexes **III-1~III-3** with one equivalent of  $\text{FcPF}_6$  generated the corresponding brown  $\text{Fe}^{\text{II}}\text{Fe}^{\text{I}}$  complexes,  $(\mu\text{-pdt})(\mu\text{-CO})[\text{Fe}(\text{CO})_2(\text{PMe}_3)][\text{Fe}(\text{CO})(\text{IMes})]^+ \text{PF}_6^-$  (**III-1<sub>ox</sub>**),  $(\mu\text{-pdt})(\mu\text{-CO})[\text{Fe}(\text{CO})_2(\text{PMe}_3)][\text{Fe}(\text{CO})(\text{IMesMe})]^+ \text{PF}_6^-$  (**III-2<sub>ox</sub>**) and  $(\mu\text{-pdt})(\mu\text{-CO})[\text{Fe}(\text{CO})_2(\text{PMe}_3)][\text{Fe}(\text{CO})_2(\text{IMe})]^+ \text{PF}_6^-$  (**III-3<sub>ox</sub>**) within 0.5 h (Figure III. 2). Monitoring by IR spectroscopy indicates that the oxidized species could be returned to their respective  $\text{Fe}^{\text{I}}\text{Fe}^{\text{I}}$  forms by reduction with  $\text{Cp}_2\text{Co}$  at -78 °C. The thermal stability of the oxidized complexes decreases with decreasing steric bulk of the NHC ligand (**III-1<sub>ox</sub>**

> **III-2<sub>ox</sub>** > **III-3<sub>ox</sub>**). Thus, while **III-1<sub>ox</sub>** is modestly stable in solution at room temperature for short time periods, appreciable decomposition of **III-2<sub>ox</sub>** and **III-3<sub>ox</sub>** occurs within minutes at room temperature and solutions of these complexes must be stored at -40 °C or below.

It is noteworthy that the Fe<sup>II</sup>Fe<sup>I</sup> mixed valent species observed in this work and in that of Justice, et al.,<sup>190, 196</sup> requires the use of a non-coordinating solvent. When CH<sub>3</sub>CN or THF is used, the mixed valent species was not observed by IR spectroscopy. Presumably coordinating solvents promote disproportionation yielding Fe<sup>II</sup>Fe<sup>II</sup> species, consistent with the observations of Rauchfuss, et al., in which the solvent-coordinated diferrous species (μ-SCH<sub>2</sub>CH<sub>2</sub>S)(μ-CO)[Fe(CO)<sub>2</sub>(PMe<sub>3</sub>)[Fe(dppv)(solv)]<sup>2+</sup> (solv = CH<sub>3</sub>CN or (CH<sub>3</sub>)<sub>2</sub>C=O) was isolated from the addition of 2 equiv of Fe<sup>+</sup> to the Fe<sup>I</sup>Fe<sup>I</sup> dithiolate precursor (μ-edt)[Fe(CO)<sub>2</sub>(PMe<sub>3</sub>)[Fe(CO)(dppv)] (dppv = 1,2-(diphenylphosphino)vinylidene) in coordinating solvents such as acetone or CH<sub>3</sub>CN.<sup>197</sup>

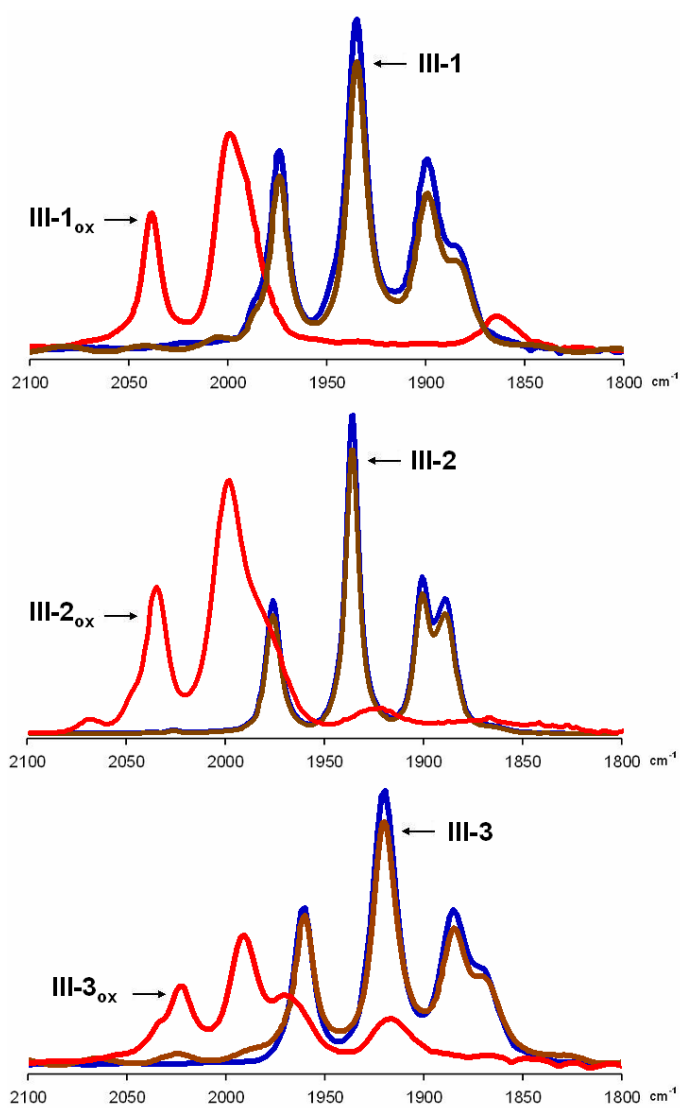


**Figure III. 2** Solution IR spectra ( $\text{CH}_2\text{Cl}_2$ ) showing the reversibility of the one-electron oxidation of **III-1** (A), **III-2** (B), and **III-3** (C). Blue IR spectrum: neutral **III-1**, **III-2**, and **III-3**; Red IR spectrum: cationic **III-1<sub>ox</sub>**, **III-2<sub>ox</sub>**, and **III-3<sub>ox</sub>** generated by treatment of **III-1**, **III-2**, and **III-3**, respectively, with  $\text{FcPF}_6$  in  $\text{CH}_2\text{Cl}_2$  at  $-78\text{ }^\circ\text{C}$ ; Brown IR spectrum: neutral **III-1**, **III-2**, and **III-3** regenerated by addition of  $\text{CoCp}_2$  (or  $\text{CoCp}^*_2$ ) to **III-1<sub>ox</sub>**, **III-2<sub>ox</sub>**, and **III-3<sub>ox</sub>**, respectively, in  $\text{CH}_2\text{Cl}_2$  at  $-78\text{ }^\circ\text{C}$ .



Complexes **III-1<sub>ox</sub>**~ **III-3<sub>ox</sub>** display quite different IR spectra from those of their reduced precursors with a blue shift of ca. 40~60 cm<sup>-1</sup>, consistent with the formation of more electron-deficient species (Figure III. 2). Within this series of mixed valent Fe<sup>II</sup>Fe<sup>I</sup> complexes, several observations concerning their IR spectra can be summarized by the following: (i) The highest energy band of the series occurs at almost identical frequency around 2036 cm<sup>-1</sup>. (ii) Overlap of the second and the third band decreases in the order of **III-1<sub>ox</sub>** (1997 (vs), 1987 (s,sh)), **III-2<sub>ox</sub>** (2000 (vs), 1983(s, sh)) and **III-3<sub>ox</sub>** (2005 (vs), 1981(s)). (iii) The fourth band of **III-1<sub>ox</sub>** (1861 (w)), indicative of a semi-bridging CO, lies at a much lower frequency relative to the value of 1929 (w) cm<sup>-1</sup> for **III-2<sub>ox</sub>** and **III-3<sub>ox</sub>**. This suggests that in the latter two complexes there is either no  $\mu$ -CO or the extent of bridging character is greatly diminished in comparison to **III-1<sub>ox</sub>**. (iv) In the case of **III-2<sub>ox</sub>**, the absorption intensity of the lowest energy CO vibration is much smaller than those of complexes **III-1<sub>ox</sub>** and **III-3<sub>ox</sub>**.

Complex **III-1<sub>ox</sub>** was also identified by electrospray ionization mass spectrometry (ESI-MS); the mass spectrum of **III-1<sub>ox</sub>** features an isotope pattern for the parent cation at  $m/z = 710$ , as well as several species resulting from CO loss. However, due to their thermal instability, **III-2<sub>ox</sub>** and **III-3<sub>ox</sub>** could not be detected by using the same technique.

The solution magnetic moments of complexes **III-1<sub>ox</sub>**~ **III-3<sub>ox</sub>**, determined by using the Evans' method,<sup>198</sup> were found to be 1.86, 1.87 and 1.89 B.M., respectively, consistent with  $S = \frac{1}{2}$  species. As expected, all three compounds are EPR active, as shown in the X-band EPR spectra given in Figure III. 3. The EPR spectrum of complex **III-1<sub>ox</sub>** features a well-defined rhombic signal with  $g$  values similar to that of the H<sub>ox</sub>

state of [FeFe]-H<sub>2</sub>ase (simulated values for **III-1<sub>ox</sub>**:  $g_1 = 2.099$ ,  $g_2 = 2.022$ ,  $g_3 = 2.007$ ; values reported for H<sub>ox</sub>: 2.10, 2.04, 1.99). In contrast, the EPR spectra of complexes **III-2<sub>ox</sub>** ( $g_1 = 2.095$ ,  $g_2 = 2.045$ ,  $g_3 = 2.014$ ) and **III-3<sub>ox</sub>** ( $g_1 = 2.104$ ,  $g_2 = 2.053$ ,  $g_3 = 2.017$ ) feature broader, more axial signals, indicating that the unpaired electron in these complexes is in a more symmetrical environment. Note that simulation of these EPR spectra did not require any <sup>31</sup>P superhyperfine coupling interactions.

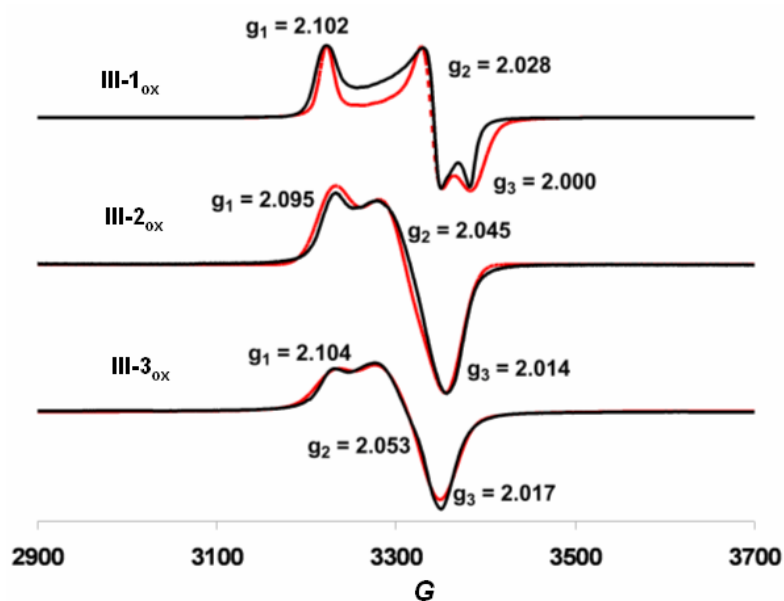


**Figure III. 3** Experimental (black) and simulated (red) EPR spectra of **III-1<sub>ox</sub>** (top), **III-2<sub>ox</sub>** (middle), and **III-3<sub>ox</sub>** (bottom). Spectra were recorded in frozen CH<sub>2</sub>Cl<sub>2</sub> at 10 K, X band. Simulation parameters: **III-1<sub>ox</sub>**:  $g_1 = 2.099$  (linewidth = 13 G),  $g_2 = 2.022$  (linewidth = 11 G),  $g_3 = 2.007$  (linewidth = 13 G); **III-2<sub>ox</sub>**:  $g_1 = 2.095$  (linewidth = 35 G),  $g_2 = 2.045$  (linewidth = 43 G),  $g_3 = 2.014$  (linewidth = 33 G); **III-3<sub>ox</sub>**:  $g_1 = 2.104$  (linewidth = 40 G),  $g_2 = 2.053$  (linewidth = 45 G),  $g_3 = 2.017$  (linewidth = 30 G).

**Molecular structures.** Crystals of **III-2<sub>NHC</sub>**, **III-1**, **III-2**, **III-3** and **III-1<sub>ox</sub>** suitable for crystallographic analysis were grown as described in the experimental section (Chapter II).<sup>190, 193</sup> Selected structural parameters these structures are listed in Table III. 3. For clarity, ball and stick drawings are used to represent all conformers as determined by solid state X-ray diffraction (Figure III. 4). All of the neutral Fe<sup>I</sup>Fe<sup>I</sup> complexes share a butterfly diiron core in which each iron adopts a square pyramidal geometry. As a general structural feature, the NHC ligand coordinates in the apical position, while a basal site is preferred for additional ligand substitution with phosphines in the disubstituted complexes **III-1~III-3**. This orientation of NHC ligand likely minimizes steric interactions of the NHC substituents with the rest of the iron coordination environment. In the solid state, the bridgehead methylene group of the pdt bridge points toward the NHC-coordinated Fe site, except in the case of complex **III-3**. In both the mono- and di-substituted series, the Fe(2)-C(11) bond distance increases with the size of the NHC ligand substituents, and undergoes little change upon PMe<sub>3</sub> addition. All of the Fe<sup>I</sup>Fe<sup>I</sup> complexes presented in this study have similar Fe-Fe distances ranging from 2.527 Å to 2.557 Å, typical for Fe<sup>I</sup>Fe<sup>I</sup> diiron dithiolates.

The solid state structure of **III-1<sub>ox</sub>** (Figure III. 5) confirms that upon one electron oxidation, the ligands about the IMes-coordinated iron (Fe(2)) center reconfigures such that a terminal CO ligand occupies the area under the Fe-Fe vector to form a semi-bridging CO.<sup>190</sup> This semi-bridging character is evident from the asymmetric Fe-C distances, with a Fe(1)-C(3) distance of 2.196 Å, and the Fe(2)-C(3) distance of 1.864 Å is significantly elongated from that of the terminal CO's (Fe(1)-C(1) = 1.808 Å, Fe(1)-

C(2) = 1.782, Fe(2)-C(4) = 1.795 Å). Interestingly, the plane of the IMes ligand also twists to a large extent ( $\sim 90^\circ$ ), likely to reduce steric interactions with the surrounding CO ligands. Overall, the structural features of **III-1<sub>ox</sub>** bear remarkable resemblance to the H<sub>ox</sub> state of [FeFe]H<sub>2</sub>ase. In the case of **III-1<sub>ox</sub>**, both IMes and PMe<sub>3</sub> can be thought of as CN<sup>-</sup> mimics on the distal (Fe<sub>d</sub>) and proximal (Fe<sub>p</sub>) iron sites, respectively. The Fe(2) of **III-1<sub>ox</sub>**, which has a five-coordinate environment and an open site, can be compared to Fe<sub>d</sub> in H<sub>ox</sub>, while the Fe(1) of **III-1<sub>ox</sub>** can be considered as Fe<sub>p</sub> of the enzymatic system, with a CO ligand in place of the cysteinyl sulfur. Unfortunately, after many frustrating attempts, complexes **III-2<sub>ox</sub>** and **III-3<sub>ox</sub>** could not be crystallized; thus DFT calculations (*vide infra*) were undertaken to guide our understanding of the geometries of **III-2<sub>ox</sub>** and **III-3<sub>ox</sub>**.

**Table III. 3** Selected interatomic distances (Å) and angles (deg) for **III-2<sub>NHC</sub>**, **III-1**, **III-2**, **III-3** and **III-1<sub>ox</sub>**.

	<b>III-2<sub>NHC</sub></b>	<b>III-1</b>	<b>III-2</b>	<b>III-3</b>	<b>III-1<sub>ox</sub></b>
Fe(1)-Fe(2)	2.527(1)	2.553(2)	2.557(8)	2.55(1)	2.566(1)
Fe(1)-P(1)	—	2.225(3)	2.20(1)	2.212(2)	2.268(2)
Fe(2)-C(11)	1.971(3)	2.013(1)	1.980(4)	1.971(6)	2.000(4)
Fe(1)-C(3)	—	—	—	—	2.194(4)
Fe(2)-C(3)	1.774(3)	1.740(1)	1.765(5)	1.748(6)	1.864(4)
Fe(2)-S(1)	2.2807(9)	2.276(3)	2.262(1)	2.281(2)	2.299(2)
Fe(2)-S(2)	2.277(1)	2.295(3)	2.274(1)	2.271(2)	2.282(1)
S(1)-Fe(2)-C(11)	104.89(8)	105.2(3)	100.0(1)	100.7(2)	160.9(1)
S(2)-Fe(2)-C(11)	105.90(8)	106.9(3)	101.2(1)	110.5(2)	92.3(1)
Fe(1)-S(1)-Fe(2)	67.52(3)	68.4(1)	68.95(3)	68.16(5)	68.2(3)
Fe(1)-C(3)-Fe(2)	—	—	—	—	77.9(1)
Fe(1)-C(3)-O(3)	—	—	—	—	129.8(3)
Fe(2)-C(3)-O(3)	—	—	—	—	151.9(3)

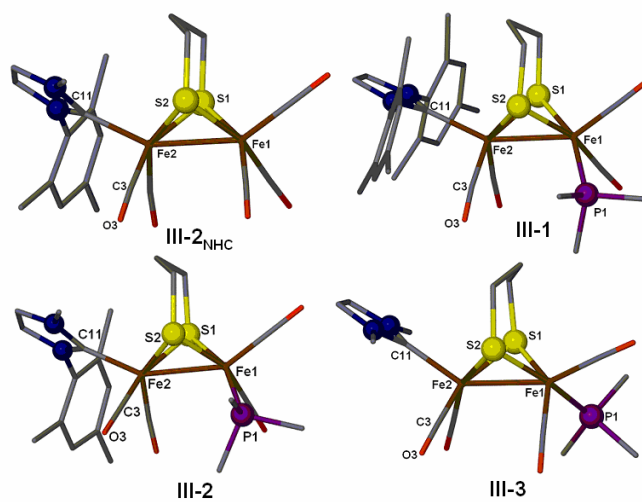


**Figure III. 4** Solid state molecular structures (ball and stick representation) of complexes III-2<sub>NHC</sub>, III-1, III-2 and III-3.

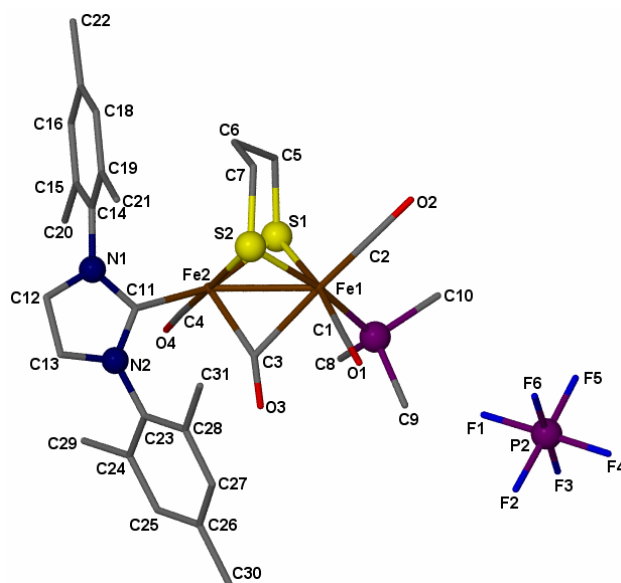


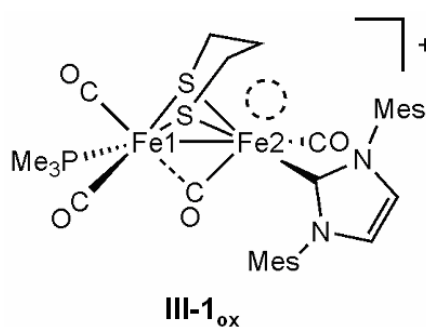
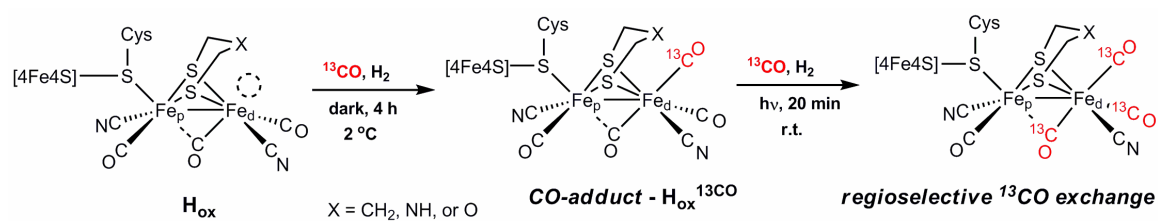
**Figure III. 5** Solid state molecular structure (ball and stick representation) of III-1<sub>ox</sub>.

Despite the formal loss of a full Fe-Fe bond as compared to its Fe<sup>I</sup>Fe<sup>I</sup> precursor, **III-1<sub>ox</sub>** shows only a minor lengthening of its Fe-Fe distance (2.553(2) Å for **III-1** vs 2.566(1) Å for **III-1<sub>ox</sub>**). In the case of previously reported Fe<sup>II</sup>Fe<sup>II</sup> species, the value is around 2.57 Å for Fe<sup>II</sup>Fe<sup>II</sup>(μ-H) hydride models and ca. 2.55 Å for Fe<sup>II</sup>Fe<sup>II</sup>(μ-CO).<sup>135, 197</sup> The similar Fe-Fe distances conserved in all three oxidation states can be rationalized by the close interactions of each Fe center with the bridging ligands, the sulfur of the dithiolate, as well as the bridging H or CO.

**Reactivities of complexes III-1<sub>ox</sub>, III-2<sub>ox</sub>, and III-3<sub>ox</sub> towards extrinsic CO: CO uptake and <sup>13</sup>CO exchange.** Consistent with the known reversible inhibition of H<sub>2</sub> oxidation activity by carbon monoxide in [FeFe]H<sub>2</sub>ase,<sup>22</sup> infrared spectroscopy and X-ray crystallography have shown that extrinsic CO binds to the open coordination site on the Fe<sub>d</sub> center generating the so-called H<sub>ox</sub><sup>CO</sup> form of the enzyme.<sup>49, 55, 57, 199</sup> In a revisit of earlier infrared studies, Roseboom et al. found that, in the absence of light at 2°C, <sup>13</sup>CO binds to the open site on Fe<sub>d</sub> and, under these conditions, does not exchange with the intrinsic CO ligands.<sup>55</sup> Upon illumination at room temperature, however, the <sup>13</sup>CO regioselectively exchanges specifically with the CO ligands on Fe<sub>d</sub>, as shown in Scheme III. 3. Since our overall characterization of complex **III-1<sub>ox</sub>** indicated that it bears similar structural, magnetic and electronic features to the enzymatic H<sub>ox</sub> state, we have explored the CO binding affinity and <sup>13</sup>CO exchange ability of **III-1<sub>ox</sub>**, **III-2<sub>ox</sub>**, and **III-3<sub>ox</sub>**. The experiments described below are interpreted based on assignments of CO stretching modes according to DFT calculation (see Figure III. 6): the bands at 2036 and 1985 can be assigned to the ν(CO)<sub>sym</sub> and ν(CO)<sub>asym</sub> of the

two terminal CO ligands on the unrotated Fe center (labeled Fe<sub>1</sub> in Scheme III. 3), while the intense band at 1998 corresponds to the terminal CO on the rotated iron center, Fe<sub>B</sub>. The less intense band at 1861 cm<sup>-1</sup> is attributed to the semi-bridging CO ligand.

### Scheme III. 3



$\nu(\text{CO})$	assignment
2036 cm <sup>-1</sup>	$\nu_{\text{sym}} \text{Fe1}(\text{CO})_2$
1998 cm <sup>-1</sup>	$\nu \text{Fe2}(\text{CO})_{\text{terminal}}$
1985 cm <sup>-1</sup>	$\nu_{\text{asym}} \text{Fe1}(\text{CO})_2$
1861 cm <sup>-1</sup>	$\nu \text{Fe2}(\text{CO})_{\text{bridging}}$

**Figure III. 6** Assignment of infrared CO stretches for complex **III-1<sub>ox</sub>**.

When a CH<sub>2</sub>Cl<sub>2</sub> solution of **III-1<sub>ox</sub>** (generated *in situ*) is sparged with CO at -78 °C for 90 minutes, changes in the  $\nu(\text{CO})$  region of the IR spectrum occur as shown in Figure

III. 7 A. The growth of a new  $\nu(\text{CO})$  band at  $2021\text{ cm}^{-1}$  is accompanied by an increase in intensity of the band(s) centered at  $\sim 1997\text{ cm}^{-1}$ . However, the band at  $1861\text{ cm}^{-1}$ , assigned to the bridging CO, undergoes little change. This apparent CO binding process is at equilibrium as it does not proceed upon further exposure to CO; its reversibility is indicated by the fact that the original spectrum **III-1<sub>ox</sub>** is reclaimed on evacuation or on bubbling the solution containing **III-1<sub>ox</sub>**<sup>CO</sup> with  $\text{N}_2$  or Ar.

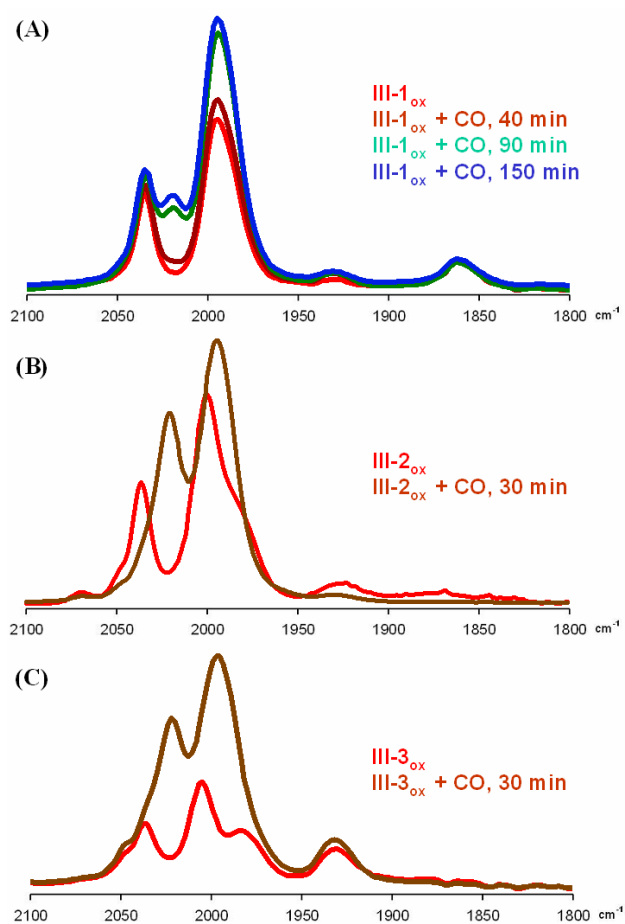


**Figure III. 7** Infrared spectra (recorded at ca.  $22^\circ\text{C}$ ) of  $\text{CH}_2\text{Cl}_2$  solutions of **III-1<sub>ox</sub>** (A), **III-2<sub>ox</sub>** (B), and **III-3<sub>ox</sub>** (C) following CO sparging at  $-78^\circ\text{C}$ .



In contrast, the reactions of complexes **III-2<sub>ox</sub>** and **III-3<sub>ox</sub>** with CO at -78 °C proceed to completion within 30 min (Figure III. 7 B and C). For both complexes, new bands at 2021 and 1996 cm<sup>-1</sup> are clearly identified in their respective IR spectra, attributed to formation of CO-adducts **III-2<sub>ox</sub><sup>CO</sup>** and **III-3<sub>ox</sub><sup>CO</sup>**. The reversibility of this process was established by recovery of the original IR spectra of **III-2<sub>ox</sub>** and **III-3<sub>ox</sub>** upon purging a solution of **III-2<sub>ox</sub><sup>CO</sup>** or **III-3<sub>ox</sub><sup>CO</sup>** with Ar or N<sub>2</sub>, or by exposure of these solutions to vacuum. The greater thermal stability of **III-2<sub>ox</sub><sup>CO</sup>** and **III-3<sub>ox</sub><sup>CO</sup>** over **III-1<sub>ox</sub><sup>CO</sup>** is indicated by a much slower rate of CO release by the less sterically congested derivatives. Interestingly, the positions of the lowest energy CO stretches at 1929 cm<sup>-1</sup> for **III-2<sub>ox</sub>** and **III-3<sub>ox</sub>** are retained in **III-2<sub>ox</sub><sup>CO</sup>** and **III-3<sub>ox</sub><sup>CO</sup>** but appear to diminish in intensity relative to the other infrared features. We have been unable to characterize **III-2<sub>ox</sub><sup>CO</sup>** and **III-3<sub>ox</sub><sup>CO</sup>** in the solid state by X-ray diffraction, but based on calculations using DFT (*vide infra*) we propose that **III-2<sub>ox</sub>** and **III-3<sub>ox</sub>** undergo CO uptake at the open site on the rotated Fe center, as in **H<sub>ox</sub><sup>CO</sup>**. A CO adduct is also observed by Rauchfuss et al. upon addition of extrinsic CO to (μ-SCH<sub>2</sub>CH<sub>2</sub>S)[Fe(CO)<sub>2</sub>(PMe<sub>3</sub>)] [Fe(CO)(dppv)]<sup>+</sup>.<sup>200</sup> As the CO binding site is presumed to be the Fe<sup>I</sup> center, containing electron density at the “open” site as in **III-1<sub>ox</sub>**, the binding of CO should result in substantial electron reorganization. This is supported by EPR spectroscopy on the exogeneous CO adducts, as described below.

The low temperature EPR spectrum (X-band, CH<sub>2</sub>Cl<sub>2</sub>, 10 K, see Figure III. 8) of **III-2<sub>ox</sub><sup>CO</sup>** is distinct from that of its precursor, **III-2<sub>ox</sub>**. Indicated by simulation to be due to a single species, the EPR spectrum of **III-2<sub>ox</sub><sup>CO</sup>** features a rhombic signal with  $g_1 = 2.093$ ,

$g_2 = 2.036$ ,  $g_3 = 2.002$ . In addition to the difference in  $g$  values between **III-2<sub>ox</sub>** and **III-2<sub>ox</sub><sup>CO</sup>**, the EPR spectrum of **III-2<sub>ox</sub><sup>CO</sup>** is best simulated with super-hyperfine coupling to <sup>31</sup>P (spin = 1/2) in  $g_3$  ( $A = 140$  MHz), coupling which is not seen in the spectrum of **III-2<sub>ox</sub>**. This implies that CO binding leads to significant delocalization of the unpaired electron onto both the NHC and PMe<sub>3</sub>-ligated iron atoms, as also predicted by computations (*vide infra*). Interestingly, electrochemical interrogation of **III-2<sub>ox</sub><sup>CO</sup>** reveals substantially different redox properties from its precursor, **III-2<sub>ox</sub>**. Unlike **III-2<sub>ox</sub>**, cyclic voltammetry data indicates that **III-2<sub>ox</sub><sup>CO</sup>** cannot be easily reduced to the Fe<sup>I</sup>Fe<sup>I</sup> oxidation state (no reductive events were observed within the solvent window of CH<sub>2</sub>Cl<sub>2</sub>).

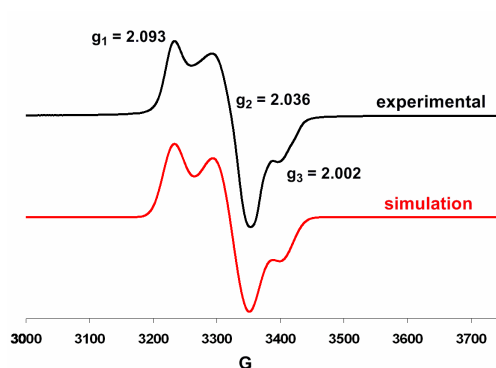


**Figure III. 8** Experimental (top) and simulated (bottom) EPR spectrum of **III-ox<sup>CO</sup>** (in CH<sub>2</sub>Cl<sub>2</sub> at 10 K, X band). Simulation parameters:  $g_1 = 2.093$  (linewidth = 32 G),  $g_2 = 2.036$  (linewidth = 44 G),  $g_3 = 2.002$  (linewidth = 35 G,  $A = 140$  MHz).

Despite the reluctance of **III-1<sub>ox</sub>** to form a stable **III-1<sub>ox</sub><sup>CO</sup>** adduct, isotopic exchange with extrinsic <sup>13</sup>CO occurs readily, mimicking the <sup>13</sup>CO/<sup>12</sup>CO exchange activity of H<sub>ox</sub>

under certain conditions. Under a blanket of  $^{13}\text{CO}$  (1 atm) at  $-78\text{ }^\circ\text{C}$  in  $\text{CH}_2\text{Cl}_2$  in the absence of light, **III-1<sub>ox</sub>** undergoes exchange with  $^{13}\text{CO}$  exclusively into the semi-bridging and terminal CO positions on the IMes-substituted, paramagnetic  $\text{Fe}^{\text{I}}$  center. This regioselective  $^{13}\text{CO}/^{12}\text{CO}$  exchange was observed by IR spectroscopy on the paramagnetic **III-1<sub>ox</sub>** and by  $^{13}\text{C}$  NMR spectroscopy on the reduced,  $^{13}\text{CO}$ -labelled product **III-1**. Upon exposure to 1 atm of  $^{13}\text{CO}$  for 15 minutes at  $-78\text{ }^\circ\text{C}$  in  $\text{CH}_2\text{Cl}_2$  in the absence of light, two new  $\nu(\text{CO})$  bands appear at  $1955\text{ cm}^{-1}$  and  $1821\text{ cm}^{-1}$  in the IR spectrum of **III-1<sub>ox</sub>** (Figure III. 1 A). The appearance of these bands is concomitant with diminished intensity in the bands at  $1997$  and  $1861\text{ cm}^{-1}$ . After 45 minutes of exposure to  $^{13}\text{CO}$ , the IR spectrum remains constant, indicating that further  $^{13}\text{CO}$  exchange does not occur at  $-78\text{ }^\circ\text{C}$ . The  $40\text{ cm}^{-1}$  shift of the band at  $1861\text{ cm}^{-1}$  to  $1821\text{ cm}^{-1}$  is consistent with  $^{13}\text{CO}$  exchange into the semi-bridging position (calculated shift =  $40\text{ cm}^{-1}$ ). The new band that appears at  $1955\text{ cm}^{-1}$  is shifted by  $42\text{ cm}^{-1}$  from the band at  $1997$  in the  $^{12}\text{CO}$ -derivative (calculated shift =  $43\text{ cm}^{-1}$ ). Based on the positions of these new  $\nu(\text{CO})$  stretches and the persistence of the bands at  $2036$  and  $1997\text{ cm}^{-1}$ , we posit that the exchange of extrinsic  $^{13}\text{CO}$  with intrinsic  $^{12}\text{CO}$  in **III-1<sub>ox</sub>** occurs at  $-78\text{ }^\circ\text{C}$  with regioselectivity, favoring the terminal and bridging CO ligands on the “rotated”  $\text{Fe}_2$ .

In an independent experiment to test this hypothesis, **III-1<sub>ox</sub>** was exposed to 1 atm  $^{13}\text{CO}$  for 30 min in  $\text{CH}_2\text{Cl}_2$  at  $-78\text{ }^\circ\text{C}$  at which time  $\text{CoCp}_2$  was added to reduce the partially  $^{13}\text{CO}$ -labeled complex to a diamagnetic  $\text{Fe}^{\text{I}}\text{Fe}^{\text{I}}$  state. The  $^{13}\text{C}$  NMR spectrum of this species revealed a single downfield  $^{13}\text{C}$  resonance at  $218.6\text{ ppm}$ , corresponding to a single type of  $^{13}\text{C}$ -labeled CO ligand (Figure III. 9 D). The absence of coupling to  $^{31}\text{P}$

(coupling that is observed in the  $^{13}\text{C}$  NMR spectrum of natural abundance samples of **III-1**) indicates that only the CO ligands on the IMes side of the molecule have been exchanged with  $^{13}\text{CO}$ .

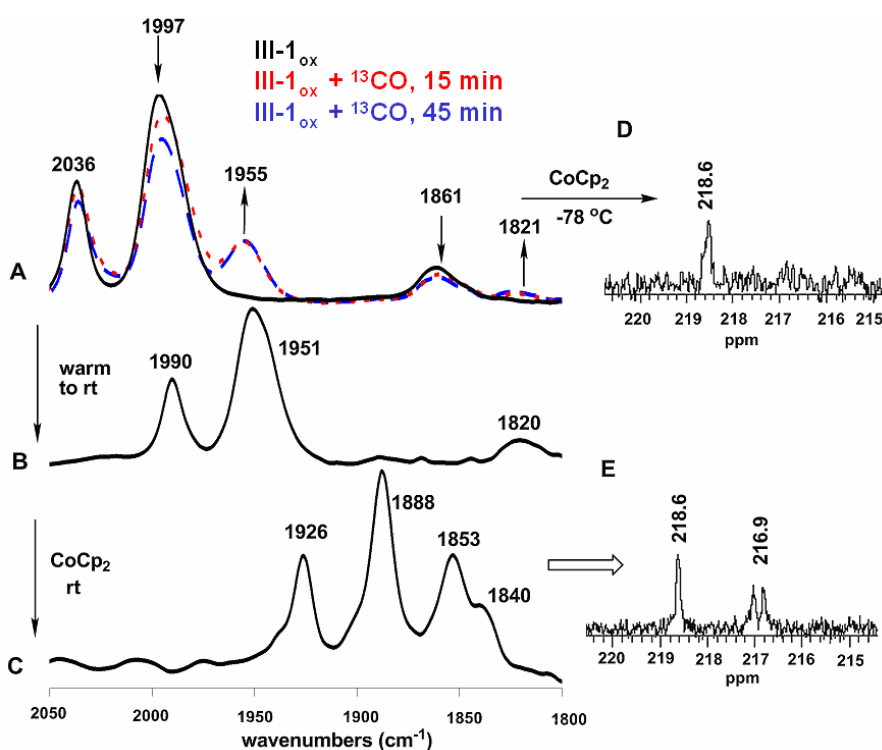


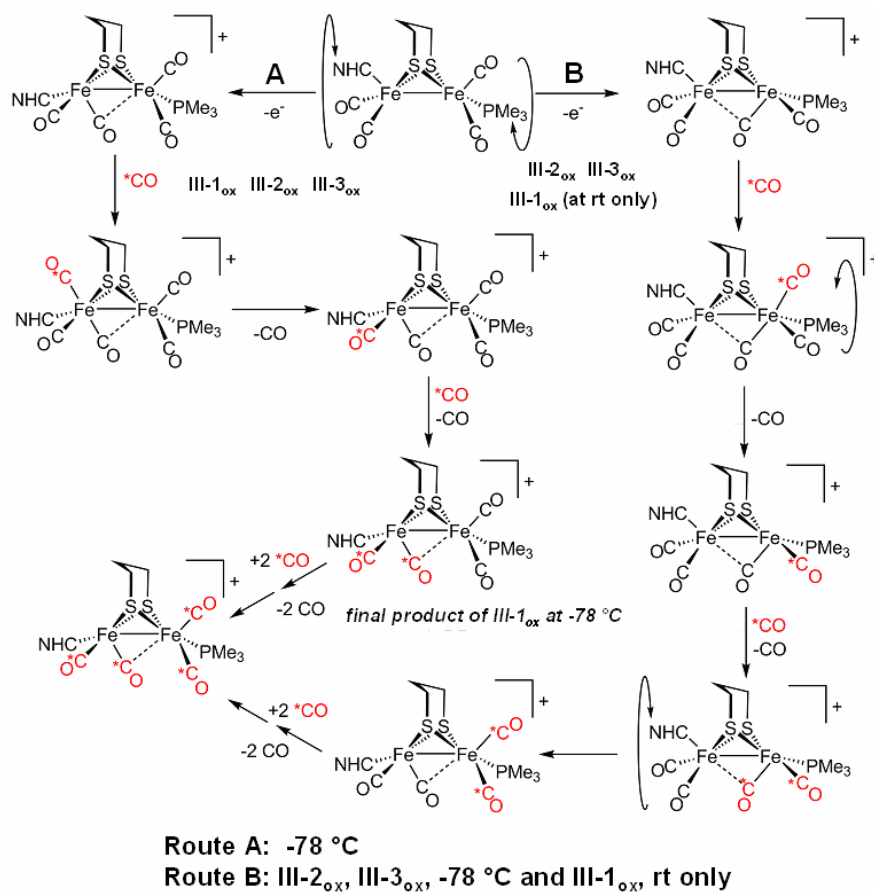
**Figure III. 9** Infrared spectra of (A) **III-1**<sub>ox</sub> upon exposure to  $^{13}\text{CO}$  at  $-78\text{ }^\circ\text{C}$  in  $\text{CH}_2\text{Cl}_2$  (in the dark) after 0 (black), 15 (red) and 45 (blue) min, (B) **III-1**<sub>ox</sub> after warming to room temperature under 1 atm of  $^{13}\text{CO}$ , and (C)  $^{13}\text{CO}$ -labeled product obtained via treatment of **III-1**<sub>ox</sub> with  $^{13}\text{CO}$  at room temperature followed by reduction with  $\text{Cp}_2\text{Co}$ . Carbonyl region of the  $^{13}\text{C}$  NMR spectrum of (D) the regioselectively labeled product generated upon exposure of **III-1**<sub>ox</sub> to  $^{13}\text{CO}$  at  $-78\text{ }^\circ\text{C}$  for 30 minutes followed by  $\text{Cp}_2\text{Co}$  reduction and (E) the fully  $^{13}\text{C}$ -labeled product obtained by addition of  $\text{Cp}_2\text{Co}$  to the labeled product generated upon exposure of **III-1**<sub>ox</sub> to  $^{13}\text{CO}$  at room temperature.

This regioselective  $^{13}\text{C}$ O exchange process is similar to that which has been observed for  $\text{H}_{\text{ox}}$ , albeit with different reaction conditions. Thus, complex **III-1<sub>ox</sub>** also undergoes  $^{13}\text{C}$ O exchange solely into positions accessible to the open coordination site on the “rotated” Fe center. While the exchange process with  $\text{H}_{\text{ox}}$  occurs near room temperature and only under illumination conditions,  $^{13}\text{C}$ O exchange occurs readily with **III-1<sub>ox</sub>** at low temperature in the absence of light, without the detection of an additional bound CO ligand.

While  $^{13}\text{C}$ O exchange into all CO positions of  $\text{H}_{\text{ox}}$  has not been observed under any conditions, such complete exchange is observed with **III-1<sub>ox</sub>**. Upon warming a solution of **III-1<sub>ox</sub>** under 1 atm of  $^{13}\text{C}$ O in  $\text{CH}_2\text{Cl}_2$  to room temperature, a new IR spectrum was obtained with bands at 1990, 1951 and 1820  $\text{cm}^{-1}$  (Figure III. 1 B). This new spectrum is consistent with  $^{13}\text{C}$ O exchange into all CO positions on both Fe centers (calculated: 1992, 1954, and 1821  $\text{cm}^{-1}$ ). Reduction of this completely  $^{13}\text{C}$ O-labeled species with  $\text{CoCp}_2$  leads to an IR spectrum consistent with what is expected for fully-labeled **III-1<sub>ox</sub>**, with bands at 1926, 1888, 1853, and 1840  $\text{cm}^{-1}$  (calculated: 1929, 1891, 1856, and 1841  $\text{cm}^{-1}$ ) (Figure III. 1 C). The  $^{13}\text{C}$  NMR spectrum of the resulting complex reveals two downfield resonances, a singlet at 218.6 and a doublet at 216.9 ppm, corresponding to  $^{13}\text{C}$ -labeled CO ligands on the IMes- and  $\text{PMe}_3$ -substituted Fe centers, respectively (Figure III. 1 E). As an important control experiment, exposure of solutions of the fully  $^{13}\text{C}$ O-labeled **III-1<sub>ox</sub>** to **III-1** atm of  $^{12}\text{C}$ O at room temperature leads to complete regeneration of the original IR spectrum of **III-1<sub>ox</sub>**.

A proposed mechanism for the regioselective isotopic exchange is presented in Scheme III. 4. In this mechanism,  $^{13}\text{CO}$  transiently binds to the open coordination site of III-1<sub>ox</sub>. Rotation about the Fe center with concomitant dissociation of a CO ligand restores the original geometry of III-1<sub>ox</sub>, but with a labeled  $^{13}\text{CO}$  ligand. Repetition of this  $^{13}\text{CO}$  binding /  $^{12}\text{CO}$  loss process generates the regioselectively labeled III-1<sub>ox</sub> following path A in Scheme III. 4. Subsequent warm-up to 22° leads to scrambling throughout III-1<sub>ox</sub>.

**Scheme III. 4**



In order to determine whether the spectroscopic and CO binding ability differences between III-1<sub>ox</sub> and its less sterically encumbered derivatives, III-2<sub>ox</sub> and III-3<sub>ox</sub>, might result in different <sup>13</sup>CO exchange behavior, the reactivity of III-2<sub>ox</sub> with extrinsic <sup>13</sup>CO was investigated. Interpretation of the spectral data was complicated by the ability of III-2<sub>ox</sub> to more easily form a CO adduct leading to possible <sup>13</sup>CO exchange into two species, III-2<sub>ox</sub> and III-2<sub>ox</sub><sup>CO</sup>. The presence of 1 atm of <sup>13</sup>CO at -78 °C (i.e., without sparging), in the dark, results in immediate changes in the IR spectrum of III-2<sub>ox</sub> (Figure III. 9). After 10 minutes, new CO stretches appear at 2029, 1973, 1958, and 1890 cm<sup>-1</sup>, while the bands at 2037, 2000 and 1929 cm<sup>-1</sup> diminish in intensity. Over the course of 1 h, the new bands continue to increase in intensity, while those corresponding to starting material decrease. As the reaction proceeds, the relative intensity of the band at 1958 cm<sup>-1</sup> increases with respect to that at 1973 cm<sup>-1</sup>, indicating that these IR bands correspond to two different species. Based on the change in reduced mass, complete exchange of <sup>13</sup>CO into all positions of III-2<sub>ox</sub> should result in an IR spectrum with bands at 1993 (m), 1957 (vs), 1940 (sh), and 1888 (w) cm<sup>-1</sup>. Thus, the new major ν(CO) stretches at 1958 and 1890 cm<sup>-1</sup> can be attributed to fully-labeled III-2<sub>ox</sub> – the expected band at 1993 cm<sup>-1</sup> is likely present underneath the 2000 cm<sup>-1</sup> band of the starting material. The formation of fully <sup>13</sup>CO-labeled III-2<sub>ox</sub> likely proceeds via the same mechanism proposed for III-1<sub>ox</sub>, however the barrier to rotation at both Fe centers is sufficiently low to provide two different pathways following loss of the bridging CO (Scheme III. 5). Another possible variation of this mechanism by which <sup>13</sup>CO could exchange to both sites is shown as

path B in Scheme III. 4. In this mechanism, extrinsic  $^{13}\text{CO}$  binding induces the semi-bridging CO ligand to migrate to the second Fe center with concomitant loss of  $^{12}\text{CO}$ .

**Scheme III. 5**

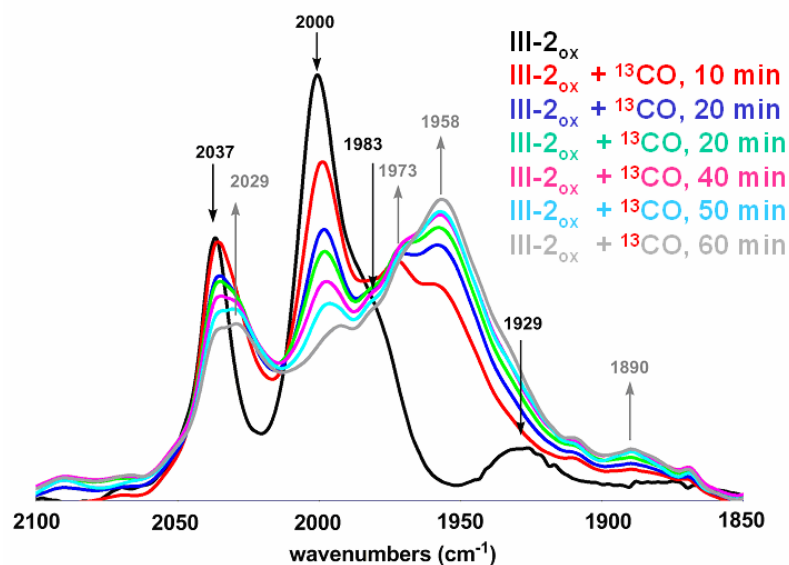
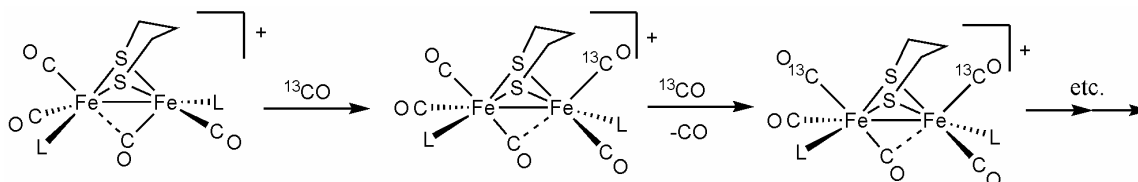


**Figure III. 10** IR spectra monitoring the reaction of **III-2<sub>ox</sub>** with  $^{13}\text{CO}$  at  $-78\text{ }^\circ\text{C}$  in  $\text{CH}_2\text{Cl}_2$  over a 1 hour time period in the absence of light.

The following experiments were performed to shed some light on the assignment of the IR stretches at  $2029$  and  $1973\text{ cm}^{-1}$ , which cannot be assigned as either starting material (**III-2<sub>ox</sub>**) or product ( $^{13}\text{CO}$ -labeled **III-2<sub>ox</sub>**) in the  $^{13}\text{CO}$  exchange reaction with



**III-2<sub>ox</sub>**. After 60 minutes of exposure to <sup>13</sup>CO, the resulting solution of labeled **III-2<sub>ox</sub>** was reduced with CoCp<sub>2</sub> at -78 °C (eq III. 1). New bands attributed to the neutral Fe<sup>I</sup>Fe<sup>I</sup> complex **III-2** appeared at 1932, 1896 cm<sup>-1</sup> (calc'd: 1931, 1892, 1857, 1843 cm<sup>-1</sup>), but the bands at 2029 and 1973 cm<sup>-1</sup> persisted (Figure III. 10). Exposure of **III-2<sub>ox</sub>** to <sup>13</sup>CO for 60 minutes at -78 °C followed by bubbling of <sup>12</sup>CO through the resulting solution for 30 minutes resulted in a single species identified by IR spectroscopy: the bands at 2021 and 1996 cm<sup>-1</sup> are attributed to exclusive formation of **III-2<sub>ox</sub><sup>CO</sup>** (Figure III. 11, eq III. 2). Since the unidentified species with bands at 2029 and 1973 cm<sup>-1</sup> is not reduced by CoCp<sub>2</sub> ( $E^\circ = -1.33$  V vs Fc/Fc<sup>+</sup>) and reacts with <sup>12</sup>CO to generate the CO-adduct **III-2<sub>ox</sub><sup>CO</sup>**, we assign this species as a <sup>13</sup>CO-adduct, **III-2<sub>ox</sub><sup>13CO</sup>**. As examined by control experiments, **III-3<sub>ox</sub>** undergoes CO exchange similar as **III-2<sub>ox</sub>**.

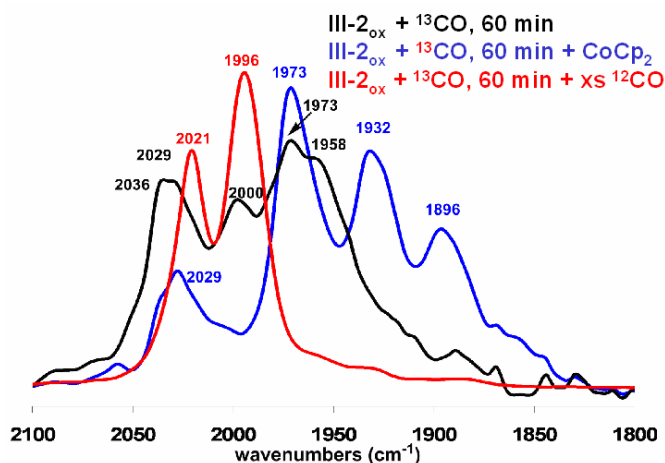
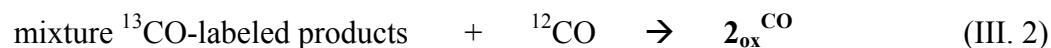


**Figure III. 11** IR spectra of the mixture of isotopically-labeled products formed upon exposure of **III-2<sub>ox</sub>** to <sup>13</sup>CO (black), and the products of reaction of this mixture with CoCp<sub>2</sub> (blue) and excess <sup>12</sup>CO (red).



In conclusion, the inherent differences between **III-1<sub>ox</sub>** and its less sterically-hindered congeners **III-2<sub>ox</sub>** and **III-3<sub>ox</sub>** lead to distinctly different reactivity of these complexes towards extrinsic CO. While **III-2<sub>ox</sub>** and **III-3<sub>ox</sub>** readily bind an additional CO ligand, complex **III-1<sub>ox</sub>** reacts sluggishly with excess CO. In addition, while regioselective exchange with <sup>13</sup>CO is observed at -78 °C for **III-1<sub>ox</sub>**, <sup>13</sup>CO scrambles into all positions of **III-2<sub>ox</sub>** even at low temperatures, with formation of an intermediate <sup>13</sup>CO-adduct observed by IR spectroscopy. This confirms our proposed associative mechanism for <sup>13</sup>CO exchange – the nonregioselective <sup>13</sup>CO scrambling into **III-2<sub>ox</sub>** is likely a result of more fluxionality in this less sterically hindered derivative (i.e. the barrier to rotation at both Fe centers is low, *vide infra*).

**Computational investigations using DFT.** To complement our experimental investigations of the rotated mixed valent Fe<sup>II</sup>Fe<sup>I</sup> models, these complexes have been examined using density functional theory (DFT) by Dr. Christine M. Thomas.<sup>192</sup> Results from the computational study of the IMes derivative indicated that the unpaired spin density in the  $S = \frac{1}{2}$  complex lies mostly on the rotated iron center, indicating that the oxidation state assignment is (IMes)(CO)Fe<sup>I</sup>(μ-CO)(μ-pdt)Fe<sup>II</sup>(PMe<sub>3</sub>)(CO)<sub>2</sub>. In addition, examination of the frontier molecular orbitals of the neutral and cationic complexes indicated that rotation about the (IMes)(CO)<sub>2</sub>Fe center leads to a disruption in the Fe-Fe bond, raising the energy of the HOMO and stabilizing the oxidized, mixed valent species

(Figure III. 12). We turned our attention now to a more detailed investigation of these  $\text{Fe}^{\text{II}}\text{Fe}^{\text{I}}$  complexes, with the ultimate goal of providing an explanation for the spectroscopic, and, perhaps, structural differences between the different NHC derivatives as well as their different reactivities towards extrinsic CO.

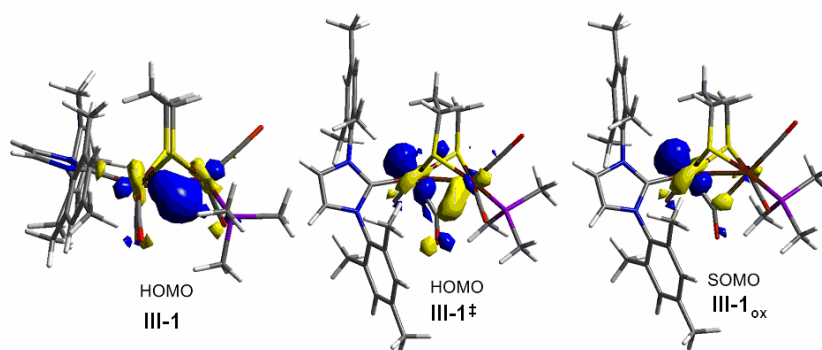


**Figure III. 12** Pictorial representations of the highest occupied molecular orbitals (or singly occupied molecular orbital, in the case of  $\text{III-1}_{\text{ox}}$ ) of the neutral complex  $\text{III-1}$ , the rotated transition state  $\text{III-1}^{\ddagger}$ , and the cation  $\text{III-1}_{\text{ox}}$ .

As noted above, the mixed-valent IMes derivative  $\text{III-1}_{\text{ox}}$ , whose structure is known definitively (X-ray), possesses distinctly different spectroscopic features (IR, EPR) from the IMesMe and IMe derivatives  $\text{III-2}_{\text{ox}}$  and  $\text{III-3}_{\text{ox}}$ . In particular, the IR spectrum of  $\text{III-1}_{\text{ox}}$  features a  $\nu(\text{CO})$  stretch corresponding to the semi-bridging CO at  $1861\text{ cm}^{-1}$ , while the lowest energy bands in the IR spectra of  $\text{III-2}_{\text{ox}}$  and  $\text{III-3}_{\text{ox}}$  are at  $1929$  and  $1930\text{ cm}^{-1}$ , respectively. These spectroscopic differences suggest that  $\text{III-2}_{\text{ox}}$  and  $\text{III-3}_{\text{ox}}$  adopt a different structure from their structurally-characterized analogue  $\text{III-1}_{\text{ox}}$ . In light of our inability to obtain single crystals of either  $\text{III-2}_{\text{ox}}$  or  $\text{III-3}_{\text{ox}}$ , we have turned to

DFT to get a better idea of the most likely structure adopted by these two mixed valent derivatives.

Starting from rotated structures similar to that determined crystallographically for **III-1<sub>ox</sub>**, and fully corroborated by DFT calculations, geometry optimizations and vibrational frequency calculations were carried out on **III-1<sub>ox</sub>**, **III-2<sub>ox</sub>**, and **III-3<sub>ox</sub>** using the B3LYP functional with modified LANL2DZ basis sets on the Fe, S, and P atoms and the D95 basis set on all C, N, O and H atoms. In all three derivatives, a rotated structure with a semi-bridging carbonyl, nearly identical to the experimental structure of **III-1<sub>ox</sub>**, was found as a minimum, with the unpaired spin density lying almost entirely on the rotated iron center. In fact, geometry optimization of **III-3<sub>ox</sub>** starting from an unrotated geometry, as in the Fe<sup>I</sup>Fe<sup>I</sup> complex **III-3**, leads to the same structure obtained if starting from a rotated geometry. The geometric parameters calculated for **III-1<sub>ox</sub>**, **III-2<sub>ox</sub>**, and **III-3<sub>ox</sub>** are similar (Table III. 4), with the most variations occurring in the parameters associated with the semi-bridging carbonyl moiety. An interesting variation in these structures is the orientation of the NHC (i.e., the CN<sub>2</sub>C<sub>2</sub> plane formed by the 5-membered imidazolylidene ring). By both calculation and experiment, the carbene in **III-1<sub>ox</sub>** is oriented such that the CN<sub>2</sub>C<sub>2</sub> plane eclipses the Fe-S bond vector *trans* to it. In **III-3<sub>ox</sub>**, however, the carbene plane is calculated to be tilted 27° away from the Fe-S vector. In the case of the asymmetric IMesMe derivative **III-2<sub>ox</sub>**, rotation of the carbene about the Fe-C bond leads to two potential isomers: one in which the NHC mesityl group points upwards in the direction of the dithiolate linker, and another in which the mesityl group points down towards the semi-bridging CO. Both potential isomers were

calculated and it was found that the “up” isomer is more stable, while the “down” isomer is a transition state at slightly higher energy ( $\Delta G^\circ = 1.5$  kcal/mol). In general, the barrier to rotation about the Fe-C<sub>NHC</sub> bond is low, as has been observed for other transition metal NHC complexes.

The vibrational frequencies calculated for the terminal CO ligands of **III-1<sub>ox</sub>** agree reasonably well with experiment when a minimal scaling factor (1.0107) is used (Table III. 5). However, the stretching frequency predicted for the bridging CO ligand (1836 cm<sup>-1</sup>) is substantially lower than the experimental value (1861 cm<sup>-1</sup>). Similar difficulties in predicting the  $\nu(\text{CO})$  stretches of bridging carbonyl ligands using DFT calculations have been previously documented.<sup>201</sup> The calculated vibrational frequencies for the terminal CO ligands of **III-2<sub>ox</sub>** and **III-3<sub>ox</sub>** also agree remarkably well with experiment; however, the calculations find low frequency bands at 1803 and 1836 cm<sup>-1</sup> for **III-2<sub>ox</sub>** and **III-3<sub>ox</sub>**, respectively, values which are some 100 cm<sup>-1</sup> lower than the lowest  $\nu(\text{CO})$  measured in solution (1929 cm<sup>-1</sup> for both **III-2<sub>ox</sub>** and **III-3<sub>ox</sub>**). This discrepancy between theory and experiment led us to examine a number of other potential structural isomers of **III-3<sub>ox</sub>** to ascertain whether other low energy structures might be accessed that would yield more compatible  $\nu(\text{CO})$  values.

Considering both rotated and unrotated structures, there are 11 possible conformational isomers of **III-3<sub>ox</sub>**, differing in the relative apical or basal positions of the NHC and PMe<sub>3</sub> ligands.<sup>193</sup> Upon full geometry optimization using DFT (B3LYP), **III-2** of the unrotated/eclipsed isomers, including the aforementioned structure identical to the neutral precursor **III-3**, spontaneously adopted rotated structures. In addition,

optimization of one of the possible rotated structures led to an unrotated geometry as a minimum. Thus, only the 8 structural isomers of **III-3<sub>ox</sub>** shown in Scheme III. 6 will be considered as minima. The ring flip of the metallocyclohexane ring was found to be worth a mere  $\sim 1$ -2 kcal/mol,<sup>193</sup> so for simplicity our discussion here will be limited to isomers in which the central methylene group points towards the NHC-coordinated Fe center.

**Table III. 4** Unpaired spin density and relevant geometrical parameters calculated for **III-1<sub>ox</sub>~III-3<sub>ox</sub>**, starting from the crystallographic coordinates of **III-1<sub>ox</sub>**.

	Spin density (Fe2/Fe1) <sup>a</sup>	Fe1-CO <sub>br</sub>	Fe2-CO <sub>br</sub>	Fe2-C-O	Fe1-Fe2
<b>III-1<sub>ox</sub></b>	1.18 / 0.00	2.162 Å	1.881 Å	149.1°	2.611 Å
<b>III-2<sub>ox</sub></b>	1.28 / -0.04	2.162 Å	1.904 Å	144.5°	2.624 Å
<b>III-3<sub>ox</sub></b>	1.17 / 0.00	2.224 Å	1.852 Å	150.8°	2.584 Å

<sup>a</sup> Fe1 refers to the PMe<sub>3</sub>-ligated Fe atom, while Fe2 refers to the NHC-bound Fe center.

**Table III. 5** Calculated<sup>a</sup> and experimental  $\nu(\text{CO})$  stretching frequencies for complexes **III-1<sub>ox</sub>~ III-3<sub>ox</sub>**.

	Calculated (cm <sup>-1</sup> )	Experimental (cm <sup>-1</sup> )
<b>III-1<sub>ox</sub></b>	2030, 1993, 1993, 1836	2037, 1997, 1987, 1861
<b>III-2<sub>ox</sub></b>	2035, 1997, 1993, 1803	2036, 2000, 1983, 1929
<b>III-3<sub>ox</sub></b>	2035, 2004, 1999, 1836	2036, 2005, 1981, 1929

<sup>a</sup> A scaling factor of 1.0107 was determined by plotting the experimental vibrational frequencies for **III-1<sub>ox</sub>** vs those calculated using an identical computational method ( $\nu(\text{CO})_{\text{exp}} = 1.0107\nu(\text{CO})_{\text{calc}}$ , R = 0.99).

Five of the possible structures of **III-3<sub>ox</sub>** feature a rotated geometry at one of the Fe centers (Scheme III. 6, **A-E**). The isomer calculated to be most stable is **A**, in which the

NHC-bound Fe center rotates and the  $\text{PMe}_3$  ligand maintains a basal position *trans*-oid to the NHC. The corresponding *cis*-oid isomer, **C**, is 1.4 kcal/mol higher in energy, while the isomer with  $\text{PMe}_3$  in an apical position is 5.3 kcal/mol higher in energy. Two possible isomers in which the ligands about the  $\text{PMe}_3$ -substituted Fe center rotate, one with the NHC in an apical position (**D**) and one with a basal NHC (**E**), were calculated to be higher in energy than **A** by 5.5 and 6.9 kcal/mol, respectively. Notably, in of these rotated possibilities, the unpaired spin density resides almost exclusively on the rotated Fe center (Scheme III. 6, italics). The optimized structures of **A-E** differ substantially, particularly with respect to the bridging CO ligand (Table III. 6). *Indeed, the Fe-C-O angle varies substantially over a range of 20° and the distance between the unrotated Fe center and the C atom of the  $\mu$ -CO varies over a range of 0.7 Å in the structural isomers of III-3<sub>ox</sub> calculated.*

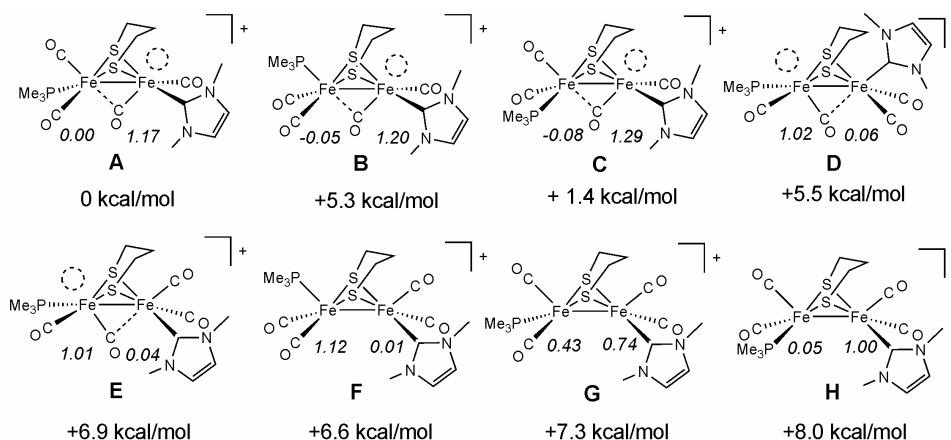
**Table III. 6** Relevant geometrical parameters calculated for the 8 possible conformational isomers of **III-3<sub>ox</sub>** in both rotated and unrotated structures.

	Fe1-CO	Fe2-CO	Fe2-C-O	Fe1-Fe2
<b>A</b>	2.224 Å	1.852 Å	150.8°	2.584 Å
<b>B</b>	2.550 Å	1.820 Å	164.7°	2.583 Å
<b>C</b>	2.182 Å	1.863 Å	147.9°	2.578 Å
<b>D</b>	1.817 Å	2.590 Å	164.9°	2.634 Å
<b>E</b>	1.798 Å	2.919 Å	170.6°	2.707 Å
<b>F</b>	1.813 Å	2.949 Å	169.7°	2.685 Å
<b>G</b>	1.791 Å	3.533 Å	179.1°	2.666 Å
<b>H</b>	1.798 Å	3.106 Å	173.9°	2.747 Å

The other three possibilities possess an unrotated geometry (Scheme III. 6, **F-H**) and are all higher in energy than the lowest energy rotated isomer (**A**). It is noteworthy that

in all three unrotated isomers the NHC occupies a basal position – initial geometries with the NHC in an apical position lead to rotation during geometry optimization. The optimized structures of **F-H** reveal a slight rotation, such that the ligands about the two Fe centers no longer eclipse each other; however, there is no evidence for a semi-bridging carbonyl ligand or an open coordination site in these structures. The unrotated isomer in which the  $\text{PMe}_3$  ligand is apical while the NHC ligand is basal (**F**) is 6.6 kcal/mol higher in energy than **A**, while the *trans*-oid (**G**) and *cis*-oid (**H**) basal/basal isomers are even higher in energy (7.3 and 8.0 kcal/mol, respectively). The location of the unpaired spin density is less predictable in these isomers – in **F**, the unpaired spin resides on the  $\text{PMe}_3$ -substituted Fe, in **H** the unpaired spin resides on the NHC-substituted Fe, and in **G** the unpaired electron is distributed over both Fe centers. The optimized geometries of **F-H** feature nearly linear Fe-C-O angles and relatively long Fe-Fe bond lengths (Table III. 6).

**Scheme III. 6** The 8 possible conformational isomers of **III-3<sub>ox</sub>** and their relative energies ( $G^\circ$ ) and unpaired spin densities (in italics).





The significant structural differences in the optimized geometries of isomers A-H lead to dramatic differences in their calculated  $\nu(\text{CO})$  stretching frequencies (Table III. 7). While the three highest energy computed  $\nu(\text{CO})$  stretches vary by only 10-15  $\text{cm}^{-1}$  and agree well with experiment, substantial differences are seen in the calculated positions of the lowest frequency band (Table III. 7). As mentioned previously, the lowest frequency band calculated for the isomer **A** (1836  $\text{cm}^{-1}$ ) agrees poorly with the experimentally observed CO vibration for **III-3<sub>ox</sub>** (1929  $\text{cm}^{-1}$ ). The calculated low frequency  $\nu(\text{CO})$  band for the isomer closest in energy (**C**, 1823  $\text{cm}^{-1}$ ) is also significantly lower than the observed frequency. On the other hand, the lowest frequency CO stretch calculated for unrotated isomer **H** (1964  $\text{cm}^{-1}$ ), is much higher than that observed experimentally. The remaining structural isomers have computed low frequency at 1913  $\text{cm}^{-1}$  (**B**), 1910  $\text{cm}^{-1}$  (**D**), 1925  $\text{cm}^{-1}$  (**E**), 1929  $\text{cm}^{-1}$  (**F**), and 1931  $\text{cm}^{-1}$  (**G**), and thus show better agreement with experiment ( $\nu(\text{CO}) = 1929 \text{ cm}^{-1}$ ). However, since all of these isomers are higher in energy than **A**, there is insufficient evidence to assign **III-3<sub>ox</sub>** as one of these alternative structural isomers. It should be noted that the use of different density functionals and different basis sets leads to similar energy differences between the possible isomers of **III-3<sub>ox</sub>** (the detailed information available in the supporting information of reference <sup>193</sup> ). On the other hand, the vibrational frequencies are much more sensitive to different functionals, basis sets, and small structural changes; for example, with respect to relative frequency of the semi-bridging CO, flipping the metallocyclohexane ring causes a shift of  $\sim 40 \text{ cm}^{-1}$  to higher frequency and the larger basis sets causes a shift of  $\sim 20 \text{ cm}^{-1}$  to higher frequency.<sup>193</sup> In

general, it appears that both the structural parameters and the vibrational frequencies associated with the semi-bridging CO ligand are remarkably sensitive to details of the electronic and molecular structure.

**Table III. 7** Calculated  $\nu(\text{CO})$  stretching frequencies for isomers A-H (using a scaling factor of 1.0107).

	$\nu(\text{CO})$ ( $\text{cm}^{-1}$ )			
<b>A</b>	2035	2004	1999	1836
<b>B</b>	2038	2008	2000	1913
<b>C</b>	2039	2011	2000	1823
<b>D</b>	2044	2006	2000	1910
<b>E</b>	2028	1991	1989	1925
<b>F</b>	2034	1994	1990	1929
<b>G</b>	2037	1993	1988	1931
<b>H</b>	2018	1993	1979	1964

It is also interesting to note that, while rotation of the carbene side of these mixed valent cations is always preferred, the extent to which this isomer is favored varies with the identity of the NHC ligand. As mentioned in the preceding paragraphs, the rotated NHC-substituted Fe side is favored by 5.5 kcal/mol in the IMe derivative **III-3<sub>ox</sub>**. However, this energy difference increases to 6.5 kcal/mol with the IMesMe derivative **III-2<sub>ox</sub>** and to 10.1 kcal/mol for the IMes derivative **III-1<sub>ox</sub>**. Thus, the NHC-substituted Fe center rotation is favored in the order **III-1<sub>ox</sub>** >> **III-2<sub>ox</sub>** > **III-3<sub>ox</sub>**. Based on this trend, as well as the preference for the more sterically bulky N-substituent in **III-2<sub>ox</sub>** to point upwards towards the open coordination site, a reasonable conclusion is that steric protection of the open coordination site plays an important role in stabilizing the rotated geometry of these mixed valent derivatives.

Computations were also used to examine the binding of extrinsic CO to **III-3<sub>ox</sub>**. As noted in the experimental section, **III-3<sub>ox</sub>** reversibly binds extrinsic CO to generate a new  $S = 1/2$  species, **III-3<sub>ox</sub><sup>CO</sup>** with a distinctly different IR spectrum than that of **III-3<sub>ox</sub>**. Since isomers of **III-3<sub>ox</sub>** in which the IMe and PMe<sub>3</sub> side rotate are relatively close in energy ( $\sim 5$  kcal/mol), two possible isomers of the CO adduct can be envisioned: one in which CO is bound to the IMe-substituted Fe center, **III-3<sub>ox</sub><sup>CO</sup>**, and one in which CO is bound to the PMe<sub>3</sub>-substituted Fe center, **III-3<sub>ox</sub>\*<sup>CO</sup>**. As shown in Scheme III. 7, CO binding to an isomer in which the PMe<sub>3</sub> side is rotated, **III-3<sub>ox</sub>\***, is energetically favorable, while CO binding to **3<sub>ox</sub>** is essentially energetically neutral. Thus, calculations suggest that the CO adducts observed experimentally upon binding of CO to **III-2<sub>ox</sub>** and **III-3<sub>ox</sub>** have CO bound to the PMe<sub>3</sub>-substituted Fe center. This hypothesis is consistent with several experimental observations, including: (1) the <sup>31</sup>P super-hyperfine coupling observed in the EPR spectrum of the CO adduct **III-2<sub>ox</sub><sup>CO</sup>** that is not observed in the EPR spectrum of the precursor **III-2<sub>ox</sub>**, and (2) the propensity of **III-2<sub>ox</sub>** and **III-3<sub>ox</sub>** to bind CO much more readily than **III-1<sub>ox</sub>**: rotation of the PMe<sub>3</sub> side of the molecule must occur before CO binding becomes favorable, and this rotation is  $\sim 5$  kcal/mol more uphill for **III-1<sub>ox</sub>**.

The structural parameters and electron distribution in the optimized structures of the CO adducts **III-3<sub>ox</sub><sup>CO</sup>** and **III-3<sub>ox</sub>\*<sup>CO</sup>** are also worthy of discussion. Relevant bond distances and angles are tabulated in Table III. 8. Interesting, upon binding of extrinsic CO, the semi-bridging CO becomes fully bridging. In the isomer in which CO binds to the IMe-substituted Fe (**III-3<sub>ox</sub><sup>CO</sup>**), the geometry about the  $\mu$ -CO is completely

symmetric, with identical Fe-C distances (2.020 Å) and Fe-C-O angles (136.3°). On the other hand, the  $\mu$ -CO geometry is slightly asymmetric in  $\text{III-3}_{\text{ox}}^*\text{CO}$ , with the bridging CO remaining slightly more tightly bound to the  $\text{PMe}_3$ -substituted side.

### Scheme III. 7

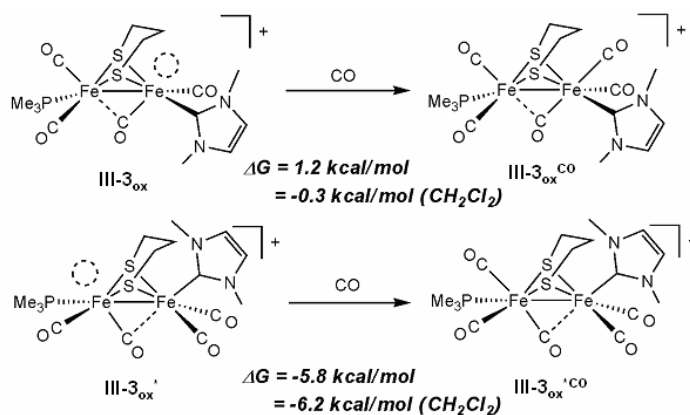


**Table III. 8** Relevant bond distances and angles calculated for the two possible CO adducts,  $\text{3}_{\text{ox}}^{\text{CO}}$  and  $\text{3}_{\text{ox}}^*\text{CO}$ .

	Fe1-C <sub>br</sub>	Fe2-C <sub>br</sub>	Fe2-C-O	Fe1-C-O	Fe1-Fe2
$\text{III-3}_{\text{ox}}^{\text{CO}}$	2.020 Å	2.020 Å	136.3°	136.3°	2.793 Å
$\text{III-3}_{\text{ox}}^*\text{CO}$	1.983 Å	2.074 Å	133.3°	138.7°	2.820 Å

These changes in geometry are accompanied by more symmetrical electron delocalization for both isomers  $\text{III-3}_{\text{ox}}^{\text{CO}}$  and  $\text{III-3}_{\text{ox}}^*\text{CO}$ . The unpaired spin density in both structural isomers is distributed over both Fe centers with a substantial spin population on the carbon and oxygen atoms of the bridging carbonyl (see Figure III. 13). Consistent with the more symmetric structure predicted for  $\text{III-3}_{\text{ox}}^{\text{CO}}$ , the unpaired spin

is localized equally on both Fe centers, while the unpaired electron of **III-3<sub>ox</sub>\*CO** is delocalized in a more asymmetric fashion, with slightly more spin density on the IMe-substituted Fe center. The Fe oxidation states in each of these CO adducts are better described as Fe<sup>1.5</sup>Fe<sup>1.5</sup>, in contrast to the Fe<sup>II</sup>Fe<sup>I</sup> oxidation state assignment for the precursor **III-3<sub>ox</sub>**. This electronic delocalization is also reflected in the frontier molecular orbitals of the CO adducts, illustrated for **III-3<sub>ox</sub><sup>CO</sup>**. Both the HOMO (SOMO) and LUMO are delocalized symmetrically over both of the iron centers as well as the bridging CO moiety.

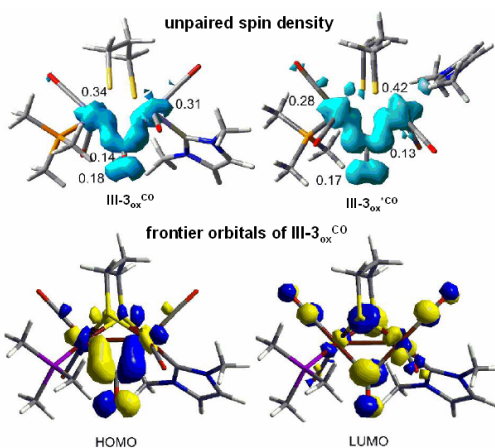


**Figure III. 13** Top: unpaired spin density surface (isodensity = 0.03) of **III-3<sub>ox</sub><sup>CO</sup>** and **III-3<sub>ox</sub><sup>\*CO</sup>**; Bottom: representative frontier orbitals (isovalue = 0.03) of **III-3<sub>ox</sub><sup>CO</sup>**.

The computational results regarding electronic delocalization in the CO adduct can be used to rationalize the shifts in infrared CO stretching frequencies experimentally observed upon CO binding. The symmetric and asymmetric stretches associated with the terminal CO ligands on the (CO)<sub>2</sub>(PMe<sub>3</sub>)Fe unit in **III-3<sub>ox</sub>** (2036 cm<sup>-1</sup> and 1983 cm<sup>-1</sup>,

respectively) would be expected to shift to lower frequencies upon a change in oxidation state from  $\text{Fe}^{\text{II}}$  to  $\text{Fe}^{1.5}$  once CO is bound. Simultaneously, the band associated with the terminal CO ligand on the  $(\text{CO})_2(\text{IMe})\text{Fe}$  unit ( $2004\text{ cm}^{-1}$ ) should split into a symmetric and asymmetric stretch and shift to higher frequency with binding of extrinsic CO.

### Conclusions and comments

As described in Chapter III, from the serial approach to establishing fundamental properties of the diiron-dithiolate complexes which have certain features in common with the  $[\text{FeFe}]$ - $\text{h}_2\text{ase}$  active site, the following salient points are noted:

- The N-heterocyclic carbene ligands IMes, IMesMe and IMe ligands are effectual in accessing thermally and moderately air-stable hetero-ligated ( $\mu$ -pdt) $[\text{Fe}^{\text{I}}(\text{CO})_2\text{PMe}_3][\text{Fe}^{\text{I}}(\text{CO})_2\text{NHC}]$  complexes in which the  $\text{PMe}_3$  and NHC ligands are of sufficient donating abilities to stabilize a one-electron oxidized form. At the reduced  $\text{Fe}^{\text{I}}\text{Fe}^{\text{I}}$  redox level, the complexes crystallize as identical conformational isomers. At the  $\text{Fe}^{\text{I}}\text{Fe}^{\text{II}}$  level, only the complex **III-1<sub>ox</sub>** has yielded to crystallization and it adopts a rotated structure with semi-bridging carbonyl remarkably analogous to the two-iron subsite of **H<sub>ox</sub>**.
- Consistent with literature reports of the properties of NHC ligands in monometallic complexes,<sup>202</sup> changes in R-group substitution at N in the NHC ligands have minimal effect on the donor abilities of such ligands as evidenced by  $\nu(\text{CO})$  IR spectroscopy of members of the series. The complexes differ from one another only in the steric bulk which flanks the carbene carbon donor site.

- Assuming (from the  $\nu(\text{CO})$  IR data of the  $\text{Fe}^{\text{I}}\text{Fe}^{\text{I}}$  complexes) differences in electron density at iron are small within the series, we are led to the conclusion that disparities in the accessibility and reversibility of the  $\text{Fe}^{\text{I}}\text{Fe}^{\text{I}}/\text{Fe}^{\text{II}}\text{Fe}^{\text{I}}$  redox couple, decreasing in the order **III-1** > **III-2** > **III-3**, must be due to steric differences in the substituent NHC ligands. These differences might determine a) stabilization of the rotated  $\text{Fe}^{\text{I}}\text{Fe}^{\text{II}}$  product imparted from steric protection of the “open” site by, in the case of **III-1<sub>ox</sub>**, an aryl group; or, b) stability of conformational isomers for various rotated or unrotated structural possibilities for the product (Scheme III. 7).
- There is an impressive variation in solution structures and stabilities of the  $\text{Fe}^{\text{I}}\text{Fe}^{\text{II}}$  complexes that also relates to steric differences of the NHC ligands. The IMe and IMesMe derivatives do not display the low energy  $\nu(\text{CO})$  band (at ca.  $1860\text{ cm}^{-1}$ ) that characterizes the semi-bridging CO group in the IMes derivative, **III-1<sub>ox</sub>**. Likewise, differences in the EPR spectra of **III-2<sub>ox</sub>** and **III-3<sub>ox</sub>** indicate that the unpaired electron is in a different environment and may not be localized on a single Fe atom as in **III-1<sub>ox</sub>**.
- DFT calculations predict the lowest energy structure of all NHC derivatives to be of the rotated type with semi-bridging carbonyl arising from the rotated  $\text{Fe}(\text{CO})_2(\text{NHC})$  unit,  $(\mu\text{-pdt})(\mu\text{-CO})[\text{Fe}^{\text{II}}(\text{CO})_2\text{PMe}_3][\text{Fe}^{\text{I}}(\text{CO})(\text{NHC})]^+$ , i.e., the same as the experimentally found structure that exists both in solid and in solution for the IMes derivative **III-1<sub>ox</sub>** and with the same assignment of oxidation state from the calculated unpaired electron density. Nevertheless, for the less sterically hindered **III-2<sub>ox</sub>** and **III-3<sub>ox</sub>** derivatives this rotated structure is inconsistent with experimental

(solution IR) data. A number of structural isomers calculated to check both rotated and unrotated geometries at either iron center are within 7 kcal/mol in energy and match the IR data more closely.

- Reversible formation of a CO adduct is seen in all three  $\text{Fe}^{\text{I}}\text{Fe}^{\text{II}}$  derivatives, with order of stability as follows:  $\text{III-3}_{\text{ox}} \geq \text{III-2}_{\text{ox}} \gg \text{III-1}_{\text{ox}}$ . We suggest this CO adduct is pivotal in the  $^{13}\text{CO}$  exchange process which is regioselective for  $\text{III-1}_{\text{ox}}$  at  $-78^\circ\text{C}$ , but not for  $\text{III-3}_{\text{ox}}$  or  $\text{III-2}_{\text{ox}}$  under the same conditions. Thus, we conclude that the open site in  $\text{III-1}_{\text{ox}}$  is sterically protected by its larger NHC ligand.

The rotated structure of a mixed-valent  $\text{Fe}^{\text{I}}\text{Fe}^{\text{II}}$  from the Rauchfuss group,  $(\mu\text{-S}_2\text{C}_2\text{H}_4)[\text{Fe}(\text{CO})_2\text{PMe}_3][\text{Fe}(\text{CO})(\text{dppv})]^+$ , bears similarity to  $\text{III-1}_{\text{ox}}$  in that the dppv ligand also has aryl rings which are directed toward the open site of the rotated iron, presumably offering steric protection/stabilization.<sup>196</sup> It differs from  $\text{III-1}_{\text{ox}}$  in that the CO that lies under the Fe-Fe vector is nearly linear and, consistently, the lowest energy  $\nu(\text{CO})$  IR band at  $1883\text{ cm}^{-1}$  is higher than that from the semi-bridging CO ligand of  $\text{III-1}_{\text{ox}}$ . It is clear that the synthetic, abiological ligands chosen by Rauchfuss and by us, yield analogues in coordination and basic  $\text{Fe}_2\text{S}_2$  framework to that adopted by nature for the  $[\text{FeFe}]\text{-H}_2\text{ase}$  active site. The composition is remarkably sensitive to ligands that provide intramolecular interactions, displayed in the synthetic analogues by aryl groups. As shown in the enzymatic mechanism (Figure I-4), in the mixed valent, rotated form of diiron units an  $\text{Fe}^{\text{I}}$  is primed to be reduced and protonated, an electron/proton coupled process, producing a terminal  $\text{Fe}^{\text{II}}\text{-H}$ . Alternatively with little structural reorganization, the same penta-coordinate  $\text{Fe}^{\text{I}}$  can have an electron withdrawn and become a



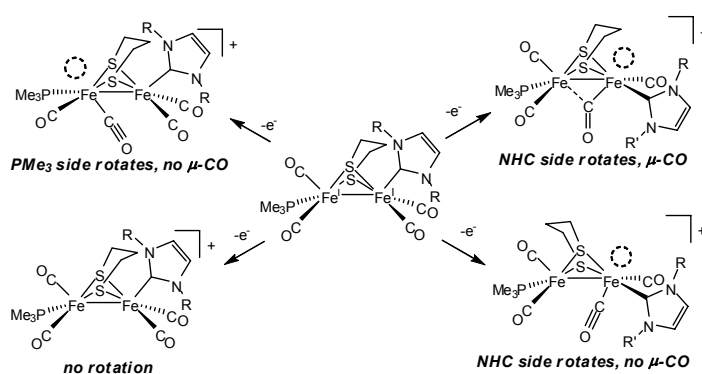
coordinatively unsaturated  $\text{Fe}^{\text{II}}$  with ideal Lewis acidity to bind  $\text{H}_2$  and begin the  $\text{H}_2$  cleavage reaction required for the known reversible activity of the enzyme.

Note that the enzyme possesses a  $4\text{Fe}4\text{S}$  redox active unit directly attached to the Fe subsite whose influence on the distal iron can change the potential for  $e^-/\text{H}^+$  attraction. As found by Brunold and coworkers, this iron sulfur cluster also plays an important role in modulating the geometric and electronic structure of the  $2\text{Fe}2\text{S}$  subsite of the H cluster.<sup>203</sup> The current models, successful as they are in mimicking structural features, do not have this capacity. Nevertheless, the sterically encumbered NHC ligand IMes appears to fulfill some of the second coordination sphere requirements that exist in the enzyme in the form of <sup>234</sup>Pro and <sup>417</sup>Phe residues close to the open site of the distal iron.<sup>44, 45</sup> Evidently, the protein matrix is sufficient to maintain this rotated structure throughout various redox levels either through hydrogen bonding or steric interactions; however, the mixed valent model complexes known to date return to their unrotated form upon re-reduction. The current study thus highlights two future challenges for developing more accurate molecular models of the active site of the  $[\text{FeFe}]\text{-H}_2\text{ase}$ : (1) replacement of  $\text{PMe}_3$  by a redox active ligand, and (2) the development of an intra- or intermolecular means for locking the rotated structure into place.

In conclusion, a comment regarding the difference between the three members of the NHC series is appropriate. Electron spin resonance, and  $\nu(\text{CO})$  IR spectral data recorded in solution may be readily interpreted according to the solid state structure of **III-1<sub>ox</sub>**. DFT calculations are consistent with a mixed valent  $\text{Fe}(\text{II})\text{Fe}(\text{I})$  compound with charge separation and the unpaired electron localized on the rotated iron. In addition, DFT

calculations provide a reasonable match of the  $\nu(\text{CO})$  IR spectrum. While the derivative with only one mesityl group and one Me substituent on the imidazolium nitrogens, **III-2<sub>ox</sub>**, would have the capability to provide the same steric protection of the open site by orienting the mesityl group over the rotated iron, such a structure was not observed. Nevertheless the DFT calculation suggested a structure similar to **III-1<sub>ox</sub>** as the lowest energy form for both **III-2<sub>ox</sub>** and **III-3<sub>ox</sub>**. However other theoretical structures are now closer in energy for the less bulky NHC derivatives. Furthermore from experiments, the IR band corresponding to the semi-bridging CO was not observed for **III-2<sub>ox</sub>** or **III-3<sub>ox</sub>**. And the EPR spectrum showed a significantly broader signal. Hence, the less sterically hindered NHC ligands, rather than locking in a single stable structure may provide a plethora of other possibilities, summarized in Scheme III. 8.

**Scheme III. 8**



## CHAPTER IV

### SULFUR OXYGENATES OF BIOMIMETICS OF THE DIIRON SUBSITE OF THE [FeFe]-HYDROGENASE ACTIVE SITE\*

#### Introduction

The well known oxygen sensitivity of hydrogenase (H<sub>2</sub>ase) enzymes<sup>17</sup> and their active site biomimetics poses a problem for their development as alternatives to platinum in fuel cell applications. As noted by Vincent, et al., the deleterious effects of O<sub>2</sub> on the enzymes vary widely and are highly dependent on the type and source of the enzymes.<sup>77</sup> For example, the membrane-bound [NiFe]-H<sub>2</sub>ase from *Ralstonia eutropha* is O<sub>2</sub> tolerant, while the [FeFe]-H<sub>2</sub>ase from *Desulfovibrio desulfuricans* is irreversibly inactivated when exposed to O<sub>2</sub> in its H<sub>ox</sub> state.<sup>77</sup> In its anaerobically over-oxidized state, the O<sub>2</sub> damage may be reversed by reductive activation. Technological targets for synthetic biomimetic compounds<sup>43, 96-98, 204-206</sup> and for genetically modified enzymes<sup>207</sup> lie in approaches to minimize or circumvent O<sub>2</sub> reactivity at the active metal catalyst site.

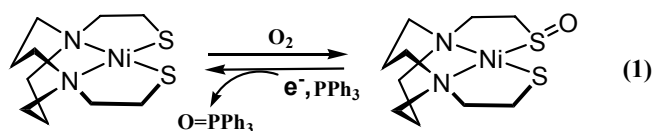
We have had interest in the ability of sulfur to act as potential moderators of O<sub>2</sub> reactivity via formation of sulf-oxy species such as metallosulfinates and metallosulfenates.<sup>208</sup> Studies of cis-dithiolato complexes of nickel, NiN<sub>2</sub>S<sub>2</sub>, established O-atom capture by thiolate sulfurs that modified redox activity of the complexes, but did

---

\*Reprinted with permission from a manuscript. Liu, T.; Li, B.; Singleton, M. L.; Hall, M. B.; Darensbourg, M. Y. Sulfur Oxygenates of Biomimetics of the Diiron Subsite of the [FeFe]-Hydrogenase Active Site: Properties and Oxygen Damage Repair Possibilities. *J. Am. Chem. Soc.* **2009**, *131* (23), 8296-8307, Copyright [2009] by the American Chemical Society.

not alter the Ni-S connectivity.

In one case, reclamation of the thiolate was demonstrated to be possible by electrochemical reduction in the presence of an O-atom acceptor, eq (1).<sup>209</sup> Such a process is possibly related to repair of oxygen-damaged [NiFe]-H<sub>2</sub>ase, which have found myriad levels of activity recovery from oxidation.<sup>210-212</sup> The nickel in [NiFe]H<sub>2</sub>ase is surrounded by cysteine S-donors, two of which serve as bridges to an adjacent Fe(CO)(CN)<sub>2</sub>, and two of which are directed towards a hydrophobic channel within the protein, presumed to provide access or egress of diatomics, such as H<sub>2</sub> or unwanted, adventitious O<sub>2</sub> molecules, Figure IV. 1.<sup>7</sup> An attractive hypothesis is that the temporary formation of sulf-oxy species might preserve enzyme active site integrity following moderate exposure to O<sub>2</sub>, and be more easily repaired than metal oxide formation.<sup>209</sup>



The two-iron subsite in the active site of [FeFe]-H<sub>2</sub>ase is sketched in Figure IV. 1: it contains three thiolate S-donors, two of which serve as a bidentate bridging ligand to the two irons.<sup>7</sup> A popular precursor to biomimetics of this site is the (μ-S(CH<sub>2</sub>)<sub>3</sub>S-)[Fe<sup>I</sup>(CO)<sub>3</sub>]<sub>2</sub> or (μ-pdt)[Fe<sup>I</sup>(CO)<sub>3</sub>]<sub>2</sub>.<sup>213</sup> Modifications by CO ligand substitution with better donor ligands L are known to enhance reactivity towards electrophiles such as

$H^+$ ,<sup>132, 136, 214, 215</sup>  $RS^{+143}$  and  $R^+$ .<sup>142</sup> In the case of  $(\mu\text{-pdt})[Fe^I(CO)_2PMe_3]_2$ ,  $H^+$  and  $RS^+$  attack the Fe-Fe bond density generating oxidative addition products  $[(\mu\text{-E})(\mu\text{-pdt})[Fe^{II}(CO)_2L]_2]^+$  with bridging  $E^-$  groups.<sup>142, 143</sup> The  $R^+$  electrophile attacks the bridging thiolate sulfur, yielding a stable  $[(\mu\text{-edt-R})[Fe^I(CO)_2L]_2]^+$ ,<sup>142</sup> Scheme IV. 1. As suggested from computational studies, the better covalent bond between S and C accounts for the regiospecificity of alkylation, while iron-based protonation, generating the bridging hydride, is some 30 kcal/mol more stable than the product of S-based protonation, generating a bridging thiol.<sup>216</sup>

Since  $\mu\text{-oxo}$  iron derivatives are well known,<sup>217, 218</sup> we questioned whether O-atom addition to  $(\mu\text{-pdt})[Fe^I(CO)_2L]_2$  might provide examples of both S-site and metal-site reactivity. These studies are described herein. A sulfur-based O-atom adduct of the  $\mu\text{-1,2-ethanesulfenatothiolate}$  ( $\mu\text{-est}$ ) complex,  $[(\mu\text{-est})[Fe^I(CO)_3]_2]$  similar to those described below was reported by Messelhauser, et al. in 1987;<sup>182</sup> and more recently, Weigang, *et al.* published complexes in the same class.<sup>219</sup> To our knowledge, those are the rare descriptions of sulf-oxy species of organoiron compounds prior to our study.

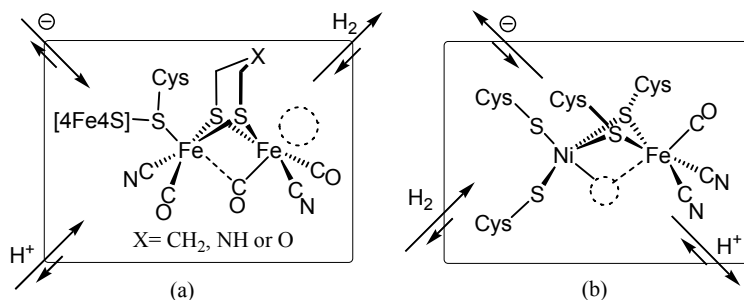
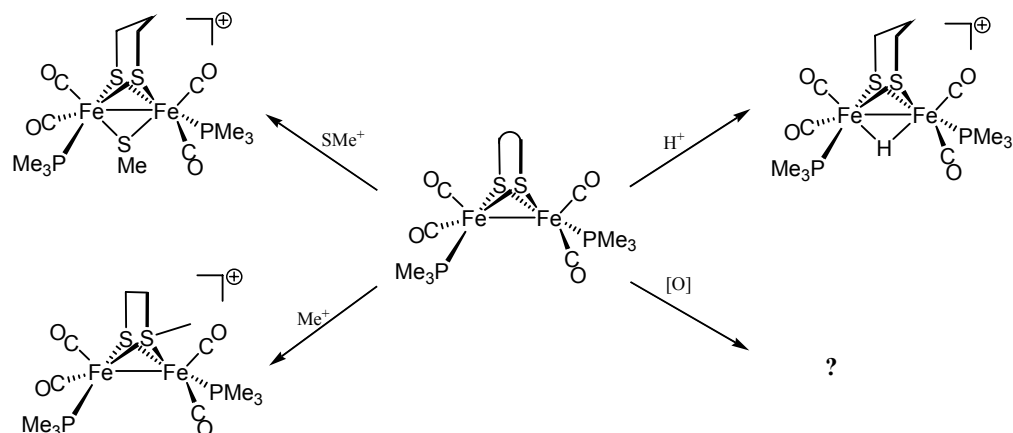


**Figure IV. 1** Sketches of the [NiFe]- and [FeFe]-H<sub>2</sub>ase active sites

Scheme IV. 1



## Results and discussion

**Theoretical predictions from DFT computations.** Prior to experimental oxygenation studies, DFT computations were carried out in an attempt to predict metal vs sulfur oxygenation of the active site paradigm of [FeFe]-H<sub>2</sub>ase,  $[(\mu\text{-pdt})[\text{Fe}(\text{CO})_3]_2$  (**IV-1**). Initially, geometry optimizations and vibrational frequency calculations were carried out on complex **IV-1**, its oxygenated product isomers  $(\mu\text{-pst})[\text{Fe}^{\text{I}}(\text{CO})_3]_2$  ( $\mu\text{-pst} = \text{-SC}_2\text{H}_6\text{S}(\text{O})\text{-}$ , propanesulfenatothiolate) (**IV-1-O**) and  $(\mu\text{-pdt})(\mu\text{-O})[\text{Fe}^{\text{II}}(\text{CO})_3]_2$  (**IV-1- $\mu$ -O**) using the B3LYP functional with modified LANL2DZ basis sets for Fe and S and D95 basis sets for other atoms. The optimized structures of **IV-1**, **IV-1-O** and **IV-1- $\mu$ -O** were confirmed as energy minima by frequency calculations. The optimized structures of complexes **IV-1** and **IV-1-O** well match the metric data of that found experimentally by x-ray diffraction, which lends confidence to the correctness of the computation. Figure IV. 2 displays the frontier molecular orbitals of **IV-1**. As was earlier presented,<sup>92</sup>

the HOMO is essentially the Fe-Fe bond density while the HOMO-1 is characterized by the remaining lone pair on the bridging sulfur.

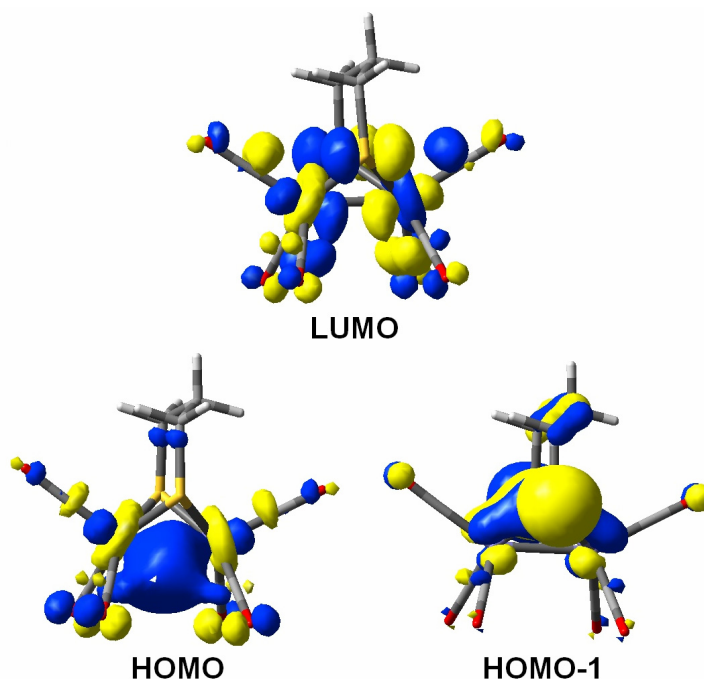


**Figure IV. 2** Frontier molecular orbitals (with isovalue = 0.04) of complex **IV-1**,  $(\mu\text{-pdt})[\text{Fe}(\text{CO})_3]_2$

Table IV. 1 lists total free energies of isomeric forms of **X-O** and **X- $\mu$ -O** (**X** = complexes **IV-1**, **IV-2**, **IV-3** and **IV-4**) obtained from the DFT calculations. For the all-CO complex **IV-1**, the sulfur oxygenate is some 9.60 kcal/mol *less* stable than the diiron oxidative addition product, **IV-1- $\mu$ -O**. As this is opposite the known experimental result of S-oxygenation determined for the  $[(\mu\text{-est})[\text{Fe}^{\text{I}}(\text{CO})_3]_2]$  complex,<sup>182</sup> other basis sets were examined as a possible source of the discrepancy. When the computation was

performed at the level of B3LYP/cc-PPVDZ&LANL2DZ (see Table IV. 1, values in parenthesis), it was found that the total energy difference ( $\Delta G1$ ) between **IV-1-O** and **IV-1- $\mu$ -O** is 10.76 kcal /mol, which is compatible with the result of 9.67 kcal /mol obtained from the initial calculation. In all cases, calculations at the level of B3LYP/cc-PPVDZ&LANL2DZ yield slightly higher energies. Replacement of the B3LYP functional with TPSS led to the calculated  $\Delta G1$  value = 11.66 kcal /mol. Thus, qualitatively, the calculated  $\Delta G1$  is not dependent on functionals or basis sets. From these data, theory predicts that the **IV-1- $\mu$ -O** isomer is thermodynamically favored.

**Table IV. 1** Total free energy (kcal/mol) comparison between sulfur oxygenated species and corresponding metal oxygenated isomers from the computations with functional and basis sets of B3LYP/D95&LANL2DZ (in parentheses, B3LYP/cc-PPVDZ&LANL2DZ), values of  $\mu$ -O complexes referenced to 0 kcal/mol; <sup>a</sup>The selected value is derived from the structure with alternate direction of bridgehead carbon in the propane S to S linker (the dash line).

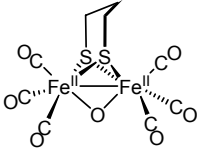
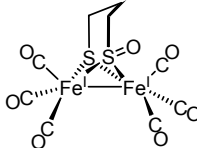
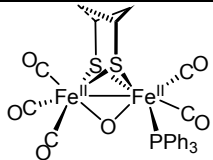
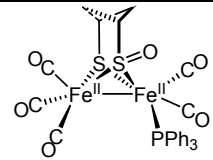
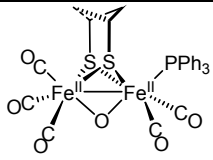
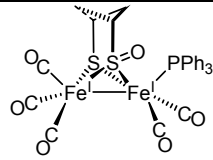
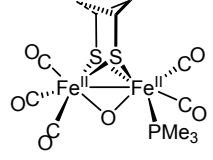
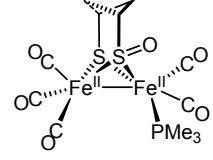
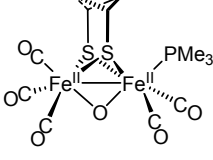
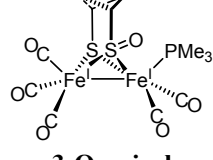
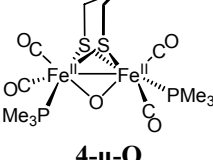
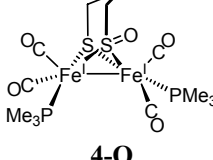
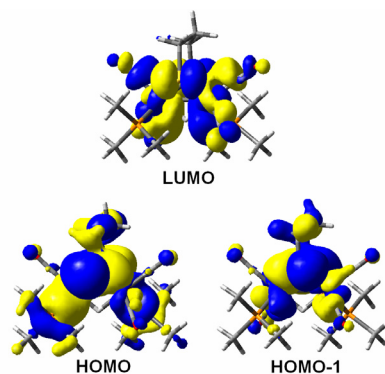
Isomeric oxygenates	
 <p><b>1-<math>\mu</math>-O</b></p> <p>G = 0 (G = 0)</p>	 <p><b>1-O</b></p> <p><math>\Delta G1 = +9.60</math> (<math>\Delta G1 = +10.96</math>)</p>



Table IV. 1 Continued.

Isomeric oxygenates	
 <p><b>2-<math>\mu</math>-O-basal</b></p> <p><math>G = 0</math> (<math>G = 0</math>)</p>	 <p><b>2-O-basal</b></p> <p><math>\Delta G_{2b} = +16.70/17.00^a</math> (<math>\Delta G_{2b} = +16.70/17.00^a</math>)</p>
 <p><b>2-<math>\mu</math>-O-apical</b></p> <p><math>G = 0</math> (<math>G = 0</math>)</p>	 <p><b>2-O-apical</b></p> <p><math>\Delta G_{2a} = +5.90/4.40^a</math> (<math>\Delta G_{2a} = +18.20/17.59^a</math>)</p>
 <p><b>3-<math>\mu</math>-O-basal</b></p> <p><math>G = 0</math> (<math>G = 0</math>)</p>	 <p><b>3-O-basal</b></p> <p><math>\Delta G_{2b} = +16.41/15.63^a</math> (<math>\Delta G_{2b} = +17.59/16.60^a</math>)</p>
 <p><b>3-<math>\mu</math>-O-apical</b></p> <p><math>G = 0</math> (<math>G = 0</math>)</p>	 <p><b>3-O-apical</b></p> <p><math>\Delta G_{2a} = 6.81/5.33^a</math> (<math>\Delta G_{2a} = +8.56/6.96^a</math>)</p>
 <p><b>4-<math>\mu</math>-O</b></p> <p><math>G = 0</math> (<math>G = 0</math>)</p>	 <p><b>4-O</b></p> <p><math>\Delta G_4 = +19.50</math> (<math>\Delta G_4 = +19.88</math>)</p>

Similarly, in all cases, the  $\mu$ -O isomeric form is calculated to be the more stable for complexes **IV-2- $\mu$ -O** vs. **IV-2-O**, **IV-3- $\mu$ -O** vs. **IV-3-O** and **IV-4- $\mu$ -O** vs. **IV-4-O**. Again, as seen in Table IV. 1, there is little difference in values determined from the two basis sets. Note that the positional isomers in complex **IV-2**, i.e. PPh<sub>3</sub> in apical or basal positions, greatly affect the  $\Delta G$  values ( $\Delta G_{2a}$  vs  $\Delta G_{2b}$ ) of the isomeric oxygenates. Relative to the basal isomer, the S-oxygenate is favored when the phosphine is in the apical position. For example, the total energy difference of **IV-2- $\mu$ -O-basal** vs. **IV-2-O-basal** ( $\Delta G_{2b}$ ) is some 17 kcal/mol while  $\Delta G_{2a}$  is only ca. 5 kcal/mol, i.e. 10 kcal/mol less than the former. DFT computations at both levels suggest the flip of the S-S linker has little effect (ca. 2 kcal/mol) on the total energy of the oxygenate isomers from **IV-2**. For example, **IV-2-O-apical** (5.90 kcal/mol) is 1.5 kcal/mol less stable than its S-S linker flipped isomer (4.40 kcal/mol, the structure with dash line in Table IV. 1). Ligand position and linker bridgehead position have similar effects on the total energy of the oxygenate isomers from **IV-3**.



**Figure IV. 3** Frontier molecular orbitals (with isovalue = 0.04) of **IV-5<sup>+</sup>**,  $\{(\mu\text{-pdt})(\mu\text{-H})[\text{Fe}(\text{CO})_2(\text{PMe}_3)_2]\}^+$

Figure IV. 3 displays the frontier orbitals of the  $\text{Fe}^{\text{II}}\text{Fe}^{\text{II}}$  complex,  $\{(\mu\text{-pdt})(\mu\text{-H})[\text{Fe}(\text{CO})_2(\text{PMe}_3)]_2\}^+$  (**IV-5<sup>+</sup>**). Unlike the  $\text{Fe}^{\text{I}}\text{Fe}^{\text{I}}$  species, the HOMO of complex **IV-5<sup>+</sup>** is largely the sulfur lone pair; i.e. addition of the proton into the Fe-Fe bond orbital greatly stabilizes what was the HOMO of complex **IV-3**. Therefore, the orbital-directing oxygenation of **IV-5<sup>+</sup>** should be at sulfur.

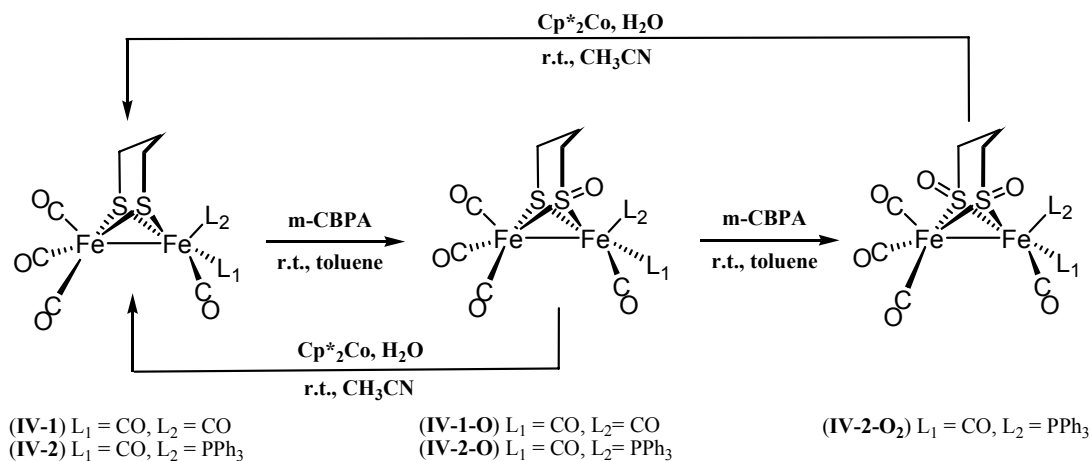
**Synthesis and characterizations.** Attempts to oxygenate  $(\mu\text{-pdt})[\text{Fe}(\text{CO})_3]_2$  (**IV-1**) (in acetonitrile and MeOH) with molecular  $\text{O}_2$  resulted in slow precipitation of insoluble, non-CO containing solids over the course of days without detection of any intermediate by IR spectroscopy. Complex **IV-1** in acetone or acetonitrile was found to be inert towards  $\text{H}_2\text{O}_2$  at 22 °C and at temperatures up to 80 °C. Therefore, we revisited the method used by I. Lorenz, et al. to produce an oxygenate of  $(\mu\text{-edt})[\text{Fe}(\text{CO})_3]_2$ , i.e.  $(\mu\text{-est})[\text{Fe}(\text{CO})_3]_2$ , using *m*-chloroperoxybenzoic acid (*m*-CPBA) as O-atom donor.<sup>182</sup> It was found out that the oxygenation of **IV-1** by 1.5 equiv of *m*-CPBA in toluene proceeds smoothly within 0.5 h at 22 °C as indicated by the IR monitor which showed on average a  $10\text{ cm}^{-1}$  positive shift in  $\nu(\text{CO})$  values. The reaction is accompanied by an obvious color change from red to golden yellow. Complex  $(\mu\text{-pst})[\text{Fe}(\text{CO})_3]_2$  (**IV-1-O**) was isolated as the sole product in 84% yield and its identity was established by ESMS, IR, NMR and X-ray diffraction. When an additional portion of oxidant was used after the formation of **IV-1-O**, no new species was observed.

Similarly to *m*-CPBA, Dimethyldioxrane (DDO) oxygenates **IV-1** to **IV-1-O** in a quantitative yield. The advantage of using DDO over *m*-CPBA is the ease of purification

of the oxygenated product since acetone is the only byproduct. The disadvantages lie in the low yield of DDO synthesis and its instability on storage.

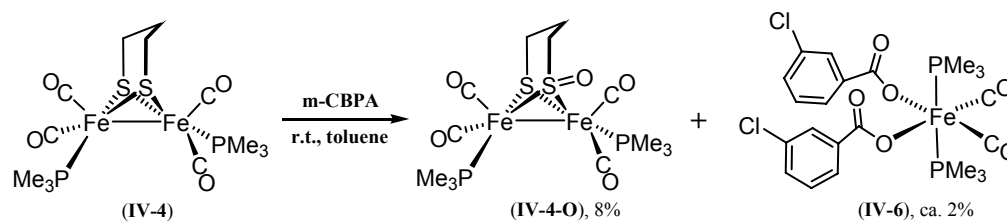
The oxygenations of various  $(\mu\text{-pdt})[\text{Fe}(\text{CO})_2\text{L}]_2$  were carried out as outlined in Scheme IV. 2. Complex **IV-2**,  $(\mu\text{-pdt})[\text{Fe}(\text{CO})_3][\text{Fe}(\text{CO})_2\text{PPh}_3]$ , behaves like complex **IV-1** upon treatment with  $\text{O}_2$  and  $\text{H}_2\text{O}_2$  but it readily reacts with 1.5 equiv of *m*-CPBA to give complex **IV-2-O**,  $(\mu\text{-pst})[\text{Fe}_2(\text{CO})_3][\text{Fe}_2(\text{CO})_2\text{PPh}_3]$  (82% yield). In contrast to complex **IV-1-O**, on addition of another 1.5 equiv of *m*-CPBA, **IV-2-O** undergoes further oxygenation at the remaining thiolate as confirmed by various characterizations. Although the  $\nu(\text{CO})$  IR monitor indicated a quantitative conversion, the isolated yield of  $(\mu\text{-pds})[\text{Fe}_2(\text{CO})_3][\text{Fe}_2(\text{CO})_2\text{PPh}_3]$ , **IV-2-O<sub>2</sub>**, ( $\text{pds} = -(\text{O})\text{S}(\text{CH}_2)_3\text{S}(\text{O})-$ ) is ca. 29% due to loss during purification.

**Scheme IV. 2**



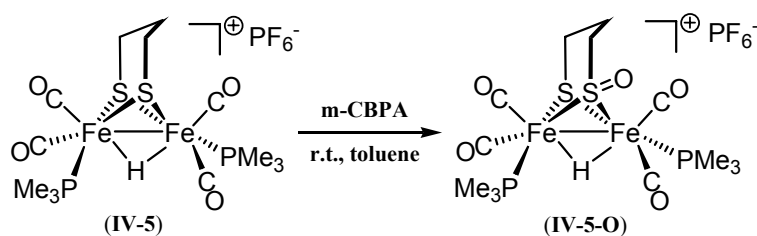
The reactivity of complex **IV-2** prompted study of the oxygenation of the more electron rich, and thus more air sensitive, complex **IV-4**,  $(\mu\text{-pdt})[\text{Fe}_2(\text{CO})_2\text{PMe}_3]_2$ , for which the stabilizing effect of better donors was expected to be more likely to form metal-based  $\text{Fe}^{\text{II}}(\mu\text{-O})\text{Fe}^{\text{II}}$  species as suggested by the above DFT investigation. Complex **IV-4** rapidly reacts with  $\text{O}_2$  to generate a dark insoluble residue. Unlike complexes **IV-1** and **IV-2**, complex **IV-4** vigorously reacts with  $\text{H}_2\text{O}_2$  in acetone at 22 °C to form light orange precipitates with gas evolution (assumed to be CO or  $\text{CO}_2$ ). The orange non-CO containing product is only slightly soluble in water and remains uncharacterized. When oxygenation of **IV-4** with *m*-CPBA was performed following the procedure as for **IV-1** and **IV-2**, a small amount of product,  $(\mu\text{-pst})[\text{Fe}_2(\text{CO})_2\text{PMe}_3]_2$  (**IV-4-O**) was slowly formed while most of the starting material decomposed (see Scheme IV. 3). The final yield of **IV-4-O** was ca. 8%. Another trace byproduct characterized by higher CO stretching frequencies (2033 and 1981  $\text{cm}^{-1}$ ) was also detected. This species was isolated by co-crystallization with **IV-4-O** in hexane solution. X-ray diffraction analysis revealed that the byproduct is a mono iron(II) dicarboxylate dicarbonyl,  $\text{Fe}(\text{CO})_2(\text{PMe}_3)_2(\text{m-Cl-PhCOO}^-)_2$ , **IV-6** (see Scheme IV. 3). This product implicates at least some Fe-based oxidation.

**Scheme IV. 3**



In order to probe the effect of Fe oxidation state on the oxygenation of diiron complexes, complex **5**, a Fe<sup>I</sup>Fe<sup>II</sup> species, was exposed to m-CPBA (Scheme IV. 4). At 22 °C, in CH<sub>2</sub>Cl<sub>2</sub>, quantitative conversion to its S-oxygenate was observed. The **IV-5-O** complex is stable to excess m-CPBA, as no additional oxygenated species was observed.

**Scheme IV. 4**



During attempts to deoxygenate **IV-1-O** by phosphines, an alternate route to complexes **IV-2-O** and **IV-4-O** was discovered, Scheme IV. 5. Pursuing this synthetic approach, we noticed that ligand substitution of **IV-1-O** required harsher conditions than with **IV-1**. For example, complex **IV-1-O** does not show obvious reactivity with  $\text{PMe}_3$  in hexane at 22 °C and only slowly forms the mono- $\text{PMe}_3$  substituted product,  $(\mu\text{-pst})[\text{Fe}(\text{CO})_3][\text{Fe}(\text{CO})_2\text{PMe}_3]$  (**IV-3-O**) at 68 °C. In refluxing toluene (110 °C), complex **IV-4-O** was prepared from complex **IV-1-O** and excess  $\text{PMe}_3$  by the ligand exchange process. In contrast, **IV-1** readily reacts with  $\text{PMe}_3$  in hexane at 22 °C to generate mono- $\text{PMe}_3$  substituted product,  $(\mu\text{-pdt})[\text{Fe}(\text{CO})_3][\text{Fe}(\text{CO})_2\text{PMe}_3]$  (**IV-3**); and di-substitution by  $\text{PMe}_3$  occurs at 68 °C. For comparison, the rates of CO/ $\text{PMe}_3$  exchange reactions of **IV-1** and **IV-1-O** in toluene were investigated under similar pseudo-1<sup>st</sup> order conditions for **IV-1** and **IV-1-O** using 20 equivalents of  $\text{PMe}_3$ . Through monitoring the

disappearance of the  $\nu(\text{CO})$  IR band at 2076 (m) for **IV-1** at 22 °C, the observed pseudo-1<sup>st</sup> order rate constant is  $1.47 \times 10^{-4} \text{ s}^{-1}$ , while the exchange reaction for **IV-1-O** is immeasurably slow. At 90°C, the observed rate constant for **IV-1-O**/ $\text{PMe}_3$  is  $4.2 \times 10^{-5} \text{ s}^{-1}$  (disappearance of  $\nu(\text{CO})$ , 2083 (m)). Detailed kinetic studies will be reported in a separate publication.

### Scheme IV. 5

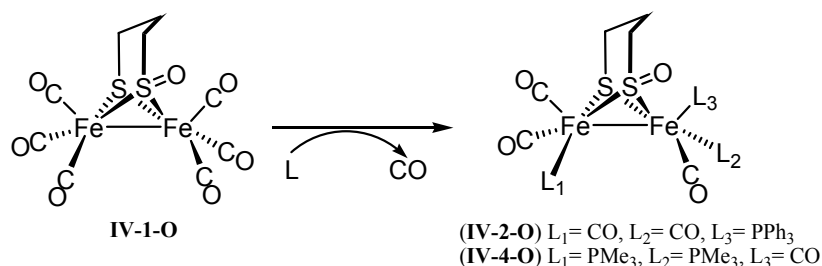


**Table IV. 2** Infrared spectroscopic data,  $\nu(\text{CO})$  region, for sulfur-oxygenated complexes (**IV-1-O**, **IV-2-O**, **IV-2-O<sub>2</sub>**, **IV-4-O**, **IV-5-O** and **IV-6**) in  $\text{CH}_2\text{Cl}_2$ , and their corresponding precursors in solvents as listed.

complex	$\nu(\text{CO})$ ( $\text{cm}^{-1}$ )
$(\mu\text{-pdt})[\text{Fe}(\text{CO})_3]_2$ ( <b>IV-1</b> )	2073 (m), 2035 (vs), 1992 (s, br)( $\text{CH}_3\text{CN}$ )
$(\mu\text{-pdt})[\text{Fe}(\text{CO})_3][\text{Fe}(\text{CO})_2\text{PPh}_3]$ ( <b>IV-2</b> )	2044 (s), 1982 (vs, br), 1931 (w) ( $\text{CH}_3\text{CN}$ )
$(\mu\text{-pdt})[\text{Fe}(\text{CO})_2\text{PMe}_3]_2$ ( <b>IV-4</b> )	1979 (w), 1942 (s), 1898 (s) ( $\text{CH}_3\text{CN}$ )
$(\mu\text{-pdt}) (\mu\text{-H})[\text{Fe}(\text{CO})_2\text{PMe}_3]_2$ ( <b>IV-5</b> )	2048(w, sh), 2033 (s), 1990 (s) ( $\text{CH}_2\text{Cl}_2$ )
$(\mu\text{-pst})[\text{Fe}(\text{CO})_3]_2$ ( <b>IV-1-O</b> )	2083 (m), 2045 (vs), 2017 (s), 2000 (s)
$(\mu\text{-pst})[\text{Fe}(\text{CO})_3][\text{Fe}(\text{CO})_2\text{PPh}_3]$ ( <b>IV-2-O</b> )	2056 (s), 1998 (vs), 1971 (w), 1953 (w)
$(\mu\text{-pds})[\text{Fe}(\text{CO})_3][\text{Fe}(\text{CO})_2\text{PPh}_3]$ ( <b>IV-2-O<sub>2</sub></b> )	2066 (s), 2014 (vs), 1981 (m), 1952 (w)
$(\mu\text{-pst})[\text{Fe}(\text{CO})_2\text{PMe}_3]_2$ ( <b>IV-4-O</b> )	1994 (w), 1985 (w), 1958 (vs), 1917 (br, m)
$(\mu\text{-pst})[\text{Fe}(\text{CO})_2\text{PMe}_3]_2$ ( <b>IV-5-O</b> )	2061 (w, sh), 2044 (s), 2002 (s)
$\text{Fe}(\text{CO})_2(\text{PMe}_3)_2(\text{m-Cl-PhCOO}^-)_2$ ( <b>IV-6</b> )	2033 (s), 1981 (s)

IR data in the CO stretching region of all sulfur-oxygenated complexes including reference complexes are compared in Table IV. 2. Complex **IV-1-O** features a similar  $\nu(\text{CO})$  IR absorption pattern as complex **IV-1** with  $\nu(\text{CO})$  values shifted ca.  $10\text{ cm}^{-1}$  higher than complex **IV-1**, indicative of the poorer donating ability of propanesulfenato thiolate ( $-\text{S}(\text{CH}_2)_3\text{S}(\text{O})-$ ) compared to propanedithiolate ( $-\text{S}(\text{CH}_2)_3\text{S}-$ ). Similarly the  $\nu(\text{CO})$  order in the series of **IV-2** < **IV-2-O** < **IV-2-O<sub>2</sub>** corresponds to decreasing donating strength of bidentate bridging ligands of  $-\text{S}(\text{CH}_2)_3\text{S}-$ ,  $-\text{S}(\text{CH}_2)_3\text{S}(\text{O})-$  and  $-(\text{O})\text{S}(\text{CH}_2)_3\text{S}(\text{O})-$ . Similar trends can be also deduced from comparison of **IV-4** and **IV-4-O**, **5** and **IV-5-O**. The byproduct, **6**, isolated from the oxygenation of **IV-4**, exhibits two strong CO absorptions at 2033(s) and 1981(s), consistent with the vibrational modes of a cis-dicarbonyl species.

**Table IV. 3** Cyclic voltammetry data versus  $\text{Fc}^+/\text{Fc}$  for the sulfur-oxygenated complexes (**IV-1-O**, **IV-2-O**, **IV-2-O<sub>2</sub>** and **IV-4-O**) and reference complexes in  $\text{CH}_3\text{CN}$  electrolyte ( $0.1\text{ mM Bu}_4\text{N}^+\text{BF}_4^-$ ; scan rate,  $100\text{ mV/s}$ )

Comple x	oxidation		Fe(I)Fe(I)/ Fe(I)Fe(0)	Further reduction
<b>IV-1</b>	—	0.82	-1.70	-2.32
<b>IV-2</b>	0.66	0.27	-1.87	-2.24
<b>IV-4</b>	0.65, 0.23	-0.14	-2.37	—
<b>IV-1-O</b>	—	0.95	-1.58	-1.70, -2.25
<b>IV-2-O</b>	—	0.48	-1.77	-1.97, -2.3
<b>IV-2-O<sub>2</sub></b>	—	0.65	-1.72	-1.98
<b>IV-4-O</b>	0.67	0.03	-2.21	-2.38



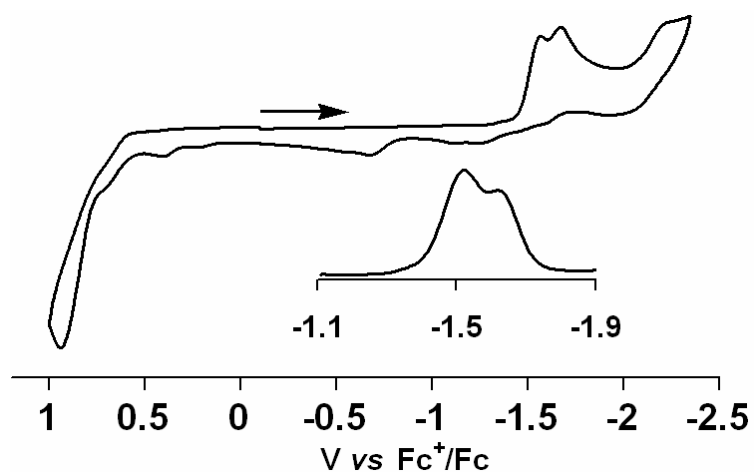


**Figure IV. 4** CV and DPV (inset) curves of the sulfur oxygenated complex **IV-1-O** in  $\text{CH}_3\text{CN}$ . All potentials are referenced vs  $\text{Fc}^+/\text{Fc}$  (scan rate = 100 mV/s, 0.1 M  $[\text{nBu}_4\text{N}]^+ [\text{BF}_4]^-$ , 22 °C).

**Electrochemical studies of IV-1-O, IV-2-O, IV-2-O<sub>2</sub> and IV-4-O.** The redox properties of sulfur-oxygenated complexes were studied by electrochemical methods of cyclic voltammetry (CV) and differential pulse voltammetry (DPV). The electrochemical data is given in Table IV. 2. According to previous reports, the first reduction event is assigned to  $\text{Fe(I)Fe(I)}/\text{Fe(I)Fe(0)}$ .<sup>146, 195</sup> The oxidative features may relate to a  $\text{Fe(I)Fe(II)}/\text{Fe(I)Fe(I)}$  process, however S-based oxidation is also possible. Figure IV. 4 presents the CV and DPV curves of **IV-1-O**. Recorded CV and DPV curves for **IV-2-O**, **IV-2-O<sub>2</sub>** and **IV-4-O** are in the supporting information of reference <sup>220</sup>. In comparison to their non-oxygenated analogous, S-oxygenates exhibit redox couples at more positive potentials, consistent with the electron withdrawing ability of  $-(\text{O})\text{S}(\text{CH}_2)_3\text{S}(\text{O})-$  and  $-(\text{O})\text{S}(\text{CH}_2)_3\text{S}-$  as inferred from IR studies.

In addition to the redox event at -1.58 V, complex **IV-1-O** displays a second redox event at -1.70 V as shown in Figure IV. 4 . The later reduction potential is identical to that of the Fe(I)Fe(I)/Fe(I)Fe(0) couple of complex **IV-1**. According to the DPV studies, the extracted Faradaic current intensity of the first reduction of **IV-1-O** is more dominant than that of the second reduction. A similar phenomenon is seen for complex **IV-4-O**. The second reduction at -2.38 of **IV-4-O** is 170 mV more negative than its first reduction and lies at almost the same position as the first reduction of complex **IV-4**. Complex **IV-2-O** displays two additional reduction events at -1.97 and -2.3 V, ca. 200 mV more negative than its Fe(I)Fe(I)/Fe(I)Fe(0) couple. For complex **IV-2-O<sub>2</sub>**, only one additional reduction event at -1.98 V was observed. The most reasonable explanation of these results is that some reductive deoxygenation process produces the precursor dithiolate *in situ*. Countering this argument is the fact that repeated scans did not change the relative intensities of the two reduction events in any of oxygenates.

**Molecular structures of oxygenated species (IV-1-O, IV-2-O, IV-2-O<sub>2</sub> and IV-4-O).** The molecular structures of these complexes verified S-oxygenation, Figure IV. 5. Selected metric data are listed in Table IV. 3. All structures adopt the well-known butterfly Fe<sub>2</sub>S<sub>2</sub> core geometry with Fe-Fe distances in the 5.6 Å range, slightly longer than their non-oxygenated counterparts.<sup>127, 132, 163</sup> The Fe-Fe distance of complex **IV-4-O** is even longer by ca. 0.094 Å than that of  $\{(\mu\text{-pdt})(\mu\text{-H})[\text{Fe}(\text{CO})_3]_2\}^+\text{PF}_6^-$  (2.578 Å). The S-O vector in each is roughly perpendicular to the Fe-Fe vector. The PPh<sub>3</sub> ligands of complexes **IV-2-O** and **IV-2-O<sub>2</sub>** occupy apical positions, which is the same as the reported structure of complex **IV-2**. The PMe<sub>3</sub> ligands of complex **IV-4-O** are both at

basal sites. One molecule of water binds with two molecules of **IV-4-O** via hydrogen bonding interactions. The hydrogen bond defined by O $\cdots$ O distance between S=O and H<sub>2</sub>O is 2.899 Å (the calculated distance of OH $\cdots$ OS is 2.030 Å).

For the mono-oxy complexes **IV-1-O**, **IV-2-O**, and **IV-4-O**, the Fe-S(O) distance is shorter than the corresponding Fe-S distance while the bis-oxy complex, **IV-2-O<sub>2</sub>**, possesses identical, short Fe-S distances. The S-O distance of complex **IV-1-O** is 1.495 Å, ca. 0.09 Å longer than that of **IV-2-O** (1.405 Å). Further oxygenation of **IV-2-O** led to longer S-O distances in **IV-2-O<sub>2</sub>**, symmetry generated identical at 1.487 Å. Complex **IV-4-O** exhibits the longest S-O distance of the series. This result is explained by the S-O bond polarization from H-bonding to water (*vide supra*). While these comparisons suggest a small influence of the S-attached O atom on the core structure of diiron dithiolates, there is no apparent trend in the S=O distances with electron-richness of the diiron complex.

The mono-Fe dicarbonyl, **IV-6**, is a typical octahedral complex. In its structure, the cis-COs and two cis-carboxylates are found in equatorial plane and two trans-PMe<sub>3</sub> ligand occupy axial positions.

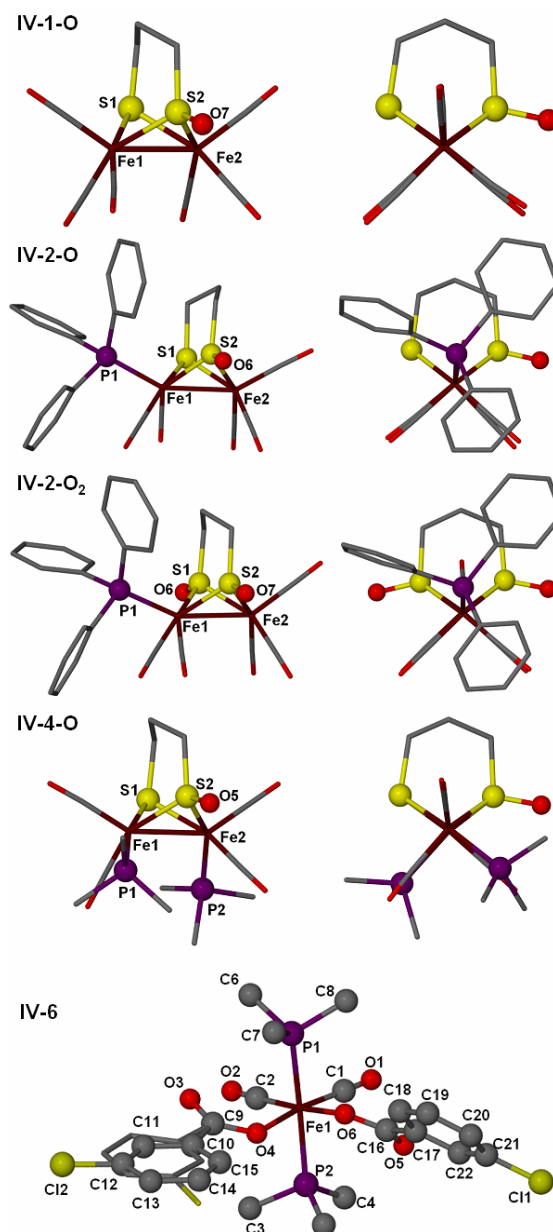


**Figure IV. 5** Molecular structures of the sulfur oxygenated complexes (**IV-1-O**, **IV-2-O**, **IV-2-O<sub>2</sub>**, **IV-4-O** and **IV-6**) given in two perspectives: along the Fe-Fe bond and perpendicular to the Fe-Fe vector. For **IV-2-O** and **IV-2-O<sub>2</sub>**, the PPh<sub>3</sub> ligand is in the front.

**Table IV. 4** Selected metric data for the sulfur oxygenated complexes (**IV-1-O**, **IV-2-O**, **IV-2-O<sub>2</sub>** and **IV-4-O**). In parenthesis and italics are the values of Fe-Fe distance of parent non-oxygenates.

Complex	<b>IV-1-O</b>	<b>IV-2-O</b>	<b>IV-2-O<sub>2</sub></b>	<b>IV-4-O</b>
Fe1- Fe2 (Å)	2.5765 (8) (2.5103 (11))	2.5583 (16) (2.5247 (6))	2.5783 (13) (2.5247 (6) )	2.6173 (12) (2.555 (2))
Fe1- S1 (Å)	2.2563 (12)	2.226 (2)	-----	2.2794 (13)
Fe1- S1(=O) (Å)	-----	-----	2.1840 (17)	-----
Fe1-S2(=O) (Å)	2.1654 (12)	2.219 (2)	2.1906 (16)	2.1650 (17)
S2=O	1.495 (2)	1.405 (7)	1.487 (4)	1.5168 (19)
Fe-P1	-----	2.228 (2)	2.2312 (17)	2.2133 (17)
S1- Fe1-S2	82.40 (4)	81.21 (7)	80.63 (6)	81.65 (6)
Fe1-S2-Fe2	73.04 (4)	70.41 (7)	72.18 (5)	74.36 (5)

**CO site-Exchange processes of complex IV-1-O and variable temperature <sup>13</sup>C NMR studies.** A fundamental property of the (μ-SRS)[Fe(CO)<sub>3</sub>]<sub>2</sub> molecule is the intramolecular site exchange which takes place on each Fe(CO)<sub>3</sub> unit, interchanging apical and basal CO groups.<sup>162, 189, 221</sup> The barrier to this rotation is affected by substituent ligands.<sup>162, 189, 221</sup> Hence the S-oxygenates provide an opportunity to investigate the effect of S-modification in the bridging propane dithiolate linker on the CO intramolecular exchange processes in (μ-SRS)[Fe(CO)<sub>3</sub>]<sub>2</sub> vs. (μ-SRSO)[Fe(CO)<sub>3</sub>]<sub>2</sub> complexes. The NMR studies described below were collaborated with group member, M. Singleton.

Variable temperature <sup>13</sup>C NMR spectra of **IV-1-O**, recorded on a 500 MHz NMR spectrometer in the temperature region of 30 °C to -60 °C, are displayed in Figure IV. 6

top, (Figure IV. 6, bottom, contains spectra for **IV-1** recorded under identical conditions). At 20 °C, **IV-1-O** displays a broad resonance at  $\delta = 207.8$  ppm which is assigned to the six rapidly exchanging CO ligands. With increase of the temperature to 30 °C, the signal sharpens, while upon cooling the sample the resonance broadens with coalescence occurring at -10 °C. Below -10 °C, the signal began to split into separate signals; and by -40 °C, complete resolution into three single resonances is observed, with chemical shifts at  $\delta = 207.8$ , 207.4 and 207.0 ppm and in a ratio of approximately 1:1:1. As the broadening resulting from decreased motion of the S to S linker should affect the signals corresponding to the basal CO's approximately the same, the fact that the resonance at 207.4 ppm changes rapidly upon cooling further indicates that it should correspond to the apical CO. The assignments of the resonances at 207.8 and 207.0 ppm can be made by comparison of this complex to previously reported diiron models where CO has been substituted by a better donor ligand.<sup>162, 221</sup> In the spectra of these complexes all CO signals show a marked downfield shift likely resulting from increased  $\pi$ -backbonding. Since the CO's trans to the sulfenato should experience a smaller amount of backbonding than the CO's trans to the thiolate, the resonance at 207.0 is assigned to the former and the remaining resonance at 207.8 to the latter.

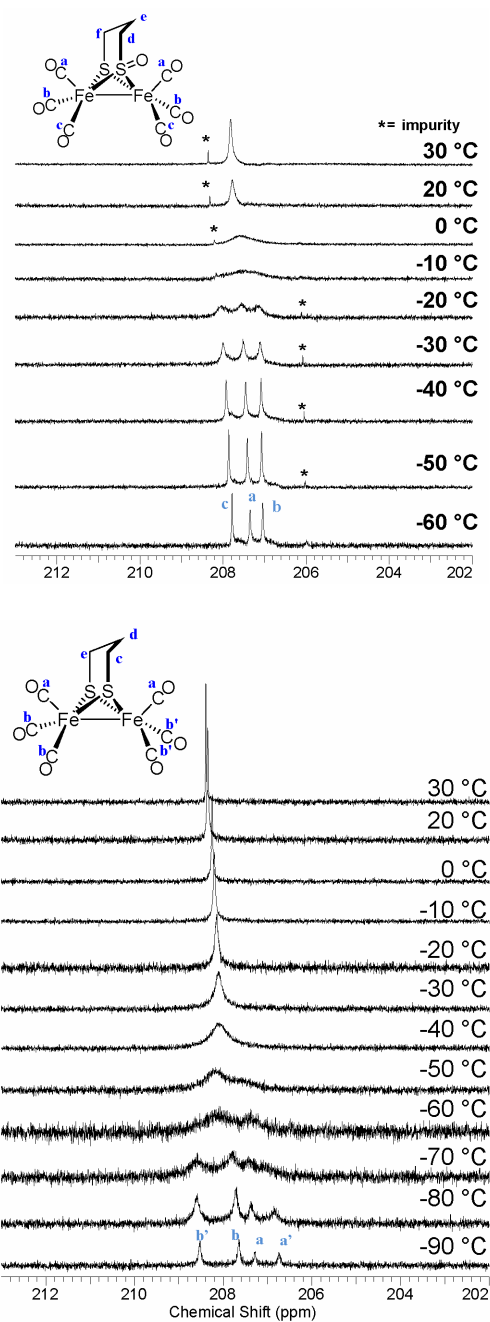


**Figure IV. 6** Top: variable temperature  $^{13}\text{C}$  NMR studies of complex **IV-1-O** from -60 to 30 °C ( $\text{CD}_2\text{Cl}_2$  solution, in CO region); signals indicated with “\*” are unknown impurities. Bottom: Variable temperature  $^{13}\text{C}$  NMR studies of complex **IV-1** from -80 to 30 °C.

Ideally, six CO's should be characterized by individual signals when the bridge flip of  $-\text{S}(\text{CH}_2)_3\text{S}(\text{O})-$  is stopped; however, this was not observed for the temperature range explored in this study. Estimation of  $\Delta G^\ddagger$  from the exchange rate constant at coalescence found as 45 kJ/mol (or 10.7 kcal/mol) and the full line shape analysis found a similar value of  $\Delta G^\ddagger = 48$  kJ/mol (or 11.4 kcal/mol).

Under similar experimental conditions to **IV-1-O**, the spectra for complex **IV-1** were recorded over a larger temperature range than previously reported.<sup>162</sup> Based on new spectra, the coalescence temperature was observed at  $-50$  °C for complex **IV-1**, which is about  $40^\circ$  lower than that of complex **IV-1-O**, and the peak separation between apical and basal signals was greater than twice that observed for **IV-1-O** (see Figure IV. 6, bottom). Both of these facts indicate that the  $\text{Fe}(\text{CO})_3$  unit of complex **IV-1** is more mobile than that of complex **IV-1-O**. In fact, the  $\Delta G^\ddagger$  from the exchange rate constant at coalescence for complex **IV-1** was estimated to be 36 kJ/mol (or 8.6 kcal/mol) which is  $\sim 10$  kJ/mol less than that of the sulfenate derivative. This difference indicates that modification of the thiolate S into a sulfenate increases the barrier for CO site exchange on the all-CO complex.

**Computational (DFT) results.** While DFT computations that defined the transition state structure resulting from the intramolecular interchange of apical and basal CO groups in complex **IV-1** were earlier reported,<sup>162, 189</sup> it has been reexamined in order to compare results under the same computational settings as complex **IV-1-O**. Figure IV. 7 (top) displays the geometry optimized ground state structure, [**IV-1-O**], of complex **IV-1-O**, along with two transition states, [**IV-1-O**]<sup>‡</sup> and [**IV-1-O**]<sup>'‡</sup>, calculated for the CO



site-exchange process of one  $\text{Fe}(\text{CO})_3$  unit. The latter differs in the orientation of the bridgehead carbon in the S to S linker. Note that the  $\text{Fe}(\text{CO})_3$  unit experiencing rotation inverts its square pyramidal geometry with the inverted apical CO lying under the Fe-Fe vector at a semi-bridging position, similarly to what is observed for mixed valent  $\text{Fe}^{\text{I}}\text{Fe}^{\text{II}}$  species.<sup>193, 196, 222, 223</sup> The total energy difference between the ground state and the transition state is 13.97 kcal/mol calculated at the level of B3LYP/D95&LANL2DZ. In Figure IV. 7 (bottom) is given the ground state structure and the transition state structures of **IV-1** along one  $\text{Fe}(\text{CO})_3$  rotation. The energy barrier required for such site-exchange is 11.88 kcal/mol.<sup>189</sup> The DFT results find the CO site-exchange process is more accessible for **IV-1** than that for **IV-1-O** since  $\Delta E_{(\text{IV-1-O})^\ddagger}$  is smaller than  $\Delta E_{(\text{IV-1})^\ddagger}$  by both calculations. The bridging S-S linker flip would disfavor the CO site exchange process by ca. 3 kcal/mol for both **IV-1** and **IV-1-O**. For instance, isomer  $[\text{IV-1}]^\ddagger$  is 2.85 or 2.69 kcal/mol more stable than the bridge flipped isomer,  $[\text{IV-1}]'^\ddagger$ . Calculations of both complexes at the level of B3LYP/cc-PVDZ&LANL2DZ yield similar results (see Figure IV. 7, the second values in parenthesis). Qualitatively these theoretical results are acceptable, although in both cases the calculated values are higher than the experimental values of IV-10.07 kcal/mol for **IV-1-O** and 8.6 kcal/mol for **IV-1**.

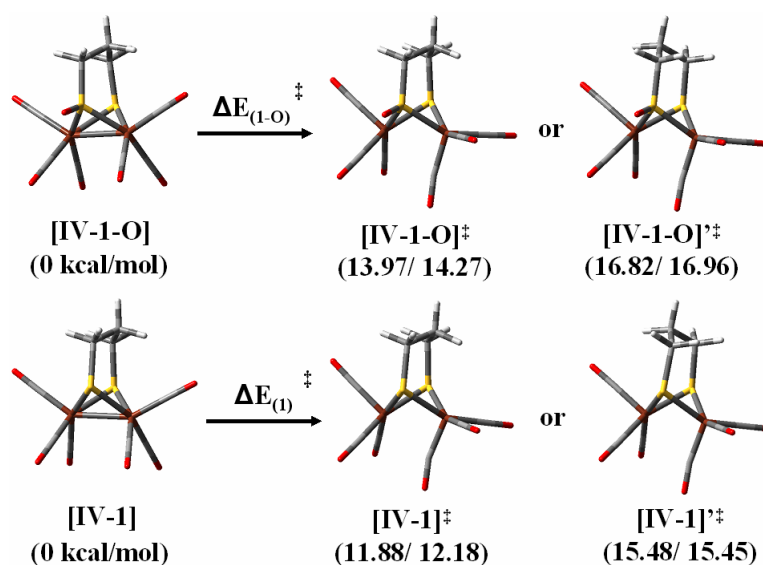


**Figure IV. 7** Ground state and transition state structures of **IV-1-O** (top) and **IV-1** (bottom) with corresponding energies given in kcal/mol obtained by DFT computations (In parenthesis, for e.g., (13.97/ 14.27): the former value obtained from the level of B3LYP/D95&LANL2DZ and the later value from the level of B3LYP/cc-pVDZ&LANL2DZ) for one Fe(CO)<sub>3</sub> unit rotation.

**Chemical and electrochemical deoxygenation studies.** Deoxygenation of the sulfur-oxygenated complexes is of particular importance as it might be related to the reductive reactivation mode of the active site of aerobically isolated [FeFe]-H<sub>2</sub>ase. In addition, deoxygenation with suitable oxygen transfer reagents could indicate relative S=O bond energies in such complexes.<sup>224</sup> We have attempted to use phosphines as O-atom acceptors, however, as discussed above, with PPh<sub>3</sub> and PMe<sub>3</sub>, only phosphine-substituted diiron complexes were identified as products. In the presence of the bulky (*t*-Bu)<sub>3</sub>P, which did not demonstrate CO substitution with complex **IV-1**, complex **IV-1-O**

remained intact under various reaction conditions. Whether the lack of O-atom transfer to phosphines is a reflection of poor kinetics or the actual thermodynamic preference is, at this stage, unclear as examples of very slow rates of uncatalyzed O-atom transfer reaction are well known.<sup>224</sup>

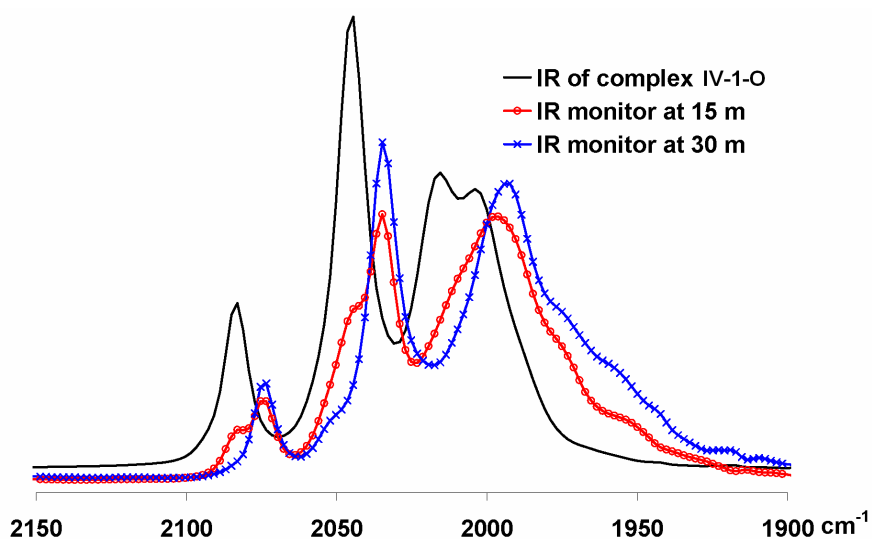


**Figure IV. 8** IR monitor of deoxygenation of **IV-1-O** with  $\text{Cp}^*_2\text{Co}$  in  $\text{CH}_3\text{CN}$  in the presence of  $\text{H}_2\text{O}$  (2% V/V)

Reductive deoxygenation of **IV-1-O** was examined using  $\text{Cp}^*_2\text{Co}$  (ca. -1.9 V vs  $\text{Fc}^+/\text{Fc}$ ) as reductant. In the presence of  $\text{CH}_3\text{CN}:\text{H}_2\text{O}$  (50:1, V/V), complex **IV-1-O** was reduced by 2 equiv of  $\text{Cp}^*_2\text{Co}$ , resulting in the formation of complex **IV-1** over the course of 30 min in an isolated yield of 50% (see Scheme IV. 2 and Figure IV. 8). Replacement of  $\text{CH}_3\text{CN}$  by THF gave the same results. However the use of anhydrous  $\text{CH}_3\text{COOH}$  and  $\text{CF}_3\text{COOH}$  as proton source was not effective as both directly react with

the Cp\*<sub>2</sub>Co reductant. In the absence of H<sub>2</sub>O, complex **IV-1-O** was reduced by Cp\*<sub>2</sub>Co in CH<sub>3</sub>CN to an unknown air sensitive species with multiple CO stretches, a species that was not observed in the presence of H<sub>2</sub>O. Subsequent treatment of the *in situ* generated complex with H<sub>2</sub>O slowly led to the formation of complex **IV-1** in low yield.

By following the deoxygenation procedure for complex **IV-1-O**, complexes **IV-2-O** and **IV-2-O<sub>2</sub>** were transformed to complex **IV-2** with 2 and 4 equiv of Cp\*<sub>2</sub>Co, respectively, in ca. 10% yield. Unknown CO-containing species were detected by IR in the deoxygenation processes of both complex **IV-2-O** and **IV-2-O<sub>2</sub>**.

Complexes **IV-3-O** and **IV-5-O** were also examined for deoxygenation in the same manner. Deoxygenation of **IV-5-O** was complicated by concurrent reductive deprotonation. The  $\nu(\text{CO})$  IR monitor indicated that a small amount of complex **5** was reclaimed from **IV-5-O** while complex **IV-4-O** was also generated via proton loss from the bridging hydride. Complex **IV-4-O** was not reduced by Cp\*<sub>2</sub>Co in the absence or presence of H<sub>2</sub>O.

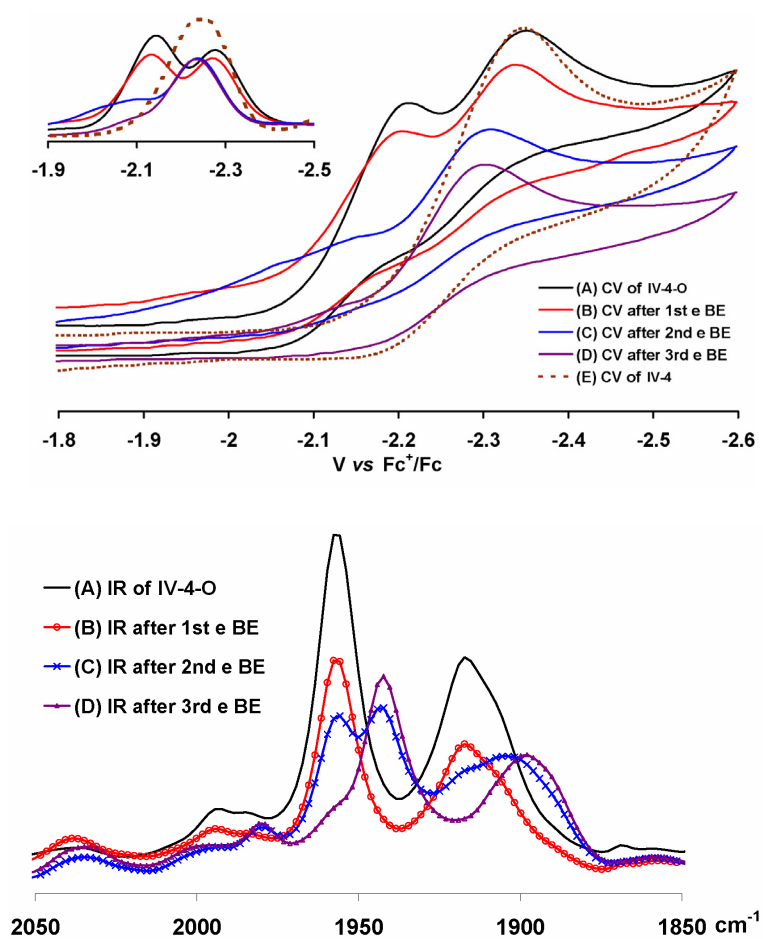


**Figure IV. 9** CV (top), DPV (top, inset) and IR measurements (bottom) of deoxygenation studies of **IV-4-O** via bulk electrolysis.

Alternatively, electrochemical methods were used to control the reduction potential for deoxygenation of complex **IV-4-O**. In CH<sub>3</sub>CN:H<sub>2</sub>O (50:1, V/V), cathodic bulk electrolysis was set at 2.3 V vs Fc<sup>+</sup>/Fc, which is about 100 mV more negative than the Fe<sup>I</sup>Fe<sup>I</sup>/Fe<sup>I</sup>Fe<sup>0</sup> couple of complex **IV-4-O**. In Figure IV. 9 (top), curve A represents the CV of **IV-4-O** and in Figure IV. 9 (bottom), the red line (IR A) displays the IR spectrum of **IV-4-O**. After a total charge of 0.43 Q, ca. 1 equiv of electrons, was passed at the

controlled potential, the second CV, which is plotted as curve B, was recorded. In the CV labeled as B, the current intensity of the 1<sup>st</sup> reduction diminished while the second peak intensified and shifted anodically. At this point a sample was taken from the electrochemical cell and its IR spectrum was recorded. A decrease in  $\nu(\text{CO})$  IR intensities indicated consumption of **IV-1-O** during bulk electrolysis, although no new species was identified. When the second equiv of electrons was supplied, the difference of the current intensity between the first and the second reduction waves was further noticeable. The IR spectrum (IR B) taken subsequently suggests the formation of complex **IV-4** with its characteristic band at  $1942\text{ cm}^{-1}$  and the presence of remaining complex **IV-4-O**. The first reduction peak completely disappeared in the third CV (CV C) which was measured after the third equiv of electrons was passed through the working electrode. The observed reduction at  $-2.35\text{ V}$  shifted ca.  $30\text{ mV}$  anodically in comparison to the original second reduction. The corresponding IR (D) exhibited CO stretches exclusively for complex **IV-4**. The yield of complex **IV-4** from this approach was estimated ca. 25% based on the relative CO stretch intensity of **IV-4-O** and **IV-4**.

The bulk electrolysis was also monitored by the DPV mode of analysis (inset in Figure IV. 9, top), which more clearly displays the changes of the reduction events during the stepwise bulk electrolysis. To further verify the efficiency of the electrochemical approach, deoxygenation by bulk electrolysis was applied to complex **IV-1-O**. Under the same experimental conditions, the electrochemical deoxygenation of complex **IV-1-O**, which was monitored by CV, DPV and IR in situ (see Figure IV. 10),

was shown to take up two equiv of electrons, similar to its chemical reduction and deoxygenation.

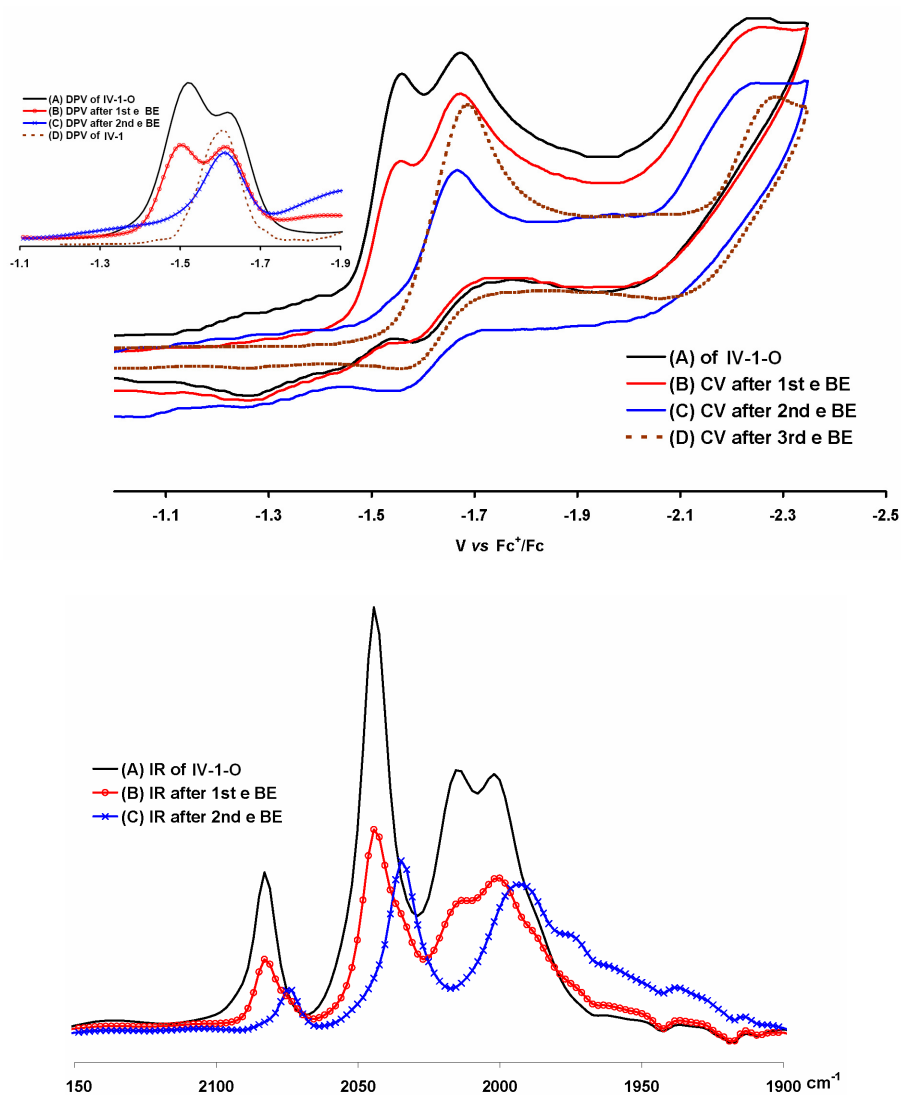


**Figure IV. 10** CV (top), DPV (top, inset) and IR measurements (bottom) of deoxygenation studies of **IV-1-O** via bulk electrolysis.

## Conclusions and comments

**Oxygenates and deoxygenation.** The series of diiron complexes with S-oxygenated bridging ligands demonstrates good stability and physical properties similar to the parent dithiolates that have served to provide insight into the unique diiron subsite of [FeFe]-H<sub>2</sub>ase. Electronic modulation of ( $\mu$ -pdt)[Fe(CO)<sub>3</sub>]<sub>2</sub> via CO/L exchange influences the O-atom uptake from m-CPBA of the parent diiron dithiolates. The less electron rich complexes allowed isolation of the kinetically controlled S-oxygenate products. The more electron rich complexes led to decomposition, presumably from the thermodynamic (DFT predicted) Fe-based oxygenation. As Fe<sup>II</sup> complexes have weak Fe-CO bonds, the decomposition is to be expected. The isolation of monoiron(II) complex **IV-6** is evidence of such Fe-based reactivity, however whether inner sphere or outer sphere oxidation is not known.

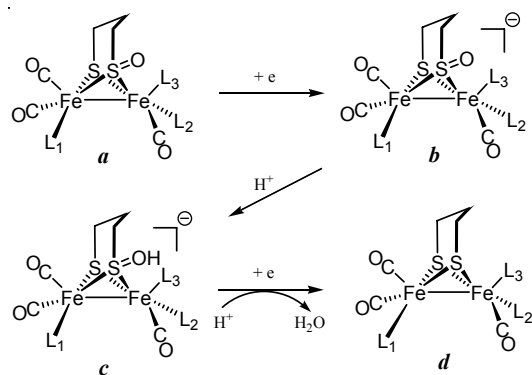
Sulfur oxygenation presents an additional way to influence the fundamental properties of the versatile ( $\mu$ -SRS)[Fe(CO)<sub>3</sub>]<sub>2</sub> complex. Sensitivity to CO substitution,<sup>163, 197, 225</sup> redox levels,<sup>188</sup> the nature of R,<sup>204, 226</sup> S/Se or P exchange<sup>227-229</sup> is now augmented by sulfur oxygenation. While still a good bidentate bridging ligand, the sulfenato moiety is a poorer electron donor, reducing electron density at iron and resulting in slower rates of ligand substitution and in greater barriers to intramolecular CO site exchange.

Reductive deoxygenation was observed both by electrochemical and bulk chemical reduction. In both cases water served as an optimal proton source presumably following the mechanism, described in Scheme VIII. 2 as a proton-coupled electron transfer,



PCET, process. The sequence proposes an initial one electron reduction of **a**, the neutral sulfur-oxygenated species to form anion **b** via an electron transfer (ET) process. The first step cannot be protonation at O of S=O because protonation should lead to changes in  $\nu(\text{CO})$  values, which are not observed in the presence of  $\text{H}_2\text{O}$ ,  $\text{CH}_3\text{COOH}$  or  $\text{CF}_3\text{COOH}$  as proton sources. The ET step is followed by or concurrent with a proton transfer (PT) process to form species **c** of Scheme IV. 6 since the second electron reduction is not accessible by the reducing ability of  $\text{Cp}^*\text{Fe}$  in the presence of  $\text{H}_2\text{O}$  or at the reduction potential applied in the bulk electrolysis. Subsequently, the second ET and the second PT will take place to give the deoxygenated product **d**. More likely, the second ET will occur first because the second PT is relatively difficult while the first PT should make the second ET favorable. The nature of the deoxygenation of the  $\text{Fe}^{\text{II}}\text{Fe}^{\text{II}}$  complex **IV-5-O** should follow the same mechanism as for the  $\text{Fe}^{\text{I}}\text{Fe}^{\text{I}}$  S-oxygenated complexes. A definite conclusion to be taken from the deoxygenation studies is as follows: *sulfur deoxygenation is a 2-electron process.*

**Scheme IV. 6**



**CHAPTER V**

**THE INFLUENCE OF SULF-OXYGENATION ON CO/L  
SUBSTITUTION AND Fe(CO)<sub>3</sub> ROTATION IN THIOLATE-  
BRIDGED DIIRON COMPLEXES\***

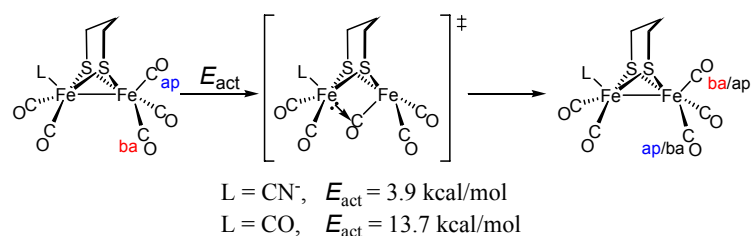
**Introduction**

Synthetic analogues of the dithiolate bridged diiron unit developed by nature to be a critical component of the active site of the all iron hydrogenase, [FeFe]-H<sub>2</sub>ase, provide opportunity to explore the influences of specific changes on the fundamental properties of dinuclear complexes in general. One such property in ( $\mu$ -pdt)[Fe(CO)<sub>3</sub>]<sub>2</sub>, a popular starting point for biomimetics, is the intramolecular CO<sub>ap</sub>/CO<sub>ba</sub> site exchange that occurs on individual iron centers, Scheme V. 1.<sup>186, 230</sup> The barrier to this site exchange is a transition state whose computationally derived structure is an edge-bridged square pyramid/inverted square pyramid that mimics the "rotated" geometry of the active site.<sup>230, 231</sup> Thus, as compared to the all-CO precursor complex, ( $\mu$ -pdt)[Fe(CO)<sub>3</sub>]<sub>2</sub>, the effect of CN<sup>-</sup>/CO replacement was to lower the barrier to Fe(CO)<sub>3</sub> rotation in ( $\mu$ -pdt)[Fe(CO)<sub>3</sub>][Fe(CO)<sub>2</sub>CN]<sup>-</sup> through stabilization of the transition state via formation of a semi-bridging carbonyl, Scheme V. 1.<sup>186, 230</sup>

---

\*Reprinted with permission from a manuscript. Li, B.; Liu, T.; Singleton, M. L.; Darensbourg, M. Y. Influence of Sulf-Oxygenation on CO/L Substitution and Fe(CO)<sub>3</sub> Rotation in Thiolate-Bridged Diiron Complexes. *Inorg. Chem.* **2009**, *48* (17), 8393-8403, Copyright [2009] by the American Chemical Society.

**Scheme V. 1** Intramolecular CO-Site Exchange



Earlier we concluded that rates of CO/CN<sup>-</sup> ligand substitution processes correlate with fluxionality in the Fe(CO)<sub>3</sub> rotors, i.e., the intramolecular site exchange described above.<sup>232</sup> The reaction of (μ-pdt)[Fe(CO)<sub>3</sub>]<sub>2</sub> with a cyanide salt, even with a deficiency of CN<sup>-</sup>, resulted in the dicyano complex (μ-pdt)[Fe(CO)<sub>2</sub>(CN)]<sub>2</sub><sup>2-</sup>.<sup>232</sup> In order to isolate the mono-cyanide, (μ-pdt)[Fe(CO)<sub>3</sub>][Fe(CO)<sub>2</sub>CN]<sup>-</sup>, the Na<sup>+</sup>[N(SiMe<sub>3</sub>)<sub>2</sub>]<sup>-</sup> reagent was used to convert a single CO into CN<sup>-</sup> through nucleophilic attack and elimination of O(SiMe<sub>3</sub>)<sub>2</sub>.<sup>232</sup> In this way, kinetic studies of sequential CO/CN<sup>-</sup> substitution processes were possible. Each reaction was found to follow a second order rate expression, with  $k_2' > k_2$ ,

Scheme V. 2. As the second nucleophilic attack of CN<sup>-</sup> was expected to be depressed by the anionic charge on (μ-pdt)[Fe(CO)<sub>3</sub>][Fe(CO)<sub>2</sub>CN]<sup>-</sup>, we proposed that the activation barrier must be apportioned into two contributory factors, defined in Figure V. 1.<sup>186</sup> The lower barrier of the second CO/CN<sup>-</sup> substitution in

Scheme V. 2 resulted from the smaller contribution to the activation barrier from the rotation of the unsubstituted Fe(CO)<sub>3</sub> unit which overwhelmed the increase in barrier due to nucleophilic attack.

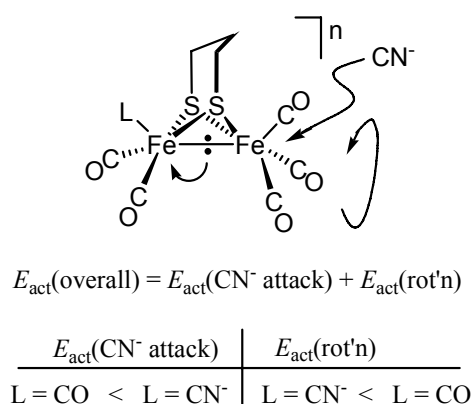
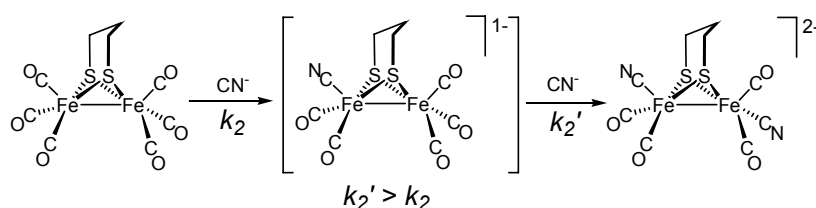


**Figure V. 1** Representation of events along reaction coordinate for cyanide nucleophilic attack on diiron carbonyl,  $L = \text{CO}$  or  $\text{CN}^-$ ,  $n = 0$  or  $-1$ , and the equation describing contributing factors to the overall activation energy barrier.

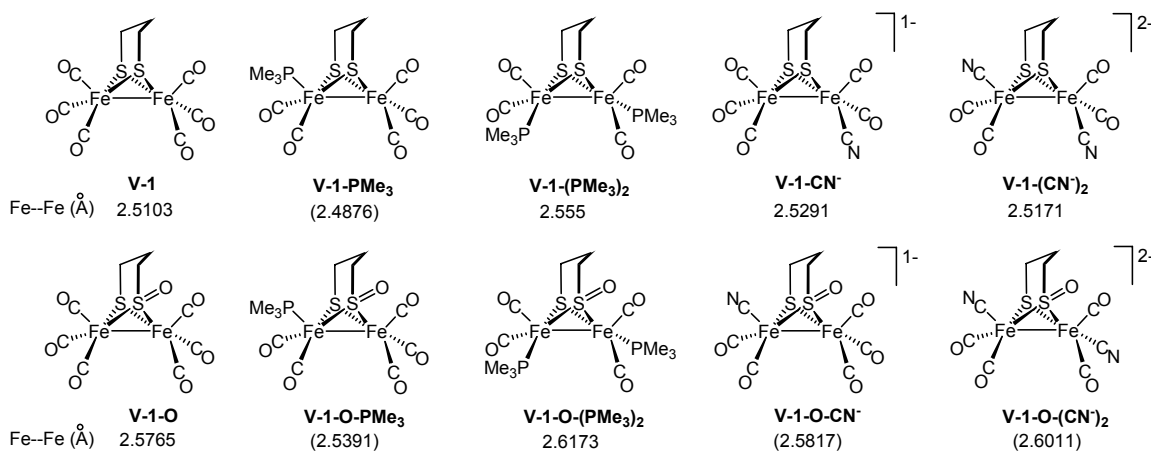
**Scheme V. 2** Sequential  $\text{CN}^-/\text{CO}$  Substitution.



Myriad derivatives of the  $(\mu\text{-pdt})[\text{Fe}(\text{CO})_3]_2$  complex have been prepared via CO/L substitution, replacement of the bridgehead C in the pdt by NR, O, S, Se,<sup>233-238</sup> steric modification by introducing substituents on the bridgehead C,<sup>221</sup> and replacement of the S donors by Se.<sup>239</sup> All such adaptations result in subtle differences in reactivity or redox properties. During recent studies of the S-oxygenate,  $(\mu\text{-pst})[\text{Fe}(\text{CO})_3]_2$  complex, we noted that while phosphines did not extract oxygen from the sulfenato sulfur, they displaced CO ligands at elevated temperatures as compared to the  $(\mu\text{-pdt})[\text{Fe}(\text{CO})_3]_2$

complex.<sup>220</sup> Thus the following kinetic studies of CO substitution by phosphines as well as cyanide were pursued in attempts to further test the mechanistic proposals above, as well as to establish the effect of the sulfenato group on the fluxionality and reactivity of the diiron complex. The complexes in this study and their abbreviations to be used hereafter are shown in Chart V. 1. Experimental values of Fe-Fe bond distance are given where available;<sup>240-242</sup> those in parentheses are DFT calculated values.<sup>13</sup> These kinetic studies were collaborated with Ben Li, an exchange student from Tianjin University, China. Mr. Li did major contribution to this work.

**Chart V. 1\***



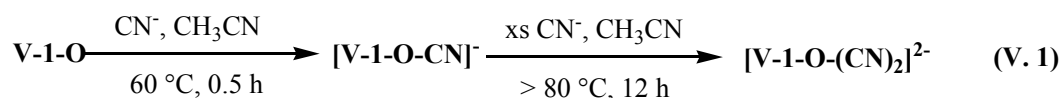
\* Experimental or (DFT Calculated) Fe-Fe distances underneath each structure.

## Results and discussion

### Properties of complexes IV-1, IV-1-O, and CN<sup>-</sup>/PMe<sub>3</sub> substituted derivatives.

With the exception of IV-1-O-CN<sup>-</sup> and IV-1-O-(CN)<sub>2</sub><sup>2-</sup>, all complexes in this study, Chart 1, are from literature preparations. The sulfenato-monocyanide complex was

readily obtained (30 min to completion) from CO/CN<sup>-</sup> (as its Et<sub>4</sub>N<sup>+</sup> salt) exchange into **IV-1-O** at 60°C, while excess CN<sup>-</sup> at CH<sub>3</sub>CN reflux overnight was required to obtain **IV-1-O-(CN)<sub>2</sub><sup>2-</sup>**, eq V. 1. Note that these conditions are much harsher than those used for similar CN<sup>-</sup> incorporation into complex **IV-1** where only the dicyanide **IV-1-(CN)<sub>2</sub><sup>2-</sup>** was observed even at sub-stoichiometric amounts of CN<sup>-</sup> and at -8°C.<sup>232</sup> Our efforts to obtain the extremely air-sensitive **1-O**-cyano complexes in pure crystalline form were unsuccessful.



The structures of reactants and products in this study are largely known, Chart V. 1. In the case of the calculated structures shown in Chart V. 1, differences in apical/basal isomers may be as large as 4 kcal/mol, while isomeric forms derived from the chair/boat configuration possibilities of the pseudo-cyclohexane FeS<sub>2</sub>C<sub>3</sub> ring are on the order of 2 kcal/mol.<sup>220</sup>

Table V. 1 contains the  $\nu(\text{CO})$  and  $\nu(\text{CN})$  infrared spectral data for the complexes of Chart 1. Notably, complexes based on complex **IV-1** vs. **IV-1-O** of analogous composition display similar IR patterns, however  $\nu(\text{CO})$  values of the ( $\mu$ -pst)[Fe(CO)<sub>2</sub>L]<sub>2</sub> thiolate/sulfenate bridged compounds shift to higher energies by 10 to 20 cm<sup>-1</sup> as compared to the dithiolate ( $\mu$ -pdt)[Fe(CO)<sub>2</sub>L]<sub>2</sub> derivatives. This reflects the

poorer electron donating ability of the sulfenato sulfur and a decrease of electron density at the [FeFe] unit as compared to the dithiolate bridge ligand in the  $\mu$ -pdt complexes.

**Table V. 1** Infrared spectroscopic ( $\nu(\text{CO})$  and  $\nu(\text{CN})$ ) data for  $(\mu\text{-pdt})[\text{Fe}(\text{CO})_2(\text{L})]_2$  and  $(\mu\text{-pst})[\text{Fe}(\text{CO})_2(\text{L})]_2$  derivatives (reported in toluene solution unless otherwise noted).

Compound	$\nu(\text{CN}), \nu(\text{CO}) (\text{cm}^{-1})$
$(\mu\text{-pdt})[\text{Fe}(\text{CO})_3]_2$ ( <b>IV-1</b> )	2072(m), 2032(s), 2000(m), 1987(m)
$(\mu\text{-pst})[\text{Fe}(\text{CO})_3]_2$ ( <b>IV-1-O</b> )	2081(m), 2042(s), 2017(m), 1995(m)
$(\mu\text{-pdt})[\text{Fe}(\text{CO})_3][\text{Fe}(\text{CO})_2\text{PMe}_3]$ ( <b>IV-1-PMe<sub>3</sub></b> )	2036(m), 1981(s), 1960(m), 1923(m)
$(\mu\text{-pst})[\text{Fe}(\text{CO})_3][\text{Fe}(\text{CO})_2\text{PMe}_3]^b$ ( <b>IV-1-O-PMe<sub>3</sub></b> )	2049(m), 1992(s), 1973(m), 1934(m)
$(\mu\text{-pdt})[\text{Fe}(\text{CO})_2\text{PMe}_3]_2$ ( <b>IV-1-(PMe<sub>3</sub>)<sub>2</sub></b> )	1982(w), 1944(s), 1902(s)
$(\mu\text{-pst})[\text{Fe}(\text{CO})_2\text{PMe}_3]_2$ ( <b>IV-1-O-(PMe<sub>3</sub>)<sub>2</sub></b> )	1983(w), 1956(s), 1919(m), 1906(m)
$(\mu\text{-pdt})[\text{Fe}(\text{CO})_3][\text{Fe}(\text{CO})_2\text{CN}]^a$ ( <b>IV-1-CN<sup>-</sup></b> )	2094(w); 2029(s), 1974(s), 1955(s), 1941(vs), 1917(s br)
$(\mu\text{-pst})[\text{Fe}(\text{CO})_3][\text{Fe}(\text{CO})_2\text{CN}]^b$ ( <b>IV-1-O-CN<sup>-</sup></b> )	2099(w); 2042(m), 1993(s), 1975(s), 1958(m), 1934(m)
$(\mu\text{-pdt})[\text{Fe}(\text{CO})_2\text{CN}]_2^b$ ( <b>IV-1-(CN)<sub>2</sub><sup>2-</sup></b> )	2076 (w), 2032 (w); 1964 (s), 1923 (s), 1883 (s)
$(\mu\text{-pst})[\text{Fe}(\text{CO})_2\text{CN}]_2^b$ ( <b>IV-1-O-(CN)<sub>2</sub><sup>2-</sup></b> )	2075(m); 1979(s), 1939(s), 1903(s)

<sup>a</sup> Spectra recorded in THF; <sup>b</sup> Spectra recorded in acetonitrile; Et<sub>4</sub>N<sup>+</sup> counter ion.

**Kinetic studies of PMe<sub>3</sub>/CO substitution in  $(\mu\text{-pdt})[\text{Fe}(\text{CO})_3]_2$  (**IV-1**).** Reactions of complex **IV-1** with PMe<sub>3</sub> to yield **IV-1-PMe<sub>3</sub>**, eq V. 2, were carried out in toluene solution, under pseudo-first-order conditions of 20-fold and greater excesses of PMe<sub>3</sub>. Figure V. 2 (a) presents stacked plots of



$$\text{Rate} = k_{\text{obs}} [\text{IV-1}] = k_2 [\text{IV-1}] [\text{PMe}_3] \quad (\text{V. 3})$$

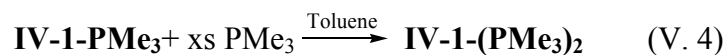
infrared spectra in the 2000  $\text{cm}^{-1}$  region which illustrate the rate data obtained for this reaction; in the example, spectra were recorded at 2 min intervals. Kinetic parameters for the reactions of complex **IV-1** with  $\text{PMe}_3$  were determined by monitoring the disappearance of the  $\nu(\text{CO})$  band at 2073  $\text{cm}^{-1}$  with time. The disappearance of the  $\nu(\text{CO})$  band at 2000  $\text{cm}^{-1}$  yielded similar results. The data measured at 22 °C were used to determine the rate expression; plots of  $\ln(A_0/A_t)$  vs time showed good linearity over 5 half-lives, Figure V. 3 (a). The derived values of  $k_{\text{obs}}$  at various  $\text{PMe}_3$  concentrations are given in Table V. 2, entries 1-4. Each  $k_{\text{obs}}$  was obtained from a single kinetic run, with ~30 spectral accumulations per run. The plot of  $k_{\text{obs}}$  vs  $[\text{PMe}_3]$  shows good linearity, Figure V. 3 (b), and its zero intercept indicates that the reaction described in eq 2 follows a second-order rate expression, eq V. 3.

**Table V. 2** Rate data for determination of rate expression for the reaction of  $\text{PMe}_3$  with complex **IV-1** measured at 22 °C and with **IV-1-PMe<sub>3</sub>** measured at 50 °C in toluene solution.

Entry	Rxn	$[\text{PMe}_3]$ , M	$10^4 k_{\text{obs}}$ , $\text{sec}^{-1}$
1	<b>IV-1</b> $\rightarrow$ <b>IV-1-PMe<sub>3</sub></b> <sup>a</sup>	0.10	1.47
2	<b>IV-1</b> $\rightarrow$ <b>IV-1-PMe<sub>3</sub></b>	0.15	2.15
3	<b>IV-1</b> $\rightarrow$ <b>IV-1-PMe<sub>3</sub></b>	0.20	2.85
4	<b>IV-1</b> $\rightarrow$ <b>IV-1-PMe<sub>3</sub></b>	0.30	4.55
$\text{av } k_2 = 14.6 (\pm 0.6) \times 10^{-4} \text{ M}^{-1} \text{ sec}^{-1}$			
5	<b>IV-1-PMe<sub>3</sub></b> $\rightarrow$ <b>IV-1-(PMe<sub>3</sub>)<sub>2</sub></b> <sup>a</sup>	0.10	1.28
6	<b>IV-1-PMe<sub>3</sub></b> $\rightarrow$ <b>IV-1-(PMe<sub>3</sub>)<sub>2</sub></b>	0.15	1.97
7	<b>IV-1-PMe<sub>3</sub></b> $\rightarrow$ <b>IV-1-(PMe<sub>3</sub>)<sub>2</sub></b>	0.20	2.62
8	<b>IV-1-PMe<sub>3</sub></b> $\rightarrow$ <b>IV-1-(PMe<sub>3</sub>)<sub>2</sub></b>	0.30	4.00
$\text{av } k_2' = 13.1 (\pm 0.3) \times 10^{-4} \text{ M}^{-1} \text{ sec}^{-1}$			

<sup>a</sup>  $[\text{Fe}_2] = 5.0 \times 10^{-3} \text{ M}$  with 20 – 60-fold excess  $\text{PMe}_3$ .





$$\text{Rate} = k_{obs} [\text{IV-1-PMe}_3] = k_2' [\text{IV-1-PMe}_3] [\text{PMe}_3] \quad (\text{V. 5})$$

Under similar conditions, sample stacked plots for the reaction of **V-I-PMe<sub>3</sub>** with **PMe<sub>3</sub>** in toluene solution at 50°C, eq V. 4, are shown in Figure V. 2 (b). The disappearance of the band at 2036 cm<sup>-1</sup> showed linearity in the ln(A<sub>0</sub>/A<sub>t</sub>) vs time plot, as well as a first-order dependence on [PMe<sub>3</sub>], eq V. 5. The rate constants *k*<sub>2</sub> derived from these data, entries 5-8 in Table V. 2, are smaller than those obtained from the first-step, (μ-pdt)[Fe(CO)<sub>3</sub>]<sub>2</sub>/PMe<sub>3</sub> substitution reaction measured at 22°C, entries 1-4.

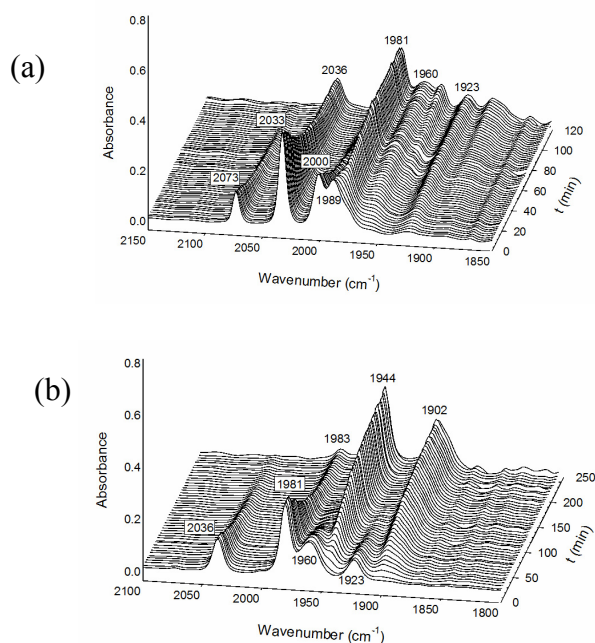


**Figure V. 2** Infrared spectra, in the 1800 – 2150 cm<sup>-1</sup> region, as CO / PMe<sub>3</sub> exchange takes place to produce (a) **IV-1-PMe<sub>3</sub>** from **IV-1**; and (b) to produce **IV-1-(PMe<sub>3</sub>)<sub>2</sub>** from **IV-1-PMe<sub>3</sub>**.

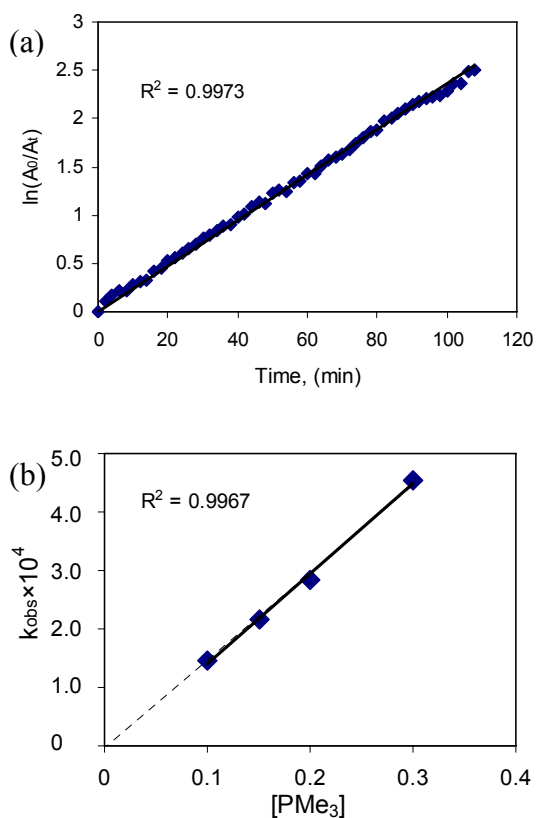
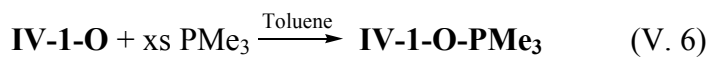


**Figure V. 3** (a) Example of plot of  $\ln(A_0/A_t)$  vs time over five half-lives, Entry 4, Table V. 2. (b) Plot of  $k_{\text{obs}}$  vs  $[\text{PMe}_3]$  for the formation of complex **IV-1-PMe<sub>3</sub>** from complex **IV-1** measured at 22°C.

**Kinetic studies of  $\text{PMe}_3/\text{CO}$  exchange into  $(\mu\text{-pst})[\text{Fe}(\text{CO})_3]_2$  (**IV-1-O**).** Reactions of  $(\mu\text{-pst})[\text{Fe}(\text{CO})_3]_2$  (**1-O**) with  $\text{PMe}_3$  to yield  $(\mu\text{-pst})[\text{Fe}(\text{CO})_3][\text{Fe}(\text{CO})_2\text{PMe}_3]$  (**IV-1-O-PMe<sub>3</sub>**), eq V. 6, were carried out in toluene solution at 80, 90, 95 and 100 °C, under pseudo-first-order conditions of 20-fold and greater excesses of  $\text{PMe}_3$ . Kinetic parameters for the reactions of **IV-1-O** with  $\text{PMe}_3$  were determined by monitoring the disappearance of the  $\nu(\text{CO})$  band at 2081  $\text{cm}^{-1}$  with time, augmented by the disappearance of the  $\nu(\text{CO})$  band at 2017  $\text{cm}^{-1}$ , Figure V. 4. The plots of  $\ln(A_0/A_t)$  vs

time showed good linearity; Figure V. 5 (a). The derived values of  $k_{\text{obs}}$  at various  $\text{PMe}_3$  concentrations and reaction temperatures, as determined by infrared spectroscopy, are given in Table V. 3, entries 1-12. Each  $k_{\text{obs}}$  was obtained from a single kinetic run, with at least  $\sim 12$  spectral accumulations per run. The plot of  $k_{\text{obs}}$  vs  $[\text{PMe}_3]$ , Figure V. 5 (b) ( $90^\circ\text{C}$ ), shows linearity, however a nonzero intercept indicates the reaction does not follow a strict second-order rate expression, but rather both associative (A) and dissociative (D) substitution processes are assumed to be involved at the higher reaction temperatures, eq V. 7. Hence, the plot of  $k_{\text{obs}}$  vs  $[\text{PMe}_3]$ , Figure V. 5 (b) and eq V. 8, yields the dissociative substitution rate constant,  $k_1 = 1.92 \times 10^{-5} \text{ sec}^{-1}$ , derived from the intercept and the associative substitution rate constant,  $k_2 = 1.58 \times 10^{-4} \text{ M}^{-1}\text{sec}^{-1}$ , is determined from the slope. It should be noted that the IR traces appeared to represent a quantitative reaction and reproducibility at  $95^\circ\text{C}$  is on the order of 95%. However some decomposition cannot be ruled out.



$$\text{Rate} = k_1[\text{IV-1-O}] + k_2[\text{IV-1-O}][\text{PMe}_3] \quad (\text{V. 7})$$

$$\text{Rate} = k_{\text{obs}}[\text{IV-1-O}]; \quad k_{\text{obs}} = k_1 + k_2[\text{PMe}_3] \quad (\text{V. 8})$$

The reaction of  $\text{IV-1-O-PMe}_3$  with  $\text{PMe}_3$  to yield  $\text{IV-1-O-(PMe}_3)_2$  is extremely slow under similar conditions as above, and kinetic measurements were not conducted.

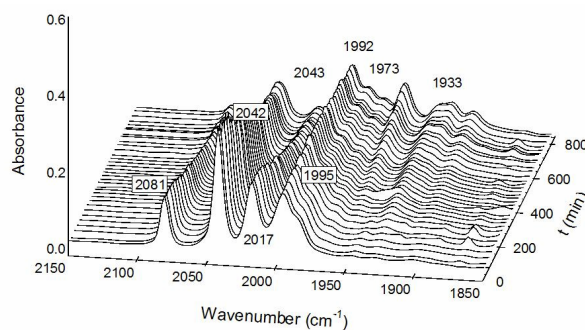


**Figure V. 4** Infrared spectra, in the 1800 – 2150  $\text{cm}^{-1}$  region, as CO /  $\text{PMe}_3$  exchange takes place to produce complex **IV-1-O- $\text{PMe}_3$**  from **IV-1-O**.

**Table V. 3** Rate data for the reaction of  $\text{PMe}_3$  with  $(\mu\text{-pst})[\text{Fe}(\text{CO})_3]_2$  (**IV-1-O**) as a function of temperature in Toluene.

Entry	Temp., $^{\circ}\text{C}$	$[\text{PMe}_3]$ , M	$10^4 k_{\text{obs}}$ , $\text{sec}^{-1}$
1	80	0.20	0.28
2	80	0.30	0.33
3	80	0.40	0.45
4	90	0.20	0.50
5	90	0.30	0.68
6	90	0.40	0.82
7	95	0.20	0.80
8	95	0.30	0.90
9	95	0.40	1.18
10	100	0.20	1.23
11	100	0.30	1.58
12	100	0.40	1.73

$[\text{Fe}_2] = 5.0 \times 10^{-3}$  M with 40 — 80-fold excess  $\text{PMe}_3$ .

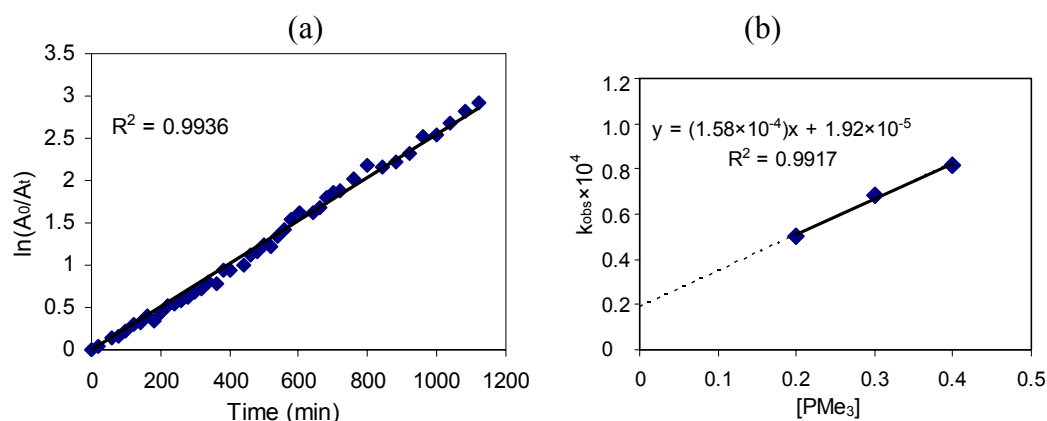


**Figure V. 5** (a) Example of plot of  $\ln(A_0/A_t)$  vs. time over four half-lives, Entry 7, Table V. 3 (b) Plots of  $k_{\text{obs}}$  vs.  $[\text{PMe}_3]$  for the formation of **IV-1-O-PMe<sub>3</sub>** from **IV-1-O** measured at 90°C.

**Temperature dependence of reactions of complexes IV-1, IV-1-PMe<sub>3</sub> and IV-1-O with PMe<sub>3</sub>.** The temperature-dependence of rate constants for the formation of complex **IV-1-PMe<sub>3</sub>** starting from complex **IV-1** and the formation of complex **IV-1-(PMe<sub>3</sub>)<sub>2</sub>** starting from complex **IV-1-PMe<sub>3</sub>** are given in Table V. 4. Table V. 4 lists values for the enthalpy and entropy of activation derived from Eyring plots, Figure V. 6, as well as  $E_{\text{act}}$  derived from Arrhenius plots. Consistent with the second-order rate expressions for the respective associative or  $I_a$  mechanisms,  $\Delta H^\ddagger$  values are small to moderate and  $\Delta S^\ddagger$  values are large and negative. The similar values of  $\Delta S^\ddagger$  and increased values of  $\Delta H^\ddagger$  and  $E_{\text{act}}$  of the reactions described by eqs 2 and 4, suggest the addition of the second  $\text{PMe}_3$  is the overall rate-limiting step in the production of complex **IV-1-(PMe<sub>3</sub>)<sub>2</sub>** starting from **IV-1**.

The temperature dependence of rate constants for both the D and A pathways for formation of complex **IV-1-O-PMe<sub>3</sub>** from **IV-1-O**, are also given in Table V. 4 and presented graphically as Eyring and Arrhenius plots, Figure V. 7; the calculated values for the enthalpy and entropy of activation as well as the  $E_{\text{act}}$  derived from Arrhenius plots are listed. The small values of  $\Delta H^\ddagger$  and large negative values for  $\Delta S^\ddagger$  are consistent with the associative pathway. For the dissociative pathway,  $\Delta H^\ddagger$  and  $E_{\text{act}}$  values of ca. 100 kJ/mol are as expected for dissociation of the CO ligand in the rate-determining step.

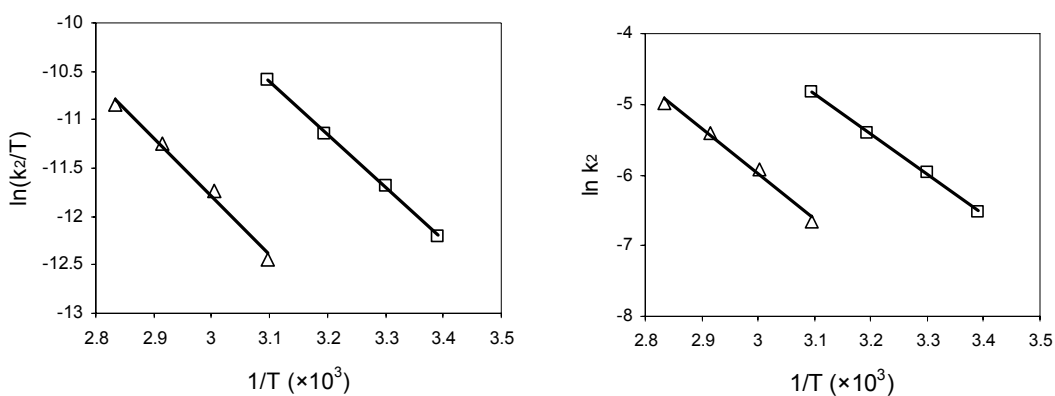


**Figure V. 6** Left: Eyring plots for the formation of complex **IV-1-PMe<sub>3</sub>** from complex **IV-1** (□) and for the formation of **IV-1-(PMe<sub>3</sub>)<sub>2</sub>** from **IV-1-PMe<sub>3</sub>** (Δ). Right: Arrhenius plot for the formation of **IV-1-PMe<sub>3</sub>** from  $(\mu\text{-pdt})[\text{Fe}(\text{CO})_3]_2$  (1) (□) and for the formation of **IV-1-(PMe<sub>3</sub>)<sub>2</sub>** from **IV-1-PMe<sub>3</sub>** (Δ).

**Table V. 4** Temperature dependence of reaction of  $\text{PMe}_3$  with  $(\mu\text{-pdt})[\text{Fe}(\text{CO})_3]_2$  (**IV-1**),  $(\mu\text{-pdt})[\text{Fe}(\text{CO})_3][\text{Fe}(\text{CO})_2\text{PMe}_3]$  (**IV-1-PMe<sub>3</sub>**) and  $(\mu\text{-pst})[\text{Fe}(\text{CO})_3]_2$  (**IV-1-O**).

Rxn path	T, °C	<i>k</i>	activation parameters <sup>c</sup>
<b>IV-1</b> → <b>IV-1-PMe<sub>3</sub></b> <sup>a</sup>		$10^3 k_2, \text{M}^{-1}\text{s}^{-1}$	
	22	1.47	$E_a = 48 \text{ kJ/mol}$
	30	2.55	$\Delta H^\ddagger = 45 (\pm 1) \text{ kJ/mol}$
	40	4.50	$\Delta S^\ddagger = -145 (\pm 3) \text{ J/mol K}$
	50	8.08	
<b>IV-1-PMe<sub>3</sub></b> → <b>IV-1-(PMe<sub>3</sub>)<sub>2</sub></b> <sup>a</sup>		$10^3 k_2', \text{M}^{-1}\text{s}^{-1}$	
	50	1.28	$E_a = 53 \text{ kJ/mol}$
	60	2.67	$\Delta H^\ddagger = 50 (\pm 4) \text{ kJ/mol}$
	70	4.48	$\Delta S^\ddagger = -146 (\pm 11) \text{ J/mol K}$
	80	6.87	
<b>IV-1-O</b> → <b>IV-1-O-PMe<sub>3</sub></b> <sup>b</sup> (A path)		$10^4 k_2, \text{M}^{-1}\text{s}^{-1}$	
	80	0.83	$E_a = 60 \text{ kJ/mol}$
	90	1.58	$\Delta H^\ddagger = 56 (\pm 3) \text{ kJ/mol}$
	95	1.92	$\Delta S^\ddagger = -163 (\pm 9) \text{ J/mol K}$
	100	2.50	
<b>IV-1-O</b> → <b>IV-1-O-PMe<sub>3</sub></b> <sup>b</sup> (D path)		$10^5 k_1, \text{s}^{-1}$	
	80	1.06	$E_a = 107 \text{ kJ/mol}$
	90	1.92	$\Delta H^\ddagger = 104 (\pm 18) \text{ kJ/mol}$
	95	3.86	$\Delta S^\ddagger = -50 (\pm 49) \text{ J/mol K}$
	100	7.67	

<sup>a</sup>  $[\text{Fe}_2] = 5.0 \times 10^{-3} \text{ M}$ ;  $[\text{PMe}_3] = 0.1 \text{ M}$ .

<sup>b</sup>  $[\text{Fe}_2] = 5.0 \times 10^{-3} \text{ M}$ ;  $[\text{PMe}_3] = 0.2 - 0.4 \text{ M}$ .

<sup>c</sup> Errors in activation parameters reported at 95% confidence level.

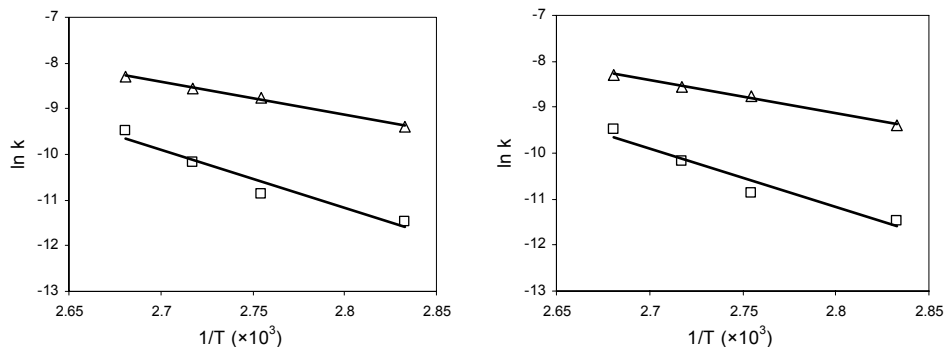
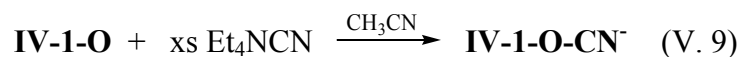


**Figure V. 7** Eyring plot (left) and Arrhenius plot (right) for the formation of  $(\mu\text{-pst})[\text{Fe}(\text{CO})_3][\text{Fe}(\text{CO})_2\text{PMe}_3]$  (**1-O-PMe<sub>3</sub>**) from  $(\mu\text{-pst})[\text{Fe}(\text{CO})_3]_2$  (**1-O**) follow dissociative path ( $\square$ ) and associative path ( $\Delta$ ).

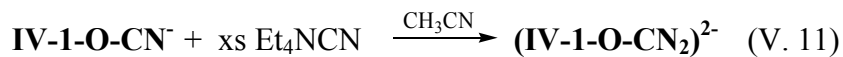
Kinetic Studies of  $\text{CN}^-/\text{CO}$  Exchange into  $(\mu\text{-pst})[\text{Fe}(\text{CO})_3]_2$  (**IV-1-O**). The reaction of complex **1-O** with  $\text{Et}_4\text{N}^+\text{CN}^-$  carried out in  $\text{CH}_3\text{CN}$  solution at  $0^\circ\text{C}$  under pseudo-first-order conditions of a 20-fold excess of  $\text{Et}_4\text{N}^+\text{CN}^-$  was found to produce only the mono-substituted  $[\text{Et}_4\text{N}]\{(\mu\text{-pst})[\text{Fe}(\text{CO})_3][\text{Fe}(\text{CO})_2\text{CN}]\}$  (**IV-1-O-CN<sup>-</sup>**), eq V. 9. The rapid disappearance of the band at  $2038\text{ cm}^{-1}$ , Figure V. 8 (a), allowed only 14 data points for the determination of  $\ln \text{Abs}$  vs  $T$  and the  $k_2$  value, given as entry 1 in Table V. 5. The large  $k_2$  values indicated the ease of attack of complex **IV-1-O** by  $\text{CN}^-$ . A second study performed at a 10-fold excess of  $\text{CN}^-$  yielded a  $k_2$  value roughly 1/2 that of the 20-fold excess; hence, we suggest the rate expression of eq V. 10 holds as well for this reaction.



$$\text{Rate} = k_{\text{obs}} [\text{IV-1-O}] = k_2 [\text{IV-1-O}][\text{CN}^-] \quad (\text{V. 10})$$



The mono-cyanide-substituted complex **1**  $\text{V--O--CN}^-$ , produced *in situ* at low temperature, was used in subsequent kinetic studies of the addition of the second  $\text{CN}^-$ , eq V. 11.



$$\text{Rate} = k_{\text{obs}}' [\text{IV-1-O-CN}] = k_2' [\text{IV-1-O-CN}^-][\text{CN}^-] \quad (\text{V. 12})$$

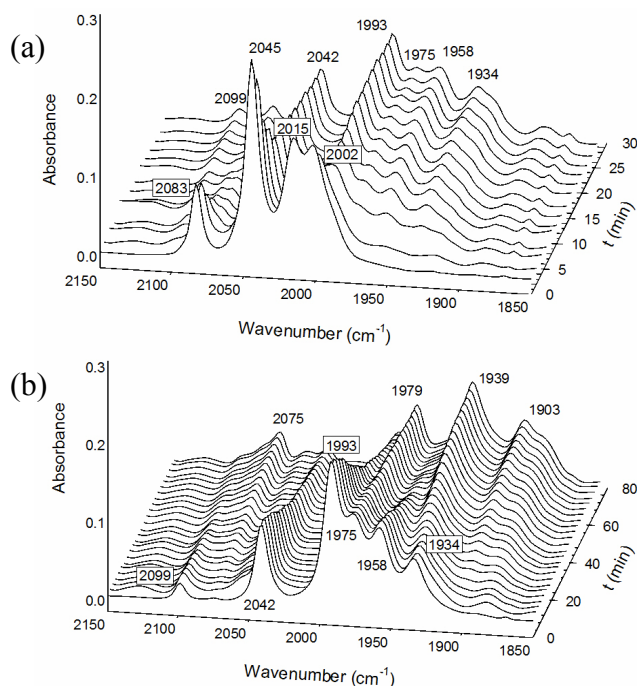


**Figure V. 8** Infrared spectra, in the 1850 – 2150  $\text{cm}^{-1}$  region, as CO /  $\text{CN}^-$  exchange takes place: (a) to produce  $\text{IV-1-O-CN}^-$  from  $\text{IV-1-O}$  at 0 °C in  $\text{CH}_3\text{CN}$ , and (b) to produce  $(\text{IV-1-O-CN}_2)^{2-}$  from  $\text{IV-1-O-CN}^-$  at 40 °C in  $\text{CH}_3\text{CN}$ .

Figure V. 8 (b) presents stacked plots of  $\nu(\text{CO})$  IR spectra for the reaction of **IV-1-O-CN<sup>-</sup>** with **CN<sup>-</sup>** taken at 3 min intervals. By monitoring the disappearance of the  $\nu(\text{CO})$  band at  $2042\text{ cm}^{-1}$  with time, the data measured at  $40^\circ\text{C}$  were used to determine the rate expression. Plots of  $\ln(A_0/A_t)$  vs time showed good linearity over 4 half-lives, Figure V. 9 (a). The derived values of  $k_{\text{obs}}$  at various  $\text{Et}_4\text{N}^+\text{CN}^-$  concentrations, entries 2-5 measured at  $40^\circ\text{C}$  in Table V.5, are much smaller than that obtained from the first-step  $(\mu\text{-pst})[\text{Fe}(\text{CO})_3]_2/\text{CN}^-$  reaction measured at  $0^\circ\text{C}$ . The plot of  $k_{\text{obs}}$  vs  $[\text{CN}^-]$  shows good linearity, Figure V. 8 (b), the zero intercept indicates the rate determining step for the overall reaction follows a second-order rate expression, eq V. 12.

**Table V. 5** Rate data for the reaction of  $\text{Et}_4\text{N}^+\text{CN}^-$  with complex **IV-1-O** measured at  $0^\circ\text{C}$  and with **IV-1-O-CN<sup>-</sup>** measured at  $40^\circ\text{C}$  in  $\text{CH}_3\text{CN}$  solution

entry	rxn	$[\text{CN}^-]$ , M	$10^4 k_{\text{obs}}$ , $\text{sec}^{-1}$
1	<b>IV-1-O</b> $\rightarrow$ <b>IV-1-O-CN<sup>-</sup></b> <sup>a</sup>	0.05	6.57
2	<b>IV-1-O</b> $\rightarrow$ <b>IV-1-O-CN<sup>-</sup></b> av $k_2 = 138.8 (\pm 7.4) \times 10^{-4} \text{ M}^{-1} \text{ sec}^{-1}$	0.10	14.6
3	<b>IV-1-O-CN<sup>-</sup></b> $\rightarrow$ <b>IV-1-O-</b> <b>(CN)<sub>2</sub><sup>2-</sup></b> <sup>b</sup>	0.10	0.83
4	<b>IV-1-O-CN<sup>-</sup></b> $\rightarrow$ <b>IV-1-O-</b> <b>(CN)<sub>2</sub><sup>2-</sup></b>	0.15	1.08
5	<b>IV-1-O-CN<sup>-</sup></b> $\rightarrow$ <b>IV-1-O-</b> <b>(CN)<sub>2</sub><sup>2-</sup></b>	0.20	1.62
6	<b>IV-1-O-CN<sup>-</sup></b> $\rightarrow$ <b>IV-1-O-</b> <b>(CN)<sub>2</sub><sup>2-</sup></b> av $k_2 = 7.94 (\pm 0.8) \times 10^{-4} \text{ M}^{-1} \text{ sec}^{-1}$	0.30	2.43

<sup>a</sup>  $[\text{Fe}_2] = 5.0 \times 10^{-3} \text{ M}$  with 10 – 20-fold excess **CN<sup>-</sup>**;  $0^\circ\text{C}$ .

<sup>b</sup>  $[\text{Fe}_2] = 5.0 \times 10^{-3} \text{ M}$  with 20 – 60-fold excess **CN<sup>-</sup>**;  $40^\circ\text{C}$ .

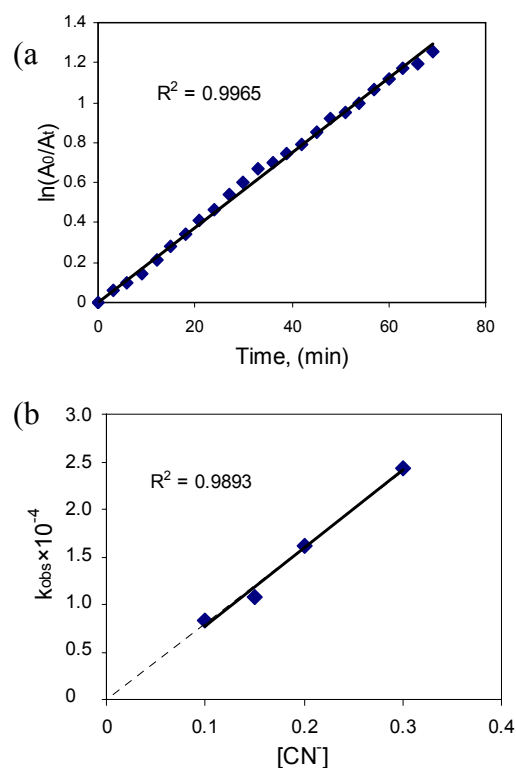


**Figure V. 9** (a) Example of plot of  $\ln(A_0/A_t)$  vs. time over three half-lives; (b) Plot of  $k_{\text{obs}}$  vs.  $[\text{CN}^-]$  for the formation of  $(\text{IV-1-O-CN}_2)^{2-}$  from  $\text{IV-1-O-CN}^-$  measured at  $40^\circ\text{C}$ .

#### Temperature dependence of reactions of complex $\text{IV-1-O-CN}^-$ with $\text{Et}_4\text{N}^+\text{CN}^-$ .

Table V. 6 lists values for the enthalpy and entropy of activation for the formation of complex  $(\text{IV-1-O-CN}_2)^{2-}$  starting from complex  $\text{IV-1-O-CN}^-$  derived from Eyring plots, as well as  $E_{\text{act}}$  derived from Arrhenius plots, Figure V. 10. As described above for the  $\text{PMe}_3$  associative reactivity,  $\Delta H^\ddagger$  values are small to moderate and  $\Delta S^\ddagger$  values are large and negative.

**Table V. 6** Temperature dependence of reaction of  $\text{Et}_4\text{N}^+\text{CN}^-$  with complex (**IV-1-O-CN**)

rxn	T, °C	$(10^3) k_2$ , $\text{M}^{-1}\text{s}^{-1}$	activation parameters <sup>b</sup>
<b>IV-1-O-CN</b> $\rightarrow$ <b>IV-1-O-(CN)<sub>2</sub><sup>2-</sup></b> <sup>a</sup>			
	40	0.83	$E_a = 61$ kJ/mol
	50	1.63	$\Delta H^\ddagger = 58 (\pm 2)$ kJ/mol
	60	3.12	$\Delta S^\ddagger = -119 (\pm 7)$ J/mol K
	70	6.55	

<sup>a</sup>  $[\text{Fe}_2] = 5.0 \times 10^{-3}$  M;  $[\text{CN}^-] = 0.1$  M.

<sup>b</sup> Errors in activation parameters reported at 95% confidence level.

The monitor of  $\text{CN}^-/\text{CO}$  substitution into complex  $(\mu\text{-pst})[\text{Fe}(\text{CO})_3]_2$  (**IV-1-O**) shows faster rates and lower  $E_{\text{act}}$  barriers to the first and second  $\text{CN}^-$  ligand additions as compared to the  $\text{PMe}_3$  exchange into complex **IV-1-O**, but is otherwise kinetically and mechanistically analogous. The formation of **IV-1-O-CN** was observed clearly to be an intermediate step for the overall ligand exchange reaction to produce **IV-1-O-(CN)<sub>2</sub><sup>2-</sup>**. The harsher reaction conditions and large activation parameters of  $\text{CN}^-/\text{CO}$  exchange into **IV-1-O-CN** indicate the second substitution to be rate-limiting, with the association of the  $\text{CN}^-$  and the diiron complex following a similar pathway as found for the  $\text{PMe}_3$  reactions. This relative ordering of the first and second step is different from the  $\text{CN}^-/\text{CO}$  exchange into complex **1**. Values of  $E_a$  (61 kJ/mol),  $\Delta H^\ddagger$  (58 kJ/mol) of the  $\text{CN}^-/\text{CO}$  exchange into **IV-1-O-CN** to form **IV-1-O-(CN)<sub>2</sub><sup>2-</sup>** are almost twice larger than the  $E_a$  (36 kJ/mol) and  $\Delta H^\ddagger$  (34 kJ/mol), of the  $\text{CN}^-/\text{CO}$  exchange into **IV-1-CN** to form **IV-1-(CN)<sub>2</sub><sup>2-</sup>**.<sup>232</sup> Thus the activation energy barrier for  $\text{CN}^-/\text{CO}$  exchange in **IV-1-O-CN** has been increased by the presence and effect of the sulfenato-oxygen. *As the*

electrophilicity of the iron centers in the **IV-1-O** derivatives should increase relative to **IV-1**, we look to the fluxionality of the diiron complex for explanation of this switch in reactivity.

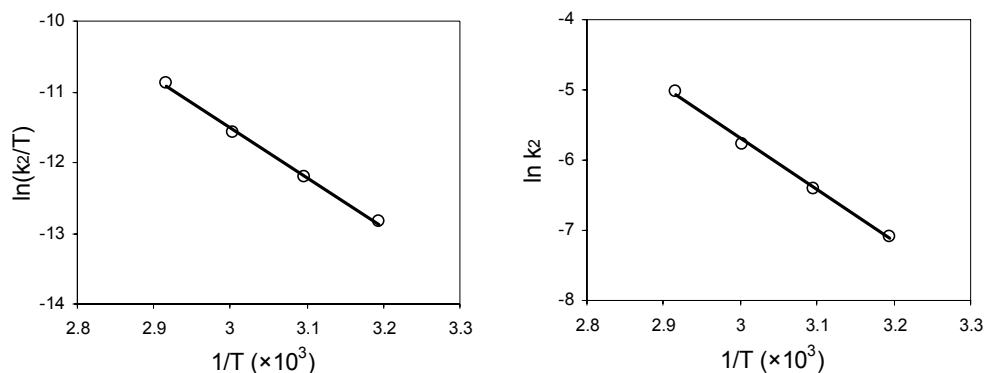


**Figure V. 10** Eyring plot (left) for the formation of complex **IV-1-O-(CN)<sub>2</sub><sup>2-</sup>** from complex **IV-1-O-CN<sup>-</sup>**. Arrhenius plot (right) for the formation of complex **IV-1-O-(CN)<sub>2</sub><sup>2-</sup>** from complex **IV-1-O-CN<sup>-</sup>**.

**Intramolecular CO site-exchange processes of complex IV-1-O-CN<sup>-</sup> via variable temperature <sup>13</sup>C NMR studies.** In a recent study we showed that the intramolecular exchange of CO groups in **IV-1-O** had a larger barrier for the Fe(CO)<sub>3</sub> rotor process than that found for complex **IV-1**.<sup>220</sup> Here we explore the effect of Fe-bound CN<sup>-</sup> on the CO-site exchange in **IV-1-O-CN<sup>-</sup>**. **Figure V. 11** displays <sup>13</sup>C NMR spectra in the CO region of the **IV-1-O-CN<sup>-</sup>** complex over the temperature range of -100 to 20 °C. At -100°C, three separate resonances are seen at 209.0, 210.8, and 211.6 ppm, which on warming are found to coalesce by -80°C, reforming into a single sharp resonance at -40 °C and above. This resonance is assigned to the carbons of the Fe(CO)<sub>3</sub> unit which are in rapid

intramolecular exchange at 20°C. In contrast, the two resonances at 215.2 and 216.2 at 20°C, assigned to the carbonyl carbons of the Fe(CO)<sub>2</sub>(CN) unit, remain distinct on cooling to -90°C, but display a gradual broadening that gives rise to an apparent broad signal at 214.8 ppm at -100°C. Our interpretation of this phenomenon is that over this temperature regime, even at room temperature, the Fe(CO)<sub>2</sub>(CN) unit is fixed, rendering each CO in distinct chemical environments due to the asymmetry in the pst bridge. This result is consistent with computational studies described below which find a high energy barrier for the Fe(CO)<sub>2</sub>(CN) rotation. The low temperature resonance broadening is likely due to slowing of the 3-carbon ring flip motion in the pst unit.

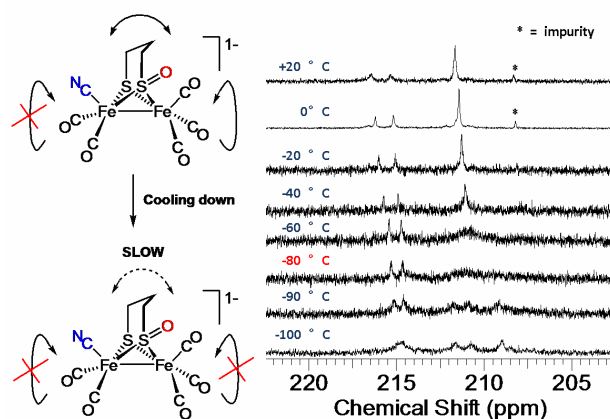


**Figure V. 11** Variable temperature <sup>13</sup>C NMR studies of complex **IV-1-O-CN<sup>-</sup>** from -100 °C to 20 °C (CD<sub>2</sub>Cl<sub>2</sub> solution, in CO region); signal indicated with “\*” are impurities

The intramolecular, apical/basal CO exchange on individual  $\text{Fe}(\text{CO})_3$  units in the parent **IV-1-O** complex, ceases by  $-60\text{ }^\circ\text{C}$  and has an activation barrier of  $\sim 47\text{ kJ/mol}$  ( $11.2\text{ kcal/mol}$ ) In contrast, the same process in complex **IV-1** has a barrier of  $35\text{ kJ/mol}$  ( $8.3\text{ kcal/mol}$ ) . A similar barrier,  $33\text{ kJ/mol}$  ( $7.85\text{ kcal/mol}$ ) is found for the  $\text{Fe}(\text{CO})_3$  unit in the **IV-1-O-CN<sup>-</sup>** complex. Thus the deactivation effect of the pst bridge on rotation in the  $\text{Fe}(\text{CO})_3$  unit is counter balanced by the activating effect of the  $\text{CN}^-$  ligand on the adjacent iron.

**Theoretical results.** To complement experimental results, the intramolecular CO exchange process for **IV-1-O-CN<sup>-</sup>** was explored by DFT computations. The optimized ground state and corresponding transition state structures en route to apical/basal CO exchange in the isomers of **IV-1-O-CN<sup>-</sup>** are given in Figure V. 12.

The CN-apical conformation is the most stable ground-state isomer by ca.  $4\text{ kcal/mol}$  as compared to the two CN-basal isomers. The activation barriers for both  $\text{Fe}(\text{CO})_3$  and  $\text{Fe}(\text{CO})_2\text{CN}$  rotation were calculated for all three isomers. Since similar results were obtained for the two CN-basal isomers, only the CN-basal isomer with cyanide cis to the S-O vector is given in Figure V. 12. The  $\text{Fe}(\text{CO})_3$  rotation barrier for the CN-apical isomer (Figure V. 12, (a)) is  $6.06\text{ kcal/mol}$ , ca.  $1.8\text{ kcal/mol}$  less than that required for the CN-basal isomer (Figure V. 12, (b)). The difference can be rationalized by better delocalization of the charge of the cyanide onto the bridging CO when the cyanide is in apical position and trans to the CO that migrates underneath the Fe--Fe bond vector. As indicated in Figure V. 12 by the metric data derived from the calculations, this is reflected by the Fe1-C1 distances and the greater bridging character of the CO that

rotates under the Fe-Fe bond vector for the CN-apical isomer as compared to the CN basal isomer.

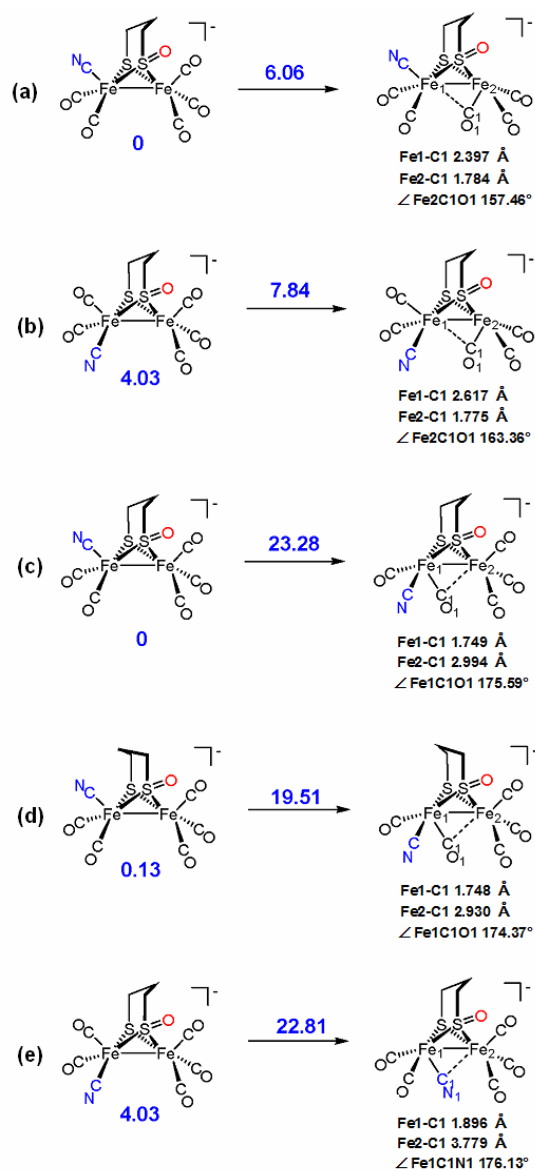


**Figure V. 12** Ground state and transition state structures for the rotation of Fe(CO)<sub>3</sub> and Fe(CO)<sub>2</sub>CN<sup>-</sup> units in the complex IV-1-O-CN<sup>-</sup> with corresponding energies given in kcal/mol from DFT computations; see text for parameters used.

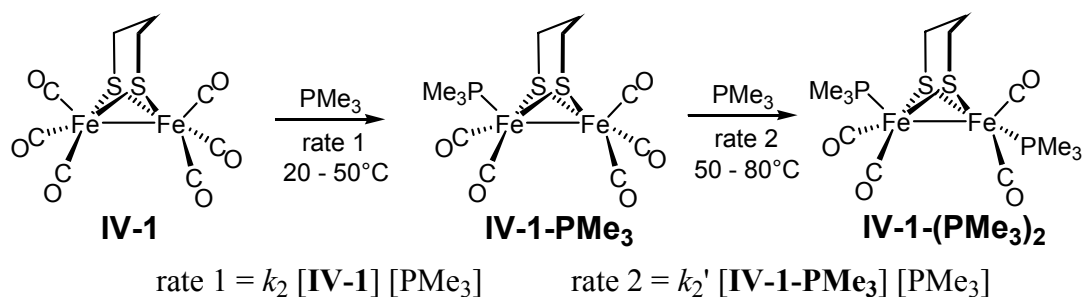


Consistent with conclusions from the VT  $^{13}\text{C}$  NMR study, the  $\text{Fe}(\text{CO})_2\text{CN}$  unit rotation (Figure V. 12, (c) and (d)) requires a much higher energy--up to 19 kcal/mol. As suggested before, the orientation of the bridgehead carbon toward the rotated Fe site stabilizes the transition state (TS); the rotation barrier in (d) is ca. 3.7 kcal/mol less than that in (c). Note that the high energy TS structures correlate with almost linear CO's. For the CN-basal isomer, a rotated TS with cyanide underneath the Fe--Fe bond vector (Figure V. 12, (e)) was found to have a barrier of 22.8 kcal/mol. The Fe1C1N1 angle and the Fe2--C1 distance indicates the CN ligand has little interaction with Fe2 site.

### Conclusions and comments

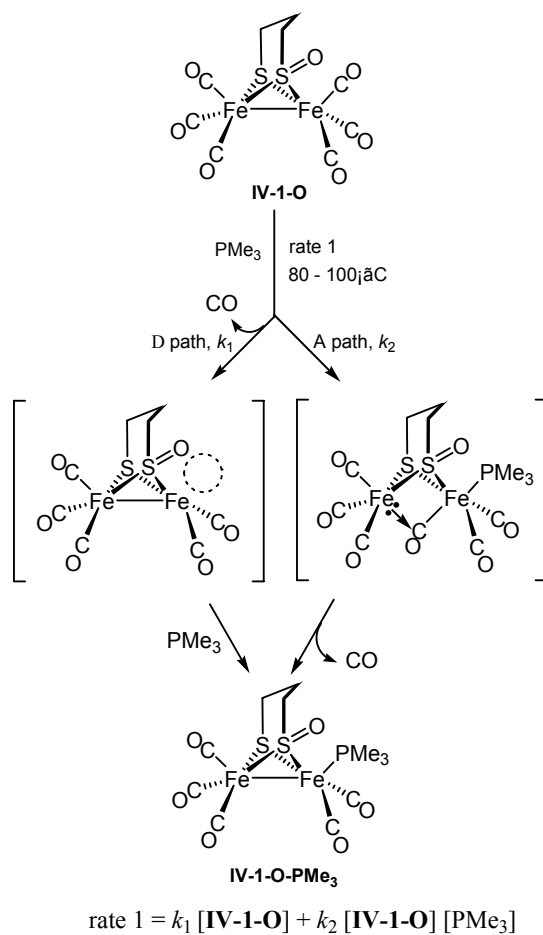
A summary of the  $\text{CO}/\text{PMe}_3$  reactivities of complexes **IV-1** and **IV-1-O** is given in Schemes V. 3 and V. 4. As noted above, the rate expressions for all reactions studied indicate associative processes. The expected increased electrophilicity of **IV-1-O** over **IV-1** towards  $\text{PMe}_3$  was not realized; under identical conditions, the barrier to  $\text{PMe}_3$  addition is higher for the former. For both **IV-1** and **IV-1-O**, the rate of  $\text{PMe}_3$  nucleophilic attack on iron is slower for the second addition than for the first, consistent with diminished electrophilicity of the diiron unit after CO substitution with the first  $\text{PMe}_3$  ligand. The **IV-1-O** complex reacts much more sluggishly than **IV-1**, leading into a temperature regime for practical measurements where CO dissociation competes with and obscures the associative path, Scheme V. 4. The addition of a second  $\text{PMe}_3$  to **IV-1-O-PMe}\_3** was so slow, even at elevated temperatures, that kinetic studies were not attempted.

## Scheme V. 3



The better nucleophilicity of  $\text{CN}^-$  as compared to  $\text{PMe}_3$  is apparent in  $\text{CO}/\text{CN}^-$  substitutions in both **IV-1** and **IV-1-O**. Scheme V. 5 summarizes observations for the  $\text{CO}/\text{CN}^-$  exchange reactions. The kinetic studies established that in both **IV-1** and **IV-1-O** the individual  $\text{CO}/\text{CN}^-$  exchange steps proceed via associative paths; an elaborated version of Scheme V. 2 is shown as Figure V. 13 specifically for the  $\mu$ -pdt complex. While the sequential step mechanism involving  $\text{Fe}(\text{CO})_3$  rotation concomitantly with  $\text{CN}^-$  nucleophilic attack on Fe holds for both, the reaction profiles differ in the relative values of  $E_{\text{act}}$  vs.  $E'_{\text{act}}$ , Figure V. 14. The analysis of this switch in order invokes the contributing factors of nucleophilic attack, the  $E_{\text{act}}(\text{CN}^- \text{ attack})$  of the equation in Figure V. 1, and the coordination sphere fluxionality, the  $E_{\text{act}}(\text{rot'n})$ , of the equation in Figure V. 1. As established by experiment from VT NMR studies, and corroborated by DFT computations, the rotational contribution for both complexes is lowered after the addition of the first  $\text{CN}^-$  ligand. For the  $\mu$ -pdt complex this enhancement of rotation overwhelms the decrease in electrophilicity due to the negative charge of complex **IV-1-CN<sup>-</sup>**.<sup>1</sup>

## Scheme V. 4



Because of the poorer donating ability of the S-oxygenate as compared to the thiolates, both  $\mu$ -pst complexes, **IV-1-O** and **IV-1-O-CN<sup>-</sup>**, are better electrophiles than the analogous  $\mu$ -pdt complexes. However they have significantly higher  $\text{Fe}(\text{CO})_3$  rotational barriers. Thus the decrease in electrophilicity in **IV-1-O-CN<sup>-</sup>** is not counter balanced by an increase of fluxionality as it was in **IV-1-CN<sup>-</sup>**. This results in slower reaction rates and greater  $E_{\text{act}}$  barriers for the second  $\text{CN}^-$  substitution in **IV-1-O-CN<sup>-</sup>**.

## Scheme V. 5

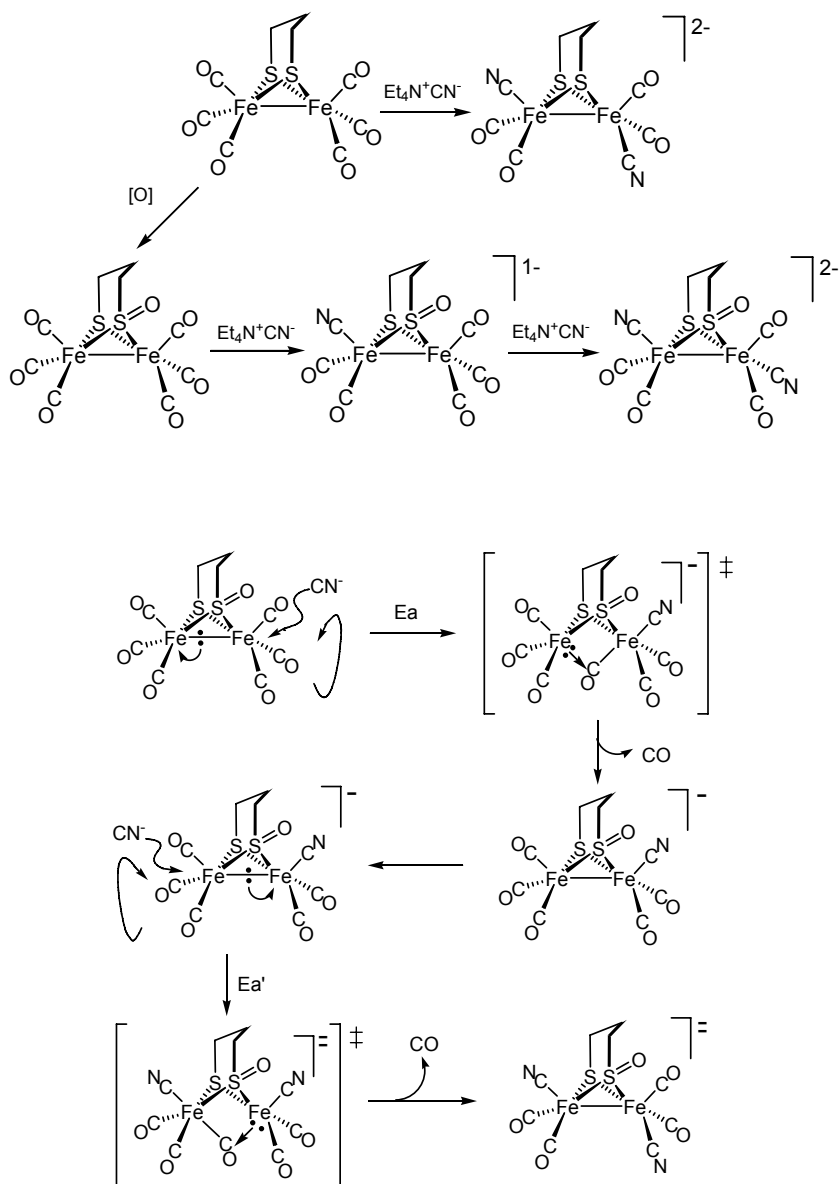


**Figure V. 13** Mechanism for  $\text{CN}^-/\text{CO}$  exchange reaction in  $(\mu\text{-pst})[\text{Fe}(\text{CO})_3]_2$  (IV-1-O).

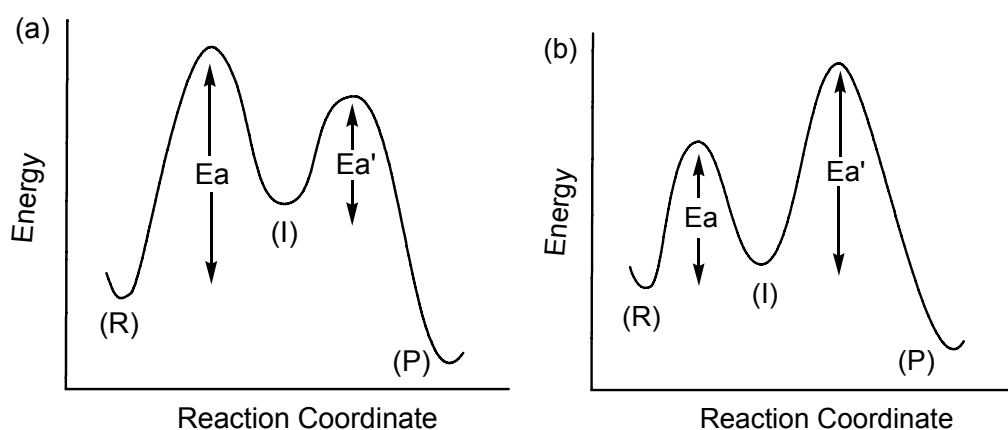


**Figure V. 14** Reaction profiles of CN<sup>-</sup>/CO substitution reaction of (a)  $(\mu\text{-pdt})[\text{Fe}(\text{CO})_3]_2$  (**IV-1**)<sup>1</sup> and (b)  $(\mu\text{-pst})[\text{Fe}(\text{CO})_3]_2$  (**IV-1-O**).

While  $\text{PMe}_3$  and  $\text{CN}^-$  have similar donor properties, kinetic studies find that "nature's phosphine", cyanide,<sup>186, 16</sup> is a much better nucleophile in CO substitution reactions. The ligand dependence is additional evidence of the associative character of the mechanism of ligand substitution, noted in early studies of  $(\mu\text{-SR})_2[\text{Fe}(\text{CO})_3]$  to be rare examples of associative mechanisms in 6-coordinate metal complexes, the sixth position being held by the Fe-Fe bond.<sup>243</sup>

**Comment on relation to the [FeFe]-Hydrogenase active Site.** This work adds to a considerable literature which explores the features of  $(\mu\text{-SRS})[\text{Fe}(\text{CO})_3]_2$  as might explain the appearance of a modified version of this classic organometallic in nature, the diiron unit of the [FeFe]-H<sub>2</sub>ase active site. The major conclusion from the current reactivity study is that the diiron construct is extremely sensitive to all conceivable modifications resulting from electronic tuning. Rarely has the potential for

intramolecular structural fluxionality in a transition metal complex been so easily verified and so readily related to reactivity.

It is notable that the mixed-valent  $\text{Fe}^{\text{I}}\text{Fe}^{\text{II}}$  diiron unit in the  $[\text{FeFe}]\text{-H}_2\text{ase}$  active site is in a ground state configuration that is "rotated" with respect to the ground state  $\text{Fe}^{\text{I}}\text{Fe}^{\text{I}}$  complex structures of complexes **IV-1** and **IV-1-O**, Figure V. 15, *giving a geometry heretofore unknown in organometallic chemistry, yet synthetically accessed by the proper combination of donor/steric properties of ligands in a mixed valent,  $\text{Fe}^{\text{I}}\text{Fe}^{\text{II}}$  form.*<sup>190, 244, 245</sup> The transition state structures of **IV-1** and **IV-1-O** that apply to the CO site exchange process are also in the "rotated" diiron form, and such a geometry for the  $\text{Fe}^{\text{I}}\text{Fe}^{\text{I}}$  diiron unit in the reduced redox level of  $[\text{FeFe}]\text{-H}_2\text{ase}$  active site would represent an "entatic state".<sup>186</sup> As earlier described in a "de novo" design approach to building diiron complexes,<sup>231</sup> an increase of electron density at the unrotated iron should stabilize the rotated transition state due to greater delocalization of electron density through the bridging carbonyl. This prediction was affirmed through CO/L substitution by better donating ligands.<sup>231</sup> The opposite case, a destabilization of the rotated transition state through removal of electron density, could not be experimentally established by CO ligand substitution. However the modification of a thiolate to a sulfenate has this outcome, leading to a consistent view of the kinetic response of this unit to first coordination sphere effects: a reduction of electron density at iron diminishes the structural mobility of the diiron unit and its ability to expand the overall coordination number in the associative path to ligand substitution.

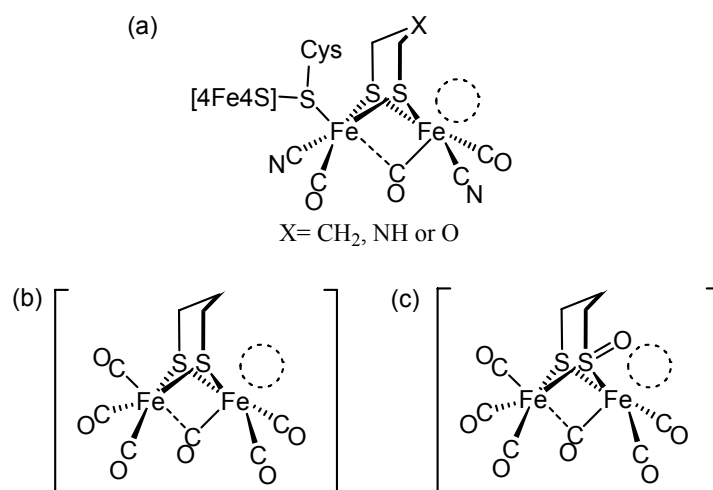


**Figure V. 15** Structures of [Fe]-H<sub>2</sub>ase active site (a)<sup>46, 59</sup> and transition state of Fe(CO)<sub>3</sub> rotation in (μ-pdt)[Fe(CO)<sub>3</sub>]<sub>2</sub> (b),<sup>1</sup> and (μ-pst)[Fe(CO)<sub>3</sub>]<sub>2</sub> (c).

**CHAPTER VI**

**IRON CARBONYL COMPLEXES  $\text{FeI}_2(\text{CO})_3\text{L}$  ( $\text{L} = \text{NHC}$   
**CARBENES, PHOSPHINES, PYRIDINE) AND  $\text{FeI}_2(\text{CO})_2\text{N}_2$  ( $\text{N}_2 = \alpha$ -  
**DIAMINES) REVELANT TO THE [Fe]-HYDROGENASE******

**Introduction**

For decades now Hieber's  $\text{Fe}^{\text{II}}\text{X}_2(\text{CO})_4$  ( $\text{X} = \text{Cl}, \text{Br}$  and  $\text{I}$ ) complexes have been utilized as synthons for development of  $\text{Fe}^{\text{II}}$  carbonyl complexes.<sup>169</sup> A recent application of  $\text{Fe}^{\text{II}}\text{I}_2(\text{CO})_4$  is in the preparation of biomimetics of [NiFe]- and the mono-iron hydrogenase or [Fe]-H<sub>2</sub>ase.<sup>111, 115</sup> The latter, also called Hmd,<sup>21, 64-67, 156</sup> contains a low-spin  $\text{Fe}^{\text{II}}$  active site surrounded by two cis-oriented CO ligands, a cysteinyl-S, an organic pyridone bidentate ligand (N and acyl carbon) and a H<sub>2</sub>O (or an open site) trans to the acyl group as sketched in Figure VI. 1. Synthetic analogues of the [Fe]-H<sub>2</sub>ase active site are of interest as it performs a stereoselective, hydride transfer reaction to a unique substrate. Furthermore, as a mono-iron complex, it should offer insight into the role of iron in the binuclear [FeFe]- and [NiFe]-H<sub>2</sub>ases. Synthetic challenges exist in the variety of ligation sites at the single active iron of Hmd site as described above, and in the strategic positioning of substrate that exists within the confinement of the protein matrix.

While x-ray crystallography gives a snapshot of the [Fe]-H<sub>2</sub>ase enzyme active site, the specific reason(s) for such a diverse ligation environment as described above, as it affects function through management of the electron density at iron, is more apt to be



found in spectroscopic analyses, specifically  $\nu(\text{CO})$  IR and Mössbauer spectroscopies. For the [NiFe]- and [FeFe]-H<sub>2</sub>ase active sites in various redox levels,  $\nu(\text{CO})$  IR spectroscopy has been helpful to this understanding through the correlation of signals from the enzymes with those of small molecule synthetic analogues or biomimetics. As Mössbauer spectroscopy is variable in its response to Fe oxidation state, to spin state, and to distortions in electron density at iron, it is particularly necessary that synthetic analogues be developed in which systematic changes are controlled and interpretable for their fundamental properties. At this time such correlations between systematic structural changes and parameters for well-characterized low-spin iron complexes are limited, at best.

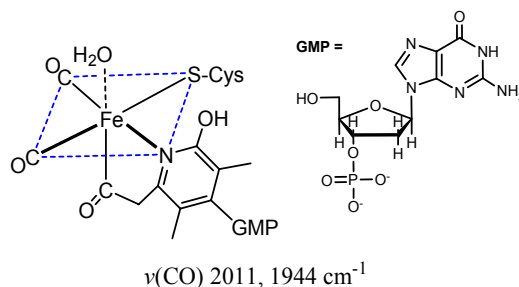


**Figure VI. 1** The active site of Hmd or [Fe]-H<sub>2</sub>ase with its CO stretching frequencies.<sup>64,</sup>

65

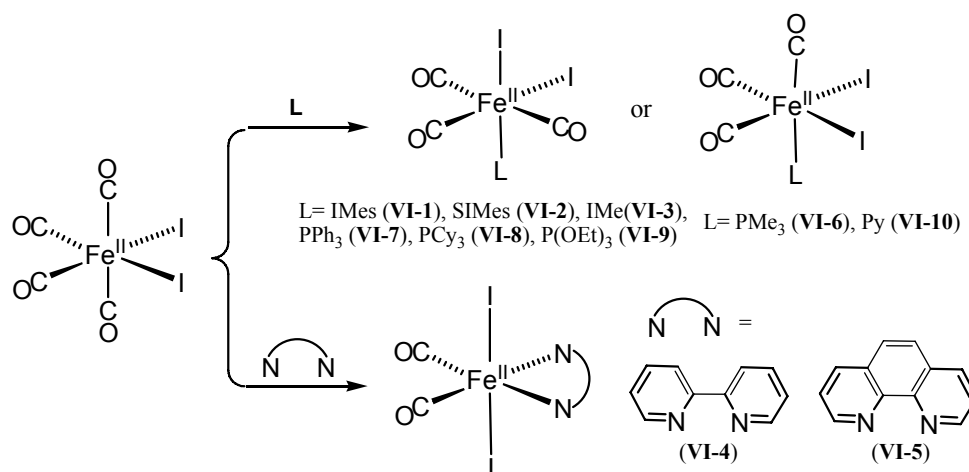
The  $\text{Fe}^{\text{II}}\text{X}_2(\text{CO})_4$  complexes have the following advantages as precursors for model complexes of [Fe]-H<sub>2</sub>ase: a) the desired  $\text{Fe}^{\text{II}}$  oxidation state, b) intrinsic carbonyls, c) facile CO replacement and halide abstraction reactivity that permits structural modifications. Herein, we report the syntheses and structures of a series of  $\text{FeI}_2(\text{CO})_3\text{L}$  (L = N-heterocyclic carbenes (NHC), phosphines, pyridine) and  $\text{FeI}_2(\text{CO})_2\text{N}_2$  ( $\text{N}_2 = \alpha$ -

diamines) complexes. These complexes are used for spectroscopic reference points as described above and they can, as well, be regarded as useful precursors for advanced models. The study on the mono-Fe complexes described in this chapter and Chapter VII was collaborated with B. Li.

## Results and discussion

**Synthesis of  $\text{FeI}_2(\text{CO})_3\text{L}$  ( $\text{L} = \text{IMes}$  (VI-1),  $\text{SIMes}$  (VI-2),  $\text{IMe}$  (VI-3),  $\text{PMe}_3$  (VI-6),  $\text{PPh}_3$  (VI-7),  $\text{PCy}_3$  (VI-8),  $\text{P(OEt)}_3$  (VI-9),  $\text{Py}$  (VI-10)) and  $\text{FeI}_2(\text{CO})_2\text{N}_2$  ( $\text{N}_2 = \text{bipyridine}$  (VI-4),  $\text{phenanthroline}$  (VI-5)).** Scheme VI. 1 outlines the scope of our synthetic endeavor. The mono-substituted  $\text{FeI}_2(\text{CO})_3\text{P}$  ( $\text{P} = \text{PPh}_3$  and  $\text{PMe}_3$ ) complexes have been reported, however, possibly due to their light and heat sensitivity, without structural characterization.<sup>183-185</sup>

**Scheme VI. 1**



N-heterocyclic carbenes are regarded as alternatives to phosphines in organometallic chemistry with certain advantages deriving from their distinctive electronic, chemical and steric properties.<sup>246</sup> Thus  $\text{FeI}_2(\text{CO})_3\text{NHC}$  complexes with  $\text{NHC} = \text{IMes}$  (1,3-bis(2,4,6-trimethylphenyl)imidazol-2-ylidene), complex **VI-1**; the saturated analogue of  $\text{IMes}$  or  $\text{SIMes}$  (1,3-bis(2,4,6-trimethylphenyl)imidazol-2-ylide), complex **VI-2**; and  $\text{IMe} = 1,3\text{-bismethylimidazol-2-ylidene}$ , complex **VI-3**, were prepared and are reported in this study. They are easily synthesized as follows: to a solution of  $\text{FeI}_2(\text{CO})_4$  in hexane the freshly prepared NHC ligand in hexane is slowly added. After stirring for 1 h at 22 °C, products precipitate out of solution (Scheme VI. 1), reflecting a solubility property of the  $\text{FeI}_2(\text{CO})_3\text{L}$  complexes consistent with higher polarity as compared to  $\text{FeI}_2(\text{CO})_4$ .

The reactions of  $\text{FeI}_2(\text{CO})_4$  with 2,2'-bipyridine afforded the disubstituted complex,  $\text{FeI}_2(\text{CO})_2(\text{bipy})$ , complex **VI-4**, under the same conditions as above. Due to the poor solubility of 1, 10-phenanthroline, phen, in hexane,  $\text{FeI}_2(\text{CO})_2(\text{phen})$ , **VI-5**, was prepared in  $\text{CH}_2\text{Cl}_2$  using equal amounts of phen and  $\text{FeI}_2(\text{CO})_4$ . The simple mixing procedure was used to prepare mono-substituted phosphine and pyridine derivatives of  $\text{FeI}_2(\text{CO})_4$  ( $\text{FeI}_2(\text{CO})_3\text{L}$ ,  $\text{L} = \text{PMe}_3$  (**VI-6**),<sup>184, 185</sup>  $\text{PPh}_3$  (**VI-7**),<sup>183, 185</sup>  $\text{PCy}_3$  (**VI-8**),  $\text{P}(\text{OEt})_3$  (**VI-9**),  $\text{Py}$  (**VI-10**)<sup>184</sup>. It should be mentioned that in the case of  $\text{FeI}_2(\text{CO})_3\text{PMe}_3$  (**VI-6**), fast addition of  $\text{PMe}_3$  leads to the formation of  $\text{FeI}_2(\text{CO})_2(\text{PMe}_3)_2$ .<sup>184, 185</sup> All of these complexes are light and heat sensitive, therefore they are stored in the dark at -40 °C in the glove box.

**Infrared spectroscopy.** In comparison to the  $\text{FeI}_2(\text{CO})_4$  starting material, the CO-substituted complexes exhibit  $\nu(\text{CO})$  frequencies at lower wavenumbers with positions dependent on the donor abilities of the various substituent ligands and with patterns reflecting the symmetry of each complex. Figure VI. 2 displays the  $\nu(\text{CO})$  infrared spectra of selected complexes **VI-1**, **VI-6**, **VI-8**, **VI-10** and **VI-12** (see SI for the  $\nu(\text{CO})$  infrared spectra of complexes **VI-2~ VI-4**, **VI-7**, **VI-9** and **VI-11**). All  $\nu(\text{CO})$  IR data for **VI-1 ~ VI-12** are listed in Table VI. 1.

**Table VI. 1** Infrared Spectroscopic ( $\nu(\text{CO})$ ) Data For  $\text{FeI}_2(\text{CO})_3\text{L}$ ,  $\text{FeI}_2(\text{CO})_2\text{N}_2$  and  $\text{FeI}(\text{CO})_2\text{LPyS}$  Derivatives (reported in  $\text{CH}_2\text{Cl}_2$  solution unless otherwise noted).

Compound	Geometry	$\nu(\text{CO})$ ( $\text{cm}^{-1}$ )
<b>(VI-1)</b> $\text{FeI}_2(\text{CO})_3\text{IMes}$	<i>mer</i>	2087 (w), 2040 (s), 2018 (m)
<b>(VI-2)</b> $\text{FeI}_2(\text{CO})_3\text{SIMes}$	<i>mer</i>	2082 (w), 2039 (s), 2019 (m)
<b>(VI-3)</b> $\text{FeI}_2(\text{CO})_3\text{Ime}$	<i>mer</i>	2082 (w), 2034 (s), 2023 (sh)
<b>(VI-4)</b> $\text{FeI}_2(\text{CO})_2\text{bipy}$	<i>cis</i>	2043 (s), 2002 (s)
<b>(VI-5)</b> $\text{FeI}_2(\text{CO})_2\text{phen}$	<i>cis</i>	2044 (s), 2003 (s)
<b>(VI-6)</b> $\text{FeI}_2(\text{CO})_3\text{PMe}_3$	<i>fac</i>	2093 (s), 2047 (s), 2022 (s)
<b>(VI-7)</b> $\text{FeI}_2(\text{CO})_3\text{PPh}_3$	<i>mer</i>	2093 (w), 2045 (s), 2032 (m)
<b>(VI-8)</b> $\text{FeI}_2(\text{CO})_3\text{PCy}_3$	<i>mer</i>	2081 (w), 2031 (vs), 2017 (s, sh)
<b>(VI-9)</b> $\text{FeI}_2(\text{CO})_3\text{P(OEt)}_3$	<i>mer</i>	2104 (w), 2053 (s, br)
<b>(VI-10)</b> $\text{FeI}_2(\text{CO})_3\text{Py}$	<i>fac</i>	2095 (s), 2050 (ms), 2041 (ms)
<b>(VI-11)</b> $\text{FeI}(\text{CO})_2\text{PCy}_3(\text{PyS})^a$	<i>cis</i>	2019 (s), 1971 (s)
<b>(VI-12)</b> $\text{FeI}(\text{CO})_2\text{PPh}_3(\text{PyS})^a$	<i>cis</i>	2031 (s), 1983 (s)
Hmd	<i>cis</i>	2011 (s), 1944 (s) <sup>156</sup>
Hmd·CO	<i>fac</i>	2074 (s), 2020 (s), 1981 (s) <sup>156</sup>

<sup>a</sup> Spectra recorded in THF

According to the  $\nu(\text{CO})$  IR patterns, mono-substituted complexes can be classified into two subtypes of geometries: *fac*- $\text{FeI}_2(\text{CO})_3\text{L}$  ( L =  $\text{PMe}_3$  (**VI-6**); py (**VI-10**)) and *mer*- $\text{FeI}_2(\text{CO})_3\text{L}$  ( L = IMes (**VI-1**); SIMes (**VI-2**); IMe (**VI-3**);  $\text{PPh}_3$  (**VI-7**);  $\text{PCy}_3$  (**VI-8**);  $\text{P(OEt)}_3$  (**VI-9**)). The patterns of the two types are very distinctive; the first band of

the *fac*-FeI<sub>2</sub>(CO)<sub>3</sub>L complexes is strong while the first band of the *mer*-FeI<sub>2</sub>(CO)<sub>3</sub>L is weak. The assignments are well supported by crystal structures (*vide infra*) of complexes **VI-1**~ **VI-3** and **VI-10**. The pattern of the *fac*-FeI<sub>2</sub>(CO)<sub>3</sub>L complexes matches well to that of the CO-inhibited active site of [mono-Fe] hydrogenase.<sup>156</sup> Therefore, as structural models these complexes provide evidence for the geometry of the CO-inhibited state of the enzyme. The CO frequencies of the *fac*-FeI<sub>2</sub>(CO)<sub>3</sub>L complexes (e.g., (**VI-10**), 2095, 2049, 2023 cm<sup>-1</sup>) are ca. 20 cm<sup>-1</sup> higher than those of the inhibited enzyme (2074, 2020, 1981 cm<sup>-1</sup>).

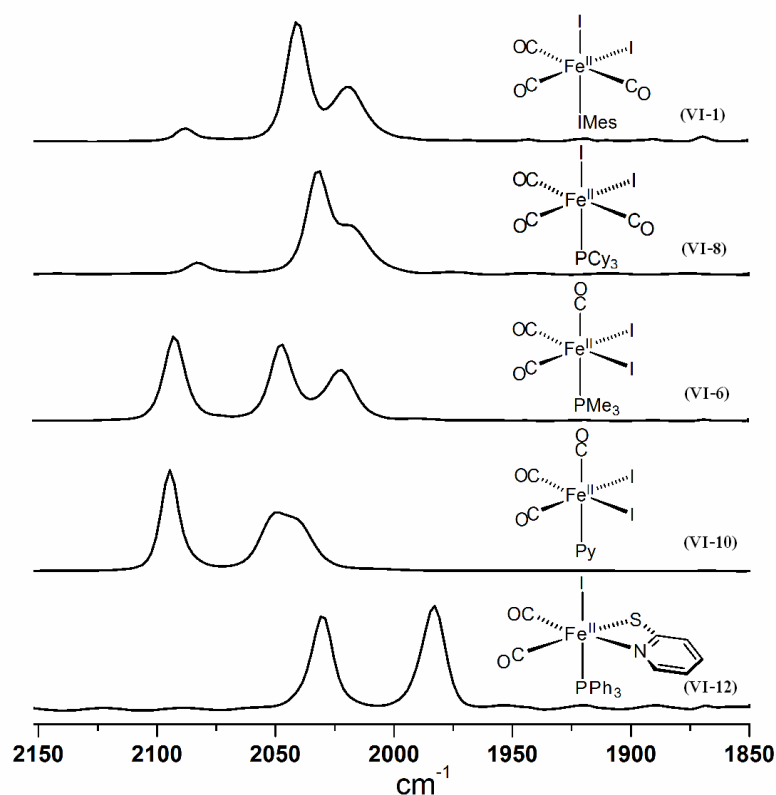


**Figure VI. 2** The infrared spectra of mono-Fe<sup>II</sup> complexes **VI-1**, **VI-6**, **VI-8**, **VI-10** and **VI-12**.

Disubstituted complexes **VI-4** and **VI-5** exhibit interesting solution behavior as detected by infrared spectroscopy. When freshly dissolved in  $\text{CH}_2\text{Cl}_2$ , both complexes show two strong CO bands at 2043 and 2002  $\text{cm}^{-1}$  for **VI-4** and 2044 and 2004  $\text{cm}^{-1}$  for **VI-5** (see Figure VI. 3 (A) and Figure VI. 4 (A)). After several minutes, a new set of two CO bands at 2077 and 2033  $\text{cm}^{-1}$ , species **X**, were observed to grow in the  $\nu(\text{CO})$  IR spectra for both **VI-4** and **VI-5** ((see Figure VI. 3 (B) and figure VI. 4 (B)), shifting positively by 30  $\text{cm}^{-1}$  relative to the original bands. While the identity of species **X** is not known with certainty, isomeric forms of  $\text{Ru}(\text{bpy})(\text{CO})_2(\text{Cl})_2$  have been structurally characterized as *cis*-(CO),*trans*-(Cl)- $\text{Ru}(\text{bpy})(\text{CO})_2(\text{Cl})_2$  and *cis*-(CO),*cis*-(Cl)- $\text{Ru}(\text{bpy})(\text{CO})_2(\text{Cl})_2$ .<sup>247</sup> Therefore a reasonable assumption is that the new CO bands reported in Figure VI. 2 are due to iodo-iron analogues. DFT computations find the *cis*-(CO),*trans*-(I)- $\text{Fe}(\text{phen})(\text{CO})_2(\text{I})_2$  complex to be thermodynamically favored by 5.6 kcal/mol over the *cis*-(CO),*cis*-(I)- $\text{Fe}(\text{phen})(\text{CO})_2(\text{I})_2$  isomer. The calculations also show that the two IR bands for the carbonyls of the *cis*-(CO),*cis*-(I)- $\text{Fe}(\text{phen})(\text{CO})_2(\text{I})_2$  are ca. 10 - 12  $\text{cm}^{-1}$  lower than those of the *trans* iodo isomer. Hence, following this assumption, we would conclude that the *cis*-iodo form was the kinetic product which was isolated and when first dissolved, spectrum A, Figure VI. 3, proceeded to isomerize into the more stable *trans*-iodo isomer that shows a 2-band  $\nu(\text{CO})$  IR spectrum at higher wavenumbers, spectra B and C, Figure VI. 3. Note that by this analysis, we would also conclude that the crystal that was chosen for x-ray diffraction study was of the thermodynamically favored product, the *trans*-iodo form.

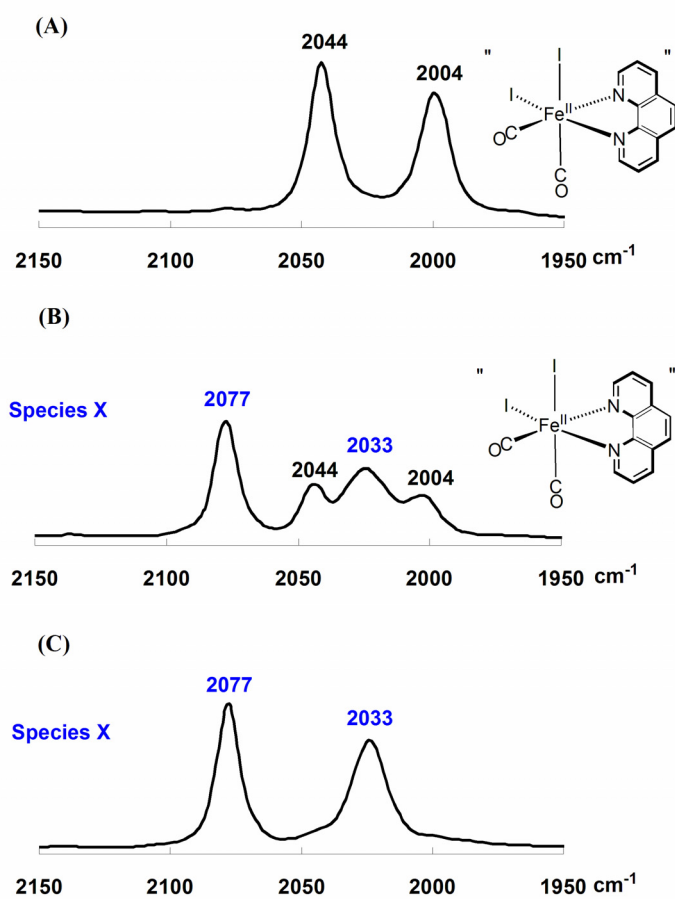


**Figure VI. 3** Infrared spectral monitoring of  $\text{CH}_2\text{Cl}_2$  solution of complex **VI-5** at  $22^\circ\text{C}$ . (A) Immediately after dissolving complex **VI-5**; (B) IR spectrum recorded 2 h later; (C) IR spectrum after overnight (RT and in the dark).

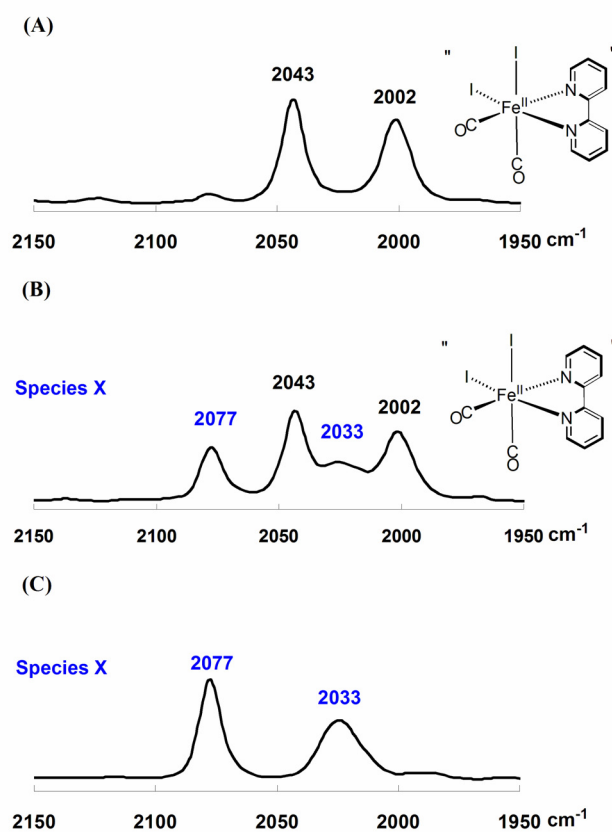


**Figure VI. 4** Infrared spectral monitoring of  $\text{CH}_2\text{Cl}_2$  solution of complex **VI-5** at  $22^\circ\text{C}$ . (A) Immediately after dissolving complex **VI-5**; (B) IR spectrum recorded 2 h later; (C) IR spectrum after overnight (RT and in the dark).

The solution behavior described above for complexes **VI-4** and **VI-5** is also observed in THF solvent and the results are identical under Ar and  $\text{N}_2$  atmospheres, thus excluding the possibility of  $\text{N}_2$ -bound adducts. Interestingly, in a mixture of complex **VI-4** isomers, only the (assumed) cis-iodo isomer undergoes  $^{13}\text{C}$ O exchange (presumably via a CO dissociation/readdition process), Figure VI. 5. This selectivity possibly offers an example of cis-labilization effects of iodide in that the operative pentacoordinate, square



pyramidal intermediate {cis-(I)-Fe(phen)(CO)(I)<sub>2</sub>} with open site trans to the poorer π-donating amine donor, would arise preferentially from the cis-(CO),cis-(I)-Fe(phen)(CO)<sub>2</sub>(I)<sub>2</sub> complex.

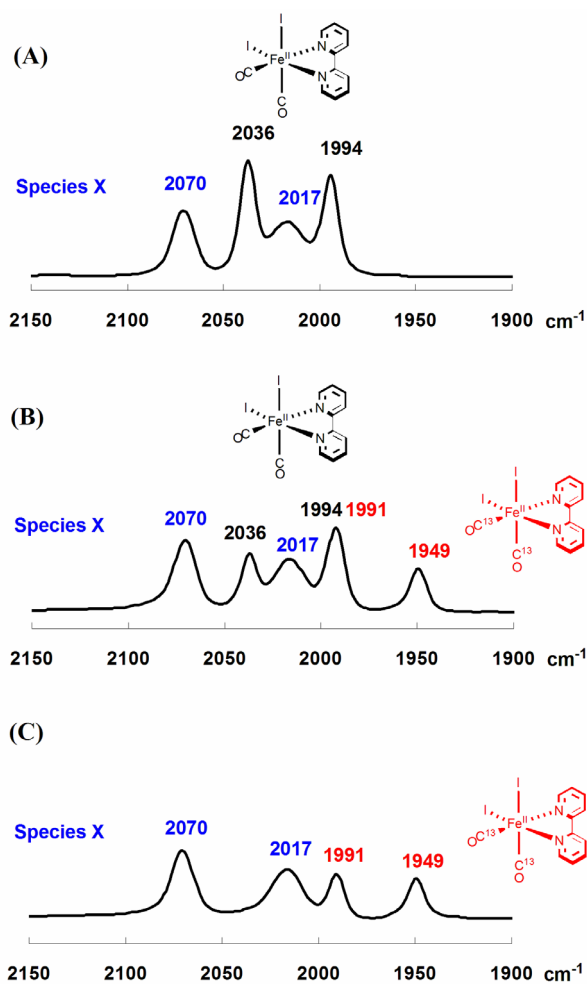


**Figure VI. 5**  $\nu(\text{CO})$  region of IR spectra of complex VI-4 in THF under  $^{13}\text{CO}$  atmosphere: (A) IR spectra of complex VI-4 in THF. (B) IR spectra of complex VI-4 in THF under 2atm  $^{13}\text{CO}$  after 3 h. (C) IR spectra of complex 4 in THF under 2atm  $^{13}\text{CO}$  after 18 h.

The above analysis relies on the two isomeric forms hypothesis. The possibility of iodide dissociation yielding a pentacoordinate intermediate susceptible to CO uptake and exchange cannot at this stage be completely ruled out. Thus, firmer evidence is needed as to the identity of the species **X** of  $\nu(\text{CO}) = 2077$  and  $2033 \text{ cm}^{-1}$  prior to further speculation.

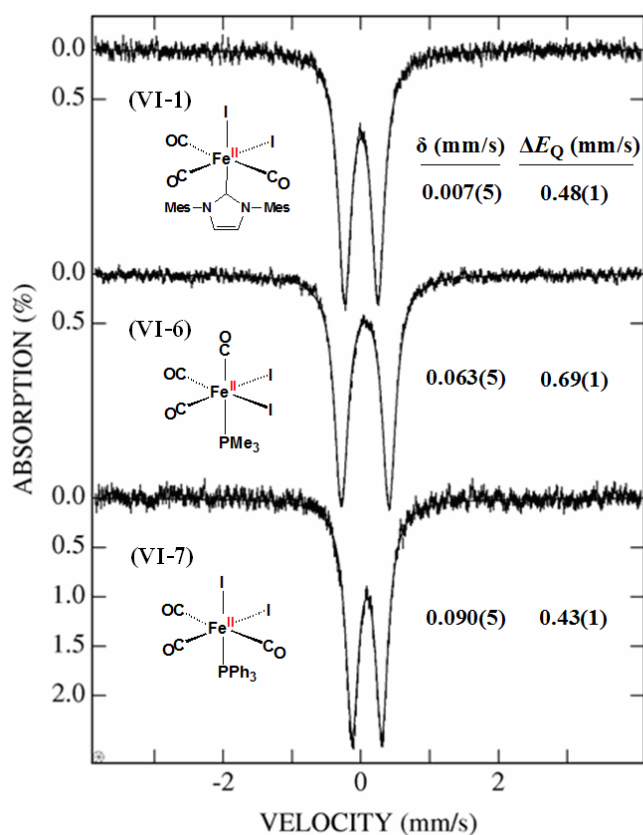


**Figure VI. 6** 6 K Mössbauer spectra for complexes **VI-1**, **VI-6**, and **VI-7** in an applied field of 0.03 T.

**Mössbauer spectroscopy** This study and description thereafter was carried by Dr. Codrina Popescu at Ursinus College. Complexes **VI-1**, **VI-6**, and **VI-7** exhibit sharp quadrupole doublets at 6 K (Figure VI. 3),<sup>248</sup> with isomer shifts ranging from 0.007 to 0.090 mm/s, and small quadrupole splittings, consistent with hexacoordinate low-spin ferrous carbonyls.<sup>249</sup> The isomer shifts of low-spin iron complexes are less sensitive to oxidation state and coordination environment than those of high-spin complexes, thus structure-spectroscopy correlations based on isolated compounds are of little value. However, as shown by Parish<sup>249</sup> examination of Mossbauer and other spectroscopic data of a set of related compounds leads to valuable correlations between structure and spectroscopy. While in general, introduction of CO ligands has the effect of lowering the isomer shift, the isomer shift of a particular set of compounds also depends on the nature of supplementary ligands that complete the coordination sphere. For instance, a series of low-spin ferrous pentacoordinate dicarbonyl complexes, where the CO's are in the company of an extremely good  $\pi$ -donating,  $\pi$ -delocalizing 2-amidothiophenolate, (PhNHS)<sup>2-</sup> ligand, and a phosphine donor showed negative isomer shifts (vide infra and Chapter VII). The present series of six-coordinate tri-carbonyls, where the non-innocent,  $\pi$ -delocalizing (N,S)<sup>2-</sup> donors are replaced by two iodide ligands, exhibit positive isomer shifts.

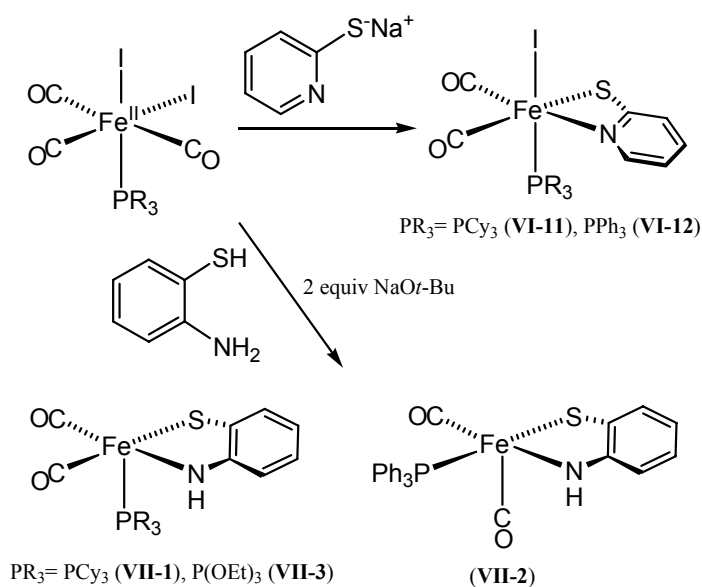
This series illustrates the effect on the isomer shift of substitution of a phosphine with the N-heterocyclic carbene IMes. The isomer shift of complex **VI-1**,  $\delta = 0.007$  mm/s, is smaller than that of complexes **VI-6** and **VI-7**, consistent with the better  $\sigma$ -donating ability of IMes compared to phosphines (PMe<sub>3</sub> and PPh<sub>3</sub>). The trend in isomer

shifts parallels the observed increase in CO stretching frequencies in the series. A change in oxidation state has a more marked effect on the isomer shift. Thus the  $\text{Fe}^0$  complex  $(\text{Fe}(\text{CO})_4\text{NHC})$ , where  $\text{NHC} = \text{IMesMe}$  (1-(2,4,6-trimethylphenyl),3-methylimidazol-2-ylidene) exhibits, at 5 K, an isomer shift of  $-0.092$  mm/s and  $\Delta E_Q = 2.01$  mm/s (spectra not shown).

**Reactivities leading to advanced Hmd models.** As the active site of the  $[\text{Fe}]\text{-H}_2\text{ase}$  has been known with reasonable certainty for only a short time, there are few reports of synthetic analogues (in great contrast to the vast literature that has grown up as biomimetics of the  $[\text{FeFe}]\text{-H}_2\text{ase}$  active site).<sup>157-159, 250, 251</sup> Complexes **VI-7~ VI-9** have been utilized as precursors to more faithful models of the active site of  $[\text{Fe}]\text{-H}_2\text{ase}$ , Scheme VI. 2. On treatment of complexes **VI-7** and **VI-8** with  $\text{PyS}^-\text{Na}^+$  complexes **VI-11** and **VI-12**, respectively, are obtained. Infrared spectra of these two complexes feature two  $\nu(\text{CO})$  bands of equal intensity at  $2019, 1991\text{ cm}^{-1}$  for **VI-11**, and at  $2031, 1983\text{ cm}^{-1}$  for **VI-12**, indicating cis-carbonyls are in these molecules. The x-ray diffraction study of **VI-12** (*vide infra*) confirmed this conclusion. Thus complexes **VI-11** and **VI-12** contain four of the first coordination sphere donors of the active site, including a nitrogen from pyridine. The  $\Gamma$  ligand may be considered as the analogue of  $\text{H}_2\text{O}$  (or actual open site) in the enzymatic site since  $\Gamma$  abstraction can generate a potential open (or active) site.

In addition, complexes **VI-7**, **VI-8** and **VI-9** can be structurally modified with 2-amidothiophenolate,  $(\text{PhNHS})^{2-}$ , to produce 5-coordinate iron dicarbonyls, **VII-1~ VI-3**. A full description of complexes **VII-1~VII-3** is given in Chapter VII.

## Scheme VI. 2



**X-ray diffraction studies and molecular structures of complexes VI-1, VI-2, VI-3, VI-4, VI-10 and VI-12.** Complexes VI-1~ VI-4, VI-10 and VI-12 were studied by X-ray diffraction. Their molecular structures are given as thermal ellipsoid plots in Figure VI. 6 and selected structural parameters are listed in Table VI. 2. All are 6-coordinate and octahedral. Only in the case of the diiododicarbonyl complex VI-4 are the iodides in trans positions; in all other complexes a cis-I<sub>2</sub>Fe arrangement prevails. The Fe-I distances are in a narrow range of 2.62 - 2.69 Å with no easily interpretable trends.

The NHC carbene substituted complexes VI-1~ VI-3 are of *meridional* geometry with the three CO ligands located in a plane and each at ca. 90° to the carbene carbon donor of the NHC. The structures of complexes VI-1 and VI-2 are almost identical. The

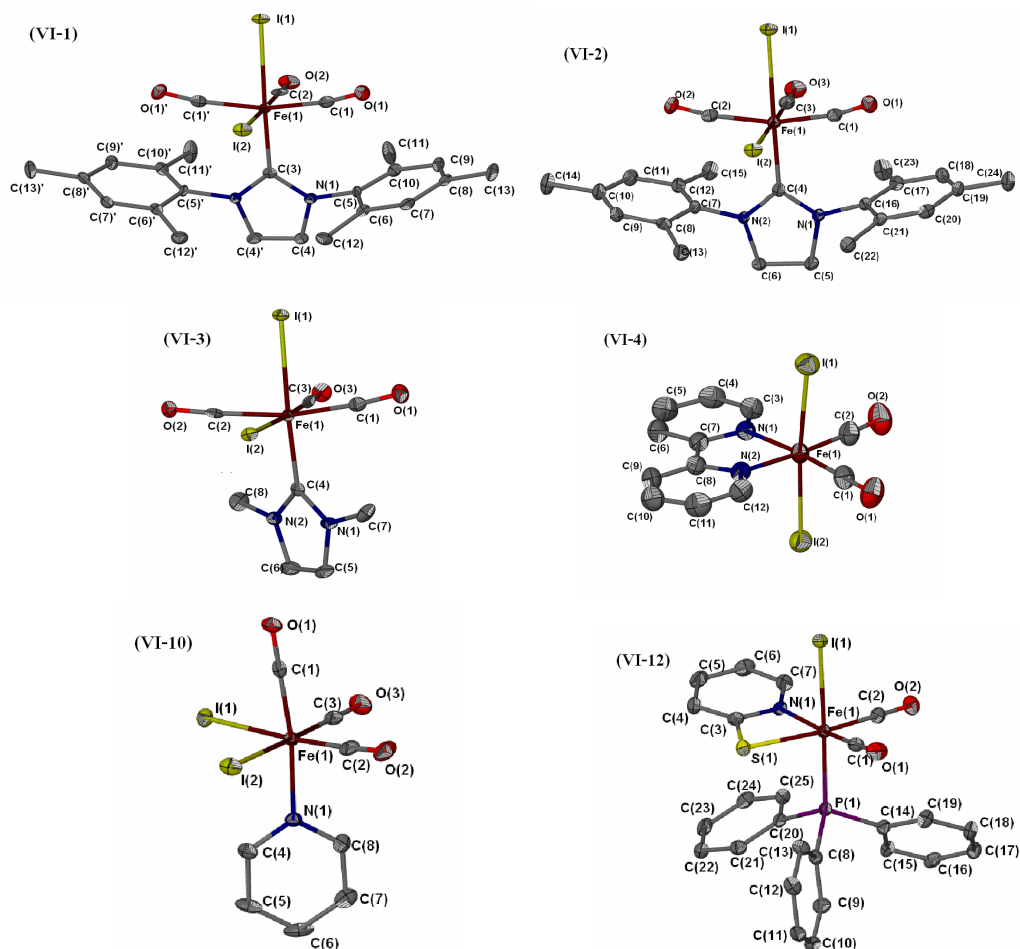


**Figure VI. 7** Thermal ellipsoid representations of the molecular structures of mono-iron complexes as indicated; hydrogen atoms omitted.

difference mainly arises in the C-C distance of the NHC five-membered ring: for **VI-1** the C(4)-C(4)' distance is that of a C=C double bond, 1.333(9) Å, and for **VI-2** the C(5)-C(6) single bond distance is 1.528(3) Å. The CN<sub>2</sub>C<sub>2</sub> heterocycle and the Fe(CO)<sub>2</sub>I are nearly coplanar. The mesityl groups flanking the carbene donor site exert a steric influence on the adjacent CO's resulting in a C1-Fe-C1' angle of 159.9 (3)° for complex

**VI-1**; the analogous C1-Fe-C2 angle in complex **VI-2** is 160.55 (11)°. For complex **VI-3**, the plane of the carbene bisects the cis ligands in the Fe(CO)<sub>3</sub>I plane with dihedral angles of 33.5 and 55.6 °. Again the steric influence of the NHC methyl substituents on N enforces a bend in the C1FeC2 angle of 166.6(2)°.

**Table VI. 2** Selected metric data for complexes **VI-1**, **VI-2**, **VI-3**, **VI-4**, **VI-10** and **VI-12**.

Complex	<b>VI-1</b>	<b>VI-2</b>	<b>VI-3</b>	<b>VI-4</b>	<b>VI-10</b>	<b>VI-12</b>
Fe1- I1 (Å)	2.674(1)	2.695(1)	2.665(1)	2.631(1)	2.640(1)	2.664(1)
Fe1- I2 (Å)	2.636(1)	2.641(1)	2.667(1)	2.625(1)	2.646(1)	-----
Fe1- C(O) (Å) trans to Fe1-I2	1.792(7)	1.794(3)	1.802(4)	-----	1.817(6)	-----
Fe1- C1(O) (Å)	1.848(5)	1.859(3)	1.824(4)	1.782(4)	1.806(6)	1.793(3)
Fe1- C(NHC) (Å)	2.002(6)	2.003(3)	1.984(4)	-----	-----	-----
Fe1-N (Å)	-----	-----	-----	1.999(3)	2.048(5)	1.962(2)
Fe1-S (Å)	-----	-----	-----	-----	-----	2.362(1)
Fe-P1 (Å)	-----	-----	-----	-----	-----	2.255(1)
cis-CO angle (°)	C(1)-Fe(1) -C(2) 96.07(14)	C(1)-Fe(1) -C(3) 94.62(12)	C(1)-Fe(1) -C(3) 90.59(18)	90.09(17)	C(1)-Fe(1) -C(2) 92.1(2)	93.57(12)
trans-CO angle (°)	159.9(3)	160.55(11)	166.58(19)	-----	-----	-----
I(2)-Fe(1) -C(O) (trans)	178.44 (19)	178.25(8)	175.57(13)	-----	178.15(18)	-----
N-Fe-S (°)	-----	-----	-----	-----	-----	70.36(7)

Complex **VI-10** has a *facial*-CO arrangement: two cis-CO's and two I<sup>-</sup> lie at the equatorial plane and an additional CO and the pyridine are positioned in trans-axial sites. The angle between two cis-COs is 92.1(2) °. The structures of complexes **VI-1**- **VI-3** and **VI-10** together with their  $\nu(\text{CO})$  IR vibration patterns provide structural references for phosphine derivatives **VI-6**- **VI-9** for which, despite many attempts, the crystal

structures are not available. Depending on the size of the phosphines, complexes **VI-6**~**VI-9** adopt *mer*-geometry or *fac*-geometry.

Complex **VI-4** was found in  $C_{2v}$  symmetry with two trans- $\Gamma$  ligands at axial positions; the phenanthroline bidentate ligand and the two cis-CO ligands occupy the equatorial plane. The angle between the cis-CO's is  $90.09 (17)^\circ$ , consistent with the  $\nu(\text{CO})$  pattern in the solution spectra.

Complex **VI-12** models the equatorial ligand set of the Hmd active site with one S, one N and two cis-CO ligands at an angle of  $93.57(12)^\circ$ . The bite angle of the NS ligand is  $70.36 (7)^\circ$ , reflecting severe strain in the NSFeC 4-membered ring. The Fe-S and Fe-N distances are  $2.362(1) \text{ \AA}$  and  $1.962(2) \text{ \AA}$  respectively, comparable with the values ( $2.335(4) \text{ \AA}$  and  $2.052(9) \text{ \AA}$ ) reported for the active site as extracted from EXAFS refinement.<sup>65</sup>

### Conclusions and comments

The structural and spectroscopic information gleaned from the series of mono- and di-substituted complexes,  $\text{FeI}_2(\text{CO})_x\text{L}_{4-x}$  suggest them to be rudimentary structural and spectroscopic models of the Hmd (or [Fe]-H<sub>2</sub>ase active site). The dicarbonyl complex **VI-11**, best matches the  $\nu(\text{CO})$  IR values of Hmd while the tricarbonyl complex **VI-6** mimics the CO-inhibited state, CO-Hmd, see Table VI. 1. In terms of the Mossbauer parameters, the tricarbonyl complex **VI-6** (Figure VI. 3) provides the best match of Hmd (in its dicarbonyl form), while the CO-Hmd finds a better match in complex **VII-2** (a dicarbonyl, however with an exceptional  $\pi$ -donating ligand!). These data beg the



question of the usefulness of Mossbauer parameters in biomimetics of apparently similar coordination spheres as the enzyme active site that they portend to mimic.

Metalloenzyme active sites have complex coordination spheres, improved by long-term evolution, which allowed fine tuning of the electron density at the iron through second coordination sphere effects and intricate hydrogen bonding that controls solvent and effects and binding of substrates such as hydride. While synthetic chemists have successfully implemented gross features of nature's design of ligands and, in some cases, unusual stereochemistry,<sup>190, 252</sup> control of finer effects from the outer coordination sphere by use of inner sphere abiological ligand constructs is still lacking.<sup>81</sup> However, this challenge is important for bioinspired catalysis as the subtle effects influence electronic structure and spectroscopy in ways that, most probably, have not been fully appreciated.<sup>119</sup>

It is well known that for high spin iron complexes Mossbauer parameters exist in dramatically different ranges depending on the oxidation state of iron. Single ligand effects are often detectable but they are smaller compared to those due to oxidation state changes.<sup>253-255</sup> This is not the case for low-spin complexes, where the isomer shift is less sensitive to oxidation state and ligand sphere.<sup>253-255</sup> However, within the above series of low-spin tricarbonyl complexes **VI-1**, **VI-6** and **VI-7**, the isomer shifts correlate well to the donating ability of the ancillary ligands. The difference from the high-spin complexes is that these differences are smaller, thus systematic sets of complexes are needed in order to document them for the newly discovered bio-organometallic chemistry. Thus Mossbauer spectroscopy is very sensitive to the subtle tuning of

electron density at iron within the same coordination sphere in low spin iron complexes. Only with such a systematic approach can useful conclusions be made regarding the enzyme and the evolutionarily perfected diverse ligation environment.

## CHAPTER VII

### THE [Fe]-HYDROGENASE MODELS: PENTA-COORDINATE IRON DICARBONYLS SUPPORTED BY A NONINNOCENT NS LIGAND

#### Introduction

The hydrogenase active sites and the chemistry they perform have inspired synthetic chemists in attempts to produce small molecule analogues<sup>7, 101, 256</sup> as potential base-metal catalysts for H<sub>2</sub> uptake, H<sub>2</sub> production, or, in the case of the mono-iron hydrogenase, [Fe]-H<sub>2</sub>ase, H<sub>2</sub> activation for a hydride reduction process.<sup>21, 64-67, 156</sup> Recent studies including X-ray diffraction<sup>64, 65</sup>, spectroscopies<sup>66, 156</sup> and DFT modeling<sup>69</sup> suggest the active site of the [Fe]-H<sub>2</sub>ase consists of a low-spin Fe<sup>II</sup>, two cis-oriented CO ligands, a cysteinyl-S, an organic pyridone bidentate ligand (N and acyl carbon), and a H<sub>2</sub>O (or an open site) trans to the acyl group as sketched in Figure VII. 1.

Synthetic analogues recently developed for the [Fe]-H<sub>2</sub>ase were described in Chapter I.<sup>156, 157, 158, 161, 160</sup> Inspired by the report of Liaw, et al.,<sup>160</sup> that pentacoordinate, 16-electron Fe<sup>II</sup> dicarbonyl complexes could be accessed in the presence of strong  $\pi$ -donor ligands such as the 2-amidothiophenolate dianion, we have developed a series of iron dicarbonyl complexes **VII-1**, **VII-2** and **VII-3**. Herein we report syntheses, electronic structures, and characterizations, including protonation-activated CO uptake

and  $^{12}\text{CO}/^{13}\text{CO}$  exchange, as influenced by the unique electronic makeup of the Fe(NS) unit.

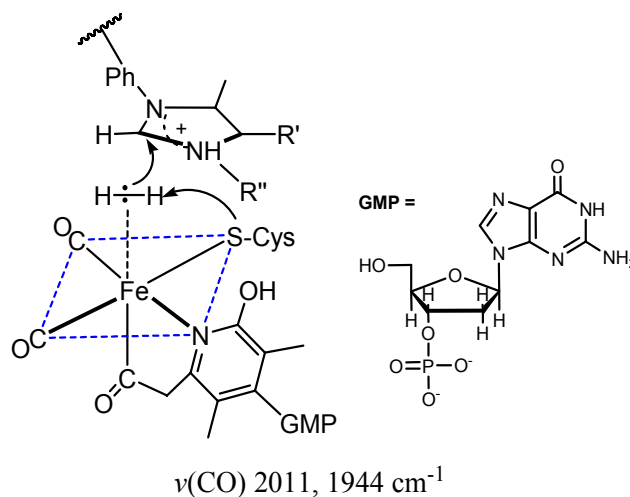


**Figure VII. 1** Formulation of the active site of the [Fe]-H<sub>2</sub>ase and a suggested mechanism of action, i.e., stereoselective hydride abstraction from  $(\eta^2\text{-H}_2)\text{Fe}^{\text{II}}$  by the  $\text{H}_4\text{MPT}^+$  substrate (see text).<sup>67</sup>

## Results and discussion

**Synthesis and characterization.** Scheme VII. 1 outlines a reliable procedure used to prepare  $(\text{NS})\text{Fe}(\text{CO})_2(\text{PR}_3)$  neutral complexes; the approach is somewhat different from that of Liaw, et al. for the cyano analogue.<sup>160</sup> The target complexes were isolated as dark brown crystalline solids in moderate to good yields. In the case of complex **VII-2**, the  $\text{Fe}^0$  complex,  $\text{trans-Fe}(\text{CO})_3(\text{PPh}_3)_2$ , was a substantial byproduct. Complexes **VII-1**, **VII-2** and **VII-3** are air stable and may be handled for short periods at room

temperature in the dark. However their thermal and light sensitivity requires that they be stored at low ( $-40^{\circ}\text{C}$ ) temperatures and always shielded from light. The light sensitivity displayed by **VII-2** and **VII-3** is also a characteristic of the [Fe]-H<sub>2</sub>ase enzyme.<sup>63</sup> Compounds **VII-1**, **VII-2**, and **VII-3** show sharp P-31 NMR resonances at 89.6, 97.4 and 173.6 ppm, respectively, confirming their diamagnetism. They are soluble in most organic solvents.

**Scheme VII. 1** A one pot synthesis of complexes **VII-1**, **VII-2** and **VII-3**.

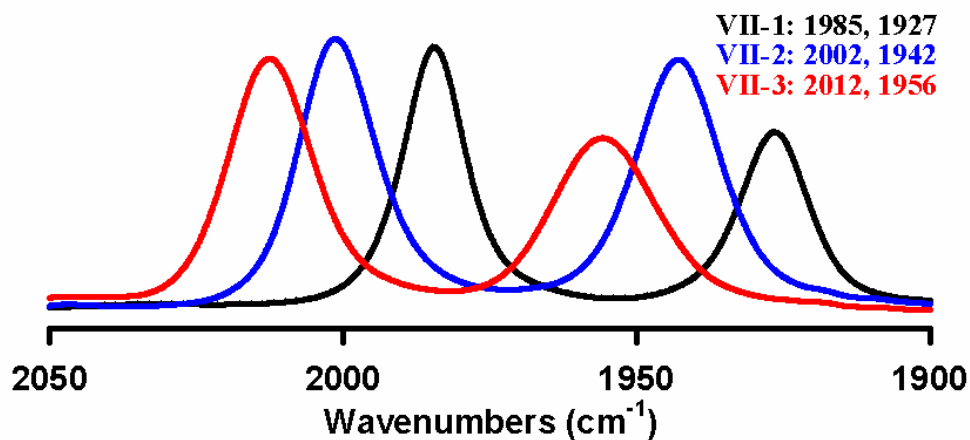
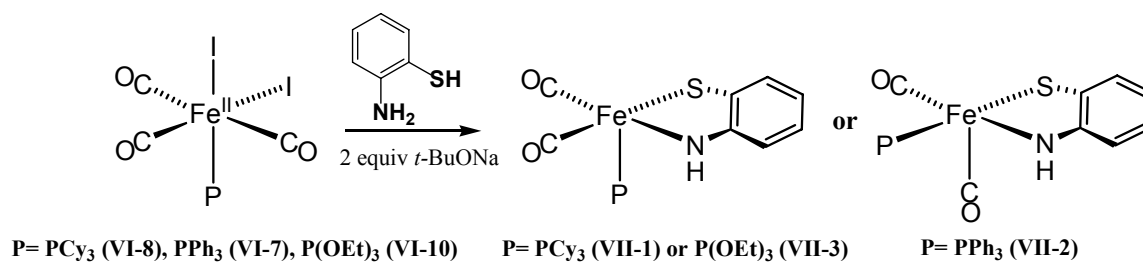


**Figure VII. 2** IR spectra ( $\nu(\text{CO})$  region) of complexes **VII-1**, **VII-2** and **VII-3** in  $\text{CH}_2\text{Cl}_2$ .

Figure VII. 2 displays the  $\nu(\text{CO})$  IR spectra for which the near equal intensity of the two bands suggests cis-dicarbonyls are at ca.  $90^\circ$  angles. The  $\nu(\text{CO})$  band positions follow that expected for the electron-donating abilities of the phosphine ligands; those of complexes **VII-2** and **VII-3** (measured in  $\text{CH}_2\text{Cl}_2$ ) are closest to those of the  $[\text{Fe}]\text{-H}_2\text{ase}$  active site (2011 and  $1944\text{ cm}^{-1}$  and likewise of equal intensities).<sup>156</sup>

Details of the x-ray diffraction studies of crystalline compounds **VII-1** and **VII-2** are fully described in the Chapter II. The ORTEP drawings of the molecular structures are presented in Figure VII. 3 so as to emphasize the square pyramidal structure of complex **VII-2** for which analysis according to Addison's  $\tau$  value<sup>257</sup> finds complex **VII-2** ( $\tau = 0.192$ , based on  $\alpha(\text{S1-Fe1-P1}) = 166.5^\circ$  and  $\beta(\text{N1-Fe1-C2}) = 155.0^\circ$ ) to be more nearly a square pyramid (similarly to Liaw's cyano complex),<sup>160</sup> while complex **VII-1** ( $\tau = 0.53$ , based on  $\alpha(\text{S1-Fe1-C2}) = 173.3^\circ$  and  $\beta(\text{C1-Fe1-N1}) = 141.0^\circ$ ) is a hybrid of square pyramidal and trigonal bipyramidal geometries.

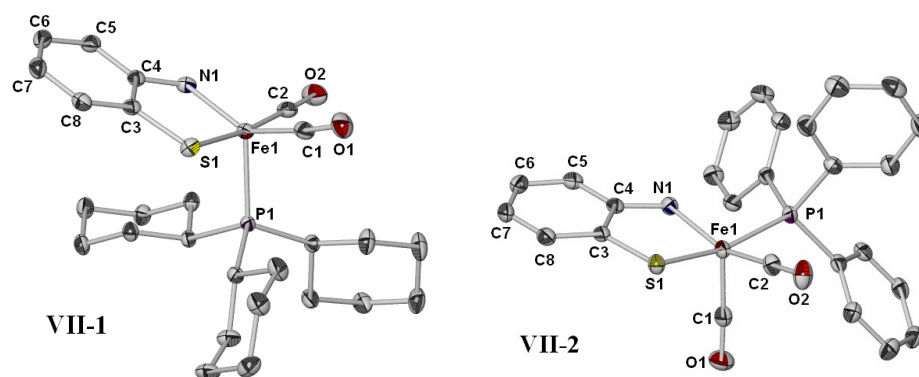


**Figure VII. 3** Molecular structures of complexes **VII-1** (top) and **VII-2** (bottom) as thermal ellipsoid representations, 50% probability, hydrogen atoms omitted. Selected metric parameters of **VII-1**: Fe1-C1, 1.764(2) Å; Fe1-P1, 2.248(4); Fe1-S1, 2.240(4); Fe1-N1, 1.855(1) ; C4-N1, 1.374(2); C3-S1, 1.724(2); C3-C4, 1.409(2); C3-C8 1.411(2); C4-C5, 1.420(2); C5-C6, 1.380(2); C6-C7, 1.401(2); C7-C8, 1.381(2); C1Fe1C2, 92.20(7)°; S1Fe1N1, 84.64(4)°; C1Fe1N1, 140.97(6)°; S1Fe1C2, 173.32(5)°; N1Fe1P1, 120.21(4)°; S1Fe1P1, 93.39(2)°; C2Fe1P1, 93.13(5)°. Selected metric parameters of **VII-2**: Fe1-C1, 1.751(3)Å; Fe1-P1, 2.241(1)Å; Fe1-S1, 2.219(2); Fe1-N1, 1.863(2); C4-N1, 1.362(3); C3-S1, 1.725(2); C3-C4, 1.410(3); C3-C8, 1.401(3); C4-C5, 1.409(3); C5-C6, 1.371(3); C6-C7, 1.397(4); C7-C8, 1.370(4); C1Fe1C2, 94.22(12)°; S1Fe1N1, 84.63(6); C2Fe1N1, 154.98(10); S1Fe1P1, 166.48(3); N1Fe1C1, 110.43(10) ; S1Fe1C, 96.86(9) ; P1Fe1C1, 96.62(9) °.

**Computational studies.** These high quality crystal structures encouraged examination of the extent of light atom metric differences that might signal interruption of the aromaticity in the aryl ring and the NS ligand's "non-innocence".<sup>258</sup> Density

functional theory (DFT) computations used in this analysis were performed with the B3LYP in a double zeta basis set (see Computational Details in the Experimental Section). The DFT optimized structures, which agree with the corresponding crystal structures (see for example, Figure VII. 4) of these complexes, were confirmed as energy minima by frequency calculations. In particular, the largest deviation of Fe-donor atom distances occur for Fe-P which is calculated to be 0.06 Å larger than the experimental value, an error that is typical for this functional and basis set. The calculations correctly predict the different geometric structures observed for complexes **VII-1** and **VII-2**. When the geometry was optimized for an isomer of **4** that corresponds to the geometry of **5**, a third isomer was predicted in which the PCy<sub>3</sub> ligand is trans to the sulfur (as in **5**) rather than trans to the open site. The third isomer of **4** is almost isoenergetic (< 0.4 kcal/mole different) with the lowest energy isomer. Thus, alternative ligand arrangements may be possible in related species.

An alternating pattern of C-C bonds in the aryl ring of the 2-amidothiophenolate ligand is found in both the calculated structures of complexes **VII-1** and **VII-2** and the experimental x-ray diffraction data. Furthermore, the pattern of C-C bond distances in the “aromatic” ring shows that the C5-C6 and C7-C8 are the two shortest bonds in both the calculated and experimental structures. The other bonds are all longer; in particular C6-C7, which in a truly aromatic ring would have the same bond distances as C5-C6/C7-C8, is 0.02 Å longer than the other bonds in both the calculated and experimental structures.



In order to examine the significance of this C-C bond pattern, DFT calculations were also performed for the free NS ligand in three redox levels: the -2 amidothiophenolate ( $\text{NS}^{2-}$ ), the -1  $\pi$ -radical or 2-iminothionebenzosemiquinoate ( $\text{NS}^{\cdot-}$ ), and the neutral 6-iminocyclohexa-2,4-dienethione forms ( $\text{NS}^0$ ).

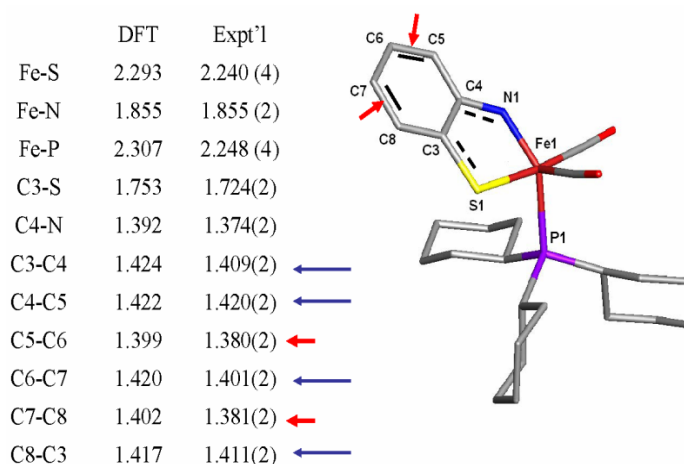
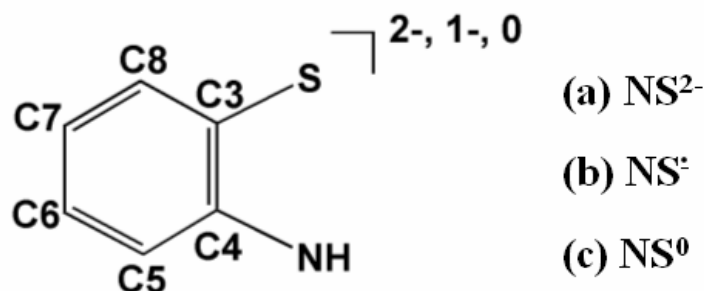


**Figure VII. 4** Comparison of DFT and experimental metric parameters for complex **VII-1**. Additional metric parameters are in the SI.

Table VII. 1 lists the calculated distances in the free ligand in these various possible forms and of the ligand within complexes **VII-1** and **VII-2**. Generally, a comparison of the bond distances could lead one to conclude that the ligand within the complexes is most like the -1  $\pi$ -radical. However, one should not take this too literally as a mixture of the dianionic amidothiolate and the neutral iminothione form could produce a similar pattern.

**Table VII. 1** Calculated distances (Å) within the NS ligand in three redox levels and within the ligand in complexes **VII-1** and **VII-2**.



	(a) NS <sup>2-</sup>	(b) NS <sup>1-</sup>	(c) NS <sup>0</sup>	NS in <b>VII-1</b>	NS in <b>VII-2</b>
C3-C4	1.493	1.482	1.512	1.424	1.425
C4-C5	1.462	1.462	1.480	1.422	1.424
C5-C6	1.414	1.388	1.364	1.399	1.398
C6-C7	1.409	1.428	1.456	1.420	1.421
C7-C8	1.433	1.398	1.373	1.402	1.401
C8-C3	1.416	1.435	1.457	1.417	1.418
C3-S	1.827	1.763	1.697	1.753	1.750
C4-N	1.369	1.355	1.314	1.392	1.388

According to Wieghardt, *et al.*, such a bonding pattern as described above, i.e., alternating short-long-short C-C distances in the C5-C6/C6-C7/C7-C8 positions, indicates that the 2-amidothiophenolate ligand is in a one-electron oxidized level, with substantial 2-iminothionebenzosemiquinonate,  $\pi$ -radical character.<sup>258</sup> If so, the formal charge of the Fe center of these complexes should be +1, and the observed diamagnetism would suggest that the unpaired electrons on ligand and metal are antiferromagnetically coupled. Alternatively, from the molecular orbital approach, the bonding pattern in Figure VII. 4 is also consistent with strong delocalization of a pair of electrons from a

formal  $\text{Fe}^0$  onto the LUMO of the neutral iminothione,  $o\text{-(S)(NH)C}_6\text{H}_4$ , ligand. The HOMO of complex **VII-1**, Figure VII. 5, shows substantial similarity to the LUMO of the neutral thione ligand, Figure VII. 6. Likewise, the SOMO of the free ligand in the radical anion form is also similar to the HOMO of the complex. If the better description is a  $-1$   $\pi$ -radical ligand antiferromagnetically coupled to a  $\text{Fe}^{\text{I}}$  radical, one would expect to find a low-lying triplet state and a spin-unrestricted singlet state with lower energy than the spin-restricted one.<sup>259</sup> In fact, calculations find a triplet state that is 14.2 kcal/mole above the singlet and attempts to find an unrestricted symmetry-breaking singlet state failed because the unrestricted singlet produced essentially the same energy and orbitals as from the restricted calculation.

**Table VII. 2** Relative energies (kcal / mol) of complex **VII-1** found by DFT calculations at different levels.

energy comparison (kcal / mol)	singlet	u-singlet	triplet
(A) B3LYP / LANL2DZ&D95	0.00	0.80	14.18
(B) B3LYP / LANL2DZ&cc-pVDZ	0.00	1.02	15.00
(C) TPSS / LANL2DZ&D95	0.00	0.33	21.69

Similar results obtained by calculations with the TPSS functional supported the conclusions from those with the B3LYP functional (See Table VII. 2 for details). Thus, all the results point to a description equivalent to a delocalized  $\text{Fe}^{\text{I}}(\text{NS}^{-1})$  electron distribution and not to an  $\text{Fe}^{\text{II}}(\text{NS}^{2-})$  assignment.

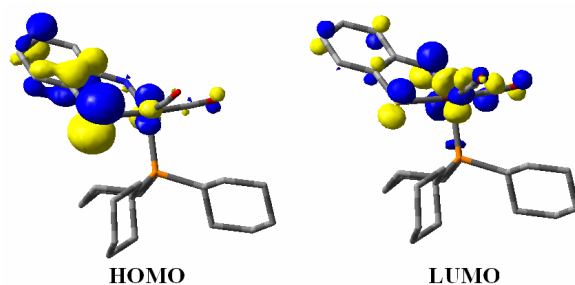


**Figure VII. 5** Frontier molecular orbitals (HOMO, left, and LUMO, right, isovalue = 0.05) of complex **VII-1** obtained from DFT calculations.

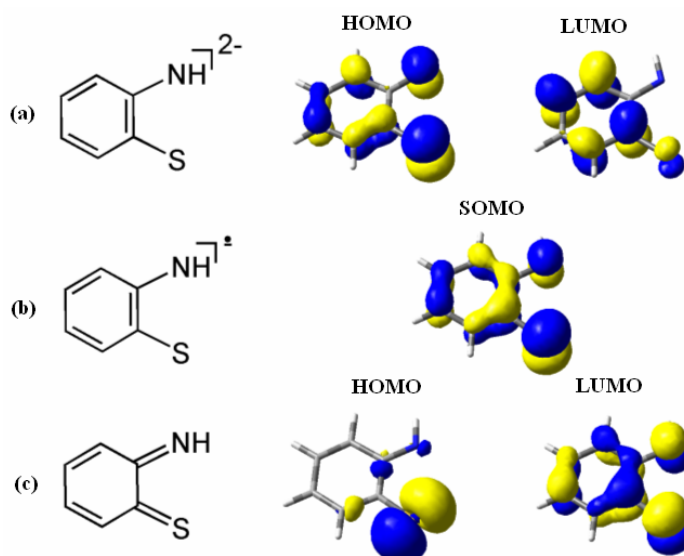


**Figure VII. 6** Frontier orbitals (isovalue = 0.05) of the free ligand forms: (a)  $NS^{2-}$ , 2-amidothiophenolate; (b)  $NS^{1-}$ , 2-iminothionebenzosemiquinonate; and (c)  $NS^0$ : 6-iminocyclohexa-2,4-dienethione.

**Mössbauer studies.** In order to experimentally probe the oxidation state of iron, Mössbauer spectroscopy was performed. Complexes **VII-1**, **VII-2**, and **VII-3** exhibited

sharp quadrupole doublets (see Figure VII. 7) in a magnetic field of 0.03 T, at 6 K. The values of the isomer shifts (Table VII. 3) are negative and are lower than those observed for low-spin Fe<sup>II</sup> sites, and in a range expected for low-spin Fe<sup>I</sup> and Fe<sup>0</sup> complexes. An Fe<sup>I</sup> center, particularly for complexes **VII-1** and **VII-2**, would be consistent with the DFT calculations which indicate substantial electron delocalization between the Fe and the NS ligand. Several low-spin ferrous mono- and dicarbonyl complexes (e.g., [( $\eta^5$ -C<sub>5</sub>Me<sub>5</sub>)Fe<sup>II</sup>(CO)<sub>2</sub>(CN)] and [( $\eta^5$ -C<sub>5</sub>H<sub>5</sub>)Fe<sup>II</sup>(CO)(CN)<sub>2</sub>]<sup>-</sup> in Table VII. 3), studied with Mössbauer spectroscopy as reference points for Fe<sup>II</sup> compounds, show small and positive isomer shifts.<sup>260</sup> The iron carbonyl pyridonate complex reported by Hu, et al., exhibits  $\delta = 0.10(2)$  mm/s and  $\Delta E_Q = 0.48(2)$  mm/s and was assigned as Fe<sup>II</sup>.<sup>158</sup> Notably, the definitive Fe<sup>II</sup> complex, *fac*-FeI<sub>2</sub>(CO)<sub>3</sub>PMe<sub>3</sub> (**7**),<sup>220</sup> exhibits very similar Mössbauer parameters to those of the [Fe]-H<sub>2</sub>ase, Table VII. 3. The isomer shift of the latter, +0.06 mm/s, is consistent with a low-spin Fe<sup>II</sup> assignment.<sup>66</sup> Thus, although the first coordination sphere donors of complexes **VII-1**, **VII-2** and **VII-3** would suggest close resemblance to the [Fe]-H<sub>2</sub>ase active site, their electronic properties as revealed by Mössbauer spectroscopy and DFT calculations described above clearly correspond to a state that is more reduced than Fe<sup>II</sup>.

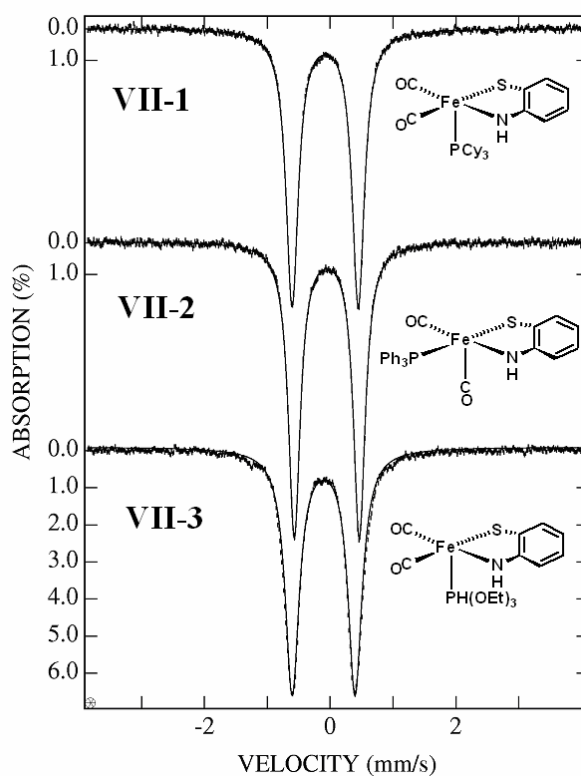


**Figure VII. 7** Mössbauer spectra of nujol suspensions of polycrystalline complexes **VII-1~VII-3** in an applied field of 300 Gauss. Two impurities accounting for ~15% of the total iron in this sample, were simulated and subtracted from the original spectrum of **VII-3**. The solid lines through the spectra are least-square fits, with the parameters listed in Table VII. 2, text.

**Table VII. 3** Selected Mössbauer parameters at 6 K, in an applied magnetic field of 0.03 T.

Complex	$\delta$ (mm/s)	$\Delta E_Q$ (mm/s)
<b>VII-1</b>	-0.078(6)	1.05(1)
<b>VII-2</b>	-0.053(6)	1.03(1)
<b>VII-3</b>	-0.0104(6)	1.00(1)
<b>VI-6</b> <sup>220</sup>	0.065	0.70
$[\text{Cp}^*\text{Fe}^{\text{II}}(\text{CO})_2(\text{CN})]^{260}$	0.076	1.97
$[\text{CpFe}^{\text{II}}(\text{CO})(\text{CN})_2]^{260}$	0.22	1.85
<b>HMD</b> <sup>66</sup>	0.06	0.65

**Chemical properties.** In contrast to the [Fe]-H<sub>2</sub>ase active site which readily binds extrinsic CO to yield a facial tricarbonyl species, only complex **VII-1** showed any tendency to (weakly and reversibly) take up CO at 1 bar. Neither did complex **VII-1** show reactivity with other Lewis bases such as PPh<sub>3</sub> and Et<sub>3</sub>N.

Nevertheless, in the presence of the strong acid, Et<sub>2</sub>O•HBF<sub>4</sub>, and CO (1 bar) solutions of complex **VII-1** in acetone (or THF) undergo a color change from dark brown to orange with concomitant  $\nu(\text{CO})$  spectral changes indicating that stoichiometric CO binding occurs (see Figure VII. 8). On deprotonation with Et<sub>3</sub>N, CO is lost and complex **VII-1** is quantitatively regenerated. While this CO adduct was not isolated, the  $\nu(\text{CO})$  bands at 2102(w) and 2046(vs) cm<sup>-1</sup> are, in position and pattern, nearly identical to that of the well-characterized *mer*-Fe(CO)<sub>3</sub>(I)<sub>2</sub>P(OEt)<sub>3</sub> complex (2102(w) and 2052(vs) cm<sup>-1</sup> in CH<sub>2</sub>Cl<sub>2</sub> solution.<sup>220</sup> N.B., the  $\nu(\text{CO})$  IR band patterns of the facial isomers within this series are distinctly different from that of the meridional.<sup>184</sup> Hence

we propose a tricarbonyl species,  $mer\text{-}[(\text{H-NS})\text{Fe}(\text{CO})_3(\text{PCy}_3)]^+$  or **VII-1(CO)-H<sup>+</sup>** with structure as shown in Figure VII. 8 is the product of this reaction.

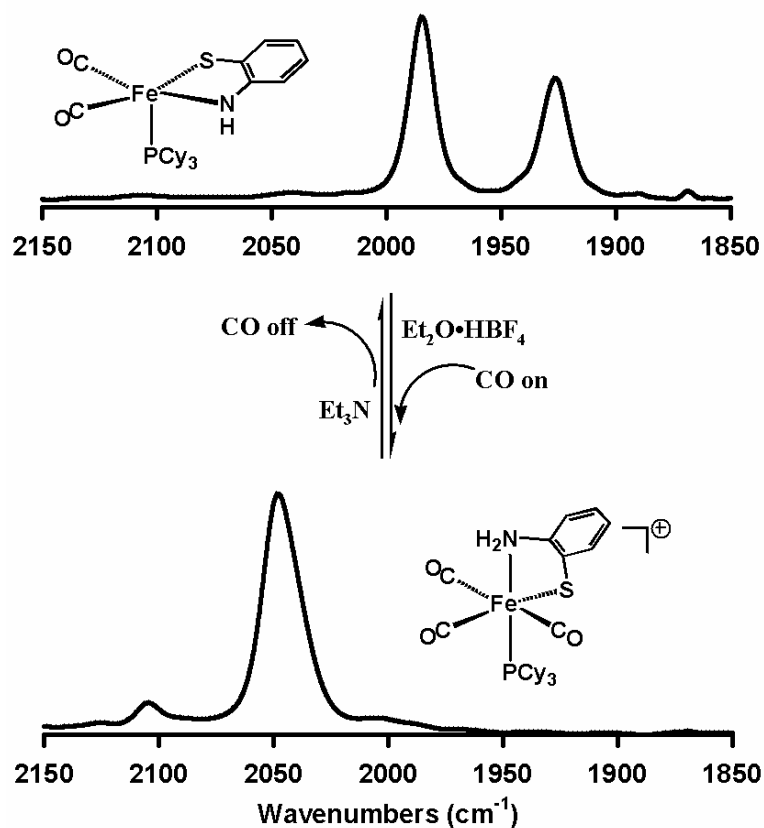


**Figure VII. 8** Protonation/deprotonation of complex **VII-1** in the presence of exogenous CO to yield **VII-1(CO)-H<sup>+</sup>**.

In a <sup>13</sup>CO atmosphere (1 bar), concomitant CO uptake and <sup>12</sup>CO/<sup>13</sup>CO exchange occurred within 15 minutes under the same conditions as above to form  $[mer\text{-}(\text{H-NS})\text{Fe}(\text{}^{13}\text{CO})_3\text{PCy}_3]^+$  (2056(w) and 2002(vs) cm<sup>-1</sup> in acetone solution, see SI, FS6). Subsequent treatment with Et<sub>3</sub>N reclaimed complex **VII-1** completely <sup>13</sup>CO labeled



(1982(s), and 1938(s)  $\text{cm}^{-1}$  in acetone solution) within 10 minutes. Notably this is a much more facile labeling process than by the direct  $^{12}\text{CO}/^{13}\text{CO}$  exchange of complex VII-1.

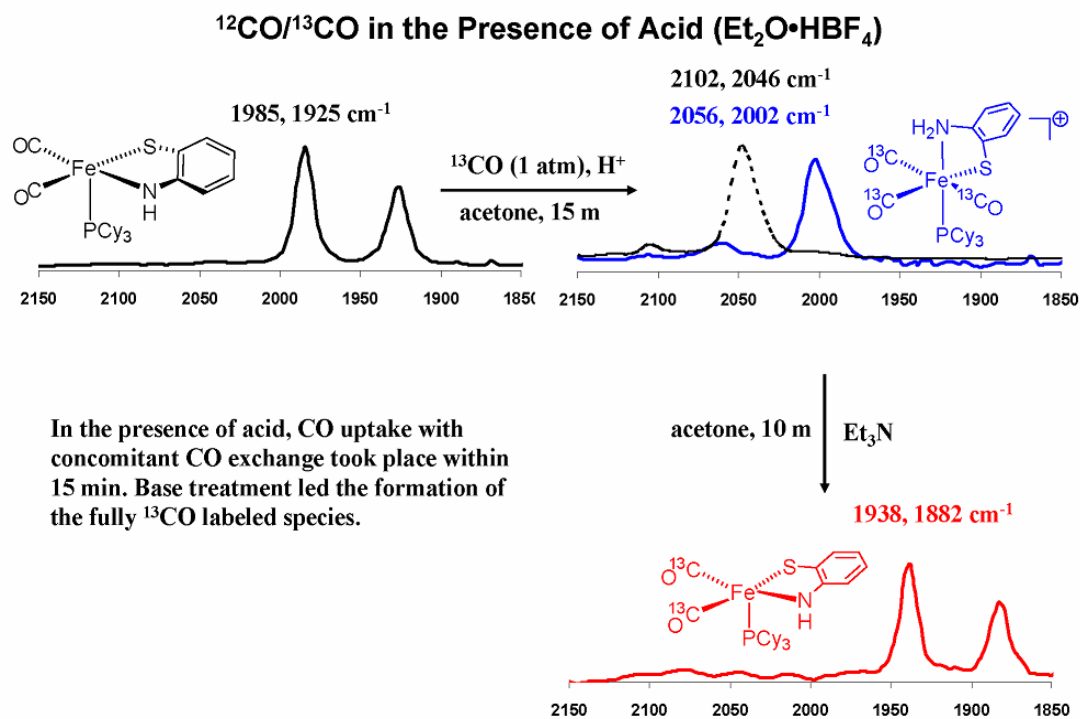


**Figure VII. 9**  $\nu(\text{CO})$  IR monitor of concomitant  $^{12}\text{CO}/^{13}\text{CO}$  exchange and  $^{13}\text{CO}$  uptake of complex VII-1 and the reclamation of complex VII-1 completely labeled with  $^{13}\text{CO}$ .

Such a change in electrophilicity of a formally  $d^6$  metal ion on ligand protonation is with precedent. Most recently, Heiden and Rauchfuss noted that N-protonation of a diamido ligand chelated to  $\text{Ir}^{\text{III}}$  “redirects  $\pi$ -bonding” resulting in several stable 18-electron base: $\text{Ir}^{\text{III}}$  adducts, including evidence for  $\eta\text{-}^2\text{H}_2$  binding and activation.<sup>261</sup>

From DFT computations here, the protonation of complex **VII-1** occurs at nitrogen of the NS ligand, and induces a dramatic change in the structure of the **VII-1-H<sup>+</sup>** complex relative to that of **VII-1**. Optimized structures of N-protonated isomers of the **VII-1-H<sup>+</sup>** complex, Figure VII. 10, find that as a result of the pyramidal nature of the amino nitrogen, the NS ligand binding is relaxed such that the  $[(\text{H-NS})\text{Fe}(\text{CO})_2(\text{PCy}_3)]^+$  or **VII-1-H<sup>+</sup>** complex is a more regular square pyramid with the C<sub>6</sub>H<sub>4</sub>SN plane of the ligand nearly coplanar with the FeNS(CO)<sub>2</sub> plane. That is, the structure is now that expected for a coordinatively unsaturated Fe<sup>II</sup>, d<sup>6</sup> complex and the bonding pattern (for example, isomer (b), see Table VII. 4) of the NS ligand in the calculated **VII-1-H<sup>+</sup>** indicates its aromaticity.<sup>258</sup> Frontier molecular orbitals of isomer b are also given in Figure VII. 10. Consistent with protonation-induced electrophilicity at iron, the LUMO of **VII-1-H<sup>+</sup>** shows considerable iron character (calculated to contribute 47.6% to the LUMO). Relative energy comparisons of the isomers are given in Figure VII. 10.

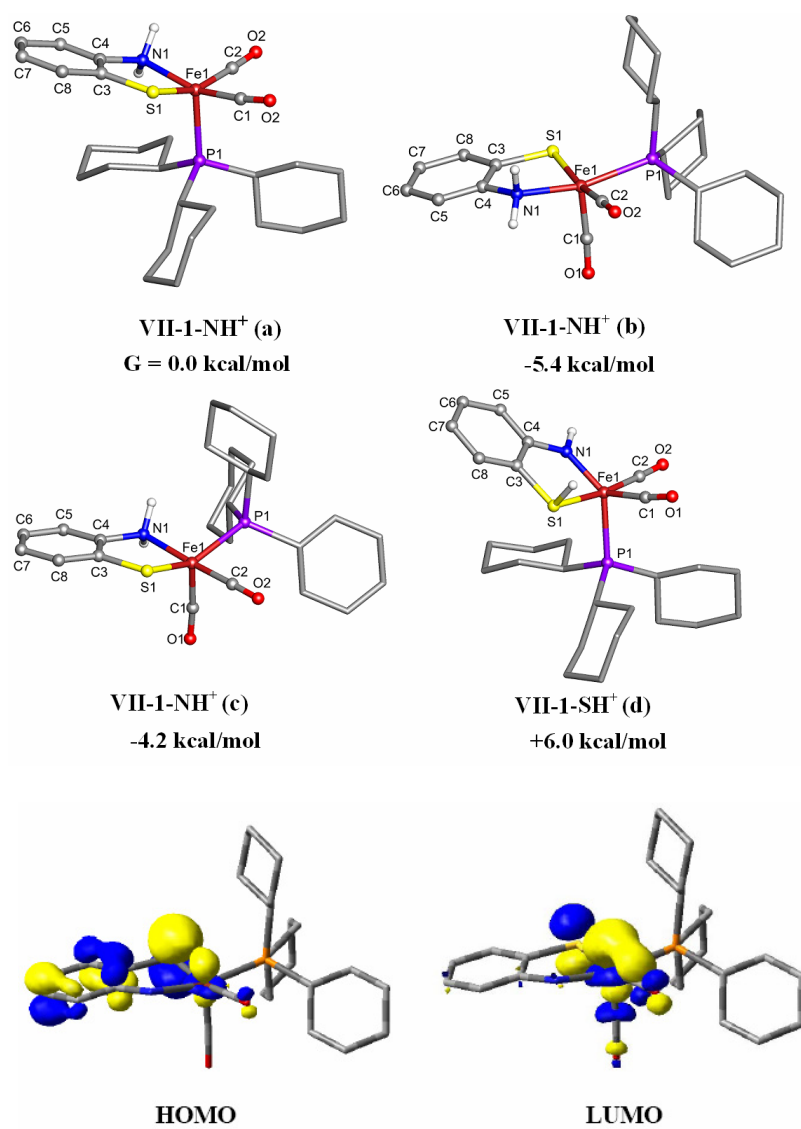


**Figure VII. 10** Top: DFT optimized structures and relative energy of the isomers of VII-1-NH<sup>+</sup> and a tautomer, VII-1-SH<sup>+</sup> (Isomer a of VII-1-NH<sup>+</sup> is defined as G = 0.0 kcal/mol). Bottom: Calculated frontier orbitals (isovalue = 0.05) of VII-1-NH<sup>+</sup> (b).

**Table VII. 4** Selected structural parameters of the lowest energy isomer of **VII-1-NH<sup>+</sup>**  
(b) found by DFT calculation.

bond (Å) and angle (°)	DFT
Fe1-C1	1.759
Fe1-P1	2.375
Fe1-S1	2.188
Fe1-N1	2.057
C4-N1	1.475
C3-S1	1.780
C3-C4	1.406
C3-C8	1.413
C4-C5	1.403
C5-C6	1.408
C6-C7	1.411
C7-C8	1.406
C1Fe1C2	96.47
S1Fe1N1	86.57
P1Fe1N1	165.38
S1Fe1C2	165.46
N1Fe1C1	97.16
S1Fe1C1	98.06
P1Fe1C1	96.47

According to the computational results, Figure VII. 10, the lowest energy isomeric form of **VII-1-H<sup>+</sup>** is N-protonated and one in which the endogeneous CO's are in the apical/basal positions (similarly to the approximate square pyramidal structure of complex **VII-2**); the open site is trans to a CO. Uptake of CO at that site would lead to the meridonal isomer, as opposed to the facial isomer. As we have yet to isolate and characterize complex **VII-1-H<sup>+</sup>** in the absence of CO we rely on computations to relate the neutral complex **VII-1** to **VII-1(CO)-H<sup>+</sup>**. Further calculations indicate that the

presumed kinetic product *mer*-[(H-NS)Fe(CO)<sub>3</sub>(PCy<sub>3</sub>)]<sup>+</sup> or **VII-1(CO)-H<sup>+</sup>** is also the thermodynamically favored isomer. That the facial isomer is observed in the CO-inhibited state of the [Fe]-H<sub>2</sub>ase likely reflects both the difference in first coordination sphere donors as well as the restrictions within the protein matrix.<sup>156</sup>

## Conclusions

The extreme  $\pi$ -delocalizing or non-innocent ligand as found in the 2-amidothiophenolate ligand described above provides access to a pentacoordinate iron dicarbonyl but renders the iron insufficiently electrophilic to perform as expected for a coordinatively unsaturated d<sup>6</sup>, Fe<sup>II</sup> center.<sup>81,82</sup> DFT computations suggest that as a result of extensive ligand/iron orbital overlap in the frontier molecular orbitals of the pentacoordinate complexes **VII-1** and **VII-2**, the iron is substantially less positive than Fe<sup>II</sup>, a conclusion that agrees with Mössbauer results. The flexibility of the  $\pi$ -character in this complex is illustrated by the effect of ligand-based protonation that decreases the electron density at iron, engendering CO uptake and the production of an 18-electron, hexacoordinate complex as expected for d<sup>6</sup>, Fe<sup>II</sup>, and as seen in the [Fe]-H<sub>2</sub>ase enzyme active site. Whether the synthetic analogue can be further tuned to bind and activate H<sub>2</sub> remains to be seen.

## CHAPTER VIII

### CONCLUSION

#### Mixed valence

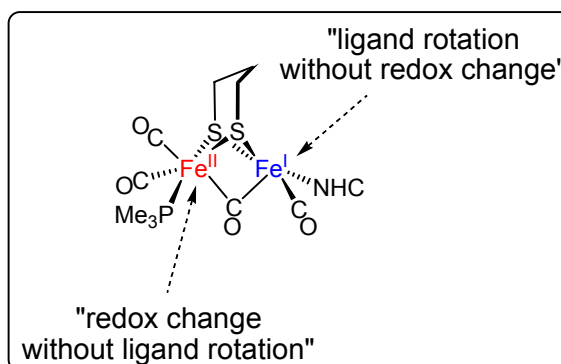
The experimental and theoretical investigation of the mixed-valent diiron  $\text{Fe}^{\text{I}}\text{Fe}^{\text{II}}$  complexes,  $(\mu\text{-pdt})(\mu\text{-CO})[\text{Fe}^{\text{II}}(\text{CO})_2\text{PMe}_3][\text{Fe}^{\text{I}}(\text{CO})(\text{NHC})]^+$  (**III-1<sub>ox</sub>**~ **III-3<sub>ox</sub>**),<sup>1-4</sup> as described in Chapter III and the parallel studies on similar mixed-valent  $\text{Fe}^{\text{II}}\text{Fe}^{\text{I}}$  complexes such as  $(\mu\text{-edt})[\text{Fe}(\text{CO})_2\text{PMe}_3][\text{Fe}(\text{CO})(\text{dppv})]^+\text{BF}_4$  and  $(\mu\text{-pdt})[\text{Fe}(\text{CO})_2\text{PMe}_3][\text{Fe}(\text{CO})(\text{dppv})]^+\text{BF}_4$  reported by Rauchfuss' group<sup>196, 200, 223</sup> opened a new regime in biomimetics of the  $[\text{FeFe}]-\text{H}_2\text{ase}$  by gaining insights into the structure and function of the  $\text{H}_{\text{ox}}$  state of the enzyme. These studies have also added novel fundamental aspects into organometallic chemistry of the class of dithiolate-bridged diiron carbonyls.

**The steric effects of NHC ligand.** The fact that the  $\text{Fe}^{\text{I}}\text{Fe}^{\text{I}}$  species (**III-1**~ **III-3**) showed similar structural and IR  $\nu(\text{CO})$  spectroscopic properties indicate that the NHC ligands, IMes, IMeM and IMe are similar in electronic properties in terms of the first coordination sphere. Distinct stability, CO reactivity, and spectroscopic (IR and EPR) features of the  $\text{Fe}^{\text{II}}\text{Fe}^{\text{I}}$  species, **III-1<sub>ox</sub>**~ **III-3<sub>ox</sub>** must be ascribed to the steric effect of the NHC ligand, more specifically, the steric bulk of the NHC N-substituents. A similar steric effect should be attributed to the dppv ligand in Rauchfuss' complexes. It was later found by both our group<sup>252</sup> and Rauchfuss' group<sup>223</sup> that even the bridging S-S linkage can engender similar steric influences as terminal ligands.

**The rotated structure.** According to DFT calculations, the most stable isomers of **III-2<sub>ox</sub>** and **III-3<sub>ox</sub>** have a similar structure as **III-1<sub>ox</sub>**, i.e. the rotated site is the NHC-Fe site (see Scheme VIII. 1). It is clear that the mixed-valent Fe<sup>II</sup>Fe<sup>I</sup> species possesses a rotated geometry in its ground state. However, the similar rotated form of the Fe<sup>I</sup>Fe<sup>I</sup> species as in (μ-pdt)[Fe<sup>I</sup>(CO)<sub>3</sub>]<sub>2</sub> exists as a transition (TS) state in the CO site exchange process of the Fe(CO)<sub>3</sub> unit.

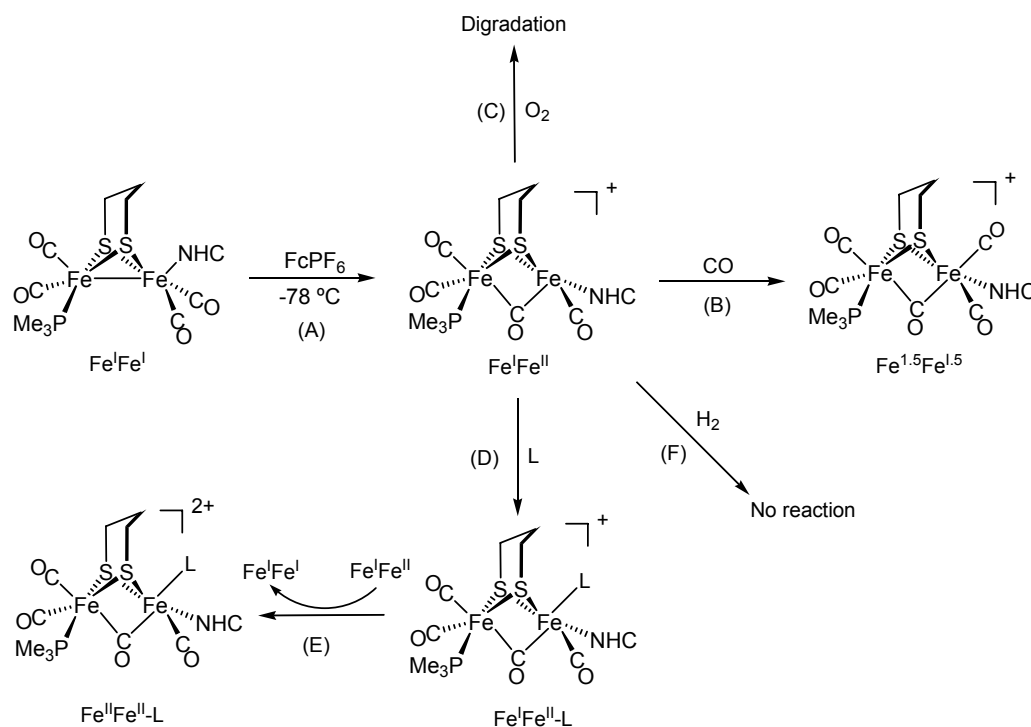
**The electronic structure.** One important fundamental issue concerned with these Fe<sup>II</sup>Fe<sup>I</sup> complexes is the assignment of the unpaired electron spin density. Consistent with the EPR studies of **III-1<sub>ox</sub>**~**III-3<sub>ox</sub>**, DFT calculations suggested that SOMO or unpaired electron spin is mainly characteristic of the rotated NHC-Fe while the other Fe site undergoes one electron oxidation without structural rearrangement. The localized electron density distribution of these complexes is sensitive to the binding of CO to the open site at the NHC-Fe<sup>I</sup>. The observed <sup>31</sup>P hyperfine coupling in the EPR spectrum of complex **III-2<sub>ox</sub>-CO** and DFT calculations suggested an assignment of Fe<sup>1.5</sup>Fe<sup>1.5</sup> to the CO adduct.

**Scheme VIII. 1**



The center point (see Scheme VIII. 1) derived from our studies<sup>190, 192-194</sup> and the studies from Rauchfuss' group<sup>196, 200, 223</sup> is: *One electron oxidation causes “geometry rearrangement without valence change” at the sterically encumbered Fe and “valence change without geometry rearrangement” at the other Fe.*

### Scheme VIII. 2



**Reactivities.** The overall reactivities of the mixed-valent complexes are summarized in Scheme VIII. 1. The mixed-valent complexes are extremely oxygen sensitive (Scheme VIII. 1, (C)) most likely due to their radical character. The mixed-valent complexes with IMeM and IMe ligands react with extrinsic CO (an  $\sigma$ -donor,  $\pi$ -acceptor ligand), to form



spectroscopically observable  $\text{Fe}^{\text{II}}\text{Fe}^{\text{I}}\text{-CO}$  adducts (Scheme VIII. 1, (B)). It can be rationalized that the acidity of the CO ligand can delocalize electron density of the diiron center and therefore stabilize the CO-adduct in comparison to an  $\sigma$ -donor (see below). We also suggested that the CO adduct is pivotal in the  $^{13}\text{C}$ O exchange process of these mixed-valent complexes.

If the incoming ligand is a pure  $\sigma$ -donor (L) such as  $\text{PMe}_3$ , the L-coordinated species,  $\text{Fe}^{\text{II}}\text{Fe}^{\text{I}}\text{-L}$  (or  $\text{Fe}^{\text{I}}\text{Fe}^{\text{II}}\text{-L}$ ), is relative electron rich and undergoes a disproportionation reaction with another molecule of the  $\text{Fe}^{\text{II}}\text{Fe}^{\text{I}}$  species to generate the original  $\text{Fe}^{\text{I}}\text{Fe}^{\text{I}}$  and a  $\text{Fe}^{\text{II}}\text{Fe}^{\text{II}}\text{-L}$  species<sup>262</sup> (Scheme VIII. 1, (D) and (E)). In terms of the effect of  $\sigma$ -donors, the weakly coordinating solvent,  $\text{CH}_2\text{Cl}_2$ , instead of coordinating solvents such acetone or acetonitrile, is critical to the one-electron oxidation of the  $\text{Fe}^{\text{I}}\text{Fe}^{\text{I}}$  precursors and the isolation of the mixed-valent complexes.

In our studies, both experimental and DFT results suggested the mixed-valent complexes are not active for  $\text{H}_2$  cleavage (Scheme VIII. 1, (F)). It was assumed that the unsaturated NHC- $\text{Fe}^{\text{I}}$  center is not sufficiently electrophilic enough for  $\text{H}_2$  uptake.

**Biological relevance.** It is clear that the synthetic, abiological ligands chosen by Rauchfuss and by us, yield the mixed-valent  $\text{Fe}^{\text{II}}\text{Fe}^{\text{I}}$  analogues with similar structure, spectroscopic (IR and EPR) features and CO reactivates as the  $[\text{FeFe}]\text{-H}_2\text{ase}$  active site in its  $\text{H}_{\text{ox}}$  state. The sterically encumbered NHC ligand, IMes, appears to fulfill some of the second coordination sphere requirements that exist in the enzyme in the form of  $^{234}\text{Pro}$  and  $^{417}\text{Phe}$  residues close to the open site of the distal iron.<sup>44, 45</sup> The above analysis of fundamental properties of the small analogues suggests the rotated mixed-

valent  $H_{ox}$  state adopted by the enzyme is intrinsic to the chemical nature of the diiron moiety as augmented by the protein matrix. Reactivities of these models with CO and  $H_2$  suggested that the biological role of  $H_{ox}$  state is probably a resting state. On the controversial oxidation state of  $H_{ox}$ , either  $Fe_p^{II}Fe_d^I$  or  $Fe_p^IFe_d^{II}$ , these mixed-valent models provide a sound precedent and support of the former assignment.

### Oxygenates and deoxygenation

In comparison to the DFT thermodynamically predicted metal oxygenation, sulfur oxygenation of  $Fe^I Fe^I$  complexes is most likely kinetically favored. Electronic modulation of  $(\mu\text{-pdt})[Fe(CO)_3]_2$  via CO/L exchange obviously influences the O-transfer from m-CPBA in that the  $Fe^I Fe^I$  diiron precursors,  $(\mu\text{-pdt})[Fe(CO)_3]_2$  (**IV-1**),  $(\mu\text{-pdt})[Fe(CO)_3][Fe(CO)_2PPh_3]$  (**IV-2**) and  $(\mu\text{-pdt}) [Fe(CO)_2PMe_3]_2$  (**IV-3**) showed diverse reactivity with the oxidant. In the case of **IV-3**, the isolation of the sulfur-oxygenate, **IV-3-O** and  $Fe(CO)_2(PMe_3)_2(m\text{-Cl-PhCOO}^-)_2$  (**IV-6**) suggested competitive sulfur vs metal oxygenation. Unlike the  $Fe^I Fe^I$  complexes, the HOMO-directed oxygenation of the  $Fe^{II} Fe^{II}$  hydride (**IV-5**) is exclusively on the sulfur. Deoxygenation of the sulfur oxygenates takes place in a proton-coupled electron transfer, PCET, process using neutral proton source ( $H_2O$ ) and appropriate electron source ( $Cp^*_2Co$  or electrochemical electrolysis).

Biological relevance of oxygenation and deoxygenation studies is described below. Using protein film electrodes, Armstrong, *et al.*,<sup>77</sup> explored the air sensitivity of  $[FeFe]\text{-}H_2ase$  from *D. desulfuricans* at the  $H_{ox}$  ( $Fe^{II} Fe^I$ ) and the anaerobically, electrochemically oxidized state (242 mV vs. SHE). As was found for the  $Fe^{II} Fe^I$  mixed-valent model

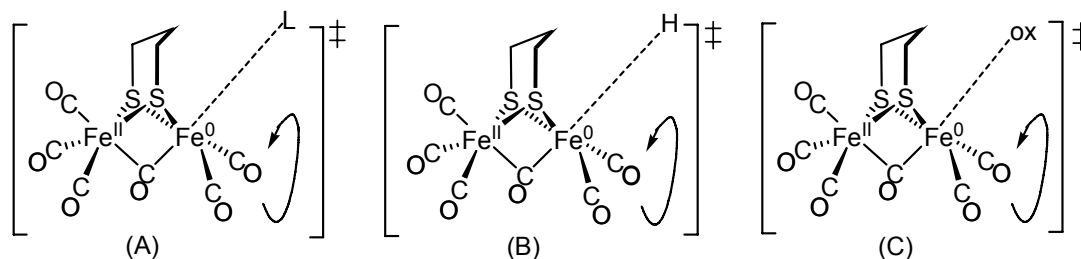
complexes,<sup>193, 196, 222, 223</sup> the  $H_{ox}$  state is highly air sensitive resulting in permanent irreversible damage/degradation, most likely due to the promotion of  $O_2$  reactivity by the radical character of  $Fe^{II}Fe^I$ . We have found that the  $Fe^{II}Fe^{II}$  complex **IV-5** is air stable and, when forced by strong O-donor agents, the O-atom uptake that occurs at sulfur can be removed under reducing conditions. Armstrong's anaerobically over-oxidized [FeFe]- $H_2$ ase enzyme,<sup>77</sup> presumed to be at the  $Fe^{II}Fe^{II}$  redox level, is said to be "protected" from permanent  $O_2$  damage in that activity can be partially regained when the potential is swept or stepped to more negative values. As the electronic structure of this anaerobically oxidized *Dd* [FeFe]- $H_2$ ase state is likely to be the same as the  $Fe^{II}Fe^{II}$  in complex **IV-5**, and as S-oxygenation is known for complex **IV-5**, we posit that a similar process may occur in the fully oxidized state of the enzyme and that reductive repair can remove S-based oxygenation as we have seen for complex **IV-5**.

A final point is that S-oxygenation of complex **IV-5** requires a peroxy species rather than molecular  $O_2$ . Whether such reactive oxygen species, such as  $OOH^-$  can be generated in the metalloprotein environment is to our knowledge unknown, and cannot be excluded as unreasonable. A simple point is clear: *if oxygen exposure of the enzyme active site results in sulfur oxygenation, then such oxygen "damage" can reductively removed.*

Unexpectedly, the sulfur modification of  $(\mu\text{-pdt})[Fe(CO)_3]_2$  significantly depresses the functionality of the  $Fe(CO)_3$  rotor by destabilizing the rotated TS state due to the poorer donating ability of the ptd ligand ( $-S(O)C_2H_6S-$ ).<sup>220, 263</sup> The observation is opposite to the effect of CO/L exchange and of the center carbon modification of the ptd

ligand on the intramolecular CO site exchange.<sup>162, 189, 221</sup> Whether the sulfur modification will produce the similar effect on the one-electron oxidation induced rotation remains to be seen. In terms of the active site in the reduced  $H_{\text{red}}$  ( $\text{Fe}^{\text{I}}\text{Fe}^{\text{I}}$ ) state, the geometry existing also as an "entatic state"<sup>186</sup> is likely enforced by the second coordination sphere, i.e. the protein matrix. The emerging synthetic challenge is how to maintain a rotated state at the  $\text{Fe}^{\text{I}}\text{Fe}^{\text{I}}$  level.

### Scheme VIII. 3



The comparative studies of the CO/L ( $L = \text{CN}^-$  or  $\text{PMe}_3$ ) exchange reaction of  $(\mu\text{-pdt})[\text{Fe}(\text{CO})_3]$  and  $(\mu\text{-pst})[\text{Fe}(\text{CO})_3]$ , revealed that the rotation of the  $\text{Fe}(\text{CO})_3$  unit plays an important role in ligand substitution. The overall reaction barrier of the CO/L exchange reaction is governed by the activation of the  $\text{Fe}(\text{CO})_3$  rotation and the nucleophilicity of L (see Figure IV. 1 and Scheme VIII. 3 (A)). The formation of a diiron terminal hydride species recently reported by Capon *et al.*<sup>136</sup> should also associate with the  $\text{Fe}(\text{CO})_3$  rotation on the Fe site undergoing protonation. As indicated by DFT calculations,<sup>92</sup> in the TS state of  $\text{Fe}^{\text{I}}\text{Fe}^{\text{I}}$  species, the major electron density is primarily localized at the rotated Fe and obviously the increased basicity of the Fe would be

amenable for or facilitate protonation at that site to form a terminal hydride (Scheme VIII. 3 (B)). In a similar consideration, it can be hypothesized that one electron oxidation described above may accompany the  $\text{Fe}(\text{CO})_2\text{L}$  rotation as well (Scheme VIII. 3 (C)). This makes the geometry and valence arrangement of the mixed-valent  $\text{Fe}^{\text{II}}\text{Fe}^{\text{I}}$  in Scheme VIII. 1 more logical; one Fe site rotation engenders the formation of a  $\text{Fe}^{\text{II}}\text{Fe}^0$  TS state and unrotated Fe site undergoes valence change from  $\text{Fe}^{\text{I}}$  to  $\text{Fe}^{\text{II}}$ ; concomitantly, the rotated Fe site resumes its original  $\text{Fe}^{\text{I}}$  oxidation state via one electron transfer. We suggested that such physical behavior has profound influences on the reactivities of  $\text{Fe}^{\text{I}}\text{Fe}^{\text{I}}$  diiron complexes.

### **Mono-Fe models**

The structural and spectroscopic (IR  $\nu(\text{CO})$  and Mössbauer) information of the series of mono- and di-substituted complexes,  $\text{FeI}_2(\text{CO})_x\text{L}_{4-x}$  engendered them to be basic models of the Hmd (or  $[\text{Fe}]\text{-H}_2\text{ase}$  active site). Structural derivation of  $\text{FeI}_2(\text{CO})_3\text{P}$  with bidentate NS ligands conveniently produces the advanced models **VI-11**, **VI-12**, and **VII-1~VII-3** featuring similar first coordination sphere as the  $[\text{Fe}]\text{-H}_2\text{ase}$  active site.

Despite the similar structure and spectroscopic (IR  $\nu(\text{CO})$ ) properties to those of the  $[\text{Fe}]\text{-H}_2\text{ase}$  active site, DFT calculations, Mössbauer data and CO reactivity of **VII-1~VII-3** indicated more reduced Fe ( $\text{Fe}^0$  or  $\text{Fe}^{\text{I}}$ ) in these complexes instead of an unsaturated  $d^6$ ,  $\text{Fe}^{\text{II}}$  as found in the active site. These properties of the pentacoordinate mono-Fe complexes are due to the “non-innocence” of the NS ligand, 2-amidophenanthiolate. Ligand based protonation of **VII-1** essentially reduces the electron

density of the Fe center to form a formally  $d^6$ ,  $Fe^{II}$  oxidation state and activate CO uptake. This example might provide a strategy to *in situ* make active unsaturated  $Fe^{II}$  dicarbonyl species that are normally unstable and difficult to prepare.

## REFERENCES

1. Pimentel, D.; Hurd, L. E.; Bellotti, A. C.; Forster, M. J.; Oka, I. N.; Sholes, O. D.; Whitman, R. J. *Science* **1973**, *182*, 443-449.
2. Lewis, N. S.; Nocera, D. G. *Proc. Natl. Acad. Sci. U. S. A.* **2006**, *103*, 15729-15735.
3. Service, R. F. *Science* **2004**, *305*, 958-961.
4. Larminie, J. *Fuel Cell Systems Explained*. SAE International: London, U.K., 2003.
5. Von Hofmann, A. W. *Introduction to Modern Chemistry: Experimental and Theoretic; Embodying Twelve Lectures Delivered in the Royal College of Chemistry*. Walton and Maberly: London, 1866, U.K.
6. Jones, A. K.; Sillery, E.; Albracht, S. P. J.; Armstrong, F. A. *Chem. Commun.* **2002**, 866-867.
7. Fontecilla-Camps, J. C.; Volbeda, A.; Cavazza, C.; Nicolet, Y. *Chem. Rev.* **2007**, *107*, 4273-4303.
8. Vignais, P. M.; Billoud, B. *Chem. Rev.* **2007**, *107*, 4206-4272.
9. Vignais, P. M.; Colbeau, A. *Curr Issues Mol Biol.* **2004**, *6*, 159-188.
10. Conrad, R. *Microbiol. Rev.* **1996**, *60*, 609-640.
11. Cammack, R.; Frey, M.; Robson, R.; Eds. *Hydrogen as a Fuel. Learning from Nature*. Taylor and Francis: London, U.K., 2001.

12. Lancaster, C. R. D.; Sauer, U. S.; Gross, R.; Haas, A. H.; Graf, J.; Schwalbe, H.; Mantele, W.; Simon, J.; Madej, M. G. *Proc. Natl. Acad. Sci. U. S. A.* **2005**, *102*, 18860-18865.
13. Appel, J.; Schulz, R. *J. Photochem. Photobiol. B: Biol.* **1998**, *47*, 1-11.
14. Deppenmeier, U. *J. Bioenerg. Biomembr.* **2004**, *36*, 55-64.
15. Ma, K. S.; Zhou, Z. H.; Adams, M. W. W. *FEMS Microbiol. Lett.* **1994**, *122*, 245-250.
16. Sawers, R. G. *Biochem. Soc. Trans.* **2005**, *33*, 42-46.
17. Adams, M. W. W. *Biochim. Biophys. Acta* **1990**, *1020*, 115-145.
18. Florin, L.; Tsokoglou, A.; Happe, T. *J. Biol. Chem.* **2001**, *276*, 6125-6132.
19. Melis, A.; Happe, T. *Photosynth. Res.* **2004**, *80*, 401-409.
20. Fournier, M.; Dermoun, Z.; Durand, M. C.; Dolla, A. *J. Biol. Chem.* **2004**, *279*, 1787-1793.
21. Shima, S.; Thauer, R. K. *Chem. Rec.* **2007**, *7*, 37-46.
22. De Lacey, A. L.; Fernandez, V. M.; Rousset, M.; Cammack, R. *Chem. Rev.* **2007**, *107*, 4304-4330.
23. Vincent, K. A.; Parkin, A.; Armstrong, F. A. *Chem. Rev.* **2007**, *107*, 4366-4413.
24. Lubitz, W.; Reijerse, E.; van Gestel, M. *Chem. Rev.* **2007**, *107*, 4331-4365.
25. Volbeda, A.; Charon, M. H.; Piras, C.; Hatchikian, E. C.; Frey, M.; Fontecillacamps, J. C. *Nature* **1995**, *373*, 580-587.
26. Higuchi, Y.; Yagi, T.; Yasuoka, N. *Structure* **1997**, *5*, 1671-1680.



27. Garcin, E.; Vernede, X.; Hatchikian, E. C.; Volbeda, A.; Frey, M.; Fontecilla-Camps, J. C. *Structure* **1999**, *7*, 557-566.
28. Matias, P. M.; Soares, C. M.; Saraiva, L. M.; Coelho, R.; Morais, J.; Le Gall, J.; Carrondo, M. A. *J. Biol. Inorg. Chem.* **2001**, *6*, 63-81.
29. Montet, Y.; Amara, P.; Volbeda, A.; Vernede, X.; Hatchikian, E. C.; Field, M. J.; Frey, M.; Fontecilla-Camps, J. C. *Nat. Struct. Biol.* **1997**, *4*, 523-526.
30. Volbeda, A.; Garcin, E.; Piras, C.; deLacey, A. L.; Fernandez, V. M.; Hatchikian, E. C.; Frey, M.; Fontecilla-Camps, J. C. *J. Am. Chem. Soc.* **1996**, *118*, 12989-12996.
31. Volbeda, A.; Martin, L.; Cavazza, C.; Matho, M.; Faber, B. W.; Roseboom, W.; Albracht, S. P. J.; Garcin, E.; Rousset, M.; Fontecilla-Camps, J. C. *J. Biol. Inorg. Chem.* **2005**, *10*, 239-249.
32. Albracht, S. P. J.; Graf, E. G.; Thauer, R. K. *FEBS Lett.* **1982**, *140*, 311-313.
33. Cammack, R.; Patil, D.; Aguirre, R.; Hatchikian, E. C. *FEBS Lett.* **1982**, *142*, 289-292.
34. Legall, J.; Ljungdahl, P. O.; Moura, I.; Peck, H. D.; Xavier, A. V.; Moura, J. J. G.; Teixeira, M.; Huynh, B. H.; Dervartanian, D. V. *Biochem. Biophys. Res. Commun.* **1982**, *106*, 610-616.
35. Bagley, K. A.; Vangarderen, C. J.; Chen, M.; Duin, E. C.; Albracht, S. P. J.; Woodruff, W. H. *Biochemistry* **1994**, *33*, 9229-9236.
36. Bagley, K. A.; Duin, E. C.; Roseboom, W.; Albracht, S. P. J.; Woodruff, W. H. *Biochemistry* **1995**, *34*, 5527-5535.

37. Happe, R. P.; Roseboom, W.; Pierik, A. J.; Albracht, S. P. J.; Bagley, K. A. *Nature* **1997**, *385*, 126-126.
38. Pierik, A. J.; Roseboom, W.; Happe, R. P.; Bagley, K. A.; Albracht, S. P. J. *J. Biol. Chem.* **1999**, *274*, 3331-3337.
39. deLacey, A. L.; Hatchikian, E. C.; Volbeda, A.; Frey, M.; FontecillaCamps, J. C.; Fernandez, V. M. *J. Am. Chem. Soc.* **1997**, *119*, 7181-7189.
40. Bleijlevens, B.; van Broekhuizen, F. A.; De Lacey, A. L.; Roseboom, W.; Fernandez, V. M.; Albracht, S. P. J. *J. Biol. Inorg. Chem.* **2004**, *9*, 743-752.
41. DeLacey, A. L.; Stadler, C.; Fernandez, V. M.; Hatchikian, E. C.; Fan, H. J.; Li, S. H.; Hall, M. B. *J. Biol. Inorg. Chem.* **2002**, *7*, 318-326.
42. Fichtner, C.; Laurich, C.; Bothe, E.; Lubitz, W. *Biochemistry* **2006**, *45*, 9706-9716.
43. Siegbahn, P. E. M.; Tye, J. W.; Hall, M. B. *Chem. Rev.* **2007**, *107*, 4414-4435.
44. Peters, J. W.; Lanzilotta, W. N.; Lemon, B. J.; Seefeldt, L. C. *Science* **1998**, *282*, 1853-1858.
45. Nicolet, Y.; Piras, C.; Legrand, P.; Hatchikian, C. E.; Fontecilla-Camps, J. C. *Structure* **1999**, *7*, 13-23.
46. Nicolet, Y.; de Lacey, A. L.; Vernede, X.; Fernandez, V. M.; Hatchikian, E. C.; Fontecilla-Camps, J. C. *J. Am. Chem. Soc.* **2001**, *123*, 1596-1601.
47. Fan, H. J.; Hall, M. B. *J. Am. Chem. Soc.* **2001**, *123*, 3828-3829.
48. Pandey, A. S.; Harris, T. V.; Giles, L. J.; Peters, J. W.; Szilagyi, R. K. *J. Am. Chem. Soc.* **2008**, *130*, 4533-4540.

49. Lemon, B. J.; Peters, J. W. *Biochemistry* **1999**, *38*, 12969-12973.
50. Huynh, B. H.; Czechowski, M. H.; Kruger, H. J.; Dervartanian, D. V.; Peck, H. D.; Legall, J. *Proceedings of the National Academy of Sciences of the United States of America-Biological Sciences* **1984**, *81*, 3728-3732.
51. Adams, M. W. W. *J. Biol. Chem.* **1987**, *262*, 15054-15061.
52. Patil, D. S.; Moura, J. J. G.; He, S. H.; Teixeira, M.; Prickril, B. C.; Dervartanian, D. V.; Peck, H. D.; Legall, J.; Huynh, B. H. *J. Biol. Chem.* **1988**, *263*, 18732-18738.
53. Hatchikian, E. C.; Forget, N.; Fernandez, V. M.; Williams, R.; Cammack, R. *Eur. J. Biochem.* **1992**, *209*, 357-365.
54. Pierik, A. J.; Hagen, W. R.; Redeker, J. S.; Wolbert, R. B. G.; Boersma, M.; Verhagen, M.; Grande, H. J.; Veeger, C.; Mutsaers, P. H. A.; Sands, R. H.; Dunham, W. R. *Eur. J. Biochem.* **1992**, *209*, 63-72.
55. Roseboom, W.; De Lacey, A. L.; Fernandez, V. M.; Hatchikian, E. C.; Albracht, S. P. J. *J. Biol. Inorg. Chem.* **2006**, *11*, 102-118.
56. VanderSpek, T. M.; Arendsen, A. F.; Happe, R. P.; Yun, S. Y.; Bagley, K. A.; Stufkens, D. J.; Hagen, W. R.; Albracht, S. P. J. *Eur. J. Biochem.* **1996**, *237*, 629-634.
57. Pierik, A. J.; Hulstein, M.; Hagen, W. R.; Albracht, S. P. J. *Eur. J. Biochem.* **1998**, *258*, 572-578.
58. De Lacey, A. L.; Stadler, C.; Cavazza, C.; Hatchikian, E. C.; Fernandez, V. M. *J. Am. Chem. Soc.* **2000**, *122*, 11232-11233.

59. Popescu, C. V.; Munck, E. *J. Am. Chem. Soc.* **1999**, *121*, 7877-7884.
60. Pereira, A. S.; Tavares, P.; Moura, I.; Moura, J. J. G.; Huynh, B. H. *J. Am. Chem. Soc.* **2001**, *123*, 2771-2782.
61. Korbas, M.; Vogt, S.; Meyer-Klaucke, W.; Bill, E.; Lyon, E. J.; Thauer, R. K.; Shima, S. *J. Biol. Chem.* **2006**, *281*, 30804-30813.
62. Shima, S.; Lyon, E. J.; Sordel-Klippert, M. S.; Kauss, M.; Kahnt, J.; Thauer, R. K.; Steinbach, K.; Xie, X. L.; Verdier, L.; Griesinger, C. *Angew. Chem. Int. Ed.* **2004**, *43*, 2547-2551.
63. Lyon, E. J.; Shima, S.; Buurman, G.; Chowdhuri, S.; Batschauer, A.; Steinbach, K.; Thauer, R. K. *Eur. J. Biochem.* **2004**, *271*, 195-204.
64. Shima, S.; Pilak, O.; Vogt, S.; Schick, M.; Stagni, M. S.; Meyer-Klaucke, W.; Warkentin, E.; Thauer, R. K.; Ermler, U. *Science* **2008**, *321*, 572-575.
65. Hiromoto, T.; Ataka, K.; Pilak, O.; Vogt, S.; Stagni, M. S.; Meyer-Klaucke, W.; Warkentin, E.; Thauer, R. K.; Shima, S.; Ermler, U. *FEBS Lett.* **2009**, *583*, 585-590.
66. Shima, S.; Lyon, E. J.; Thauer, R. K.; Mienert, B.; Bill, E. *J. Am. Chem. Soc.* **2005**, *127*, 10430-10435.
67. Vogt, S.; Lyon, E. J.; Shima, S.; Thauer, R. K. *J. Biol. Inorg. Chem.* **2008**, *13*, 97-106.
68. Vignais, P. M. *Coord. Chem. Rev.* **2005**, *249*, 1677-1690.
69. Yang, X.; Hall, M. B. *J. Am. Chem. Soc.* **2009**, *131*, 10901-10908.

70. Pershad, H. R.; Duff, J. L. C.; Heering, H. A.; Duin, E. C.; Albracht, S. P. J.; Armstrong, F. A. *Biochemistry* **1999**, *38*, 8992-8999.
71. Leger, C.; Jones, A. K.; Roseboom, W.; Albracht, S. P. J.; Armstrong, F. A. *Biochemistry* **2002**, *41*, 15736-15746.
72. Jones, A. K.; Lamle, S. E.; Pershad, H. R.; Vincent, K. A.; Albracht, S. P. J.; Armstrong, F. A. *J. Am. Chem. Soc.* **2003**, *125*, 8505-8514.
73. Lamle, S. E.; Vincent, K. A.; Halliwell, L. M.; Albracht, S. P. J.; Armstrong, F. A. *Dalton Trans.* **2003**, 4152-4157.
74. Lamle, S. E.; Albracht, S. P. J.; Armstrong, F. A. *J. Am. Chem. Soc.* **2004**, *126*, 14899-14909.
75. Armstrong, F. A.; Albracht, P. J. *Philos. Trans. R. Soc. A-Math. Phys. Eng. Sci.* **2005**, *363*, 937-954.
76. Vincent, K. A.; Cracknell, J. A.; Parkin, A.; Armstrong, F. A. *Dalton Trans.* **2005**, 3397-3403.
77. Vincent, K. A.; Parkin, A.; Lenz, O.; Albracht, S. P. J.; Fontecilla-Camps, J. C.; Cammack, R.; Friedrich, B.; Armstrong, F. A. *J. Am. Chem. Soc.* **2005**, *127*, 18179-18189.
78. Elgren, T. E.; Zadvorny, O. A.; Brecht, E.; Douglas, T.; Zorin, N. A.; Maroney, M. J.; Peters, J. W. *Nano Lett.* **2005**, *5*, 2085-2087.
79. Alonso-Lomillo, M. A.; Rudiger, O.; Maroto-Valiente, A.; Velez, M.; Rodriguez-Ramos, I.; Munoz, F. J.; Fernandez, V. M.; De Lacey, A. L. *Nano Lett.* **2007**, *7*, 1603-1608.

80. McDonald, T. J.; Svedruzic, D.; Kim, Y.-H.; Blackburn, J. L.; Zhang, S. B.; King, P. W.; Heben, M. J. *Nano Lett.* **2007**, *7*, 3528-3534.
81. Kubas, G. J. *Chem. Rev.* **2007**, *107*, 4152-4205.
82. Jessop, P. G.; Morris, R. H. *Coord. Chem. Rev.* **1992**, *121*, 155-284.
83. Bau, R.; Teller, R. G.; Kirtley, S. W.; Koetzle, T. F. *Acc. Chem. Res.* **1979**, *12*, 176-183.
84. Clapham, S. E.; Hadzovic, A.; Morris, R. H. *Coord. Chem. Rev.* **2004**, *248*, 2201-2237.
85. Besora, M.; Lledos, A.; Maseras, F. *Chem. Soc. Rev.* **2009**, *38*, 957-966.
86. Peruzzini, M.; Poli, R. *Recent Advances in Hydride Chemistry*. Elsevier: Amsterdam, 2001.
87. Davidson, E. R.; Kunze, K. L.; Machado, F. B. C.; Chakravorty, S. J. *Acc. Chem. Res.* **1993**, *26*, 628-635.
88. Darensbourg, D. J. *Adv. Organomet. Chem.* **1982**, *21*, 113-150.
89. Cable, J. W.; Sheline, R. K. *Chemical Reviews* **1956**, *56*, 1-26.
90. Aubke, F.; Wang, C. *Coord. Chem. Rev.* **1994**, *137*, 483-524.
91. Brunet, J. J.; Chauvin, R.; Diallo, O.; Kindela, F.; Leglaye, P.; Neibecker, D. *Coord. Chem. Rev.* **1998**, *178*, 331-351.
92. Georgakaki, I. P.; Thomson, L. M.; Lyon, E. J.; Hall, M. B.; Darensbourg, M. Y. *Coord. Chem. Rev.* **2003**, *238*, 255-266.
93. Bouwman, E.; Reedijk, J. *Coord. Chem. Rev.* **2005**, *249*, 1555-1581.

94. Bruschi, M.; Zampella, G.; Fantucci, P.; De Gioia, L. *Coord. Chem. Rev.* **2005**, *249*, 1620-1640.
95. Capon, J. F.; Gloaguen, F.; Schollhammer, P.; Talarmin, J. *Coord. Chem. Rev.* **2005**, *249*, 1664-1676.
96. Liu, X. M.; Ibrahim, S. K.; Tard, C.; Pickett, C. J. *Coord. Chem. Rev.* **2005**, *249*, 1641-1652.
97. Sun, L. C.; Akermark, B.; Ott, S. *Coord. Chem. Rev.* **2005**, *249*, 1653-1663.
98. Darensbourg, M. Y.; Lyon, E. J.; Smee, J. J. *Coord. Chem. Rev.* **2000**, *206*, 533-561.
99. Capon, J. F.; Gloaguen, F.; Petillon, F. Y.; Schollhammer, P.; Talarmin, J. *Coord. Chem. Rev.* **2009**, *253*, 1476-1494.
100. Marr, A. C.; Spencer, D. J. E.; Schroder, M. *Coord. Chem. Rev.* **2001**, *219*, 1055-1074.
101. Tard, C.; Pickett, C. J. *Chem. Rev.* **2009**, *109*, 2245-2274.
102. Halcrow, M. A.; Christou, G. *Chem. Rev.* **1994**, *94*, 2421-2481.
103. Rosenfield, S. G.; Armstrong, W. H.; Mascharak, P. K. *Inorg. Chem.* **1986**, *25*, 3014-3018.
104. Nguyen, D. H.; Hsu, H. F.; Millar, M.; Koch, S. A.; Achim, C.; Bominaar, E. L.; Munck, E. *J. Am. Chem. Soc.* **1996**, *118*, 8963-8964.
105. Hsu, H. F.; Koch, S. A.; Popescu, C. V.; Munck, E. *J. Am. Chem. Soc.* **1997**, *119*, 8371-8372.
106. Jiang, J. F.; Koch, S. A. *Chem. Commun.* **2002**, 1724-1725.

107. Lai, C. H.; Lee, W. Z.; Miller, M. L.; Reibenspies, J. H.; Darensbourg, D. J.; Darensbourg, M. Y. *J. Am. Chem. Soc.* **1998**, *120*, 10103-10114.
108. Liaw, W. F.; Lee, J. H.; Gau, H. B.; Chen, C. H.; Jung, S. J.; Hung, C. H.; Chen, W. Y.; Hu, C. H.; Lee, G. H. *J. Am. Chem. Soc.* **2002**, *124*, 1680-1688.
109. Chen, C. H.; Chang, Y. S.; Yang, C. Y.; Chen, T. N.; Lee, C. M.; Liaw, W. F. *Dalton Trans.* **2004**, 137-143.
110. Chiou, T. W.; Liaw, W. F. *C. R. Chimie* **2008**, *11*, 818-833.
111. Sellmann, D. L., F.; Geipel, F.; Heinemann, F. W.; Moll, M. *Angew. Chem. Int. Ed.* **2004**, *43*, 3141-3144.
112. Perra, A.; Davies, E. S.; Hyde, J. R.; Wang, Q.; McMaster, J.; Schroder, M. *Chem. Commun.* **2006**, 1103-1105.
113. Barton, B. E.; Whaley, C. M.; Rauchfuss, T. B.; Gray, D. L. *J. Am. Chem. Soc.* **2009**, *131*, 6942-6943.
114. Zhu, W. F.; Marr, A. C.; Wang, Q.; Neese, F.; Spencer, D. J. E.; Blake, A. J.; Cooke, P. A.; Wilson, C.; Schroder, M. *Proc. Natl. Acad. Sci. U. S. A.* **2005**, *102*, 18280-18285.
115. Li, Z. L.; Ohki, Y.; Tatsumi, K. *J. Am. Chem. Soc.* **2005**, *127*, 8950-8951.
116. Ogo, S.; Kabe, R.; Uehara, K.; Kure, B.; Nishimura, T.; Menon, S. C.; Harada, R.; Fukuzumi, S.; Higuchi, Y.; Ohhara, T.; Tamada, T.; Kuroki, R. *Science* **2007**, *316*, 585-587.
117. Sellmann, D.; Geipel, F.; Moll, M. *Angew. Chem. Int. Ed.* **2000**, *39*, 561-563.
118. DuBois, M. R.; DuBois, D. L. *C. R. Chimie* **2008**, *11*, 805-817.



119. DuBois, M. R.; DuBois, D. L. *Chem. Soc. Rev.* **2009**, *38*, 62-72.
120. Reihlen, H.; Gruhl, A.; Hessling, G. v. *Liebigs Ann. Chem.* **1929**, *472*, 268-287.
121. Hieber, W.; Spacu, P. *Z. Anorg. Allg. Chem.* **1937**, *233*, 353-364.
122. King, R. B. *J. Am. Chem. Soc.* **1962**, *84*, 2460-2460.
123. Apfel, U. P.; Halpin, Y.; Gorls, H.; Vos, J. G.; Schweizer, B.; Linti, G.; Weigand, W. G. *Chem. Biodiversity* **2007**, *4*, 2138-2148.
124. Seyferth, D.; Henderson, R. S.; Song, L. C. *Organometallics* **1982**, *1*, 125-133.
125. A number of routes, all involving reactions of iron carbonyls with organosulfur compounds (RSH, RSR, RSSR, and others) have served in the preparation of diverse  $(RS)_2Fe_2(CO)_6$  complexes. In "*Gmelin Handbuch der Anorganischen Chemie*", 8th ed. Fe, *Organoiron Compounds, Part C1 (Binuclear Compounds I)*; pp 74-122., Springer-Verlag, Berlin: **1979**.
126. Schmidt, M.; Contakes, S. M.; Rauchfuss, T. B. *J. Am. Chem. Soc.* **1999**, *121*, 9736-9737.
127. Lyon, E. J.; Georgakaki, I. P.; Reibenspies, J. H.; Darensbourg, M. Y. *Angew. Chem. Int. Ed.* **1999**, *38*, 3178-3180.
128. Le Cloirec, A.; Best, S. P.; Borg, S.; Davies, S. C.; Evans, D. J.; Hughes, D. L.; Pickett, C. J. *Chem. Commun.* **1999**, 2285-2286.
129. Lawrence, J. D.; Li, H. X.; Rauchfuss, T. B.; Benard, M.; Rohmer, M. M. *Angew. Chem. Int. Ed.* **2001**, *40*, 1768-1771.
130. Li, H.; Rauchfuss, T. B. *J. Am. Chem. Soc.* **2002**, *124*, 726-727.

131. Tard, C.; Liu, X. M.; Ibrahim, S. K.; Bruschi, M.; De Gioia, L.; Davies, S. C.; Yang, X.; Wang, L. S.; Sawers, G.; Pickett, C. J. *Nature* **2005**, *433*, 610-613.
132. Zhao, X.; Georgakaki, I. P.; Miller, M. L.; Yarbrough, J. C.; Darensbourg, M. Y. *J. Am. Chem. Soc.* **2001**, *123*, 9710-9711.
133. Boyke, C. A.; Rauchfuss, T. B.; Wilson, S. R.; Rohmer, M. M.; Benard, M. J. *Am. Chem. Soc.* **2004**, *126*, 15151-15160.
134. Lawrence, J. D.; Rauchfuss, T. B.; Wilson, S. R. *Inorg. Chem.* **2002**, *41*, 6193-6195.
135. van der Vlugt, J. I.; Rauchfuss, T. B.; Whaley, C. M.; Wilson, S. R. *J. Am. Chem. Soc.* **2005**, *127*, 16012-16013.
136. Ezzaher, S.; Capon, J. F.; Gloaguen, F.; Petillon, F. Y.; Schollhammer, P.; Talarmin, J. *Inorg. Chem.* **2007**, *46*, 3426-3428.
137. Wolpher, H.; Borgstrom, M.; Hammarstrom, L.; Bergquist, J.; Sundstrom, V.; Stenbjorn, S.; Sun, L. C.; Akermark, B. *Inorg. Chem. Commun.* **2003**, *6*, 989-991.
138. Ott, S.; Kritikos, M.; Akermark, B.; Sun, L. C. *Angew. Chem. Int. Ed.* **2003**, *42*, 3285-3288.
139. Li, X. Q.; Wang, M.; Zhang, S. P.; Pan, J. X.; Na, Y.; Liu, J. H.; Akermark, B.; Sun, L. C. *J. Phys. Chem. B* **2008**, *112*, 8198-8202.
140. Song, L. C.; Wang, L. X.; Tang, M. Y.; Li, C. G.; Song, H. B.; Hu, Q. M. *Organometallics* **2009**, *28*, 3834-3841.

141. Song, L. C.; Tang, M. Y.; Su, F. H.; Hu, Q. M. *Angew. Chem. Int. Ed.* **2006**, *45*, 1130-1133.
142. Zhao, X.; Georgakaki, I. P.; Miller, M. L.; Mejia-Rodriguez, R.; Chiang, C. Y.; Darensbourg, M. Y. *Inorg. Chem.* **2002**, *41*, 3917-3928.
143. Georgakaki, I. P.; Miller, M. L.; Darensbourg, M. Y. *Inorg. Chem.* **2003**, *42*, 2489-2494.
144. Zhao, X.; Chiang, C. Y.; Miller, M. L.; Rampersad, M. V.; Darensbourg, M. Y. *J. Am. Chem. Soc.* **2003**, *125*, 518-524.
145. Gloaguen, F.; Lawrence, J. D.; Rauchfuss, T. B. *J. Am. Chem. Soc.* **2001**, *123*, 9476-9477.
146. Chong, D. S.; Georgakaki, I. P.; Mejia-Rodriguez, R.; Samabria-Chinchilla, J.; Soriaga, M. P.; Darensbourg, M. Y. *Dalton Trans.* **2003**, 4158-4163.
147. Mejia-Rodriguez, R.; Chong, D.; Reibenspies, J. H.; Soriaga, M. P.; Darensbourg, M. Y. *J. Am. Chem. Soc.* **2004**, *126*, 12004-12014.
148. Liu, T. B.; Wang, M.; Shi, Z.; Cui, H. G.; Dong, W. B.; Chen, J. S.; Akermark, B.; Sun, L. C. *Chem. Eur. J.* **2004**, *10*, 4474-4479.
149. Ott, S.; Kritikos, M.; Akermark, B.; Sun, L. C.; Lomoth, R. *Angew. Chem.-Int. Edit. Engl.* **2004**, *43*, 1006-1009.
150. Vijaikanth, V.; Capon, J. F.; Gloaguen, F.; Schollhammer, P.; Talarmin, J. *Electrochem. Commun.* **2005**, *7*, 427-430.
151. Thomas, C. M.; Rudiger, O.; Liu, T.; Carson, C. E.; Hall, M. B.; Darensbourg, M. Y. *Organometallics* **2007**, *26*, 3976-3984.

152. Ibrahim, S. K.; Liu, X. M.; Tard, C.; Pickett, C. J. *Chem. Commun.* **2007**, 1535-1537.
153. Na, Y.; Wang, M.; Pan, J. X.; Zhang, P.; Akermark, B.; Sun, L. C. *Inorg. Chem.* **2008**, *47*, 2805-2810.
154. Olsen, M. T.; Barton, B. E.; Rauchfuss, T. B. *Inorg. Chem.* **2009**, *48* 7507-7509.
155. Felton, G. A. N.; Glass, R. S.; Lichtenberger, D. L.; Evans, D. H. *Inorg. Chem.* **2006**, *45*, 9181-9184.
156. Lyon, E. J.; Shima, S.; Boecher, R.; Thauer, R. K.; Grevels, F. W.; Bill, E.; Roseboom, W.; Albracht, S. P. J. *J. Am. Chem. Soc.* **2004**, *126*, 14239-14248.
157. Wang, X. F.; Li, Z. M.; Zeng, X. R.; Luo, Q. Y.; Evans, D. J.; Pickett, C. J.; Liu, X. M. *Chem. Commun.* **2008**, 3555-3557.
158. Obrist, B. V.; Chen, D. F.; Ahrens, A.; Schunemann, V.; Scopelliti, R.; Hu, X. L. *Inorg. Chem.* **2009**, *48*, 3514-3516.
159. Royer, A. M.; Rauchfuss, T. B.; Gray, D. L. *Organometallics* **2009**, *28*, 3618-3620.
160. Liaw, W.-F.; Lee, N.-H.; Chen, C.-H.; Lee, C.-M.; Lee, G.-H.; Peng, S.-M. *J. Am. Chem. Soc.* **2000**, *122*, 488-494.
161. Smith, J. M.; Lachicotte, R. J.; Holland, P. L. *Organometallics* **2002**, *21*, 4808-4814.
162. Lyon, E. J.; Georgakaki, I. P.; Reibenspies, J. H.; Darensbourg, M. Y. *J. Am. Chem. Soc.* **2001**, *123*, 3268-3278.

163. Li, P.; Wang, M.; He, C. J.; Li, G. H.; Liu, X. Y.; Chen, C. N.; Akermark, B.; Sun, L. C. *Eur. J. Inorg. Chem.* **2005**, 2506-2513.
164. Ping Li, M. W., Chengjiang He, Xiaoyang Liu, Kun Jin, Licheng Sun, *Eur. J. Inorg. Chem.* **2007**, 2007, 3718-3727.
165. Tye, J. W.; Lee, J.; Wang, H. W.; Mejia-Rodriguez, R.; Reibenspies, J. H.; Hall, M. B.; Darensbourg, M. Y. *Inorg. Chem.* **2005**, 44, 5550-5552.
166. Chu, Y.; Deng, H.; Cheng, J.-P. *J. Org. Chem.* **2007**, 72, 7790-7793.
167. Nieto-Oberhuber, C.; Lopez, S.; Echavarren, A. M. *J. Am. Chem. Soc.* **2005**, 127, 6178-6179.
168. Murray, R. W.; Jeyaraman, R. *J. Org. Chem.* **1985**, 50, 2847-2853.
169. Hieber, W.; Bader, G. *Ber. Dtsch. Chem. Ges.* **1928**, 61, 1717-1722.
170. Barbour, L. J. *J. Supramole. Chem.* **2001**, 1, 189-191.
171. Becke, A. D. *J. Chem. Phys.* **1993**, 98, 5648-5652.
172. Lee, C.; Yang, W.; Parr, R. G. *Phys. Rev. B: Condens. Matter* **1988**, 37, 785-788.
173. Frisch, M. J., Trucks, G. W., Schlegel, H. B., Scuseria, G. E., Robb, M. A., Cheeseman, J. R., Montgomery, J. A., Jr., Vreven, T., Kudin, K. N., Burant, J. C., Millam, J. M., Iyengar, S. S., Tomasi, J., Barone, V., Mennucci, B., Cossi, M., Scalmani, G., Rega, N., Petersson, G. A., Nakatsuji, H., Hada, M., Ehara, M., Toyota, K., Fukuda, R., Hasegawa, J., Ishida, M., Nakajima, T., Honda, Y., Kitao, O., Nakai, H., Klene, M., Li, X., Knox, J. E., Hratchian, H. P., Cross, J. B., Bakken, V., Adamo, C., Jaramillo, J., Gomperts, R., Stratmann, R. E., Yazyev, O., Austin, A. J., Cammi, R., Pomelli, C., Ochterski, J. W., Ayala, P. Y.,

- Morokuma, K., Voth, G. A., Salvador, P., Dannenberg, J. J., Zakrzewski, V. G., Dapprich, S., Daniels, A. D., Strain, M. C., Farkas, O., Malick, D. K., Rabuck, A. D., Raghavachari, K., Foresman, J. B., Ortiz, J. V., Cui, Q., Baboul, A. G., Clifford, S., Cioslowski, J., Stefanov, B. B., Liu, G., Liashenko, A., Piskorz, P., Komaromi, I., Martin, R. L., Fox, D. J., Keith, T., Al-Laham, M. A., Peng, C. Y., Nanayakkara, A., Challacombe, M., Gill, P. M. W., Johnson, B., Chen, W., Wong, M. W., Gonzalez, C., and Pople, J. A. *Gaussian 03, Revision B.04*; Gaussian, Inc.: Wallingford, CT, 2004.
174. Hay, P. J.; Wadt, W. R. *J. Chem. Phys.* **1985**, *82*, 270-283.
175. Wadt, W. R.; Hay, P. J. *J. Chem. Phys.* **1985**, *82*, 284-298.
176. Marc Couty, M. B. H. *J. Comput. Chem.* **1996**, *17*, 1359-1370.
177. Höllwarth, A.; Böhme, M.; Dapprich, S.; Ehlers, A. W.; Gobbi, A.; Jonas, V.; Köhler, K. F.; Stegmann, R.; Veldkamp, A.; Frenking, G. *Chem. Phys. Lett.* **1993**, *208*, 237-240.
178. Dunning, J. T. H. *J. Chem. Phys.* **1970**, *53*, 2823-2833.
179. Dunning, J. T. H.; Hay, P. J. *In Methods of Electronic Structure Theory*. Plenum Press: New York, 1977.
180. Dunning, J. T. H. *J. Chem. Phys.* **1989**, *90*, 1007-1023.
181. Capon, J. F.; El Hassnaoui, S.; Gloaguen, F.; Schollhammer, P.; Talarmin, J. *Organometallics* **2005**, *24*, 2020-2022.
182. Messelhäuser, J.; Gutensohn, K. U.; Lorenz, I.-P.; Hiller, W. *J. Organomet. Chem.* **1987**, *321*, 377-388.

183. Cohen, I. A.; Basolo, F. J. *Inorg. Nucl. Chem.* **1966**, *28*, 511-520.
184. Pankowski, M.; Bigorgne, M. *J. Organomet. Chem.* **1977**, *125*, 231-252.
185. Bellachioma, G.; Cardaci, G.; Macchioni, A.; Venturi, C.; Zuccaccia, C. *J. Organomet. Chem.* **2006**, *691*, 3881-3888.
186. Darensbourg, M. Y.; Lyon, E. J.; Zhao, X.; Georgakaki, I. P. *Proceedings of the National Academy of Sciences of the United States of America* **2003**, *100*, 3683-3688.
187. Razavet, M.; Borg, S. J.; George, S. J.; Best, S. P.; Fairhurst, S. A.; Pickett, C. J. *Chem. Commun.* **2002**, 700-701.
188. Borg, S. J.; Behrsing, T.; Best, S. P.; Razavet, M.; Liu, X. M.; Pickett, C. J. *J. Am. Chem. Soc.* **2004**, *126*, 16988-16999.
189. Tye, J. W.; Darensbourg, M. Y.; Hall, M. B. *Inorg. Chem.* **2006**, *45*, 1552-1559.
190. Liu, T.; Darensbourg, M. Y. *J. Am. Chem. Soc.* **2007**, *129*, 7008-7009.
191. Doyle, M. J.; Lappert, M. F. *J. Chem. Soc., Chem. Commun.* **1974**, 679-680.
192. Thomas, C. M.; Darensbourg, M. Y.; Hall, M. B. *J. Inorg. Biochem.* **2007**, *101*, 1752-1757.
193. Thomas, C. M.; Liu, T.; Hall, M. B.; Darensbourg, M. Y. *Inorg. Chem.* **2008**, *47*, 7009-7024.
194. Thomas, C. M.; Liu, T. B.; Hall, M. B.; Darensbourg, M. Y. *Chem. Commun.* **2008**, 1563-1565.

195. Capon, J. F.; Ezzaher, S.; Gloaguen, F.; Petillon, F. Y.; Schollhammer, P.; Talarmin, J.; Davin, T. J.; McGrady, J. E.; Muir, K. W. *New J. Chem.* **2007**, *31*, 2052-2064.
196. Justice, A. K.; Rauchfuss, T. B.; Wilson, S. R. *Angew. Chem.-Int. Edit. Engl.* **2007**, *46*, 6152-6154.
197. Justice, A. K.; Zampella, G.; De Gioia, L.; Rauchfuss, T. B.; van der Vlugt, J. I.; Wilson, S. R. *Inorg. Chem.* **2007**, *46*, 1655-1664.
198. Evans, D. F. *J. Chem. Soc.* **1959**, 2003-2005.
199. Albracht, S. P. J.; Roseboom, W.; Hatchikian, E. C. *J. Biol. Inorg. Chem.* **2006**, *11*, 88-101.
200. Justice, A. K.; Nilges, M. J.; Rauchfuss, T. B.; Wilson, S. R.; De Gioia, L.; Zampella, G. *J. Am. Chem. Soc.* **2008**, *130*, 5293-5301.
201. Tye, J. W.; Darensbourg, M. Y.; Hall, M. B. *J. Comput. Chem.* **2006**, *27*, 1454-1462.
202. Fürstner, A.; Alcarazo, M.; Krause, H.; Lehmann, C. W. *J. Am. Chem. Soc.* **2007**, *129*, 12676-12677.
203. Fiedler, A. T.; Brunold, T. C. *Inorg. Chem.* **2005**, *44*, 9322-9334.
204. Song, L. C. *Acc. Chem. Res.* **2005**, *38*, 21-28.
205. Capon, J. F.; Gloaguen, F.; Petillon, F. Y.; Schollhammer, P.; Talarmin, J. *Eur. J. Inorg. Chem.* **2008**, 4671-4681.
206. Gloaguen, F.; Rauchfuss, T. B. *Chem. Soc. Rev.* **2009**, *38*, 100-108.



207. Ghirardi, M. L.; King, P. W.; Posewitz, M. C.; Maness, P. C.; Fedorov, A.; Kim, K.; Cohen, J.; Schulten, K.; Seibert, M. *Biochem. Soc. Trans.* **2005**, *33*, 70-72.
208. Grapperhaus, C. A.; Darensbourg, M. Y. *Acc. Chem. Res.* **1998**, *31*, 451-459.
209. Farmer, P. J.; Verpeaux, J. N.; Amatore, C.; Darensbourg, M. Y.; Musie, G. J. *Am. Chem. Soc.* **1994**, *116*, 9355-9356.
210. Seefeldt, L. C.; Arp, D. J. *Biochemistry* **1989**, *28*, 1588-1596.
211. Vanderzwaan, J. W.; Coremans, J.; Bouwens, E. C. M.; Albracht, S. P. J. *Biochimica Et Biophysica Acta* **1990**, *1041*, 101-110.
212. Coremans, J.; Vanderzwaan, J. W.; Albracht, S. P. J. *Biochimica Et Biophysica Acta* **1992**, *1119*, 157-168.
213. Seyferth, D.; Womack, G. B.; Gallagher, M. K.; Cowie, M.; Hames, B. W.; Fackler, J. P.; Mazany, A. M. *Organometallics* **1987**, *6*, 283-294.
214. Dong, W. B.; Wang, M.; Liu, T. B.; Liu, X. Y.; Jin, K.; Sun, L. C. *J. Inorg. Biochem.* **2007**, *101*, 506-513.
215. Barton, B. E.; Rauchfuss, T. B. *Inorg. Chem.* **2008**, *47*, 2261-2263.
216. Tye, J. W.; Darensbourg, M. Y.; Hall, M. B. *Theochem-J. Mol. Struct.* **2006**, *771*, 123-128.
217. Kurtz, D. M. *Chem. Rev.* **1990**, *90*, 585-606.
218. Tshuva, E. Y.; Lippard, S. J. *Chem. Rev.* **2004**, *104*, 987-1012.
219. Windhager, J.; Seidel, R. A.; Apfel, U. P.; Goerls, H.; Linti, G.; Weigand, W. *Chem. Biodiversity* **2008**, *5*, 2023-2041.

220. Liu, T.; Li, B.; Singleton, M. L.; Hall, M. B.; Darensbourg, M. Y. *J. Am. Chem. Soc.* **2009**, *131*, 8296-8307.
221. Singleton, M. L.; Jenkins, R. M.; Klemashevich, C. L.; Darensbourg, M. Y. *C. R. Chimie* **2008**, *11*, 861-874.
222. Liu, T.; Darensbourg, M. Y. *J. Am. Chem. Soc.* **2007**, *129*, 7008-7009.
223. Justice, A. K.; De Gioia, L.; Nilges, M. J.; Rauchfuss, T. B.; Wilson, S. R.; Zampella, G. *Inorg. Chem.* **2008**, *47*, 7405-7414.
224. Holm, R. H.; Donahue, J. P. *Polyhedron* **1993**, *12*, 571-589.
225. Gao, W. M.; Ekstrom, J.; Liu, J. H.; Chen, C. N.; Eriksson, L.; Weng, L. H.; Akermark, B.; Sun, L. H. *Inorg. Chem.* **2007**, *46*, 1981-1991.
226. Seyferth, D.; Womack, G. G.; Song, L. C. *Organometallics* **1983**, *2*, 776-779.
227. Seyferth, D.; Henderson, R. S. *J. Organomet. Chem.* **1980**, *204*, 333-43.
228. Seyferth, D.; Brewer, K. S.; Wood, T. G.; Cowie, M.; Hilts, R. W. *Organometallics* **1992**, *11*, 2570-2579.
229. Gao, S.; Fan, J. L.; Sun, S.; Peng, X. J.; Zhao, X.; Hou, J. *Dalton Trans.* **2008**, 2128-2135.
230. Georgakaki, I. P.; Thomson, L. M.; Lyon, E. J.; Hall, M. B.; Darensbourg, M. Y. *Coord. Chem. Rev.* **2003**, 238-239, 255-266.
231. Tye, J. W.; Darensbourg, M. Y.; Hall, M. B. *Inorg. Chem.* **2006**, *45*, 1552-1559.
232. Lyon, E. J.; Georgakaki, I. P.; Reibenspies, J. H.; Darensbourg, M. Y. *J. Am. Chem. Soc.* **2001**, *123*, 3268-3278.
233. Li, H.; Rauchfuss, T. B. *J. Am. Chem. Soc.* **2002**, *124*, 726-727.

234. Wang, Z.; Liu, J.-H.; He, C.-J.; Jiang, S.; Akermark, B.; Sun, L.-C. *J. Organomet. Chem.* **2007**, *692*, 5501-5507.
235. Jochen Windhager, M. R., Silvio Bräutigam, Helmar Görls, Wolfgang Weigand, *Eur. J. Inorg. Chem.* **2007**, *2007*, 2748-2760.
236. Song, L.-C.; Yang, Z.-Y.; Bian, H.-Z.; Liu, Y.; Wang, H.-T.; Liu, X.-F.; Hu, Q.-M. *Organometallics* **2005**, *24*, 6126-6135.
237. Song, L.-C.; Yang, Z.-Y.; Hua, Y.-J.; Wang, H.-T.; Liu, Y.; Hu, Q.-M. *Organometallics* **2007**, *26*, 2106-2110.
238. Windhager, J.; Rudolph, M.; Brautigam, S.; Gorls, H.; Weigand, W. *Eur. J. Inorg. Chem.* **2007**, 2748-2760.
239. Harb, M. K.; Nicksch, T.; Windhager, J.; Görls, H.; Holze, R.; Lockett, L. T.; Okumura, N.; Evans, D. H.; Glass, R. S.; Lichtenberger, D. L.; El-khateeb, M.; Weigand, W. *Organometallics* **2009**, *28*, 1039-1048.
240. Lyon, E. J.; Georgakaki, I. P.; Reibenspies, J. H.; Darensbourg, M. Y. *Angew. Chem. Int. Ed.* **1999**, *38*, 3178-3180.
241. Schmidt, M.; Contakes, S. M.; Rauchfuss, T. B. *J. Am. Chem. Soc.* **1999**, *121*, 9736-9737.
242. Gloaguen, F.; Lawrence, J. D.; Schmidt, M.; Wilson, S. R.; Rauchfuss, T. B. *J. Am. Chem. Soc.* **2001**, *123*, 12518-12527.
243. Ellgen, P. C.; Gerlach, J. N. *Inorg. Chem.* **1973**, *12*, 2526-2532.
244. Singleton, M. L.; Bhuvanesh, N.; Reibenspies, J. H.; Darensbourg, M. Y. *Angew. Chem. Int. Ed.* **2008**, *47*, 9492-9495.

245. Justice, A. K.; Rauchfuss, T. B.; Wilson, S. R. *Angew. Chem. Int. Ed.* **2007**, *46*, 6152-6154.
246. Herrmann, W. A. *Angew. Chem., Int. Ed.* **2002**, *41*, 1290-1309.
247. Haukka, M.; Kiviaho, J.; Ahlgren, M.; Pakkanen, T. A. *Organometallics* **2002**, *14*, 825-833.
248. Bancroft, G. M.; Libbey, E. T. *Dalton Trans.* **1973**, 2103-2111.
249. Parish, R. V. *The Organic Chemistry of Iron, Vol. Mössbauer Spectroscopy*. Springer-Verlag New York, LLC: New York, 1996.
250. Guo, Y. S.; Wang, H. X.; Xiao, Y. M.; Vogt, S.; Thauer, R. K.; Shima, S.; Volkers, P. I.; Rauchfuss, T. B.; Pelmenchikov, V.; Case, D. A.; Alp, E. E.; Sturhahn, W.; Yoda, Y.; Cramer, S. P. *Inorg. Chem.* **2008**, *47*, 3969-3977.
251. Royer, A. M.; Rauchfuss, T. B.; Wilson, S. R. *Inorg. Chem.* **2008**, *47*, 395-397.
252. Singleton, M. L.; Bhuvanesh, N.; Reibenspies, J. H.; Darensbourg, M. Y. *Angew. Chem. Int. Ed.* **2008**, *47*, 9492-9495.
253. Christner, J. A.; Münck, E.; Janick, P. A.; Siegel, W. M. *J. Biol. Chem.* **1981**, *256*, 2098-2102.
254. Christner, J. A.; Muenck, E.; Kent, T. A.; Janick, P. A.; Salerno, J. C.; Siegel, L. M. *J. Am. Chem. Soc.* **1984**, *106*, 6786-6794.
255. Gutlich, P. L., R.; Trautwein, A. *Mossbauer Spectroscopy and Transition Metal Chemistry*. Springer Verlag: Berlin, 1979.
256. Lubitz, W.; Reijerse, E. J.; Messinger, J. *Energy Environ. Sci.* **2008**, *1*, 15-31.

257. Addison, A. W. R., T. Nageswara; Reedijk, Jan; Rijn, Jacobus van; Verschoor, Gerrit C. *J. Chem. Soc., Dalton Trans.* **1984**, 1349 -1356.
258. Herebian, D.; Bothe, E.; Bill, E.; Weyhermuller, T.; Wieghardt, K. *J. Am. Chem. Soc.* **2001**, *123*, 10012-10023.
259. Bachler, V.; Olbrich, G.; Neese, F.; Wieghardt, K. *Inorg. Chem.* **2002**, *41*, 4179-4193.
260. Popescu, C. V. *Ph.D. Thesis, Department of Chemistry, Carnegie Mellon University* **2000**.
261. Heiden, Z. M.; Gorecki, B. J.; Rauchfuss, T. B. *Organometallics* **2008**, *27*, 1542-1549.
262. Boyke, C. A.; van der Vlugt, J. I.; Rauchfuss, T. B.; Wilson, S. R.; Zampella, G.; De Gioia, L. *J. Am. Chem. Soc.* **2005**, *127*, 11010-11018.
263. Li, B.; Liu, T.; Singleton, M. L.; Darensbourg, M. Y. *Inorg. Chem.* **2009**, *48*, 8393-8403.

## VITA

Tianbiao Liu was born in Enshi, China. He received his Bachelor of Science degree in biochemistry from Hubei University of Technology at Wuhan, China in 2000 and his Master of Science degree in applied chemistry from Dalian University of Technology at Dalian, China in 2004. He entered Texas A&M University in May 2005 and worked under the direction of Professor M. Y. Darensbourg for his doctoral study. Tianbiao received his Doctor of Philosophy degree in chemistry in December 2009.

Mr. Liu may be reached through the address at Department of Chemistry, Texas A&M University, 3255 TAMU, College Station, 77843, Texas. His email is liu\_tianb@yahoo.com.

### Selected publications

- (1) Liu, T.; Li, B.; Popescu, C. V.; Bilko, A.; Pérez, L. M.; Hall, M. B.; Darensbourg, M. Y., "Analysis of a Pentacoordinate Iron Dicarbonyl as Synthetic Analogue of the Hmd or [Fe]-Hydrogenase Active Site" **2009**, submitted to *Chem. Eur. J.*
- (2) Liu, T.; Li, B.; Singleton, M.; Hall, M. B.; Darensbourg, M. Y., "Sulfur Oxygenation of [FeFe] Hydrogenase Biomimetics: Possible Connection to Air Sensitivity of the Enzyme" *JACS*, **2009**, *131*, 8296-8307.
- (3) Thomas, C. M.; Liu, T. (equal contribution); Hall, M. B.; Darensbourg, M. Y., "Series of Mixed Valent Fe(II)Fe(I) Complexes That Model the H<sub>ox</sub> State of [FeFe] Hydrogenase: Redox Properties, Density-Functional Theory Investigation, and Reactivities with Extrinsic CO" *Inorg. Chem.* **2008**, *47*, 7009-7024.
- (4) Liu, T.; Darensbourg, M. Y., "A Mixed Valent, Fe(II)Fe(I), Diiron Complex Reproduces the Unique Rotated State of the [FeFe]Hydrogenase Active Site", *JACS*, **2007**, *129*; 7008-7009.